

**A STUDY OF THE RECORD OF
ANCIENT SEDIMENTARY ROCKS ON
MARS USING MER, HIRISE AND CRISM
IMAGES**

Thesis by

Joannah M. Metz

In Partial Fulfillment of the Requirements for the

degree of

Doctor of Philosophy

CALIFORNIA INSTITUTE OF TECHNOLOGY

Pasadena, California

2010

(Defended March 30, 2010)

© 2010

Joannah M. Metz

All Rights Reserved

ACKNOWLEDGEMENTS

I am grateful to many people for their support over the last five years at Caltech. First and foremost, I would like to thank my advisor, John Grotzinger, whose encouragement gave me the confidence to turn from a student into a scientist. John has been great at opening doors, and whenever I got stuck he could always put me in touch with the experts or resources that I needed. I also appreciate that John truly cares about his students and has created a very friendly lab environment. I am also thankful for his advice (yes, I did try to read a paper every day), financial support, very helpful comments on all of my papers, and mentoring in the ways of science.

I would like to thank my parents, who have always been willing to listen, even when they had no idea what I was talking about, and to provide an endless source of love and encouragement. I could not have done this without your support.

There are many people at Caltech to whom I am indebted. I would have been lost without the help of Ralph Milliken, who taught me how to work with Mars data, how to use all the software I needed, as well as the principles of spectroscopy. I am also thankful to Ralph for the research discussions and advice. I would like to thank Wes Watters for his patience in teaching me Matlab, as well as Kevin Lewis and Alex Hayes for additional Matlab help. Thanks to Terri Suer for making the DEMs used in this thesis. I would also like to thank Jen Griffes for all of her help in the lab (and for the tasty baked goods). I appreciate the helpful science discussions and feedback from Joann Stock, especially on chapter 5. I would like to thank Oded Aharonson for always taking the time to ask how I was doing, as well as for help to get the DEMs that I needed made. I appreciate Mike Lamb's very helpful comments on chapter 4 as well as his always speedy replies to my questions. I am also grateful to Janice Grancich, Marcia Hudson, and Dian Buchness. You all make Caltech the friendly, caring and supportive environment that it is.

I have been truly fortunate to have undertaken a PhD during a golden age of Mars Exploration when it has first become really possible to apply studies of sedimentary geology to Mars. I have been very lucky to participate in both the Mars Exploration Rover

science team and the HiRISE science team, and I am grateful to Steve Squyres and Alfred McEwen for these opportunities. I would like to thank Gary Kocurek, John Southard, and Steven Fryberger for their helpful comments on chapter 2. I appreciate Douglas Jerolmack and Dave Mohrig's advice on calculating timescales in chapter 3. I would also like to thank Brad Prather, Carlos Pirmez, Alessandro Cantelli, and Ciaran O'Byrne for all of the fantastic discussions about submarine fans and for their suggestions on chapter 4. Thanks to Chris Okubo for the comments on chapter 5.

I cannot imagine making it through these last five years without the support of my friends, both inside and outside of Caltech. Thanks to Dave Fike, Margarita Marinova, Michelle Selvans, Amy Hofmann, and Alejandro Soto for the coffee and lunch breaks that energized me to go back to work, and the interesting discussions to remind me that there's an outside world too. Thanks to the pit crew who helped make our first year fun and not just a lot of hard work. Thank you Woody Fischer for being a great officemate and for all of your advice. Thank you to all of my friends from St. Phillips - you were always there to give me moral support, encouragement, and a home cooked meal. Thanks also to the women of the P.E.O. for your financial and moral support.

ABSTRACT

Many processes that operate on a planetary surface have the potential to create sedimentary deposits which when preserved as rocks can provide clues that allow past environmental conditions to be reconstructed. This work combines several studies using data from the Mars Exploration Rover and Mars Reconnaissance Orbiter spacecraft to examine the structure and sedimentology of the sedimentary rock record of Mars. The first study supports the dune-interdune model proposed for the formation of the deposits at the *Opportunity* landing site in Meridiani Planum and provides evidence that liquid water was involved to a greater extent in the formation of outcrops in Erebus crater. The next study identifies two depositional fan complexes on the floor of southwestern Melas Chasma and suggests that they may be sublacustrine in origin, which suggests the former presence of a significant body of water stable for at least 100 to 10,000 years. Furthermore, the basin containing the fans may be a complete source-to-sink system. The third study examines the geomorphic channel patterns present on analogue terrestrial submarine fans and deltas. The last study characterizes the extent and styles of deformation of sedimentary rocks in Valles Marineris and finds that subaerial or subaqueous gravitational slumping or sliding and soft-sediment deformation are potential mechanisms that may have caused the deformation.

TABLE OF CONTENTS

Acknowledgements	iii
Abstract	v
Table of Contents	vi
List of Illustrations	ix
List of Tables	xii
Acronyms	xiii
1 Introduction	1
1.1 The Record of Ancient Sedimentary Rocks on Mars	1
1.2 Methods	4
1.2.1 Datasets	4
1.2.1.1 Mars Global Surveyor	5
1.2.1.1 Mars Exploration Rovers	5
1.2.1.1 Mars Reconnaissance Orbiter	7
1.2.2 Software	8
1.2.1.1 ArcGIS	8
1.2.1.1 ENVI	8
1.2.1.1 MATLAB	9
2 Sulfate-Rich Bedrock in Erebus Crater, Meridiani Planum	12
2.1 Introduction	13
2.2 Regional Setting	15
2.3 Stratigraphic Framework for Erebus Crater	18
2.3.1 Methods	18
2.3.2 Results	19
2.4 Facies and Depositional Processes	24
2.4.1 Mottled Sandstone	25
2.4.2 Synsedimentary Deformed Sandstone	30
2.4.2.1 Soft-Sediment Deformation	30
2.4.2.2 Shrinkage Cracks	32
2.4.2.3 Rip-Up Clasts	33
2.4.3 Small-Scale Trough Cross-Laminated to Wavy- Laminated Sandstone	35
2.4.4 Flat-Laminated to Low-Angle Stratified Sandstone	37
2.4.5 Trough Cross-Bedded Sandstone	42
2.5 Facies Associations and Depositional Environments	43
2.5.1 Eolian Dune	43
2.5.2 Eolian Sand Sheet	44
2.5.3 Interdune	45
2.5.4 Olympia Outcrop Stratigraphy	46
2.5.5 Payson Outcrop Stratigraphy	47
2.5.6 Yavapai Outcrop Stratigraphy	49

2.6 Discussion.....	50
2.6.1 Alternative Interpretations for Depositional Processes	50
2.6.1.1 Base Surge	50
2.6.1.2 Aqueous Deposition	51
2.6.2 Climate Cycles	54
2.7 Conclusions	58
3 Sublacustrine Depositional Fans in Southwest Melas Chasma.....	60
3.1 Introduction	61
3.2 Geologic Setting	63
3.3 Methods	65
3.4 Descriptions of Fans Used for Comparison.....	67
3.5 Results.....	70
3.5.1 Morphology	70
3.5.2 Mineralogy	76
3.6 Discussion.....	80
3.6.1 Depositional Fan Comparisons	80
3.6.1.1 Alluvial Fans	80
3.6.1.2 Gully Deposits.....	81
3.6.1.3 Deltas	82
3.6.1.4 Submarine Fans	84
3.6.2 Formation of the Melas Western Fans.....	86
3.6.3 Discriminating Between Deltas and Submarine Fans	89
3.6.4 Timescales	90
3.6.1 Sublacustrine Fans as Terminal Sediment Sinks.....	95
3.7 Conclusions	98
4 Geomorphic Channel Patterns on Deltas versus Distal Submarine Fans ...	100
4.1 Introduction	101
4.2 Background.....	102
4.3 Study Sites	105
4.3.1 Submarine Fans	106
4.3.2 Deltas	111
4.3.3 Mars fans	112
4.4 Data	113
4.4.1 Submarine Fans	113
4.4.2 Deltas	114
4.4.3 Mars Fans	114
4.5 Methods	115
4.6 Results.....	124
4.7 Discussion.....	127
4.7.1 Nature of Channel Bifurcations	127
4.7.2 Mean Channel Length versus Width Trends	131
4.7.3 Sinuosity	131
4.7.4 Reservoir Model Applications	132
4.7.5 Effects of Martian Gravity	133
4.8 Conclusions	135

5 Thin-Skinned Deformation of Sedimentary Rocks in Valles Marineris.....	136
5.1 Introduction	137
5.2 Geologic Setting	140
5.3 Methods	143
5.4 Results.....	152
5.4.1 Deformation Styles.....	152
5.4.2 Map distribution and stratigraphy of deformed regions.....	157
5.4.2.1 Melas Chasma	157
5.4.2.2 Ius Chasma	166
5.4.2.3 Candor Chasma	167
5.4.3 Elevations of deformed strata	169
5.4.4 Fold orientations.....	170
5.4.5 Composition of deformed strata inferred from CRISM spectra	171
5.5 Discussion.....	173
5.5.1 Rheology of deformed strata.....	173
5.5.2 Relative age of deformed strata	175
5.5.3 Possible causes of deformation.....	184
5.5.3.1 Liquefaction.....	185
5.5.3.2 Landslides.....	190
5.5.3.3 Regional gravity gliding.....	195
5.6 Conclusions	197
References	199

LIST OF ILLUSTRATIONS

<i>Number</i>	<i>Page</i>
1.1 Distribution of layered rocks on Mars	3
1.2 Martian timescale	4
2.1 Erebus crater location map.....	14
2.2 Payson outcrop facies.....	20
2.3 Yavapai outcrop.....	21
2.4 Geometry of Yavapai beds.....	22
2.5 MI of lower Overgaard.....	23
2.6 Site Topography	24
2.7 Stratigraphy of Payson	26
2.8 Variation in recrystallization of Payson.....	27
2.9 Prism cracks in lower Overgaard	29
2.10 Shrinkage cracks in Bellemont	31
2.11 Rip up clasts.....	34
2.12 Wavy and low-angle stratification	35
2.13 Stratigraphy of Yavapai	38
2.14 Yavapai upper unit	40
2.15 Bedform transitions	40
2.16 Trough cross-bedding.....	42
2.17 Yavapai lower unit	43
2.18 Climate cycles	55
3.1 Location map of Southern Melas Basin	62
3.2 Melas sublacustrine fans and feature location map.....	71
3.3 Melas fan DEM and dips.....	72
3.4 Melas stratigraphic column.....	73
3.5 Melas fan lobes.....	75
3.6 Melas fan channels	76

3.7 Eastern Melas fans.....	77
3.8 CRISM data for Southern Melas Basin	79
3.9 Mean channel sinuosity	82
3.10 Side-scan sonar image of Mississippi submarine fan.....	84
3.11 Power law fits to length versus width trends	88
3.12 Ideal schematic of environments in Southern Melas Basin	95
4.1 Location map of fans.....	106
4.2 Channel mapping on side-scan sonar.....	109
4.3 Wax Lake Delta and channel property definitions	111
4.4 Mean channel width versus bifurcation order	115
4.5 Mean channel length versus bifurcation order	116
4.6 Log-log plot of power law fits	118
4.7 Plot of channel sinuosity versus bifurcation order	124
4.8 Channel branching angle versus bifurcation order	125
4.9 Particle settling	134
5.1 Location maps	142
5.2 Deformation map.....	145
5.3 Deformation styles	146
5.4 Histograms of block sizes	150
5.5 Valles Marineris stratigraphic columns	153
5.6 Basin cross-section	156
5.7 Fold axial trace orientations	157
5.8 Region 1 southeast map	159
5.9 Region 1 southwest map	161
5.10 Resistance blocks	163
5.11 Gradational contacts	165
5.12 Melas slump.....	168
5.13 Light-toned draping deposit in Melas.....	170
5.14 Region 7 east map	172
5.15 Region 3 west map	173

5.16 Candor DEM	175
5.17 CRISM data	177
5.18 ILD contacts	181
5.19 Landslide volume to runout	191

LIST OF TABLES

<i>Number</i>	<i>Page</i>
3.1 Characteristics of submarine fans and deltas.....	69
3.2 Characteristics of western Melas fans	74
3.3 Depositional fan characteristics	83
3.4 Martian alluvial fan gradients	99
4.1 Properties of fan systems.....	107
4.2 Channel property measurements.....	118
5.1 Mean block sizes	149
5.2 List of CRISM images.....	151
5.3 List of images showing contacts in Valles Marineris.....	183

ACRONYMS

CRISM Compact Reconnaissance Imaging Spectrometer for Mars

CTX Context Camera

DEM Digital Elevation Model

HiRISE High Resolution Imaging Science Experiment

MER Mars Exploration Rover

MGS Mars Global Surveyor

MI Microscopic Imager

MOC Mars Orbiter Camera

MOLA Mars Orbiter Laser Altimeter

MRO Mars Reconnaissance Orbiter

THERMIS Thermal Emission Infrared Spectrometer

Chapter 1

INTRODUCTION

1.1 The Record of Ancient Sedimentary Rocks on Mars

Many processes that operate at a planetary surface have the potential to create a record of sedimentary rocks, and these rocks provide clues that allow past environmental conditions to be reconstructed. Earth has a rich sedimentary rock record, and the study of these rocks has provided insights into how the climate of Earth has evolved over the last several billion years. Of all of the planetary bodies in our Solar System, Mars is the only other planet known to have an extensive sedimentary rock record.

While the study of rocks on Mars that appear sedimentary in nature began with Mariner and Viking images (Sharp 1973; Nedell et al. 1987), the field has truly blossomed with the data returned from the Mars Global Surveyor, Mars Odyssey, Mars Express, the Mars Exploration Rovers, and the Mars Reconnaissance Orbiter (Christensen et al. 2000; Malin and Edgett 2000; Malin and Edgett 2003; Glotch et al. 2005; Grotzinger et al. 2005; Ehlmann et al. 2008; Lewis et al. 2008b; Milliken et al. 2008; Metz et al. 2009a; Metz et al. 2009b). With the high-resolution images and spectral data from these spacecraft, the detailed morphology, stratigraphy and composition of sedimentary deposits can now be studied from orbit and on the surface in Meridiani Planum and Gusev crater. Sedimentary rocks from a range of depositional environments have now been identified on Mars, allowing detailed comparisons between environments and processes on Earth and Mars. These environments include eolian dune/interdune (Grotzinger et al. 2005; Metz et al.

2009a), alluvial/fluvial (Mangold et al. 2004; Moore and Howard 2005; Quantin et al. 2005; Kraal et al. 2008a; Mangold et al. 2008a), deltaic (Malin and Edgett 2003; Fassett and Head 2005; Lewis et al. 2006; Wood 2006; Ehlmann et al. 2008; Grant et al. 2008), subaqueous (Metz et al. 2009b) and volcanoclastic (Lewis et al. 2008a).

Many sedimentary environments are quite similar on Earth and Mars; however, there are a few key differences. Because the upper crust of Mars is primarily basaltic instead of intermediate to felsic as on Earth, typical particles derived from chemical weathering on Mars will have a different composition than those on Earth (McLennan and Grotzinger 2008). Chemical and spectral measurements of the rocks exposed on the surface of Mars indicate that many of them were altered in low pH environments dominated by the sulfur cycle, as opposed to moderate pH environments dominated by the carbonate cycle as on Earth (McLennan and Grotzinger 2008). Another key difference between Earth and Mars is that Mars does not have plate tectonics (Albarède and Blichert-Toft 2007; O'Neill et al. 2007), and so sedimentary basins are largely thought to form in impact craters or through rifting, as in Valles Marineris, instead of through subsidence (McLennan and Grotzinger 2008).

Exposures of rocks that may be sedimentary in nature are concentrated in a few areas on Mars, primarily within $\sim 30^\circ$ of the equator (Fig. 1.1). An ice-rich mantle has been identified on the surface of Mars between ~ 30 - 70° north and south and may obscure exposures of sedimentary rocks in those latitude bands (Mustard et al 2001). A survey of High Resolution Imaging Science Experiment (HiRISE) and Mars Orbiter Camera (MOC)

images show that layered rocks occur primarily in Valles Marineris, Meridiani Planum, Arabia Terra, Holden crater and near the western and northern rims of the Hellas impact basin (Malin and Edgett 2000; Griffes et al. 2010). This suggests that at the time these rocks formed, climatic conditions led to stratified rocks primarily deposited in these areas or preferentially preserved or exposed in these areas. Absolute ages for rocks on Mars are

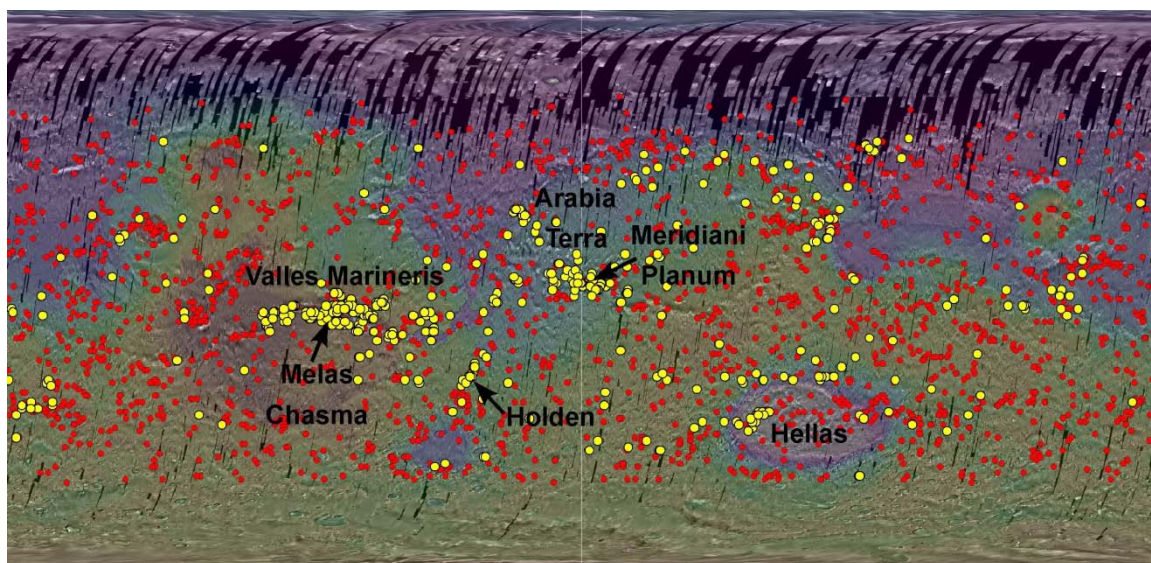


Figure 1.1 MOLA elevation map of Mars overlaid on THEMIS daytime IR mosaic. Red dots indicate locations of HiRISE images that do not show layered deposits. Yellow dots are HiRISE images with stratified bedrock (based on Fig. 1 from Griffes et al. 2010).

not known, but relative ages of rocks can be estimated based on the density of impact craters. Areas that are more heavily cratered are thought to be older and those with fewer impact craters are thought to be younger. Martian time has been divided into three epochs: the Noachian, Hesperian and Amazonian as shown in Figure 1.2.

	3.5		1.8	
Noachian		Hesperian		Amazonian

Figure 1.2 Martian timescale which divides Martian time into three epochs. Noachian refers to rocks older than 3.5 Ga, Hesperian to rocks between 3.5 and 1.8 Ga, and the Amazonian to rocks younger than 1.8 Ga.

The following chapters will describe several exposures of sedimentary rock from different depositional environments on the surface of Mars and will compare them to similar terrestrial environments. Chapter 2 describes eolian dune/interdune facies observed in Erebus crater in Meridiani Planum with the *Opportunity* rover. Chapter 3 describes a depositional fan complex in a small basin in southwestern Melas Chasma, Valles Marineris, and based on similarities to terrestrial depositional fans, infers that it is most likely sublacustrine in origin. Chapter 4 investigates some of the properties of terrestrial submarine fans that serve as a reference for comparison to the Martian sublacustrine fans. Chapter 5 describes many outcrops of deformed sedimentary rocks that are exposed in the central chasmata of Valles Marineris and evaluates potential causes for the deformation.

1.2. Methods

The work described in the following chapters uses several datasets and software programs. A short description of the most heavily used datasets is given below along with a description of the software programs.

1.2.1 Datasets

1.2.1.1 Mars Global Surveyor

The Mars Global Surveyor (MGS) spacecraft was launched in 1996 and operated for nearly a decade before it was lost in November 2006. Data from one of its instruments, the Mars Orbiter Laser Altimeter (MOLA), is used in this thesis, and I refer to data from another of its instruments, the Mars Orbiter Camera (MOC). MOC is a pushbroom camera and includes both a narrow-angle and two wide-angle cameras. Narrow-angle image swaths are roughly 3 km wide and have a ground sampling dimension up to 1.5 m/pixel (Malin et al. 1992). MOLA is an optical remote sensing instrument, and it has acquired the most accurate global topographic map of the surface of Mars to date. MOLA has a vertical accuracy of 1 m and a surface spot size of 168 m with an along track shot spacing of 300 m (Smith et al. 2001).

1.2.1.2 Mars Exploration Rovers

The Mars Exploration Rovers (MER) *Spirit* and *Opportunity* landed on the surface of Mars in January 2004, and six years later are still traversing across the surface, long past their nominal 90-sol mission. The *Spirit* rover landed in Gusev crater and the *Opportunity* rover in Meridiani Planum. Each rover contains a suite of scientific instruments including panoramic cameras (Pancam), a microscopic imager (MI), a miniature thermal emission spectrometer (Mini-TES), an alpha particle X-ray spectrometer (APXS), a Mössbauer spectrometer (MB), and a rock abrasion tool (RAT). This thesis primarily uses results from the rover cameras, although key results from the other instruments are summarized.

Pancam is used to provide imaging of the landing sites in order to study the morphology, lithology, texture and distribution of rocks and outcrops. It is a high-resolution color stereo pair of 1024×1024 -pixel CCD cameras that are mounted 30 cm apart on a camera bar on top of the rover mast (Bell et al. 2003). The cameras have a 1° toe-in, which means they are angled in, and can provide accurate range data from 5-100 m from the rover (Bell et al. 2003). Each camera has a filter wheel which provides visible and near IR coverage ranging from 400 nm to 1100 nm with stereo imaging available for red (L2/R2) and blue (L7/R1) wavelengths (Bell et al. 2003). The MI is used to provide hand-lens scale imaging of rock and soil textures. It uses the same CCD as the Pancam, but with only a single broad-band filter so images are monochromatic (Squyres et al. 2003). The field of view is 31×31 mm with $30 \mu\text{m}/\text{pixel}$ sampling (Squyres et al. 2003).

The Mini-TES is used to provide mineralogical information for rocks and soils. It is a Michelson interferometer that provides a spectral resolution of 10 cm^{-1} over the 5-29 μm range (Squyres et al. 2003). The APXS provides information that can be used to determine the elemental chemistry of rocks and soils, which can be used to help constrain mineralogical analyses. It exposes material to alpha particles and x rays from a radioactive ^{244}Cm source, and then measures the energy spectra of backscattered alphas and x rays (Squyres et al. 2003). The depth of analysis ranges from 10-100 μm , depending on the atomic number, with a detection limit of 0.5-1 weight percent. The Mössbauer spectrometer can be used to reveal the valence state, molecular structure, and magnetic properties of iron-bearing material in the rocks and soils (Squyres et al. 2003). It uses a ^{57}Co source and has a depth of sampling of 200-300 μm with a spot size of ~ 15 mm.

The RAT is used to brush dust from rock surfaces and to grind into the surface of rocks to expose fresh material. It is a diamond tipped grinding tool that can remove a cylindrical area of 4.5 cm to a depth of at least 0.5 cm (Squyres et al. 2003).

1.2.1.3 Mars Reconnaissance Orbiter

The Mars Reconnaissance Orbiter entered orbit around Mars in 2006 and hosts several high data rate instruments, including the High Resolution Imaging Experiment (HiRISE), the Context Camera (CTX), and the Compact Reconnaissance Imaging Spectrometer for Mars (CRISM). This suite of instruments provides the ability to map the surface of Mars at an unprecedented spatial and spectral resolution. The spacecraft is in a near circular, near polar 255×320 km orbit with a mean local solar time of 3:10 pm (Murchie et al. 2007).

The HiRISE camera is a pushbroom camera and has a 6 km swath width and a minimum ground sampling dimension of 25-30 cm/pixel (McEwen et al. 2007). The camera has fourteen 2048×128 element CCDs and a 3-color capability over the central 20% of the swath width. MRO has very precise stability and pointing control which allows HiRISE to acquire stereo images that can be combined to form digital elevation models (DEMs) with a vertical precision of ~25 cm (McEwen et al. 2007). The CTX camera acquires context images that can be used for the data acquired by other MRO instruments; it has a 5064 pixel wide CCD array and has a swath width of 30 km with a ground sampling dimension of 6 m/pixel (Malin et al. 2007). The CRISM instrument is a hyperspectral imager that is used to map the mineralogy of key areas of the surface of Mars

at high spatial resolution. In its targeted mode, it has a spatial resolution of 15-19 m/pixel and a spectral resolution of 362-3290 nm at 6.55 nm/channel (Murchie et al. 2007). CRISM uses gimbaling to take out along-track motion of the field of view to allow targeted images of approximately 10 km by 10 km at full spatial resolution (Murchie et al. 2007).

1.2.2 Software

The software programs used most heavily in this thesis (ArcGIS, ENVI, and Matlab) are described below. Additional programs used include Canvas, JMars, and GoogleMars.

1.2.2.1 ArcGIS

Most of the mapping that was done in the following chapters was accomplished in ArcGIS, which is a suite of geographic information system software produced by ESRI. A Thermal Emission Infrared Spectrometer (THEMIS) daytime infrared (IR) global mosaic was used as a basemap and all other images were registered to the basemap using the Mars 2000 projection. HiRISE and CRISM images were manually aligned to CTX images using prominent features in the images.

1.2.2.2 ENVI

CRISM images were processed using the CRISM Analysis Tools (CAT) in ENVI, which is a software application used to process and analyze geospatial imagery. IR and visible images were first converted from PDS format to CAT, then the IR images were

corrected for atmospheric gases and stripes were removed. Band parameter maps were calculated for both IR and visible images, and then the images were projected. Lastly, the IR and visible images were stacked.

CRISM images were analyzed using spectral band parameter maps, which are designed to capture spectral features unique to specific mineralogies (see Table 1 of Pelkey et al. 2007 for a list of CRISM spectral parameters). Band depths generally scale with the abundance of the absorbing mineral, though factors such as particle size and albedo do have an effect (Pelkey et al. 2007). Each band parameter was examined and the three most revealing were combined into the three channels of an RGB image. Regions with interesting features were then selected from a linked RGB band parameter image and the visible image. A spectrally 'neutral' area, often a dusty area, was also selected and the spectra of each region of interest were ratioed to the spectra of the neutral area.

1.2.2.3 MATLAB

The DEMs used throughout this thesis were analyzed using scripts I wrote in Matlab; these scripts allow users to directly select bedding planes or contacts in HiRISE DEMs and calculate the orientation of the bedding and the errors on these measurements. The method uses two main steps in order to find the orientation of layers in a DEM. First, a user clicks points along each layer for which the orientation is desired using a graphical user interface. These points are then used to find the orientation of the plane as well as the errors in the measurements.

The inputs to the scripts are a HiRISE orthoimage of the area of interest (along with its worldfile) and a DEM, both in tiff format. Typically, I work with only a subset of the DEM covering a particular portion of interest (usually $\sim 1/3$ of the DEM or less) to decrease computing times and memory issues. It is important to select bedding planes or contacts that have three-dimensional exposures so that a unique plane can be fit to the data. It is also important that each bedding plane or contact be relatively planar.

Once the layers have been traced out, the points are used to find a multiple linear regression least-squares plane fit. The equation of the plane is

$$Z = B_1X + B_2Y + B_3 \quad (1)$$

where B are the coefficients for the multiple linear regression with one-sigma confidence limits, X is the easting, Y is the northing and Z is the elevation. The equation for the strike (in degrees) is

$$dip = \frac{180}{\pi} \tan^{-1} \left(\sqrt{(B_1^2 + B_2^2)} \right), \quad (2)$$

and the equation for the dip (in degrees) is

$$strike = \frac{-180}{\pi} \tan^{-1}(-B_2, B_1) \quad (3)$$

where \tan^{-1} is the four quadrant inverse tangent. I used bootstrapping with replacement (1000 iterations) to derive the confidence intervals of the strike and dip. This is accomplished by first adding a random residual of the plane fit (R^*) to the elevation value, and then subtracting the residual so that the error is not doubled:

$$z^* = z + R^* - R \quad (4)$$

The multiple linear regression is then run using the x , y , z^* values, and this is repeated 1000 times. Next, we take the mean of the 1000 strikes and the mean of the 1000 dips derived from the bootstrapping to find the strike and dip, respectively. We then calculate the one-sigma confidence limits on the dip.

Next, we calculate the principal components (C_1, C_2, C_3) of the plane fit. I report the colinearity, which is defined as the ratio of the third principal component to the second principal component (C_3/C_2). This value should be close to zero for a good plane fit. If the ratio of C_3/C_2 is large, then it means that the points used to define the plane are colinear and the plane should not be used to derive strike and dip measurements.

Two figures are produced from these scripts, (1) shows the image with the location of each selected plane along with a number labeling each plane, and (2) shows the image with the strike and dip symbol and numerical measurement of each plane plotted on top.

Chapter 2

SULFATE-RICH BEDROCK IN EREBUS CRATER, MERIDIANI PLANUM

Originally published in:

Metz, J. M., Grotzinger, J. P., Rubin, D. M., Lewis, K. W., Squyres, S. W., and Bell, J. F. (2009a), Sulfate-rich eolian and wet interdune deposits, Erebus crater, Meridiani Planum, Mars, *Journal of Sedimentary Research*, 79, 247-264, doi: 10.2110/jsr2009.033.

Abstract

This study investigates three bedrock exposures at Erebus crater, an ~300 m diameter crater approximately 4 km south of Endurance crater on Mars. These outcrops, called Olympia, Payson, and Yavapai, provide additional evidence in support of the dune-interdune model proposed for the formation of the deposits at the *Opportunity* landing site in Meridiani Planum. There is evidence for greater involvement of liquid water in the Olympia outcrop exposures than was observed in Eagle or Endurance craters. The Olympia outcrop likely formed in a wet interdune and sand sheet environment. The facies observed within the Payson outcrop, which is likely stratigraphically above the Olympia outcrop, indicate that it was deposited in a damp-wet interdune, sand sheet, and eolian dune environment. The Yavapai outcrop, which likely stratigraphically overlies the Payson outcrop, has facies suggestive of deposition in primarily a sand sheet environment and also potentially in an eolian dune environment. These three outcrop exposures may indicate an overall drying-upward trend spanning the stratigraphic section from its base at the Olympia outcrop to its top at the Yavapai outcrop. This contrasts with the wetting-upward trend

seen in Endurance and Eagle craters. Thus, the series of outcrops seen at Meridiani by *Opportunity* may constitute a full climatic cycle, evolving from dry to wet to dry conditions.

2.1 Introduction

The development, testing, and refinement of facies models lies at the core of the analysis of sedimentary rocks on Earth. Multiple outcrop exposures or well information create the basis for this approach, whose application has great relevance for the interpretation of sedimentary rocks on Mars. At Meridiani Planum, randomly distributed impact craters provide spatially separated outcrops that can be interrogated for information related to depositional processes. The results obtained for each crater can be used to evaluate developing facies models.

The Mars Exploration Rover (MER) *Opportunity* has investigated several bedrock exposures in craters in Meridiani Planum. Facies models developed by studying outcrops in Eagle and Endurance craters create a framework to which each new crater can be compared. The purpose of this study was to test and refine existing models proposed for the formation of the Meridiani bedrock by investigating new outcrop exposures at Erebus crater, an ~ 300-m-diameter crater approximately 4 km south of Endurance crater (Fig. 2.1A). Erebus crater is a large simple crater, and Mars Global Surveyor-Mars Orbiter Camera stereo data and Mars Orbiter Laser Altimetry data suggest that the land surface surrounding Erebus crater is about 10-15 m higher in elevation than Endurance crater.

Assuming the bedrock to be approximately flat lying, this implies that the rocks at Erebus may be at a slightly higher stratigraphic level than Endurance. The outcrops examined at Erebus are concentrated along the rim of the crater and have been informally named Olympia, Payson, and Yavapai (Fig. 2.1B).

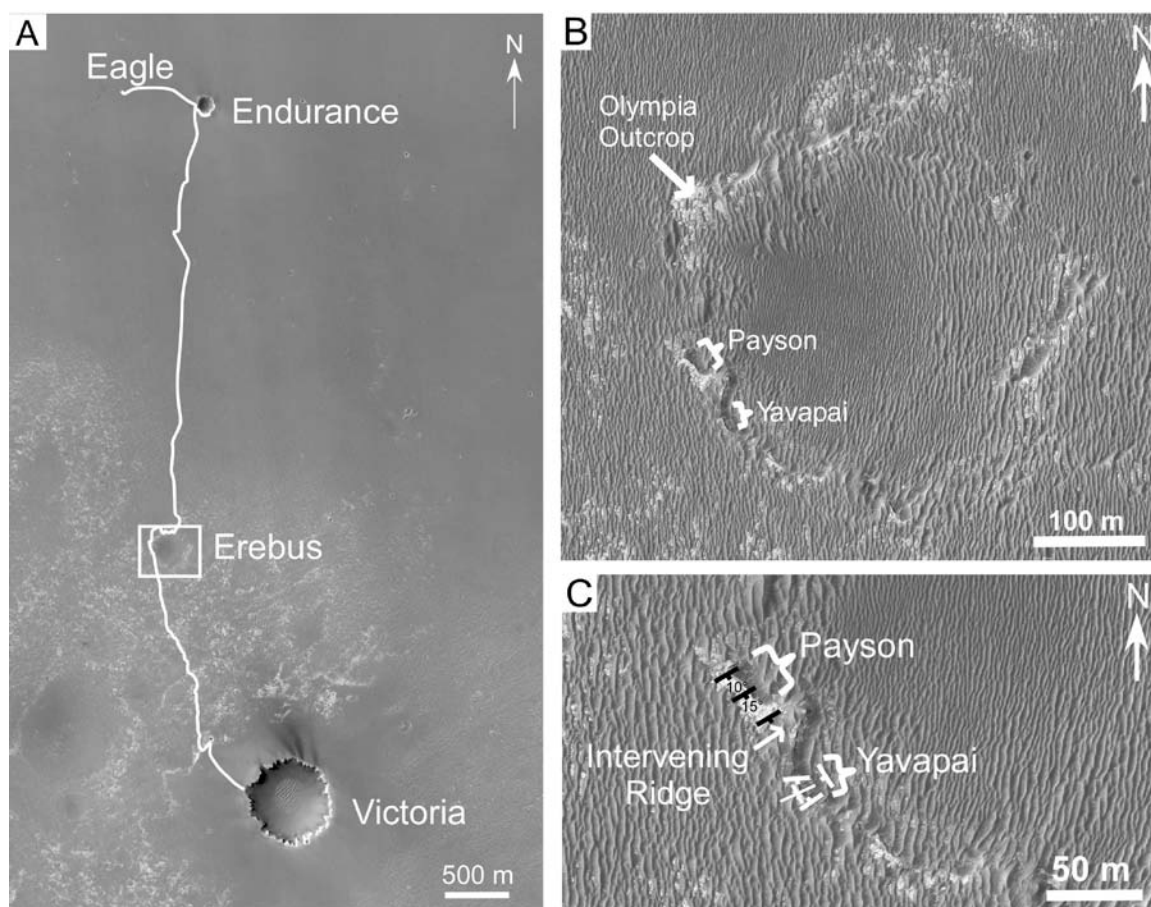


Figure 2.1. Subscenes from HiRISE image PSP_001414_1780, which was acquired on November 14, 2006 (Mars northern summer). White box indicates location of B. The image was taken at the local Mars time of 3:26 p.m., and the scene was illuminated from the west at a solar incidence angle of 54° . A.) HiRISE image showing rover traverse path in white. The rover drove from Eagle crater east to Endurance crater, and then drove 4 km south to Erebus crater en route to Victoria crater. B.) Erebus crater with locations of the Olympia Outcrop, Payson, and Yavapai marked. C.) Close-up view of the western margin of Erebus crater showing the strike and dip of bedding in the Payson, Intervening Ridge,

and Yavapai outcrops. The trend of the axis of the potential syncline at Yavapai is also indicated.

The sulfate-rich bedrock exposed along the walls at Eagle and Endurance craters has been interpreted by the MER team to have been deposited in an eolian dune-interdune environment (Grotzinger et al. 2005; Grotzinger et al. 2006; Squyres et al. 2004). This interpretation of the outcrops has been challenged by McCollom and Hynek (2005) and Knauth et al. (2005), who suggested that volcanic or impact-related sedimentation was responsible for the deposition of the Meridiani bedrock. These strongly contrasting models make specific sedimentologic predictions for Meridiani bedrock exposures; the current study documents an important new locality that provides data to help test these models. All of the observations point to a dune-interdune scenario. This allows consideration of potential climatic influences, which is a major concern for the environmental evolution of Mars.

2.2 Regional Setting

Erebus crater is located in the Terra Meridiani region of Mars. The oldest rocks constitute a Noachian-age basal unit that has been extensively dissected by channel systems (Arvidson et al. 2003). Lying disconformably on top of the dissected cratered terrain is a widespread, partially eroded, layered complex consisting of several light-toned stratigraphic units. The layered complex (“etched terrain”) has a variable morphology which includes polygonal ground separated by ridges and valleys and accumulations of strata which have been eroded into a variety of landforms (Arvidson et al. 2003). These

essentially flat-lying strata extend laterally for distances in excess of 100 km. Erosional features within the etched terrain indicate that several hundred meters have been stripped from this deposit (Arvidson et al. 2003). The etched terrain covers $2.3 \times 10^5 \text{ km}^2$ and is at least 500 m thick (Hynek 2004). The strata in the etched terrain are inferred to be lithified sedimentary rock, because they maintain nearly vertical cliffs and have high thermal inertia (Arvidson et al. 2006; Edgett and Malin 2002).

Strata of the etched terrain are capped by hematite-bearing plains which are characterized by a smooth morphology and dark tone (Arvidson et al. 2003; Arvidson et al. 2006); these materials have locally been reworked into a variety of eolian bedforms including dunes and granule ripples (Jerolmack et al. 2006). Exposure of light-toned bedrock of the etched terrain can be seen in the interdune areas. The northern part of the Meridiani region is covered by a mantle whose thickness is $\sim 10 \text{ m}$, thickening to 30 m toward the north (Arvidson et al. 2003).

Opportunity has examined the extremely flat plains and several craters within the hematite-bearing plains unit in Terra Meridiani. The bedrock exposures near and within Eagle, Endurance, and Erebus craters have allowed detailed examination of the layers in the lower part of the topmost strata in the etched terrain. Due to differential erosion, the strata exposed at the upper surface of the etched terrain vary considerably in age. A framework for interpretation of the bedrock exposures investigated by *Opportunity* was outlined in Grotzinger et al. (2005).

Endurance and Eagle craters (Fig. 2.1A) expose a combined stratigraphic thickness of 7 m of sedimentary rocks called the Burns formation (Grotzinger et al. 2005). These outcrops are composed dominantly of fine- to medium-grained sandstones. Geochemical and mineralogic data show that the grains are composed of 50% fine-grained siliciclastic materials derived from the weathering of basaltic rock, 40% sulfate minerals, and 10% hematite (Clark et al. 2005; Squyres et al. 2004). Exposed rocks are soft, as revealed through grinding using the rock abrasion tool (RAT); they have a resistance to abrasion similar to talc (Arvidson et al. 2004). Most outcrops are laminated and formed of well-rounded and well-sorted grains, bound together with intergranular cements (Grotzinger et al. 2005). Mineralogical and geochemical data support sedimentologic observations of evaporative processes and indicate the presence of abundant sulfate minerals, including jarosite ($\text{KFe}_3(\text{SO}_4)_2(\text{OH})_6$) and probable calcium and magnesium sulfates, in addition to later remobilization of evaporite mineral phases (Clark et al. 2005; McLennan et al. 2005).

The Burns formation at Endurance crater can be subdivided into lower, middle, and upper units. The lower unit contains large-scale cross-bedded sandstone and is interpreted to represent an eolian dune facies. The middle unit is dominated by several meters of planar-laminated to low-angle cross-stratified sandstone with an overprint of nodular recrystallization and is interpreted as representative of an eolian sand sheet. The upper unit contains planar lamination, low-angle stratification, and small-scale cross-stratification in sets, including rare small-scale trough cross-lamination. This unit is interpreted as having been deposited in a mixed eolian sand sheet and interdune environment (Grotzinger et al. 2005). According to this model, the sequence shows a wetting-upward succession and

records a progressive increase in the influence of groundwater and ultimately surface water on deposition and subsequent diagenesis (Grotzinger et al. 2005). Centimeter-scale trough cross-lamination in the upper unit is indicative of sediment transport in shallow subaqueous flows with current velocities of a few tens of centimeters per second (Grotzinger et al. 2005). These flows most likely resulted from the flooding of interdune-playa surfaces.

2.3 Stratigraphic Framework for Erebus Crater

2.3.1 Methods

Structural attitudes were obtained using planar fits to bedding seen in Pancam images of the Payson outcrop. Linear segments were traced out along well-exposed layers. Only layers with some natural curvature in the horizontal direction were used in order to provide accurate constraints on the three-dimensional geometry of the layer. This was done because linear segments do not provide any information on the direction perpendicular to the line. We employed the method presented in Squyres et al. (2007) and Lewis et al. (2008b), which uses principal component analysis to ensure the layers used are well fitted by a plane. Where sufficient outcrop curvature was not present, apparent dips were used.

The stratigraphy was mapped by visual tracing and correlation of key beds across the outcrop. Breaks due to lack of outcrop and possible small fault offsets were accounted for, and composite stratigraphic thicknesses were estimated by using key beds to link different parts of the outcrop.

2.3.2 Results

Opportunity obtained images of Erebus crater from sols 647 to 759. The bedrock exposures in Erebus crater include a large expanse called the Olympia outcrop (Fig. 2.1B). The outcrop appears as a relatively flat pavement due to recent eolian abrasion. The structural dips of the rocks at the Olympia outcrop are up to $\sim 15\text{-}30^\circ$, with variable strike, possibly caused by the crater-forming impact that rotated individual rocks or sections of rock (Grotzinger et al. 2006). Correlations between individual blocks at Olympia generally were not possible. Two, more prominent, outcrops are located farther south along the western rim of Erebus crater. These more prominent outcrops feature $\sim 1\text{-m}$ -high vertical exposures of outcrop that extend for $\sim 80\text{ m}$ from the north end of the northern outcrop (“Payson”) to the south end of the southern outcrop (“Yavapai”) (Fig. 2.1B). There is a small ridge separating the two outcrops (Fig. 2.1C). The stratigraphic relationship between Payson and Yavapai cannot be resolved with certainty, but from the images acquired it appears that the bedding continues beyond Payson across the intervening ridge with similar dips, and so Yavapai is likely stratigraphically higher than Payson. Together, these two outcrops represent approximately 10 m of stratigraphic section.

The northern and southern outcrops were imaged between sols 742 and 758, with Payson imaged from three different positions and Yavapai from two positions. The dip of the Payson strata ranges between 10 and 15° and all of the layers strike in a SE-NW direction (Fig 2.1C). The Payson outcrop is approximately 31 m long and ranges in height from 0.75 m to 1.6 m. The total stratigraphic thickness represented by Payson is 4.85 m. A

fracture cuts across the northern end of the outcrop (Fig. 2.2A). The bedding at the northern end of the outcrop dips at $\sim 10^\circ$ to the SE. Approximately 10 m along from the north end of the outcrop exposure at Payson, there is a change in the bedding dip (Fig. 2.2A). The apparent dips become steeper south of this area, with dips measuring around 15° to the SE.

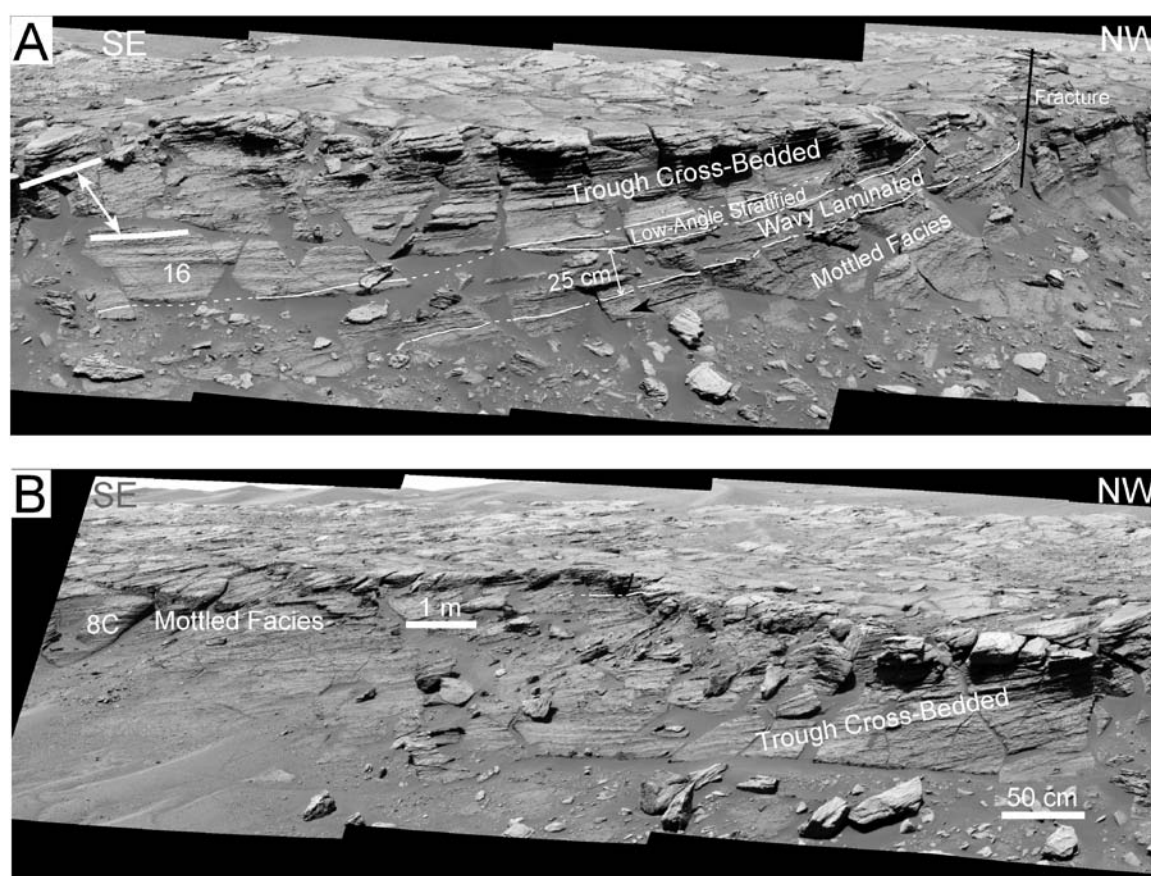


Figure 2.2 The northern two-thirds of the Payson outcrop shown as two overlapping panels. The facies transitions are marked by white lines. Solid lines are drawn where the transitions are clearly defined, and dashed lines are drawn where the transitions are inferred or partially obscured. These images were taken by the Pancam on sol 749 with the 430 nm filter. A.) Northernmost section of Payson. A fracture, likely formed during formation of Erebus crater, is marked by a black line. The mottled facies, wavy-laminated facies, low-angle stratified facies, and trough cross-bedded facies are marked. The location of figure 2.16 is indicated. The two thick white lines and the white arrow indicate the area where the

dip of the outcrop bedding increases from $\sim 10^\circ$ to $\sim 15^\circ$, measured relative to a horizontal surface. B.) The middle section of the Payson outcrop, showing the trough cross-bedded and mottled facies. The location of figure 2.8C is indicated.

Because Erebus crater is a highly eroded simple crater whose plan view departs significantly from circular (Melosh 1989), it is likely that the current walls are the result of a large amount of erosion of the original rim walls. The current walls are likely far removed from the original rim, and also potentially below the original flanks of the crater.

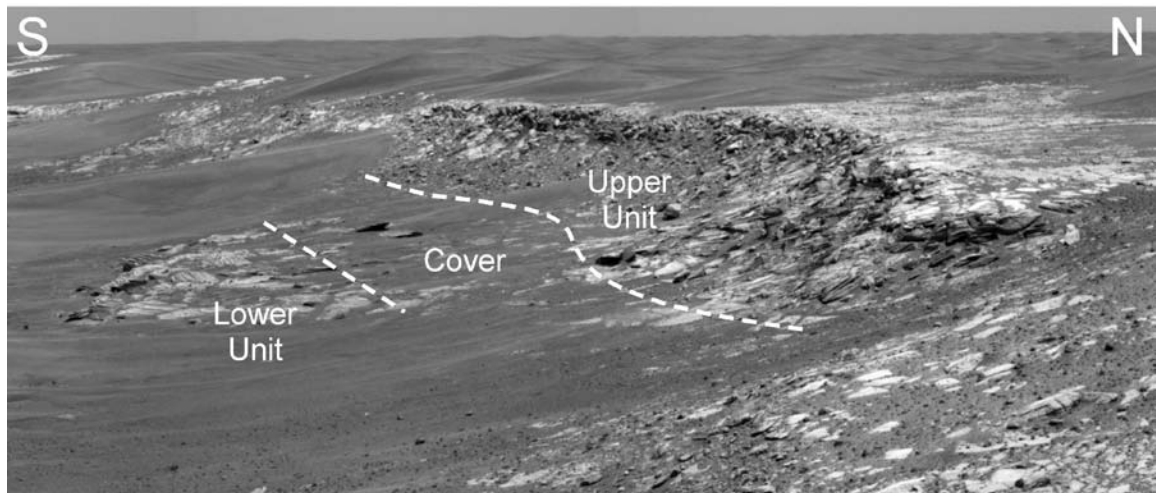


Figure 2.3 The Yavapai outcrop, showing the locations of the lower and upper units and the interval of cover between them. Dashed white lines indicate the approximate locations of the unit boundaries, in this case defined by limits of exposure. Navcam image acquired on sol 755.

The outcrop dips are also not directed radially away from the crater, as would be expected if they were the result of the crater-forming impact. Erebus crater is superposed on an older crater, Terra Nova, so the dips observed at Erebus may potentially be related to the combined deformation from both impacts. However, the observed dips at Erebus crater also do not coincide with the expected radial outward dips from the Terra Nova impact.

Terra Nova is also a heavily eroded crater, and so as described earlier for Erebus, the current exposures are probably far removed from the original walls of Terra Nova. Thus, the dips observed at Erebus may have originated from a complicated interaction of the deformation from both the Erebus and Terra Nova impacts.

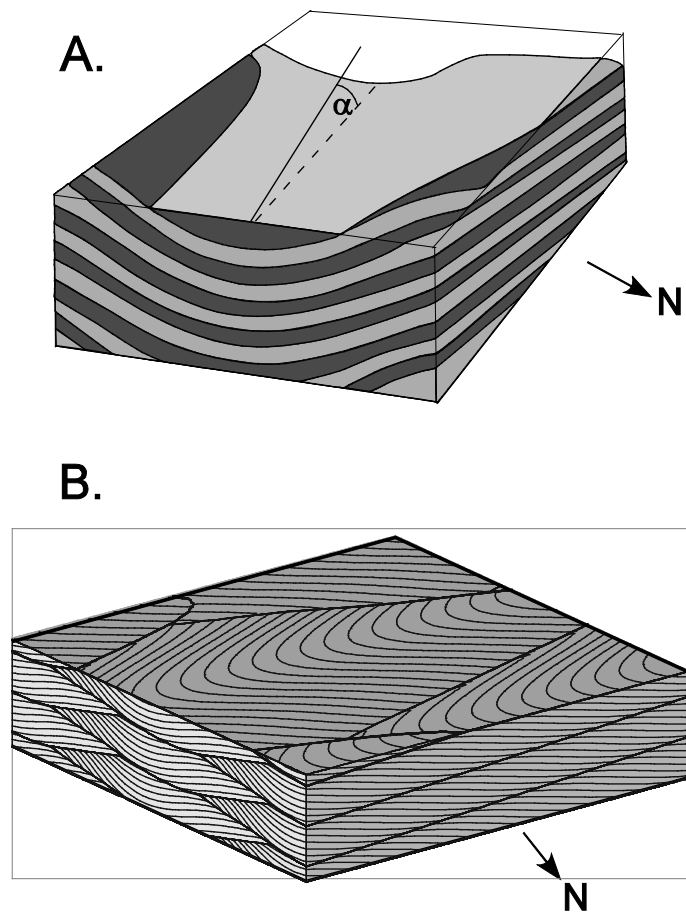


Figure 2.4. A.) Hypothetical geometry of beds in the upper unit of the Yavapai outcrop if they form a syncline. α is the plunge of the fold axis. B.) Hypothetical geometry of the beds in the upper unit of Yavapai if they represent opposite sides of large trough-shaped sets of cross-beds.

The Yavapai outcrop is approximately 30 m in length and is separated from the Payson outcrop by about 20 m. Only the northernmost 6 m of the outcrop was imaged in enough detail to characterize the diversity of sedimentary structures. The section of the Yavapai outcrop for which images were acquired can be separated into two units (Fig. 2.3). The lower unit has approximately 0.8 m of vertical relief, and the upper unit has between 1.5 to 2.5 m of vertical relief; they are separated by ~ 5 m of areal soil cover. Yavapai strata define either (1) an open syncline, with the fold axis trending roughly east-west and plunging into the outcrop (Figs. 2.1C, 2.4A) or (2) a set of large-scale trough-shaped cross-strata with the variable dip directions due to exposure of cross-bed layers on both sides of the trough bedform (Figs. 2.1C, 2.4B). The total stratigraphic thickness represented by the Yavapai outcrop is 5.15 m.

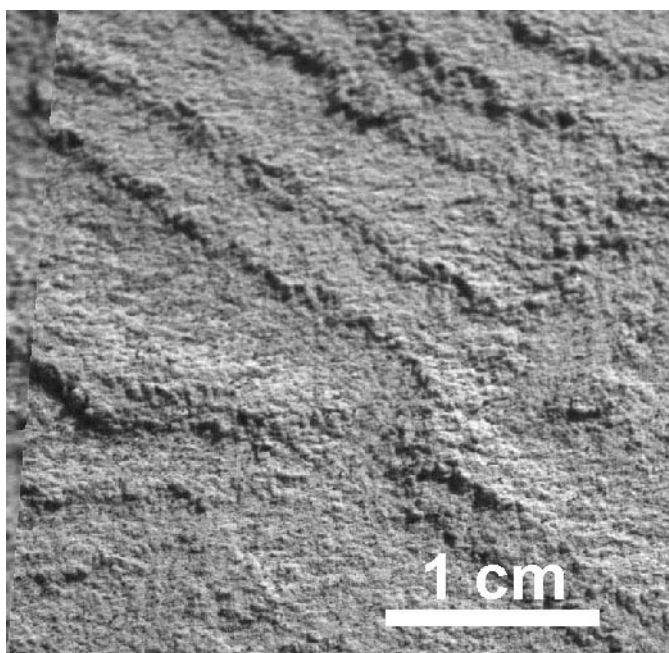


Figure 2.5 Microscopic imager photograph of the rock lower Overgaard showing the typical grain sizes and sorting within the Olympia outcrop. Grains are predominantly of

medium sand size, with interlocking textures due to cementation. Image acquired on sol 708.

2.4 Facies and Depositional Processes

All of the rocks in the Olympia, Payson, and Yavapai outcrops are interpreted to be sandstones on the basis of the predominance of clastic textures. This is supported by Microscopic Imager (MI) images of the Olympia outcrop, located 50 m north of Payson, which show predominantly medium-sand-size grains (Fig. 2.5). MI images were not obtained for the Payson or Yavapai outcrops, but grains are below the limit of the resolution of the Pancam images.

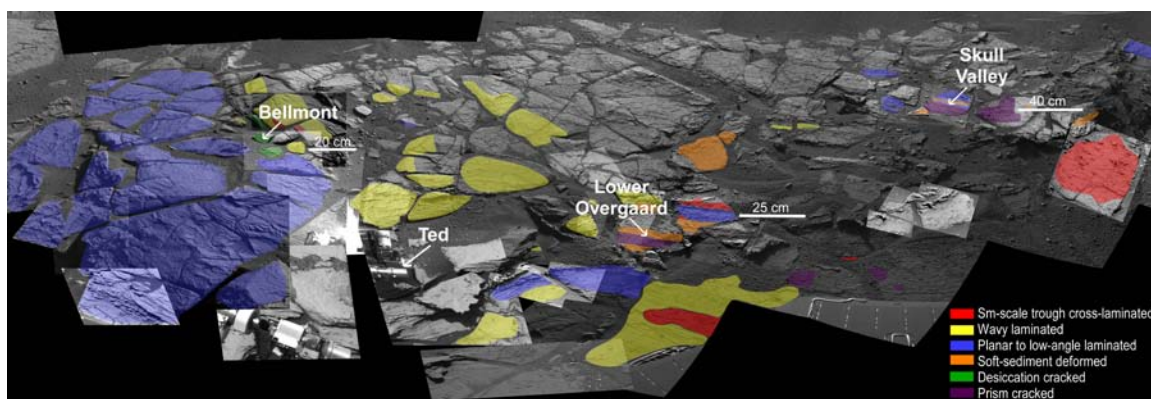


Figure 2.6 Distribution of facies at the Olympia outcrop. Where facies could be determined they are marked on the outcrop by the indicated colors. Rocks discussed in this paper (Bellemont, Lower Overgaard, and Skull Valley) are identified. Correlation of facies is severely limited due to impact-related brecciation and block rotation. These images were acquired between sols 652 and 694 with Pancam's 482 nm filter.

The composition of the rock "Ted" (Fig. 2.6) at Olympia is similar to that observed at Endurance and Eagle craters (Knoll et al. 2008) and the rock is similarly interpreted to

have been derived from reworked, siliciclastic-rich evaporites. The presence of centimeter-scale lamination in many of the facies makes it likely that these deposits accumulated as the result of bedload traction transport of sand-size particles. The facies observed at Olympia, Payson, and Yavapai include mottled sandstone, syn-sedimentary deformed sandstone, wavy-laminated to small-scale trough cross-laminated sandstone, and planar-stratified to low-angle-stratified sandstone. There are zones of intense recrystallization where the deposits appear massive, but there is also generally evidence for palimpsest layering, indicating that the original deposits were not massive.

2.4.1 Mottled Sandstone

There are several occurrences in the Payson outcrop of a mottled and disrupted texture that is poorly stratified to massive. This facies appears in both the lower unit and the upper unit at Payson (Figs. 2.2, 2.7, 2.8). Beds in the mottled facies in the lower unit are ~ 4-6 cm thick and show palimpsest millimeter-scale lamination in some areas. Although the Meridiani rocks are classified as sandstones because of their primary texture, their very unusual composition and the highly labile nature of the mineralogy lead to textures not commonly seen in sandstones (McLennan et al. 2005; Tosca et al. 2008). Therefore, we must turn to chemical sedimentary rocks for potential analogs. Mottling occurs in terrestrial carbonate rocks when part of the limestone is diagenetically replaced by dolomite, causing a difference in composition and crystallinity. This can result in

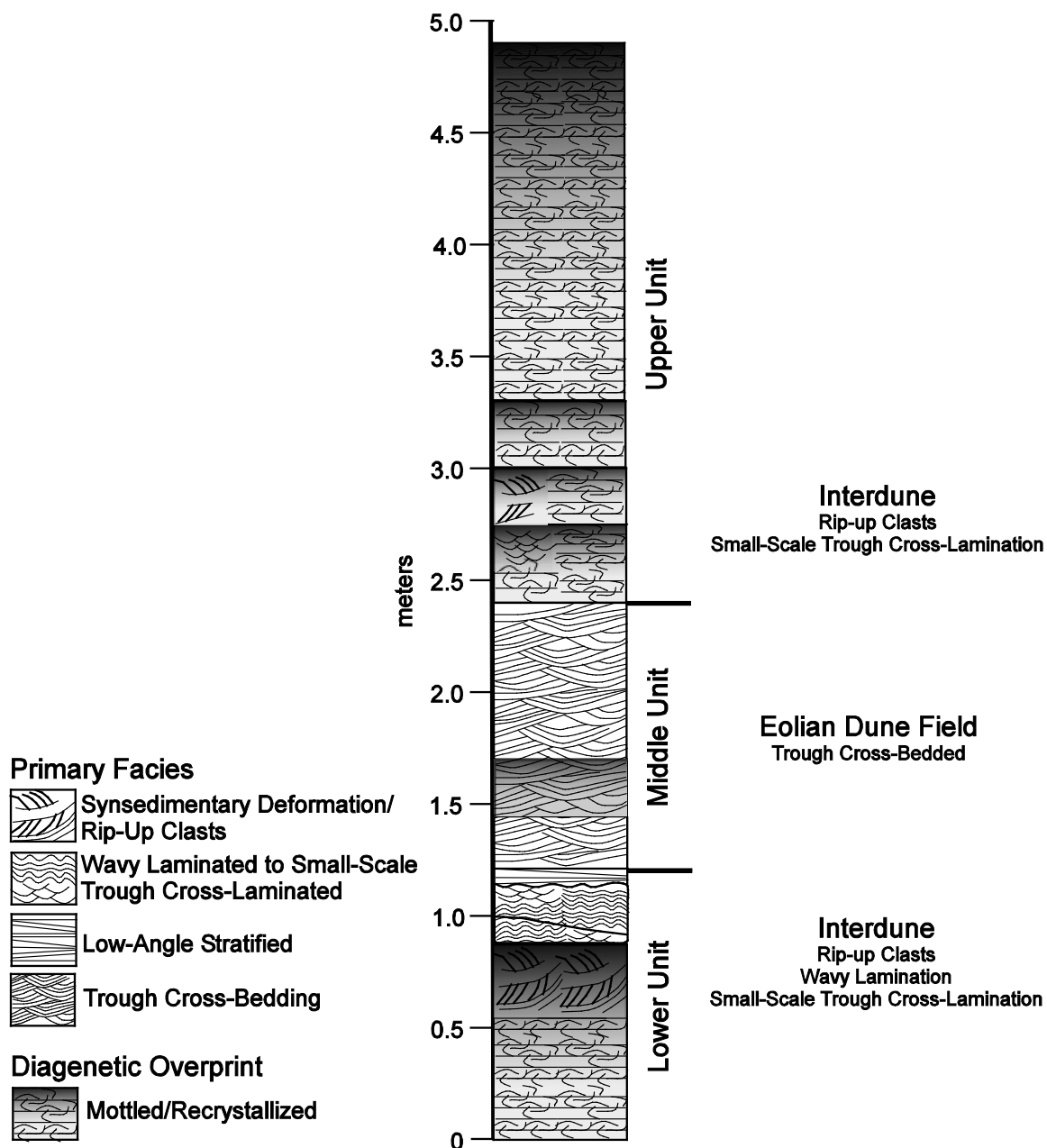


Figure 2.7 Stratigraphy of Payson. The five facies are defined on the basis of sedimentologic and diagenetic attributes. The lower mottled facies, syn-sedimentary deformed facies with rip-up clasts, and wavy- to small-scale trough cross-laminated facies are interpreted to have been deposited in an interdune environment. The low-angle stratified facies is interpreted to have been deposited in an eolian sand sheet. The ~ meter-wavelength trough cross-bedded facies is interpreted as representative of an eolian dune

field. The upper mottled facies with areas of small-scale trough cross-lamination and rip-up clasts is interpreted as representative of an interdune environment.

obliteration of primary depositional stratification (Beales 1972; Bullen and Sibley 1984). Though the rock composition for Payson is very different from these well-documented terrestrial carbonates, we envision a similar process whereby the appearance of a mottled facies at Payson is likely a diagenetic overprint and not a primary depositional facies. The

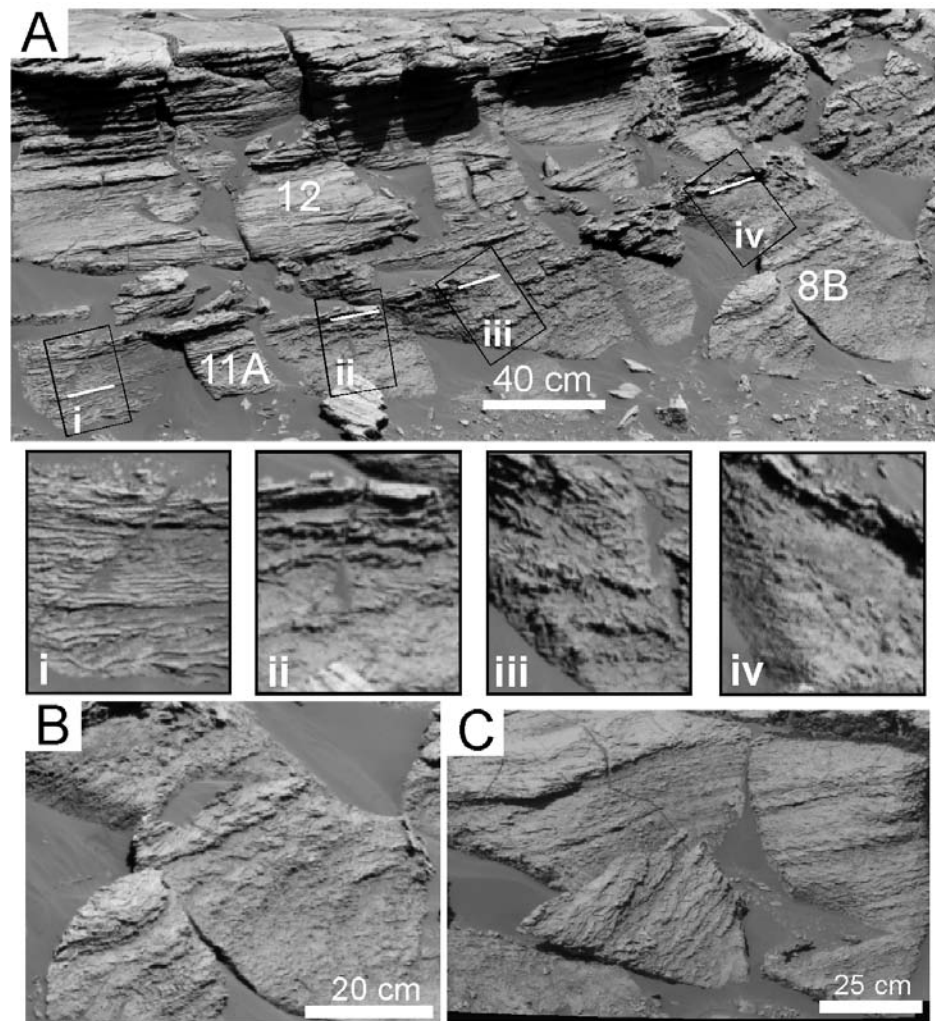


Figure 2.8 A.) Section of the Payson outcrop showing the locations of Figures 2.8B, 2.11A, and 2.12. The lateral and vertical variation in the extent of recrystallization can be seen;

the lateral variation is particularly noticeable along the stratigraphic horizon marked by the horizontal white lines. Boxes i-iv show the areas outlined in the black boxes in more detail. In box i, the original stratification is well preserved, but some of the original texture is lost farther along the same layer as shown in box ii. In box iii the recrystallization has been more intense, with much of the original stratification lost, while farther to the right in box iv the original stratification is almost completely lost. These images illustrate that although some areas of the outcrop may appear massive, they were all originally stratified at the centimeter-scale. Pancam image acquired on sol 749 with the 430 nm filter. B.) Close-up view of the mottled area below and including box iv. The original stratification is nearly absent due to recrystallization. C.) Close-up view of the upper mottled facies in the area indicated in Figure 2.2B. The mottled appearance of this area is interpreted to be the result of recrystallization. This palimpsest lamination suggests that the original stratification was likely wavy-laminated to small-scale trough cross-laminated. Pancam image acquired on sol 753 with the 430 nm filter.

intensity of the proposed recrystallization varies both horizontally and vertically in this facies in the lower unit of Payson (Fig. 2.8A i-iv). Where stratification is visible in the mottled facies in the lower unit, syndimentary deformation and possible rip-up clasts also are visible. The upper unit of Payson is composed entirely of the mottled facies which extends to the top of the outcrop (Figs. 2.2B, 2.7, 2.8c). In this area, where hints of the original stratification remain, it appears to be wavy- or small-scale trough cross-laminated (Fig. 2.8C).

Recrystallization could have occurred in the phreatic or capillary zone of a paleo-water table. Groundwater in contact with a sulfate evaporite deposit readily dissolves the rock unless the water is already saturated with respect to the specific sulfate phase (Johnson 2005; Tosca et al. 2005). Tosca et al. (2005) have modeled the evaporation of fluids derived from acid weathering of Martian basalt, and their model suggests that Mg, Ca, and Fe sulfates should be produced. They also calculated the solubility of these evaporite minerals under diagenetic conditions that were likely in Meridiani Planum and found that

epsomite (Mg sulfate) and melanterite (Fe sulfate) were the most soluble but gypsum took much longer to dissolve (Tosca et al. 2005). Since the rock in the mottled facies does not appear to have an increased porosity on a scale visible to the Pancam (minimum size of features that can be resolved is several millimeters), any fluid responsible for the diagenetic alteration must have been a brine saturated or very close to saturated with respect to the chemical composition of the rocks (Tosca et al. 2005).

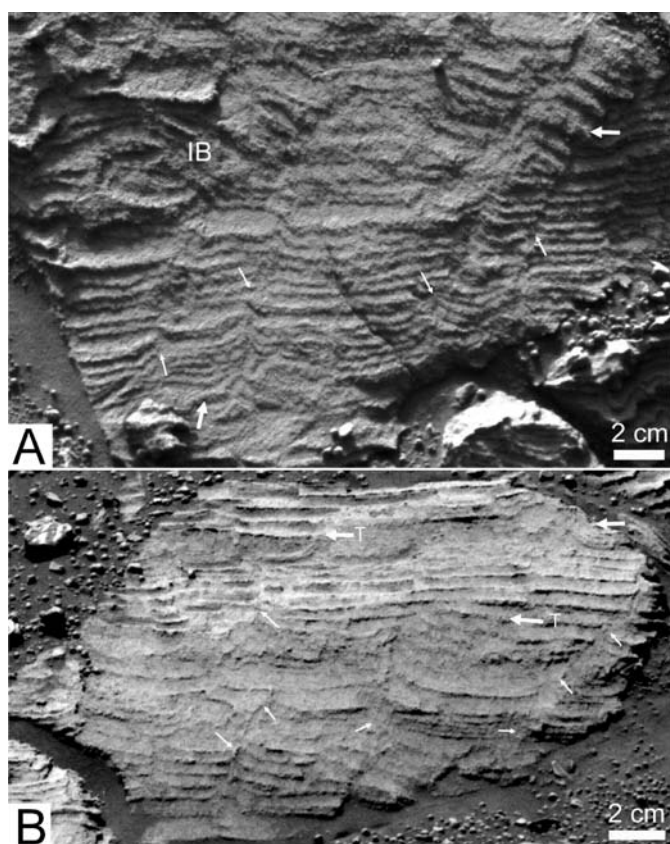


Figure 2.9 A.) Lower Overgaard. Two cracks at the right margin of Overgaard are reactivated, in the upper part of the rock, to form a soft-sediment deformation fold (upper large arrow). To the left of the fold, in equivalent strata, note generally incoherent bedding (labeled “IB”) suggesting soft-sediment deformation. Also note soft-sediment-related folding in lowermost part of rock (lower large arrow); fold is overlapped by overlying laminae. This super-resolution image was acquired on Sol 698 at 16:32:03 LTST using

Pancam's 482 nanometer filter, sequence id p2572. B.) Skull Valley. Numerous penecontemporaneous cracks (small arrows) crosscut lamination, some oblique to bedding. Note zone of soft-sediment deformation in upper right corner of rock (large arrow in upper right). Note truncation of upward-deflected laminae along discrete bedding planes in center and upper parts of rock (large arrows with T). This super-resolution image was acquired on Sol 713 at 13:48:35 LTST using Pancam's 482 nanometer filter, sequence id p2589.

2.4.2 *Synsedimentary Deformed Sandstone*

2.4.2.1 Soft-Sediment Deformation

Soft-sediment deformation features were observed at Eagle crater (see Fig. 2.13D in Grotzinger et al. 2005) and are abundant in the Olympia outcrop. At both locations such features are closely associated with the small-scale trough cross-laminated facies and synsedimentary shrinkage cracks. All observed features are of small scale, and consist of irregular zones of crude bedding that are laterally adjacent to cracks, and zones of bedding-parallel shortening and folding. These are illustrated in two rocks in the Olympia outcrop: in the middle and upper parts of Skull Valley, and in the upper part of lower Overgaard (Fig. 2.9).

The upper part of lower Overgaard contains deformed strata in which a small-scale fold along the right edge of the field of view of the rock nucleates and grows above a boundary that approximately coincides with the upper limit of underlying synsedimentary cracks (Fig. 2.9A). Strata that define this fold pass laterally (to the left) into other deformed strata. Notably, all of this deformation does not seem to affect the lower (cracked) part of lower Overgaard, suggesting bedding-parallel shortening above a distinct

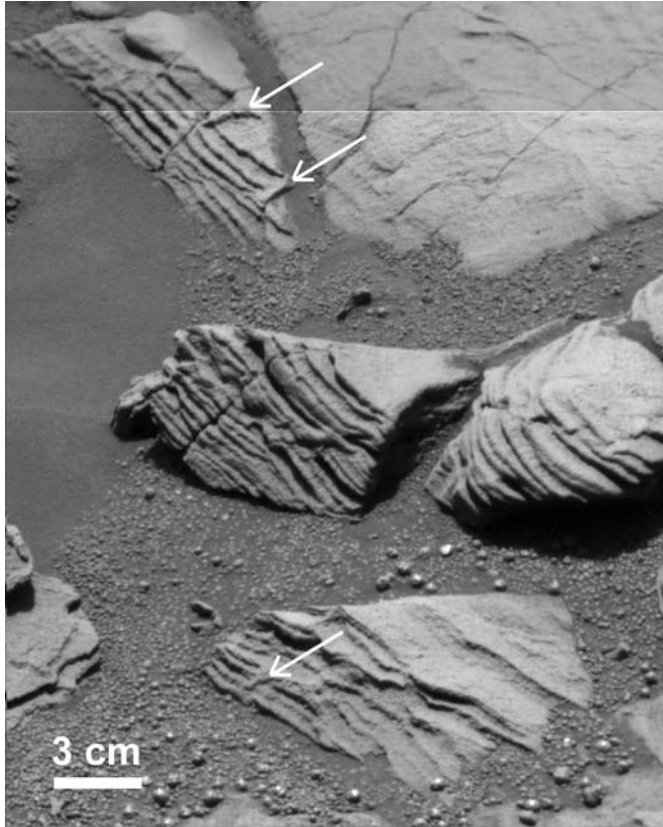


Figure 2.10 Possible shrinkage cracks in the rock Bellemont. White arrows highlight the locations of the cracks. Note how cracks taper downward in a v-shape cutting perpendicularly across several laminae. This super-resolution image was acquired on sol 665 with the 482 nm filter.

surface of detachment. However, the lowermost part of lower Overgaard also seems to contain a zone of folding; here, folds seem to be overlapped by younger laminae containing the planar cracks described in Grotzinger et al. (2006).

Skull Valley contains a distinct zone, localized near the upper part of the rock, which likely also involves soft-sediment deformation (Fig. 2.9B). At the upper left margin of the rock a cracked lamina is portioned into three pieces which are offset. The right-hand fragment is curled upward. At this stratigraphic level, in the center of the rock, all texture

is lost and the bedding is massive. Along the right margin of the rock this massive zone shows evidence of projecting upward across laminae which are also deformed in an upward direction. Underlying laminae are relatively intact, which suggests that sediments in the massive zone were fluid enough to penetrate bedding. By analogy to similar terrestrial features, this could have involved flow across upward-directed pressure gradients induced by early compaction of differentially permeable sediments.

2.4.2.2 Shrinkage Cracks

Possible shrinkage cracks are common in the Olympia outcrop. These cracks have been identified in the rock Bellemont in a cross-sectional view where they are observed to taper downward in a v-shape (Fig. 2.10). They cut perpendicularly across several sedimentary layers and have also been infilled with sediment. Putative cracks appear to start at several levels, are up to 6 mm wide at their surface of initiation, and taper downward to 1-2 mm at their base over a stratigraphic distance of 5-8 mm (3-4 laminae). MI data show that cracks are filled with sediment that is texturally similar to laminae which are cracked. Most cracks are oriented perpendicular to bedding, though some crosscut bedding at an angle and may show compaction-related deformation.

The rapid taper and large amount of shrinkage which caused these cracks is unusual for terrestrial sandstones; here it is possibly due to the unusual mineralogy of the grains. The original grains were not nonporous silicate grains, such as olivine or pyroxene, but probably a lightly cemented mudstone (McLennan et al. 2005). Geochemical measurements and modeling suggest that the grains are magnesium sulfates (McLennan et

al. 2005). If the grains were deposited as a hydrated magnesium sulfate such as epsomite (with seven waters of hydration), then dehydration may have caused the sediments to shrink enough to cause these cracks. However, this is speculative due to the uncertain timing of dehydration which may have occurred over longer time scales. More likely, shrinkage was due to a dehydration of the pore fluids, which would have existed in the lightly cemented grains as well as between grains.

Prism cracks, which are polygonal networks of cracks that form normal to bedding and break the sediment into vertical prisms (Fischer 1964), were also identified in the Olympia outcrop. These occurrences were described in Grotzinger et al. (2006) and interpreted as shrinkage cracks formed during desiccation of damp sediments. The columnar structure of the prism cracks is maintained by repeated cycles of wetting and drying, with cracking over the same polygonal cracks occurring after deposition of new lamina (Demicco and Hardie 1994).

2.4.2.3 Rip-Up Clasts

The mottled facies in the lower unit of Payson contains possible evidence of brittle synsedimentary deformation, including potential rip-up clasts (Fig. 2.11). The rip-up clasts are interpreted to represent chips and pieces of former lamination that were cemented early and then broken up and reworked. A consistent flow direction results in clast imbrication; several imbricated clasts are seen in the Payson outcrop, and they indicate a flow direction from north to south.

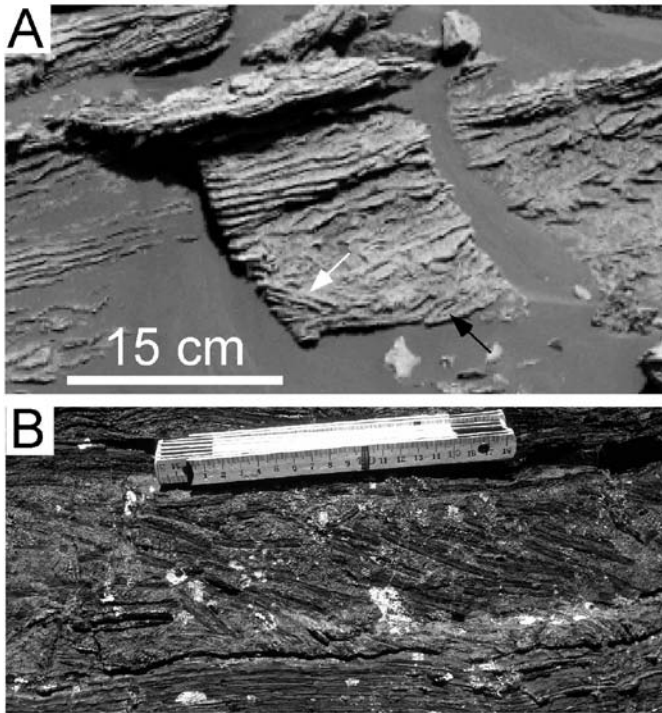


Figure 2.11 A.) Close-up of the area with putative rip-up clasts indicated in figure 2.7A. These rip-up clasts likely formed when the surface sediment became crusted over and was then later broken up, reworked, and deposited by a current. The clasts indicated by the white arrow appear to be imbricated. The clast indicated by the black arrow appears to have broken into at least two pieces. There may also be a few more clasts imbricated in the same direction as those mentioned above in the block to the right, although they are more poorly defined. B.) Earth analog showing imbricated rip-up clasts from the Rocknest Formation (1.9 Ga), northern Canada. Scale is in centimeters.

Some of the putative rip-up clasts seen in Payson appear to have still been somewhat soft when they were ripped up, since they appear curved or deformed (near black arrow in Fig. 2.11A). Others seem to have undergone brittle deformation, because they were already partially lithified; therefore, these clasts remained flat (white arrow in Fig. 2.11A.). Evidence to support the supposition that these are rip-up clasts includes the fact that the thickness of the putative rip-up clasts is the same as the intact lamination above and below the deformed area. Also, some of the pieces appear to have been laminae that

were deformed and then broken off from more continuous lamination at the same stratigraphic level. Such syndepositional deformation and rip-up structures are often found in wet interdune environments (Mountney and Thompson 2002).

It is possible that these features are related to later strain, associated with the impact-forming deformation event. However, these features are developed only in a few specific beds. Furthermore, they have not been observed in any other outcrops, including Eagle and Endurance craters where impact also occurred. Such penetrative strain would be expected to be ubiquitous, yet these features are rare. Therefore, their origin due to impact seems unlikely.

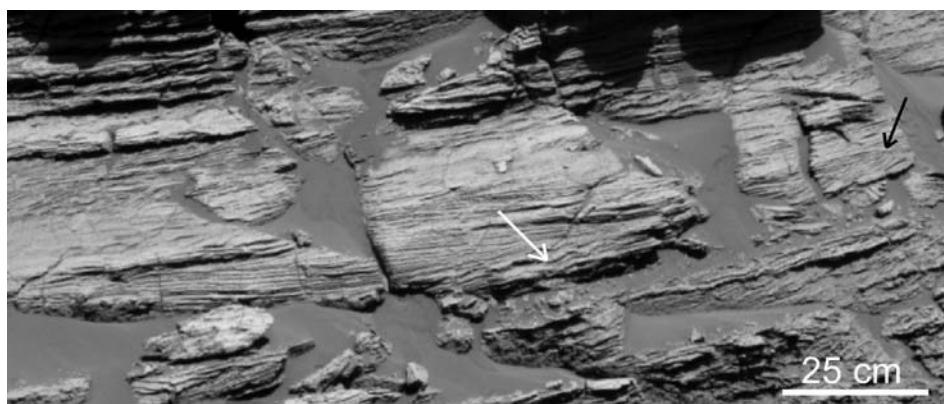


Figure 2.12 Wavy and low-angle stratification in the area of the Payson outcrop indicated in Figure 2.8A. Wavy lamination is indicated by the white arrow and low-angle stratification by the black arrow.

2.4.3 Small-Scale Trough Cross-Laminated to Wavy-Laminated Sandstone

Possible centimeter-scale trough cross-lamination occurs in some beds near the south end of Payson. The potential small-scale troughs are not well exposed, and the

resolution of the images in the areas with the potential troughs is not sufficient to identify them unambiguously. The Olympia outcrop, however, contains several areas that show well-exposed small-scale trough cross-lamination, described in Squyres et al. (2006) and Grotzinger et al. (2006). Small-scale trough cross-lamination (also known as festoon cross-lamination) is formed by migration of three-dimensional ripple bedforms with sinuous crestlines that climb at generally positive angles in flowing water (Rubin 1987). The bounding surfaces scoured by three-dimensional bedforms tend to be trough-shaped. This type of cross-lamination at this scale is common in deposits of subaqueous ripples (Hunter 1977b; Winston 1978) but very rare in deposits of eolian impact ripples. Eolian ripples typically have straight crestlines and uniform spacing, and therefore deposit thin tabular beds; these deposits are typically inversely graded rather than cross-laminated (Hunter 1977b).

Wavy-laminated strata occur in the lower unit of the Payson stratigraphy, between 0.9 m and 1.2 m (Figs. 2.7, 2.12), and in the upper unit of Yavapai, between 2.25 m and 2.70 m (Figs. 2.13, 2.14). Palimpsest lamination in the mottled facies in the upper unit of Payson indicates that wavy lamination may have been the precursor stratification in this area as well. A large portion of the Olympia outcrop is also wavy-laminated (Fig. 2.6). Wavy-laminated strata may result from shallow scours backfilled with laminae that drape the scour surface, which could be caused by local turbulence, changes in wind speed, or fluctuations in surface wetness or sediment supply (Kocurek 1981).

Wavy lamination is characteristic of damp to wet interdune environments (Kocurek 1981). In a study of eolian sandstones, Hunter (1981) described wavy bedding deposited in wet interdune areas. He attributed relatively regular waviness to ripples (wave ripples, wind ripples, or subaqueous ripples), and he attributed less regular waviness to adhesion-ripple growth, current or wind scour, gas-bubble growth and escape, dewatering, and small-scale loading.

Given the evidence for migration of small-scale subaqueous ripples described above, it is also possible that the wavy lamination could have resulted from supercritically climbing ripples (i.e., ripples that climb at angles greater than the angle of the stoss slope). If true, this would imply that the flows were decelerating with high concentrations of suspended sediment.

2.4.4 Flat-Laminated to Low-Angle-Stratified Sandstone

Flat-laminated to low-angle cross-stratified strata typically display thin lamination that is geometrically arranged in bed sets showing low-angle truncations (less than 20°). This is in contrast to the cross-strata which form by migration of dune slip faces, which are usually tangential to their underlying bounding surfaces (Fryberger et al. 1979).

The thin lamination is likely the expression of alternating finer and coarser layers deposited during sediment transport in eolian environments where wind ripples migrate under conditions of bed accretion (Hunter 1977a). This type of facies probably represents translational wind-ripple strata deposited on dune bottomset beds or in a sand sheet (Kocurek

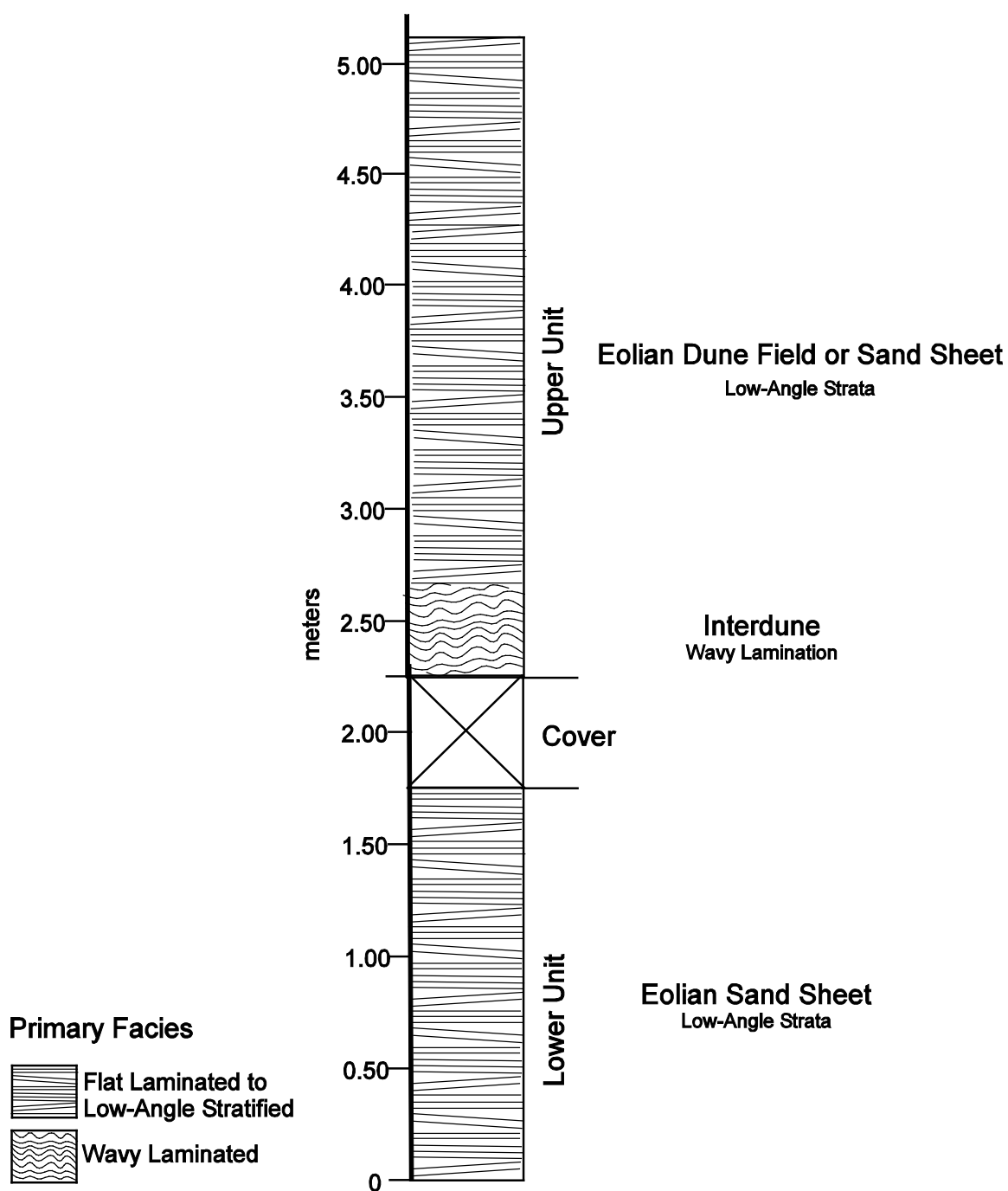


Figure 2.13 Stratigraphy of Yavapai. Two units in Yavapai are separated by an interval of soil cover. The lower unit is flat laminated to low-angle stratified and is interpreted to have been deposited as an eolian sand sheet. The upper unit can be subdivided into two facies. The lower facies is wavy-laminated and was likely deposited in an interdune area. The upper facies is flat laminated to low-angle stratified and was likely deposited in either an eolian dune field or a sand sheet.

and Nielson 1986), where each individual lamina is formed by the translation of a single wind ripple. The ripples in this case were likely subcritically climbing, since these result in well-defined tabular lamination where cross-lamination is rarely seen. Low-angle cross-stratification can also form on the lee side of a dune, where the slope is lower than the angle of repose (such as on bottomset beds), and sand is deposited by grainfall (Hunter 1977b; Hunter 1981).

Much of the Yavapai outcrop appears to be composed of this facies. In the upper unit is an ~ 2-m-thick facies which appears to be planar- to low-angle stratified. The strata in this unit are ~ 1-2 cm thick. Laminae produced by wind ripples on Earth are typically a few millimeters thick (Fryberger and Schenk 1988; Stolper et al. 2007); however, the strata in the Yavapai outcrop, which may have formed from the migration of wind ripples, are closer to 1-2 cm thick. Sands with a greater grain size range can produce ripples with a greater height, so this may imply that the ripples at Yavapai had a larger range of grain sizes (Bagnold 1941).

However, several other possible processes could have deposited the beds in the upper unit of Yavapai. One possibility is that we are not able to discern finer-scale (millimeter) laminae because of the resolution limits of the images, and so these 1-2 cm thick beds are actually bedsets of finer-scale laminae. This is a likely explanation given that the smallest features in the images that we can discern at this distance from the outcrop are ~ 8 mm. It is also possible that the centimeter-scale stratification was formed by eolian grainflows. Grainflows occur on the foresets of dunes, so if the dunes had straight

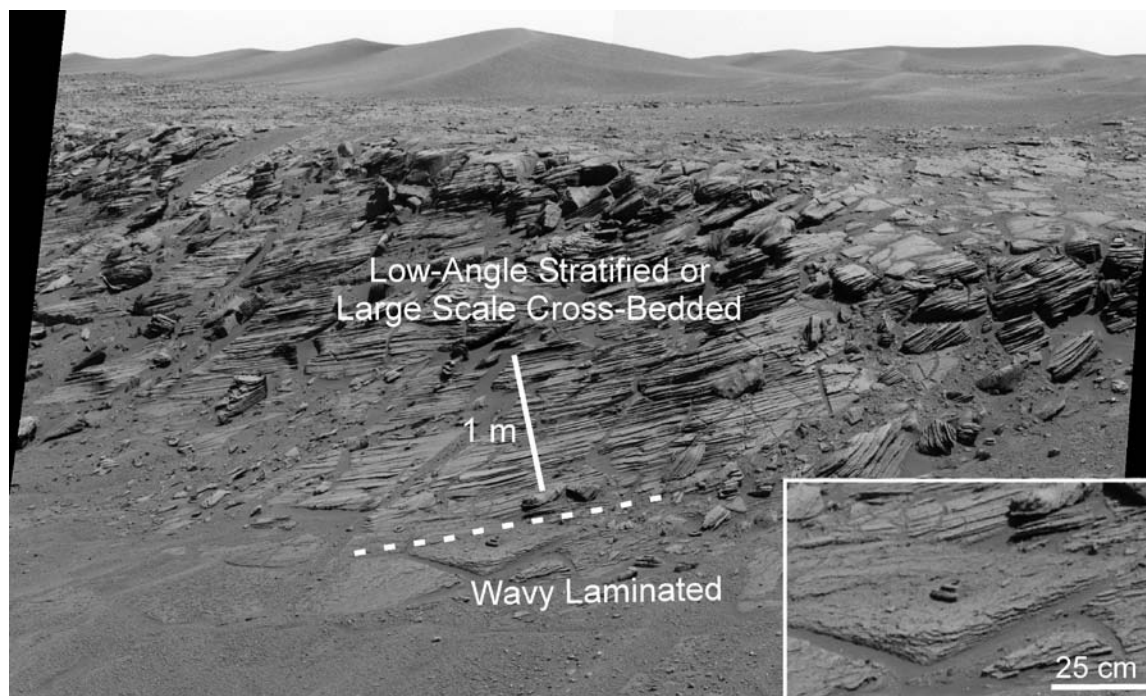


Figure 2.14 Yavapai upper unit. The lower facies is wavy-laminated, and the upper facies is either low-angle stratified (rotated by deformation) or one-half of a large trough-shaped bedform. The dashed white line indicates the facies transition. The inset shows the wavy-laminated facies up close. Pancam images acquired on sol 758 with the 430 nm filter.

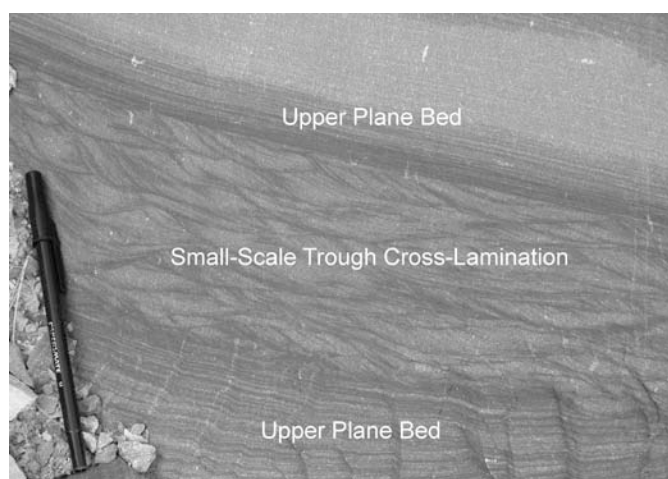


Figure 2.15 Upper flow-regime plane beds pass into to lower flow-regime small-scale trough-cross-lamination in 1.4 Ga Mt Shields Formation, Belt Supergroup, Montana. The flows responsible for this lamination were formed in shallow channels. As the flow

decelerates, it passes into small-scale trough cross-lamination. The top of the small-scale trough cross-laminated deposit was eroded away by the next event of high-velocity flow and upper-plane-bed deposition. Pen is 15 cm long.

crestlines and if this is a view that is oblique or normal to transport, then it would show centimeter-scale planar lamination. However, grainflows typically have a limited lateral extent and appear as lenses in a strike section as shown by Hunter (1977a, his Fig. 8), but these lenses may not be visible given the low resolution of the images. They could also potentially be deposits of the upper flow regime of an aqueous flow, but this is less likely given the thickness (~ 2 m) of this deposit. Planar-laminated deposits formed in the upper flow regime are often on the order of tens of centimeters thick (Bal and Lewis 1994; Langford and Bracken 1987), because they are limited by the difficulty of maintaining a constant flow without decelerating into a lower flow regime (Fig. 2.15). However, it is possible to stay in the upper-plane-bed regime and maintain high flow velocities for a long time at substantial flow depths, which can happen in fluvial environments, shallow marine environments, as well as in turbidity-current deposition in deep water. If the rate of downstream decrease in sediment transport rate is sufficiently great, a thick succession of planar-laminated sediment can be deposited. Another possibility is that these beds were formed by supercritically climbing wind ripples, which are also unlikely to persist over such long distances since they require high sediment aggradation rates or rapidly decreasing through-going sediment transport rates (Rubin and Hunter 1982).

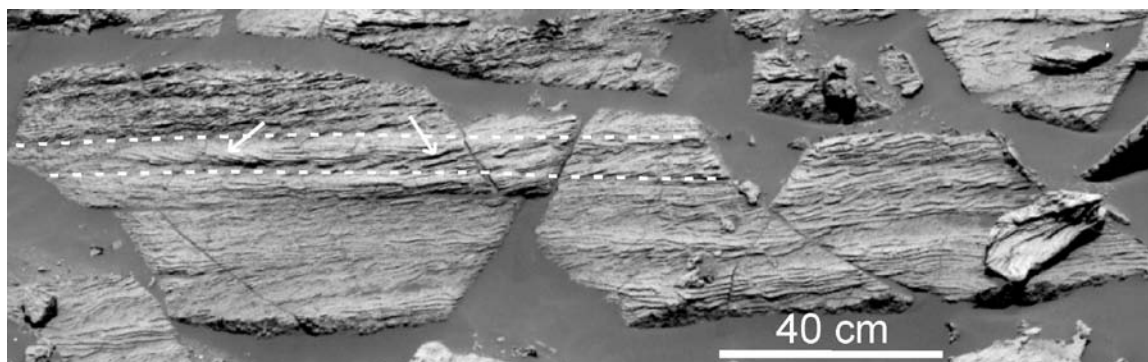


Figure 2.16 Close-up view of the area of trough cross-bedded sandstone shown in Figure 2.2A. The dashed white lines indicate a cross-bed set boundary, and the white arrows indicated the cross-beds in this layer. The cross-beds can be seen to be dipping in opposite directions, although there is a preponderance of dips to the left, suggesting a view cut obliquely to transport. If an individual cross-bed is traced across the layer, it can be seen to form a trough with a wavelength of ~ 1 m. Pancam image acquired on sol 749 with the 430 nm filter.

2.4.5 Trough Cross-Bedded Sandstone

The middle unit of Payson is composed of fairly regular ~ 3 -4 cm thick cross-stratified bedsets, with shallow trough geometry (Figs. 2.2, 2.16). The cross-beds in each set dip in opposite directions. If an individual cross-bed is traced across the layer, it can be seen to form a trough with a wavelength of ~ 1 m. More of the cross-beds dip to the left than to the right; thus there is also a component of transport from right to left, which means that the outcrop face is oblique to the paleoflow direction.

These cross-strata likely represent the toes of larger sinuous-crested eolian dunes deposited during bedform migration. If a dune migrates at a subcritical rate of climb, only a portion of the foreset of the dune is preserved and sets of cross-strata are separated by erosional bounding surfaces (Kocurek 1991). This typically leads to preservation of only the basal portions of dunes in the rock record, and hence set thickness is only a fraction of

the original bedform height (Rubin and Hunter 1982). Thus, the dunes that deposited these cross-strata were probably larger than 4 cm.

2.5 Facies Associations and Depositional Environments

The facies observed at Erebus crater form three distinct facies associations which characterize a dune-interdune system. These facies associations are eolian dune, damp-wet interdune, and eolian sand sheet. Similar facies associations were described for the Burns formation in Endurance and Eagle craters (Grotzinger et al. 2005).

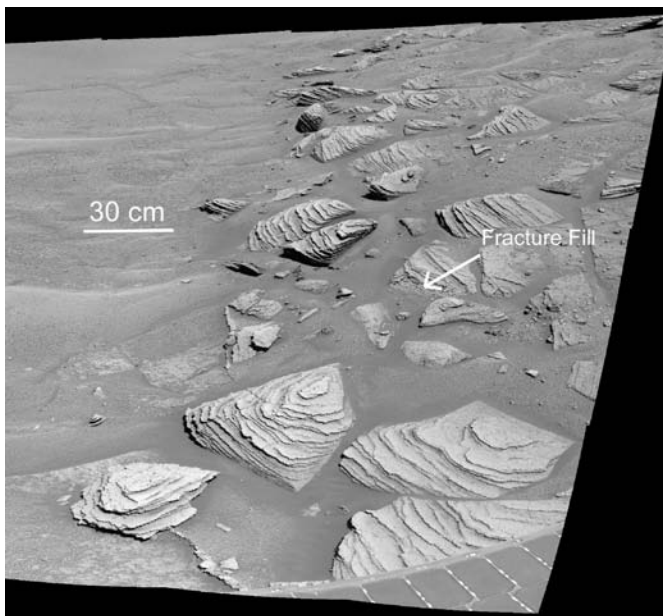


Figure 2.17 Yavapai lower unit. This unit is flat laminated to low-angle stratified and weathers to a rough appearance. The location of a fracture fill is marked. Pancam images acquired on sol 758 with the 430 nm filter.

2.5.1 Eolian Dune

The eolian-dune facies association includes the trough cross-bedded facies in the middle unit at Payson (Fig. 2.7) and potentially the flat laminated to low-angle stratified facies of the upper unit of Yavapai, if this stratification is representative of two sides of large trough cross-beds (Fig. 2.4). These trough cross-beds are indicative of sediment transport by migrating sinuous-crested dunes. This suggests at least an episodically dry climate or a low water table due to other topographic effects in the region. The extent of the paleo-dune field is uncertain, but it was likely relatively widespread since similar facies were identified in Endurance crater ~ 4 km away and layers of this formation appear to be laterally continuous as inferred from MOC and TES data.

2.5.2 Eolian Sand Sheet

There is a thin exposure of the eolian-sand sheet facies in the lower unit at Payson and it may be the dominant facies at Yavapai (Figs. 2.2, 2.14, 2.17). There are also exposures of the sand sheet facies at Olympia (Fig. 2.6). These associations are composed of flat-laminated to low-angle-stratified sandstone and consist largely of wind-ripple laminae. Sand sheet deposits are transitional facies between dune and interdune deposits and also often form on the boundaries of dune-interdune systems (Fryberger et al. 1979; Kocurek and Nielson 1986). They form from the accretion of wind-blown sand in areas where conditions are not suitable for the formation of dunes or where some factors inhibit the formation of dunes (Kocurek and Nielson 1986). Factors that favor sand sheet development are: (1) a high water table, (2) early cementation, (3) high sediment moisture content or wetting during floods, and (4) coarse-grained sediment (Kocurek and Nielson

1986). Instead of forming dunes under these conditions, these factors result in low, rolling, hummocky topography.

The thin lamination seen in sand sheet deposits is deposited by wind ripples by the saltation of sand. The low-angle discordances develop during the migration of low-relief mounds of sand, not by slip-face processes such as grainflows.

2.5.3 Interdune

An interdune depression is commonly enclosed or partly bounded by eolian dunes or sand sheets (Ahlbrandt and Fryberger 1981). Several of the facies in the Olympia and Payson outcrops, as well as the base of the upper unit of Yavapai, are indicative of a damp to wet interdune environment (Figs. 2.6, 2.7, 2.13). The association of small-scale trough cross-lamination, wavy laminae, desiccation cracks, and rip-up clasts is indicative of a damp to wet interdune environment with episodic wetting and drying, which could result from minor fluctuations in the groundwater table (Mountney and Thompson 2002). Sedimentation in interdune depressions is enhanced by a high water table and early evaporitic cements, and since interdune deposits form in topographic depressions, they are selectively preserved (Hummel and Kocurek 1984). An interdune environment can be classified as “dry,” “damp,” “wet,” or “evaporitic” on the basis of the abundance of water-induced processes (Fryberger et al. 1983; Kocurek 1981).

In a wet interdune environment, the water table is shallow, and the deposits are within the capillary fringe of the water table. Sedimentary structures typical of a wet

interdune environment are small-scale trough cross-lamination, wavy lamination (Hunter 1981), contorted or syndepositionally deformed strata, and rip-up clasts (Fryberger et al. 1983). A damp interdune commonly exhibits contorted or syndepositionally deformed strata and adhesion structures caused by sand adhering to a damp surface (Fryberger et al. 1983; Kocurek 1981). A dry interdune consists mostly of wind-ripple strata and exists where the water table is relatively deep (Fryberger et al. 1983; Kocurek 1981).

The facies associations in the Olympia outcrop indicate a mainly wet interdune environment because of its multiple exposures of small-scale trough cross-lamination, wavy lamination, and syndimentary deformed strata. The Payson outcrop is indicative of a damp-wet interdune because of its exposures of wavy lamination, possible rip-up clasts, and occasional small-scale trough cross-lamination. The thin exposure of wavy lamination at the base of the upper unit of Yavapai indicates a damp interdune environment.

2.5.4 Olympia Outcrop Stratigraphy

In attempting to develop a stratigraphy that allows correlation within outcrops as well as between outcrops, we are limited to consideration of physical attributes only, in particular the facies. Only one rock at Olympia was analyzed for its chemical and mineralogic composition, and none were analyzed at Payson and Yavapai. The analysis at Olympia of the rock “Ted” indicates that this rock is similar in composition to rocks analyzed at other localities visited by *Opportunity* (Knoll et al. 2008).

The Olympia outcrop was divided into several facies as discussed above, including planar to wavy-laminated sandstone and small-scale trough cross-laminated sandstone. Some rocks show penecontemporaneous sedimentary features including shrinkage cracks and soft-sediment deformation (Fig. 2.6). Several examples of small-scale trough cross-lamination and shrinkage cracks at Erebus crater were previously described by Squyres et al. (2006) and Grotzinger et al. (2006). Some facies could be correlated between a few adjacent outcrop blocks, but there were no facies patterns that could be correlated across the Olympia outcrop due to their displacement and rotation.

2.5.5 Payson Outcrop Stratigraphy

Payson was divided into several facies (Figs. 2.2, 2.7), which are distinguished by their sedimentary structures, secondary diagenetic textures, and color. These facies are grouped into three units: a lower unit, a middle unit, and an upper unit. The lower unit is ~1.25 m thick and is composed of three facies: a mottled facies, a wavy-laminated facies, and a low-angle-stratified facies. The mottled facies has a texture interpreted to be the result of recrystallization and grades laterally (from north to south) and vertically from strongly recrystallized, such that the original sedimentary structures cannot be distinguished, to less severely recrystallized, such that some primary structures can be identified. One structure that can be identified is the putative rip-up clasts. Figure 2.8A shows the lateral variation within the mottled facies grading from the northernmost areas, where primary textures have been almost completely destroyed, to areas where the original stratification, including rip up clasts, are visible. This lateral variation in the

recrystallization is a real effect and not an artifact of the limitations of the image resolution. The details of the textures are within the resolution limits for all described areas of the outcrop. This mottled facies is approximately 90 cm thick, and its upper contact is a scour surface. Above the mottled facies is a 20-30 cm thick wavy-laminated facies with rare sets of centimeter-scale trough cross-lamination (Figs. 2.2A, 2.7). A scour surface can be seen in this facies; its upper contact is also a truncation surface. The third facies in the lower unit of Payson is a 10-cm-thick low-angle-stratified facies whose top is a scour surface (Figs. 2.2A, 2.7).

The middle unit of Payson is composed entirely of a trough cross-bedded facies. This unit is 1.2 m thick, and the troughs have meter-scale wavelengths (Figs. 2.2, 2.7, 2.16). Since trough cross-stratification is a way-up indicator, it implies that the rocks in the Payson outcrop are the right way up and not part of an overturned flap. Overturned flaps are part of the ejecta blankets of impact craters and are sections of pre-existing stratigraphy that are ejected from the crater and are preserved in detail, but inverted (Jones 1978).

The upper unit is 2.4 m thick and is characterized by a facies with a mottled texture interpreted to be the result of recrystallization with rare zones of centimeter-scale trough cross-lamination and rip up clasts. The boundary between the middle and upper units is gradational and is the result of diagenetic alteration obscuring the lamination (Fig. 2.2B).

The geomorphic rim that defines the top of the outcrop appears to be horizontal but is not a bedding plane, since the bedding can be seen cutting across the rim in some places (Fig. 2.2). The location of the rim varies between the middle and the upper unit. The

geomorphic expression of the rim reflects differential lithification, probably the result of diagenesis that postdates deposition and deformation. This is consistent with the groundwater table rising above the tilted and buried layers. The groundwater table should be more or less horizontal, especially in porous sediments.

2.5.6 Yavapai Outcrop Stratigraphy

The lower unit of Yavapai is a planar-stratified to low-angle-stratified unit and is approximately 1.75 m thick (Figs. 2.13, 2.17). The contact between the lower and upper unit is obscured by a cover of soil (Fig. 2.3). The upper unit of Yavapai contains two facies (Figs. 2.13, 2.14). The lower facies is wavy-laminated, and its contact with the upper facies is not clearly resolved because of the quality of the images and soil cover (Fig. 2.14 inset). The upper facies is thin bedded with several low-angle truncation surfaces. Because close-up images of Yavapai were not acquired, it is not possible to see the details of this outcrop. Since the upper facies is not resolved, we propose several possible interpretations based on its similarity to other similar-scale stratification at Meridiani: (1) The stratification is large-scale cross-bedding and the two different dip directions are the two sides of a large trough bedform (Fig. 2.4B). No structural deformation is necessary for this option. (2) The planar to low-angle stratification represents preservation of the basal foresets of migrating straight-crested dunes. The outcrop exposure is a view cut perpendicular to the transport direction. Later, the beds were deformed to acquire their present day dips (Fig. 2.4A). (3) The planar to low-angle stratification is the result of migrating hummocky low-amplitude bedforms in a sand sheet. The present day dips in this case are also due to later

deformation. It is not possible to distinguish between these possibilities without higher-quality images or examination of additional outcrop exposures.

2.6 Discussion

2.6.1 Alternative Interpretations for Depositional Processes

2.6.1.1 Base Surge

Two alternative interpretations have been suggested which propose that the stratification observed at the Opportunity landing site was the result of base-surge processes, alternatively generated by volcanic (McCollom and Hynek 2005) or impact (Knauth et al. 2005) processes. However, the sedimentology of the Olympia, Payson, and Yavapai outcrops differs broadly from the attributes predicted by these interpretations. Pyroclastic surges are characterized by the following facies from a vent-proximal to vent-distal direction: decimeter- to meter-scale supercritically climbing cross-stratification, massive deposits, and planar, centimeter-scale stratification (Wohletz and Sheridan 1979). Base surges also are commonly coarse-grained and have poor sorting over meter scales. Bomb sags are common. Desiccation cracks and imbricated rip-up clasts are not described.

No decimeter- to meter-scale supercritically climbing cross-strata were observed at Olympia, Payson, or Yavapai. Massive beds that might represent mass-flow deposits are also not observed. While a mottled and poorly stratified facies was observed, which might at first glance suggest a possibly massive facies, even this has palimpsest millimeter-scale lamination, which indicates that it was emplaced as a thinly-laminated deposit. Therefore,

these beds were not deposited as mass flows, but rather as a result of traction-controlled transport. Their mottled appearance is interpreted to result from postdepositional recrystallization. Wavy lamination at the millimeter-scale and small-scale trough cross-lamination, as observed at Payson, has not been reported in surge deposits. Wavy bedding does occur in base-surge deposits, but it is an order of magnitude larger in scale (Branney and Kokelaar 2002). Planar-laminated facies are observed at Olympia, Payson, and Yavapai, and are found in both base-surge and dune-interdune deposits. No bomb sags were observed in any of the outcrops at Erebus crater (or in any other strata previously studied by *Opportunity* at Meridiani). The facies pattern at Erebus as a whole, given the lack of decimeter- to meter-scale supercritically climbing cross-strata and the presence of millimeter-scale wavy lamination and centimeter-scale trough cross-lamination, is more consistent with a dune-interdune environment than a base-surge deposit. This is further supported by the consistently fine-grained nature of the Meridiani deposits and their excellent sorting (Squyres et al. 2006). Finally, the possible desiccation cracks observed at Olympia and the imbricated rip-up clasts observed at Payson are most consistent with an eolian interdune environment.

2.6.1.2 Aqueous Deposition

Another alternative interpretation for the Meridiani strata is that they were deposited predominantly during subaqueous sedimentation. This was considered briefly in Grotzinger et al. (2005). All of the types of stratification observed in the outcrops to date could form as a result of subaqueous sedimentation.

Small-scale trough cross-lamination is exceedingly rare in purely eolian deposits. However, trough cross-beds with wavelengths of 1 m and heights between 3-4 cm (as seen in the Payson outcrop) form by migrating sinuous-crested bedforms and develop in both eolian and subaqueous settings. The scale of these bedforms does not uniquely determine their origin. Also, since only the basal portions of the bedforms were preserved, the original bedform height was likely greater than 4 cm. Subaqueous dunes typically have a height that is 10-40% of the flow depth (Leclair 2002), which implies, if these bedforms were produced subaqueously, that water flow depths exceeding ~ 40 cm would have been attained.

More problematically, large-scale cross bedding, such as that observed in the lower unit of the Burns formation in Endurance crater, could represent large subaqueous dunes. Dunes of this type could form in fluvial bar forms (Miall 1992) or shallow marine, tidally generated bar forms (Dalrymple 1992). Bedsets of large scale cross-beds in Endurance crater range in height from 5 cm up to greater than 2.2 m (Grotzinger et al. 2005). Since bed thickness is typically only a small fraction (~ 10%) of the height of the bedform that deposited it, the dunes which deposited these cross-beds could have been many meters high (Rubin and Hunter 1982). This would require water flows that were even deeper (Leclair 2002), possibly on the order of 10 meters or greater. Since tidal currents on Mars should be only 5-10% of terrestrial mean tides (de Pater and Lissauer 2001), it is unlikely that tidal currents on Mars would have been strong enough to generate these bedforms. Also, MOLA data indicate that Meridiani does not form a closed basin (Aharonson et al. 2001), so it would be difficult to contain a body of water deep enough to contain large subaqueous

dunes. Nevertheless, it is possible that these large-scale bedforms were fluvial in origin. This would imply deep and strong flows of water in order to produce subaqueous dunes many meters in height. With these significant flows, the water would be expected to channelize. While channels and inverted valleys have been found in Meridiani Planum, they are located at a lower stratigraphic level than the outcrops discussed here (Edgett 2005). Evidence for channels, such as levees or point bars (Miall 1992), has not been found by the rovers. Furthermore, grain size might be expected to locally coarsen within possible channel deposits. This has not been observed.

Low-angle to planar lamination could form as a result of sediment transport in high-velocity, upper-flow-regime subaqueous flows. However, the 1-2 m thick deposits of low-angle to planar lamination are unlikely to form subaqueously given the thickness of this deposit. In a search of the literature, 33 deposits of upper-flow-regime plane-bed lamination were found with a thickness less than a meter (Bal and Lewis 1994; Chakraborty and Bose 1992; Cheel and Middleton 1986; Dardis 1985; Langford and Bracken 1987; Plint and Wadsworth 2003; Røe 1987; Schwartz 1982; Shaw 1972; Sohn et al. 1999; Williams 1971); six deposits were found with a thickness between 1 and 2 meters (Bal and Lewis 1994; Røe 1987; Shaw 1972); and three deposits were found with a thickness of 2 meters or greater (Anderson 1976; Bristow 1993; Shaw 1972).

Wavy lamination can also form subaqueously from supercritically climbing ripples. The thicknesses of wavy lamination observed thus far are ~ 20-30 cm thick, which could be formed by supercritically climbing ripples. If the wavy lamination was formed by

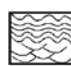
supercritically climbing ripples, then the flow which deposited them would have had to maintain high sediment aggradation rates relative to the ripple migration rates (Ashley et al. 1982).

Considered individually, each of the structures discussed in this section can form subaqueously. However, considered collectively and also considering the lack of other key features, such as channels and a fine upper limit to grain-size variations, the most parsimonious interpretation is that they formed as the result of deposits in a dune-interdune environment.

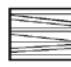
2.6.2 Climate Cycles

Sedimentary basins are sensitive to fluctuations in the climate, which can lead to variability in surface-water runoff and in the elevation of the water table (Brookfield 1977). These can affect sedimentation patterns and the extent of preservation of eolian strata. Strata in Erebus crater, like those in the Burns formation in Endurance crater, record the interaction between eolian and fluvial processes. Repeated cycles of relative water-table rise and fall in a dune-interdune system would be expected to form stacked deposits of dune-interdune facies (Grotzinger et al. 2005). The interactions between eolian and fluvial processes have been widely documented on Earth in both modern and ancient deposits, and these interactions can result in basin-wide drying-upward or wetting-upward sequences (Clemmensen et al. 1989; Frederiksen et al. 1998; Langford 1989; Scherer and Lavina 2005). Alternations in wet/dry deposition might also arise from non-climatic factors such

Primary Facies

 Damp to Wet: Subaqueous Ripple Cross-Stratified, Wavy Lamination, Soft-Sed Deformation


 Syndimentary Deformation/ Rip-Up Clasts

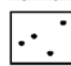
 Dry to Damp: Eolian Sand Sheet or Interdune

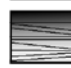
 Dry: Trough Cross-Bedding

 Dry: Large-Scale Eolian Cross-Bedding

Diagenetic Overprint

 Mottled and Recrystallized

 Hematitic Concretions Pptd in Phreatic Zone

 Recrystallization in Vadose-Phreatic Zone

 Drying-Upward Sequence

 Wetting-Upward Sequence

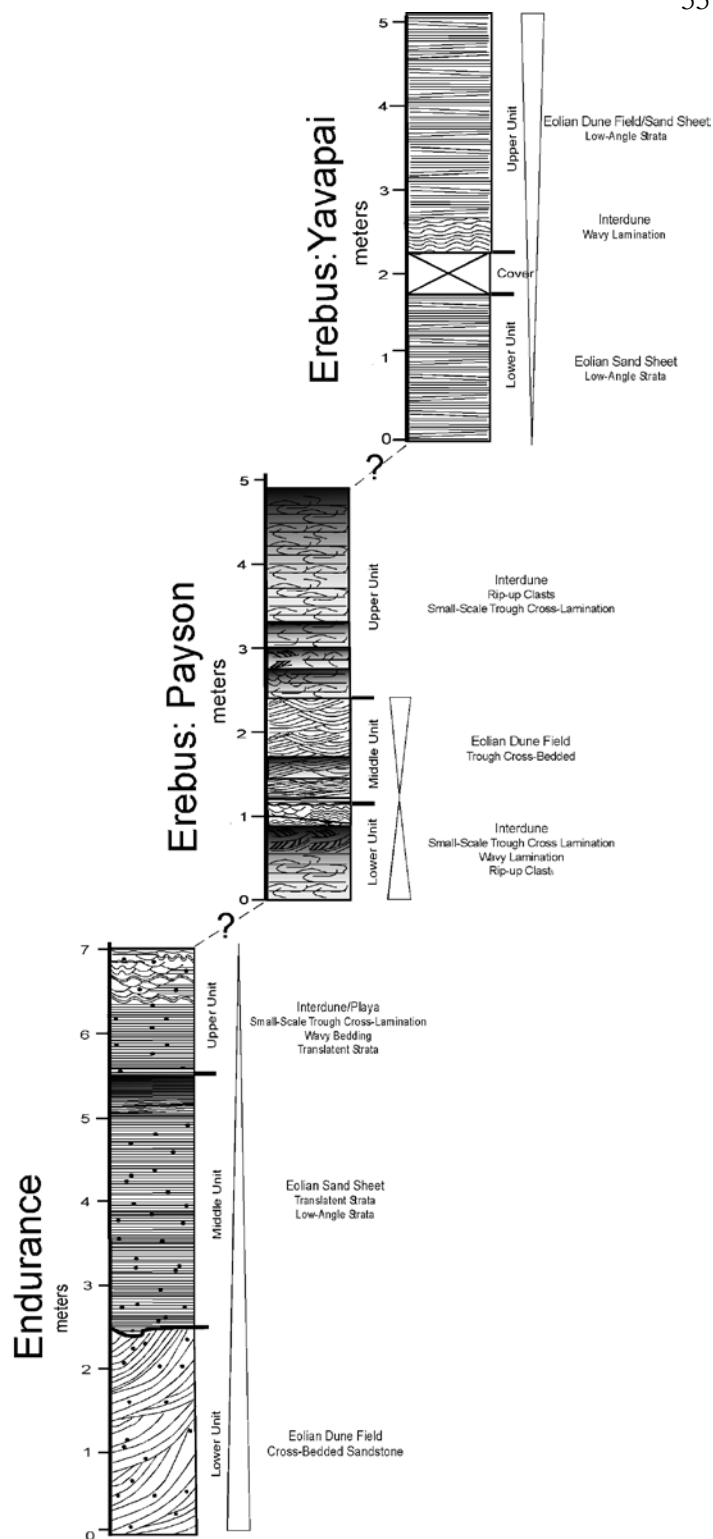


Figure 2.18 Stratigraphic columns from Endurance and Erebus craters shown in their likely stratigraphic relationship. Endurance crater shows a wetting-upward trend whereas Erebus crater shows a drying-upward trend. Together they may represent a full climate cycle.

as migration of discrete masses of sand through the depositional area. In this model, the land would be drier when topography and stratigraphy allow better drainage (e.g., more sand is present), and wetter when drainage is blocked or the water table is perched.

The Burns formation is interpreted to record eventual wetting of the surface related to a relative rise in the water table (Grotzinger et al. 2005). In contrast, Erebus crater strata may show an overall drying-upward trend through the stratigraphic section from the Olympia outcrop in the north, to the Payson and Yavapai outcrops to the south. Unfortunately, this interpretation is not certain since the upper facies of the Yavapai outcrop is not clearly resolved. However, if the upper facies of Yavapai is composed of eolian stratification, then the series of outcrops seen at Meridiani may represent a full climate cycle, evolving from dry to wet to dry (Fig. 2.18). This is consistent with the stacked set of dune-interdune facies predicted by investigation of the Burns formation at Endurance crater.

In potential terrestrial analogs, such cycles of alternating wetting/drying-upward sequences are often interpreted as the result of orbitally driven climate fluctuations or, alternatively, as a result of tectonic processes (Scherer and Lavina 2005). On Earth, climate fluctuations and tectonic processes can impress the stratigraphic record in similar ways, because both can modify sediment supply, sand availability, fluvial and eolian

transport capacity, and water-table position (Clemmensen et al. 1989; Scherer and Lavina 2005). On Mars, however, regional tectonic processes related to lithospheric plate motions can be discounted since Mars is a planet in which mantle convection occurs beneath a thick, strong and immobile lithosphere (O'Neill et al. 2007). Plate tectonics does not operate on Mars (Albarede and Blichert-Toft 2007), and so high-frequency episodic regional subsidence is not expected. This is regarded to have been the case as well during the late Noachian to early Hesperian when the Burns strata were deposited (Breuer and Spohn 2003). Finally, more localized tectonic processes such as faulting – which is widespread at other regions of Mars – can be discounted for the Meridiani region, where there is no evidence of faulting that may have contributed to localized, episodic subsidence.

Since tectonic processes can be discounted as a factor in controlling stratigraphic architecture in the Burns formation, climatic regulation provides a satisfactory alternative explanation. More arid climate periods would result in a relative fall of the water table and development of eolian dune and sand drift facies. During wet periods, the water table would rise, inhibiting formation of sand dunes and promoting sand sheet or interdune fluvial accumulations (Scherer and Lavina 2005). Modeling studies by Andrews-Hanna et al. (2007) predict that significant groundwater upwelling and evaporation should have occurred in Meridiani Planum. Thus, the Burns formation could have resulted from sustained groundwater upwelling, perhaps modulated by climatic overprinting of groundwater recharge or groundwater discharge (evaporation rate), or both.

Mars is a planet whose stratigraphic record may have been much more susceptible to climate forcing as compared to earth. One potential cause of these climate fluctuations is obliquity cycles, with the position of the water table rising or falling from changes from high to low obliquity. Obliquity-driven solar insolation is much stronger on Mars than on Earth (Head et al. 2006). While the current obliquity of Mars is 25° , the models predict that the obliquity has varied widely from its current low value. Over the last 4 Gyr the obliquity probably reached a high of 46° , but may have reached as high as 82° (Head et al. 2006). Furthermore, whereas climate on Earth is strongly influenced by its large oceans, the likely absence of any major water bodies on Mars would have ensured a much more direct link between solar insolation and stratigraphic response. Recent analysis of stratigraphic thickness distributions in the Arabia region of Mars also suggests a link between climate and sedimentary accumulation (Lewis et al. 2008a).

2.7 Conclusions

The outcrop exposures at Erebus crater provide additional evidence that support the dune-interdune model and highlight the inconsistencies with the base-surge models proposed for the emplacement of the Burns formation at the *Opportunity* landing site in Meridiani Planum. There is evidence for the greater involvement of liquid water in the outcrop exposures of the Olympia outcrop than was observed in Eagle or Endurance craters. The Olympia outcrop likely formed in a wet interdune and sand sheet environment. The facies observed in the Payson outcrop, which is likely stratigraphically above the Olympia outcrop, indicate that it was deposited in a damp-wet interdune, sand

sheet, and eolian-dune environment. The Yavapai outcrop, which is likely stratigraphically above the Payson outcrop, indicates that it was deposited in primarily a sand sheet environment and also potentially in an eolian-dune environment. These three outcrop exposures may indicate an overall drying-upward trend spanning the stratigraphic section from its base at the Olympia outcrop in the north to its top at the Yavapai outcrop in the south. This contrasts with the wetting-upward trend seen in Endurance and Eagle craters. Thus, the full series of outcrops studied by *Opportunity* may represent a full climatic cycle, evolving from dry to wet to dry conditions. Obliquity-driven climate cycles may be a more significant factor in the development of the stratigraphic record of Mars as compared to Earth.

Chapter 3

SUBLACUSTRINE DEPOSITIONAL FANS IN SOUTHWEST MELAS CHASMA

Originally published in:

Metz, J. M., Grotzinger, J. P., Mohrig, D., Milliken, R. E., Prather, B., Pirmez, C., McEwen, A. S., and Weitz, C. M. (2009b), Sublacustrine depositional fans in southwest Melas Chasma, *Journal of Geophysical Research*, 114, E10002, doi:10.1029/2009JE003365.

Abstract

Two depositional fan complexes have been identified on the floor of southwest Melas Chasma. The western fan complex is located near the center of an enclosed basin in southwest Melas Chasma and is composed of multiple lobes with dendritic finger-like terminations. These fans are very flat and have a morphology unlike any other fan that has been previously identified on Mars. Based on the morphologic similarity of the western fan complex to the Mississippi submarine fan complex, we suggest that it may be a deep subaqueous fan depositional system. There are numerous channels on the surface of the western fan complex and measurements of channel length, width, and sinuosity are consistent with channels observed on terrestrial submarine fans. The eastern Melas depositional fans are less well preserved and may be of deltaic or sublacustrine origin. Recognition of the fans supports earlier suggestions for the presence of a former lake in Melas Chasma and indicates that a significant body of water was present and stable at the surface of Mars for at least 10^2 to 10^4 years.

3.1 Introduction

Evidence for ancient lakes on Mars is based on multiple indirect criteria including constant-elevation contour lines inferred to be shorelines, the presence of flat-lying finely-layered deposits inferred to be lake-bottom sediments, terraced alluvial fans inferred to have formed in response to lake-level rise, and deltas with aggradational stratal geometries (Quantin et al. 2005; Lewis and Aharonson 2006; Grant et al. 2008; Kraal et al. 2008b). Direct evidence of a lacustrine environment requires observation of sedimentary deposits that could have formed only in fully submerged settings. The former presence of lakes, as well as the amount of time that they were stable on the surface, has important implications for the history and role of water on Mars (Baker 2001).

One area on Mars with possible evidence of a paleo-lake is Melas Chasma in Valles Marineris (Fig. 3.1). Dense, highly-organized valley networks have been identified in the topographic highs surrounding a basin in southwest Melas Chasma, hereafter referred to as Southern Melas Basin (Mangold et al. 2004). Since the heads of the valleys occur at different elevations, including near the tops of wall rock ridgelines, they have been interpreted to have been fed by precipitation (Mangold et al. 2004; Quantin et al. 2005). These valleys drain into a sub-circular closed depression within Southern Melas Basin, and this depression follows the -1800 m elevation contour (Quantin et al. 2005). Quantin et al (2005) suggest there may have been a body of standing water in the basin. The basin contains numerous light-toned flat-lying layers that can be traced over several kilometers. A set of strata that show clinoform geometries occurs in the northwest part of Southern

Melas Basin, and it has been suggested that this feature represents either a channel-levee complex or a delta complex (Dromart et al. 2007).

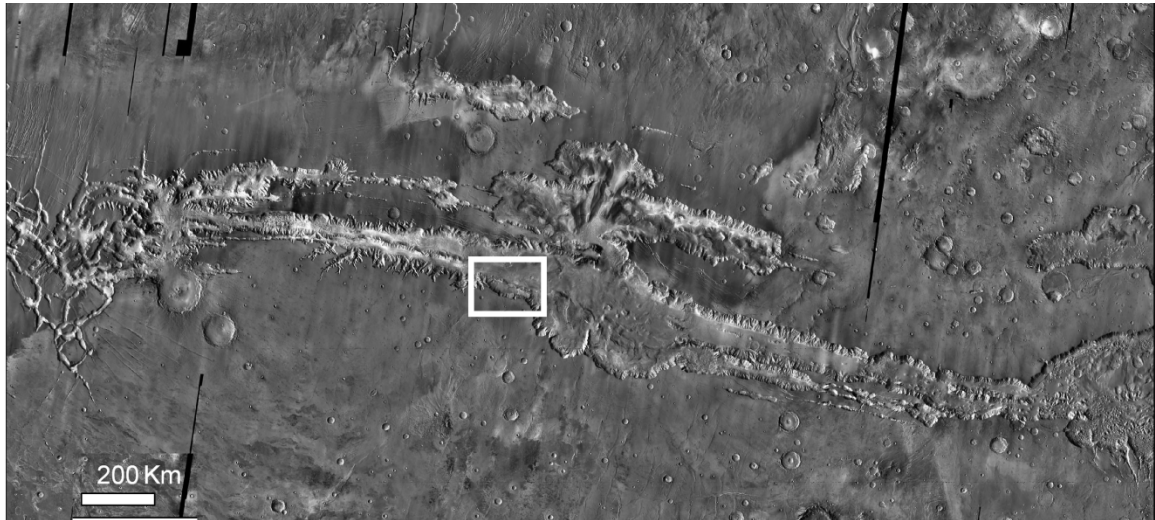


Figure 3.1 White box shows location of Southern Melas Basin within central Valles Marineris.

Channel-levee complexes are important components of deep-water depositional systems. Submarine fans are fed by turbidity currents that often flow down sinuous deep-water channels through laterally extensive channel-levee systems (Wynn et al. 2007). The channels are thought to avulse frequently with only one channel active at any given time (Damuth et al. 1983b; Damuth and Flood 1984; Wynn et al. 2007). Many studies have found similarities in the planform geometry of channels on upper and middle submarine fans and river channels (Flood and Damuth 1987; Clark et al. 1992), but with a lower occurrence of meander loop cutoffs and frequent avulsions in submarine channels as compared to subaerial channels (Kane et al. 2008). As the turbidity currents wane during flow events, deposition of lobes of sediment is common (Nelson et al. 1992). Cores

through submarine fan deposits show clays with interbedded graded sand and silt beds with distorted layers arranged in discontinuous lenses (Nelson et al. 1992). These lenses of coarser material occur where channelized flows ‘freeze’ into dendritic patterns, depositing their sediment near the edges of depositional lobes (Nelson et al. 1992). ‘Freezing’ in sediment deposition occurs due to loss of pore fluid pressure or because of frictional grain resistance and cohesive grain interactions (Dasgupta 2003).

A fan was previously identified near the western margin of Southern Melas Basin, and it was suggested that it may be of deltaic origin (Quantin et al. 2005). We identify four fans in Southern Melas Basin, two in the western part of the basin and two in the eastern part of the basin. One of the western fans was considered part of the delta in the Quantin et al. (2005) analysis. We evaluate the potential origins for the two western fans which include submarine fan, delta, alluvial fan, or gully deposit. We compare the detailed morphology, basin position, and slope of each of the possibilities to those of the western Melas fans. Although many of the features of the fans are consistent with a deltaic origin, we propose that a sublacustrine origin is also consistent with the morphology and properties of the two western fans.

3.2 Geological Setting

The area of study in Southern Melas Basin is located within central Valles Marineris (Fig. 3.1). Surface features and materials in Melas Chasma have been studied using Mars Global Surveyor data (Pelkey and Jakosky 2002) and Mars Odyssey Thermal

EMission Imaging System (THEMIS) data (Pelkey et al. 2003). These studies conclude that the recent surface in Melas Chasma has been dominated by eolian processes.

There is still much debate about how Valles Marineris formed, but mechanisms that have been suggested include structural collapse (Spencer and Fanale 1990; Schultz 1998; Rodriguez et al. 2006), tectonic rifting (Mege and Masson 1996; Schultz 1998; Peulvast et al. 2001) and gravity spreading due to loading of aurally-widespread salt deposits (Montgomery et al. 2008). The Valles Marineris canyon system is thought to have formed over several periods of tectonic activity spanning the late Noachian to late Hesperian or early Amazonian, and the material filling southwestern Melas Chasma is thought to be Hesperian to Amazonian in age based on impact crater-counting (Scott and Tanaka 1986; Pelkey and Jakosky 2002). Crater-counting of the material thought to compose the paleolake surface of Southern Melas Basin yields a complicated pattern with an age of 3 Gy followed by a period of resurfacing until 10 My (Quantin et al. 2005). The crater-size distribution of the valley networks indicates that they are younger than 3.5 Gy (Quantin et al. 2005). Thus it is possible that the fluvial and lacustrine features in Southern Melas Basin date back to the beginning of the Valles Marineris system.

There is some debate about the ages of materials on the floor of Valles Marineris, such as the interior layered deposits, which are distinct finely-layered materials located on the floors of troughs within Valles Marineris. There are many hypotheses suggested for their formation, many of which suggest they were deposited after the formation of Valles Marineris (Lucchitta 1990; Komatsu et al. 2004; Fueten et al. 2006; Okubo et al. 2008), but

some suggest they are ancient materials exhumed from below the material forming the trough walls (Malin and Edgett 2000; Montgomery et al. 2008). It is possible that both of these hypotheses are true; for example, there could be large expanses of wall rock that predate the opening of Valles Marineris, but more local topographically enclosed basins may contain deposits that formed after the depression was formed. The age of the materials on the floor of Southern Melas Basin may in fact be older than their crater-counting ages suggest if they were recently uncovered by erosion (Malin and Edgett 2001; Hartmann 2005).

3.3 Methods

Structural attitudes were obtained using planar fits to bedding seen in a Digital Elevation Model (DEM) constructed using stereo Mars Reconnaissance Orbiter (MRO) High-Resolution Imaging Science Experiment (HiRISE) images (PSP_007087_1700, PSP_007667_1700). The DEM was constructed using the methods of Kirk et al. (2008), and the vertical precision of the DEM is ~0.2 m (resolution ~1 m). Linear segments were traced out along well-exposed layers. Only layers with some natural curvature in the horizontal direction were used in order to provide accurate constraints on the three-dimensional geometry of the layer. We employed the method presented in Squyres et al. (2007) and Lewis et al. (2008b), which uses principal component analysis to ensure the layers used are well fit by a plane.

Channels on the fans were identified using both images and the DEM. There are several ways to define a channel, but for this study two new channels are defined after each

channel branch point. We define the main trunk channel as a first-order channel. When a first-order channel branches, the resulting channels are second-order channels. When a second order channel branches, the resulting channels are third order channels. Thus, the main trunk channel is a first order channel and the more distal channels are higher order. The width of each channel was measured at the beginning of each channel reach, and each width measurement has an uncertainty of about 1 m. The sinuosity of the channels was found by dividing the channel length, which is the length traced along the path of the channel, by the valley length, which is the straight-line distance from the beginning to the end of the channel (Schumm 1963).

To compare the channel patterns seen on the Melas fans against terrestrial depositional fans, we need to account for the different size of the systems. This was accomplished using non-dimensional parameters that included dimensionless width and length and sinuosity. The width of each channel was divided by the width of the main trunk channel, and length of each channel was divided by the length of the main trunk channel to make these parameters non-dimensional. The depth of each channel was measured from the DEM and has an uncertainty of ~1 m. The reported channel depths for the Melas fans are minimum estimates, since many of the channels have been at least partially filled in by eolian material and the channel levees may have been partially eroded. A minimum estimate of the channel gradient was calculated by finding the difference in elevation between the beginning and end of each channel and dividing by the length of the channel.

Ideally, the channels on the Melas fans would be compared to channels on terrestrial sublacustrine fans; however, images of the plan view morphology of terrestrial sublacustrine fans either have not been acquired or are not publicly available. Thus, the channel patterns on terrestrial sublacustrine fans could not be mapped and compared using the methods of this study. Bathymetric and seismic-reflection profiles across sublacustrine fans have been acquired and show that channels are present on sublacustrine fans (Normark and Dickson 1976b; Scholz and Rosendahl 1990; Back et al. 1998; Nelson et al. 1999).

The surface slope of the Mississippi submarine fan was found by superimposing the side-scan sonar image over the bathymetry (Gardner 2007). The slope was found by fitting a plane to a small area of the surface, similar to the methods used in Lewis et al. (2008b), and repeating this measurement for several areas on the fan. The values found were between 0.04° and 0.4° with an average of 0.08° , but there is an uncertainty of at least 0.04° in the measured values due to artifacts in the bathymetry. Despite the uncertainty, these values are close to the average seafloor slope of 0.06° reported for the Mississippi fan (Nelson et al. 1992; Schwab et al. 1996).

Fan lobes on the western Melas fans were identified and their thicknesses measured using the DEM. The lobe areas were measured, and their minimum volume calculated by multiplying lobe area by the thickness. These are all minimum estimates since some parts of the fans are obscured by overlying strata. The lobe areas and volumes were added to find the total area and volume of each fan.

3.4 Description of Fans used for Comparison

Channels identified and mapped on the Melas fans were compared to six terrestrial deep-water submarine fans (Brazos-Trinity Basin IV, Makassar, Mississippi, Pochnoi, Rhone, and Speculobe), two terrestrial deltas (Wax Lake and Lena), and one Martian delta (Eberswalde). These six terrestrial submarine fans were chosen because they were imaged at sufficient resolution to make a comparison, and we were able to obtain the data. The Brazos-Trinity Basin IV ponded apron is located in the northwestern Gulf of Mexico and is formed in the terminal basin of four linked intraslope basins (Table 3.1). The seafloor fan in Makassar Straits is a very low relief mud-rich fan located between the islands of Borneo and Sulawesi (Table 3.1). The Mississippi submarine fan is a large, mud-rich seafloor fan located in the Gulf of Mexico (Table 3.1) that was largely constructed during the Pliocene-Pleistocene (Wynn et al. 2007). The Pochnoi fan is located in the Aleutian Basin in the Bering Sea (Table 3.1), and it is thought to be a very young feature, possibly of late Pliocene-Quaternary age (Herman et al. 1996). The Rhone Neofan is part of the much larger Petit-Rhone Fan and formed from the most recent avulsion of the Rhone channel in the Gulf of Lion (Table 3.1). The Speculobe fan is a small sand-rich seafloor fan located in the Gulf of Cadiz offshore Spain (Table 3.1). As shown in Table 3.1, the six submarine fans chosen for comparison comprise the range of diversity seen on submarine fans (eg. mud-rich, sand-rich and mixed sediment; active and passive continental margin, basin floor and ponded fans).

Wax Lake Delta is a modern river-dominated bay head fan delta located at the mouth of the Wax Lake outlet, which is a man-made channel excavated in 1941 (Wellner et al 2005). The formation of this delta was tracked through time by images taken over the

last thirty years. The Wax Lake Delta is a relatively young delta that has not had much human interference and thus appears in a natural state. The Lena delta is a river-dominated delta located at the Laptev Sea coast in northeast Siberia (Olariu and Bhattacharya 2006). The Eberswalde delta is located in Eberswalde crater near the western margin of the 65-km diameter crater (Wood 2006). It is an erosional remnant of a larger paleodeltaic deposit and has numerous bifurcating distributaries preserved in positive relief (Malin and Edgett 2003).

Fan	Location	Fan Type	Fan Area (km ²)	Water Depth (m)	Drainage Basin Area (km ²)*	Grain size	Tectonic State
BT Basin IV	27°20'N 94°24'W	ponded	128	1500	1.2×10^5	mixed	passive
Makassar	0°23'S 118°37'E	seafloor	2500	2400	7.5×10^4	mud	active
Mississippi	26°30'N 85°30'W	seafloor	300,000	3200	4.76×10^6	mud	passive
Pochnoi	54°35'N 173°56'W	seafloor	20,000	?	1.2×10^5	?	active
Rhone Neofan	41°45'N 4°54'E	seafloor	1430	2400	9.0×10^4	sand	passive
Speculobe	35°30'N 7°30'W	seafloor	48	1500	5.7×10^4	sand	active
Wax Lake Delta	29°30'N	delta	40	~0	?	-	passive

	91°26'W						
Lena Delta	72°13'N 126°9'E	delta	30,000	~0	2.5×10^6	-	active
Melas North	9°49'S 76°25'W	lacustrine	2.3	?	~500	?	?
Melas South	9°49'S 76°25'W	lacustrine	4.3	?	~500	?	?

Table 3.1 Characteristics of the submarine fans and deltas compared in this study. Grain size refers to the predominant grain size on the fan and the tectonic state refers to the margin on which the fan is developed. *The drainage basin area is based on the size of the drainage basin of the main river that ultimately feeds the fan.

3.5 Results

3.5.1 Morphology

The western fan complex is located near the center of Southern Melas Basin and has two fans, each of which is composed of multiple lobes with dendritic finger-like terminations (Fig. 3.2). The lobes are elongated and the ‘fingers’ often branch off at high angles in the downstream direction (up to 90° to the overall transport direction). The mean

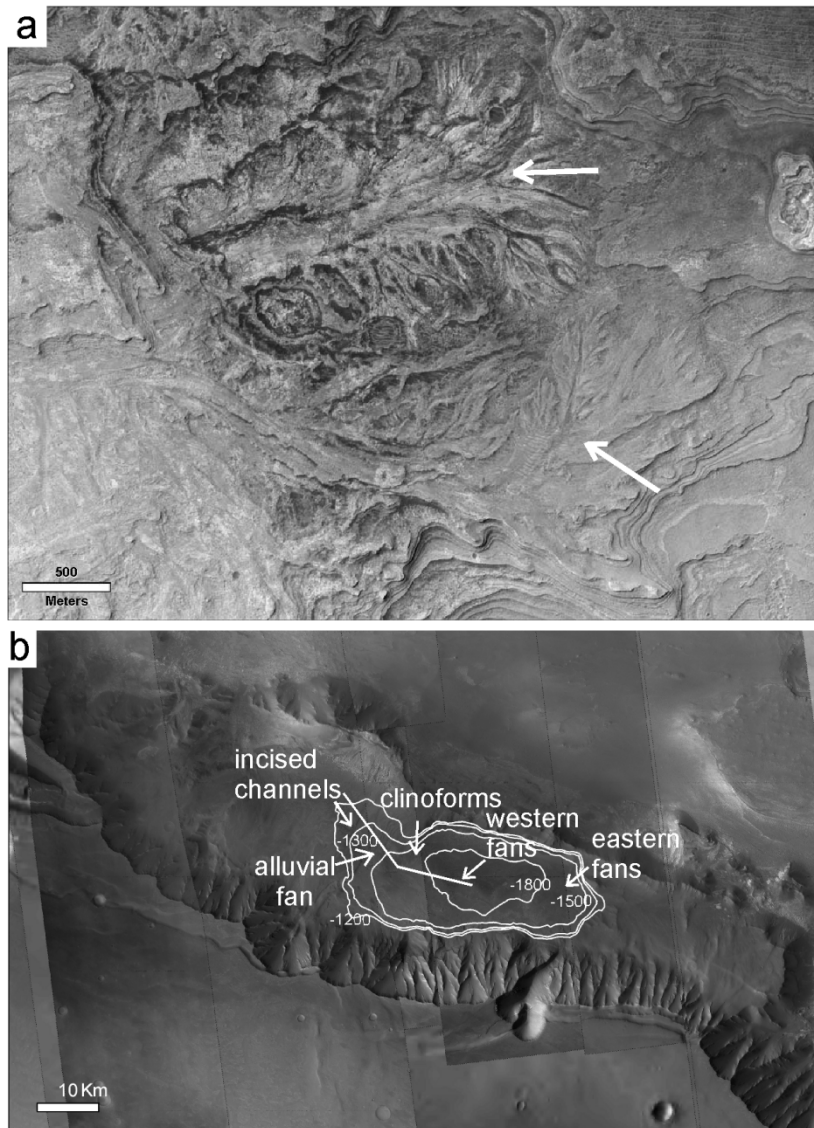


Figure 3.2 A.) Portion of HiRISE image PSP_007667_1700 with white arrows showing the location of the two putative western sublacustrine fans intercalated within the layers in Southern Melas Basin. B.) Mosaic of CTX images showing Southern Melas Basin where the putative sublacustrine fans occur. White line is actual topographic transect for schematic in Fig. 3.12.

branching angles for the fingers are 75 degrees while the median is 80 degrees. The surface of the fans in Southern Melas Basin is marked by numerous mildly sinuous

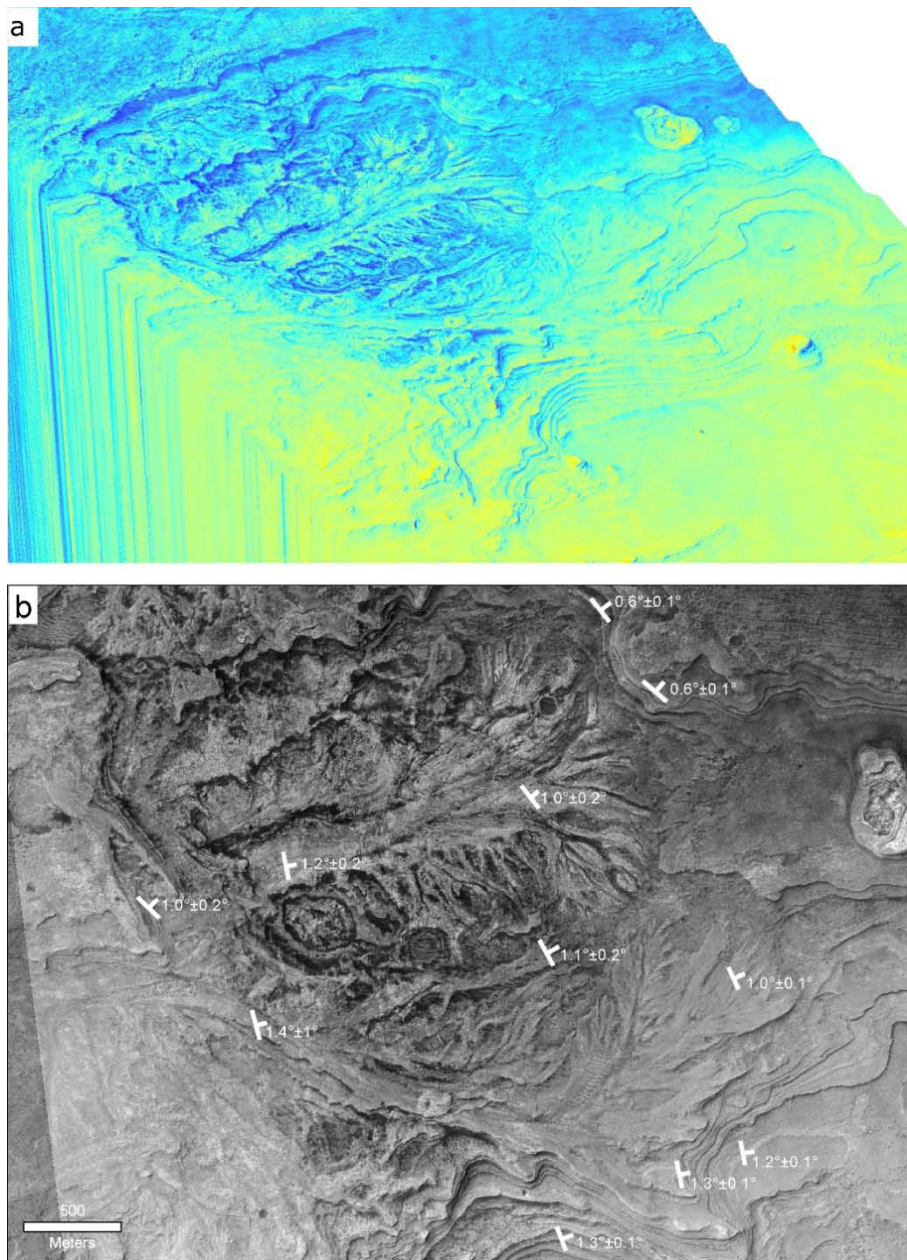


Figure 3.3. A.) Shaded relief perspective view of the western fans. The southern fan is topographically and stratigraphically above the northern fan. B.) Image of the fans showing the dips of the fan surfaces and layers. The main feeder channel of the southern fan is ~50 m above the basin plain.

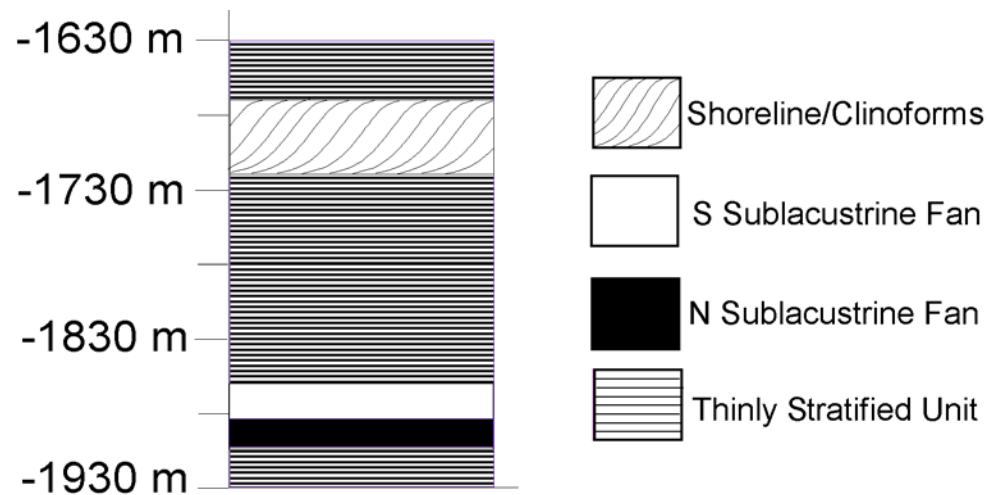


Figure 3.4. Stratigraphic column illustrating that the southern fan is located stratigraphically above the northern fan.

channels, and its average surface slope is $\sim 1^\circ$ (Fig. 3.3). The dips of the beds in the fans are also about 1° (Fig. 3.3). The fans have few craters, because they were probably buried beneath later sediments, which prevented small craters from forming on their surfaces. Subsequent exhumation has now exposed the surfaces of the fans. There are layered beds surrounding the fans, so the beds must have been joined in the past and then eroded back to expose the fans. The preservation of the channels, including a topographic signature, suggests the exhumed paleo-fan surface corresponds closely to the original fan surface.

The fans occupy different stratigraphic levels with the southern fan located stratigraphically above the northern fan, but both are located in the topographically lowest part of the basin (Fig. 3.4). The fans are surrounded by other layered material, and these beds are also relatively flat-lying with dips of between 0.6 - 1.4° (Fig. 3.3). The fans appear to be visible through an erosional window through the other layers.

Table 3.2 lists the characteristics of the western Melas fans, including slope, minimum area and volume, minimum length, mean and maximum channel depths, mean channel gradients, and channel sinuosity. Six lobes were identified on the northern fan and ten lobes on the southern fan (Fig. 3.5). The numbering of the lobes indicates the relative order that they formed in; parts of earlier formed lobes can be seen to be covered by later-formed lobes. Some of the later-formed lobes appear to have filled in the low areas surrounding earlier formed lobes. The channels identified on each fan are shown in Fig. 3.6.

Fan	Slope	Area (km ²)	Volume (km ³)	Length (km)	Channel depth (m)		Mean Channel Gradient (m/km)	Sinuosity
					Mean	Maximum		
Northern	1°	2.3	0.05	2.1	1	4	23	1.02
Southern	1°	4.3	0.10	1.3	1	2	32	1.02

Table 3.2 Characteristics of the western Melas fans.

There are two additional fans in the eastern part of Southern Melas Basin (Fig. 3.7a), but they are not as well-preserved as the western fans. They have an elongate branching morphology and are preserved in positive relief. The bulk of the fans appear to be composed of inverted channels (Fig. 3.7b), although there are a few channels on the surface of the southern fan which form topographic depressions. The channels composing

the fans can be seen to migrate and cross-cut. The northern fan appears to have formed first (1 in Fig 3.7b); the main feeder channel switched south and built up a new channel system (2 in Fig. 3.7b). The main channel appears to have ultimately switched to the north as evidenced by the cross-cutting channel relationships (3 in Fig. 3.7b). There are several large and small impact craters on the surfaces of the fans. Since these fans are not as well-preserved as the western fans, this paper will focus on the western fans.



Figure 3.5 Outlines of the six lobes composing the northern fan and the ten lobes composing the southern fan are outlined in white.

The combination of low slope, channel branching geometry, presence of distinctive small-scale lobes, and position near the center rather than near the margin of a topographic basin show that the western fans are distinct from previously identified fluvial features on Mars.

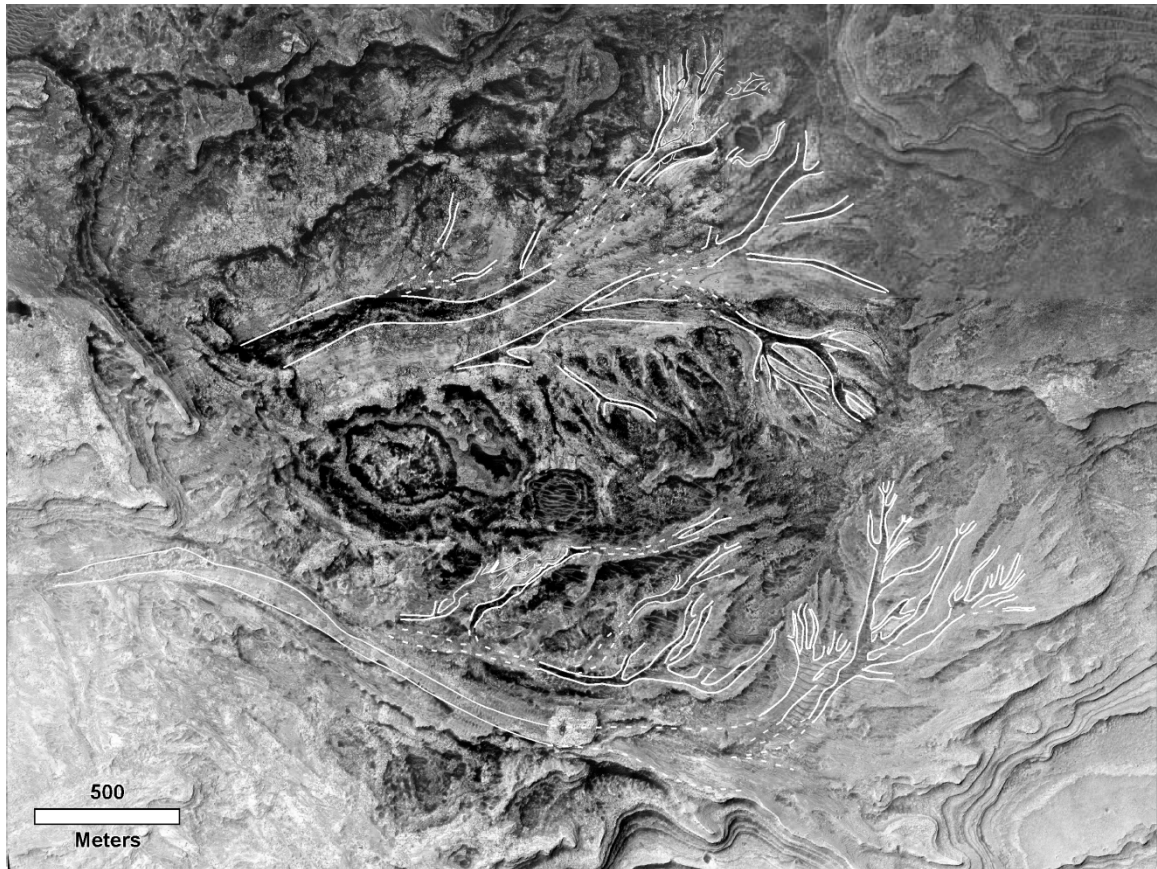


Figure 3.6 Channels on the Melas fans are outlined by the solid white lines. Dashed lines show inferred positions of channels.

2.5.2 Mineralogy

The surfaces of the fans are covered in dust, which makes mineralogical detections difficult (Fig. 3.8a). However, MRO Compact Reconnaissance Imaging Spectrometer for Mars (CRISM) spectra do show evidence for opaline silica (Fig. 3.8b,c) and jarosite (Fig.



Figure 3.7. A.) Portion of HiRISE image PSP_007377_1700 with the white arrows showing the location of the eastern Melas fans. B.) White lines show outlines of channels. Black lines show an older generation of channels. The numbers refer to the relative ages of the channels based on cross-cutting relationships.

3.8b,d) in layers near the fans, similar to the mineral assemblages seen on the plains directly south of Melas Chasma (Milliken et al. 2008; Weitz et al. 2009). The opaline silica was detected in a small hill just to the east of the northern Melas fan and in bedded outcrops to the northeast of the fan (Fig. 3.8b). These latter exposures occur in strata that lie stratigraphically above the fans. The hydrated silica was identified by the presence of absorption bands centered near 2.21-2.26 μm due to the presence of Si-OH groups. The position and shape of a doublet band at 2.23 and 2.26 μm is most consistent with laboratory spectra of opal- A/CT (Fig. 3.8c). Hydrated silica can occur as primary sedimentary deposits (McLennan 2003), altered ash deposits, precipitation as pore-filling cements, or precipitation from shallow evaporating bodies of water (Milliken et al. 2008).

Mineral spectra that show a good spectral match to jarosite were detected in the clinoforms (Fig. 3.8b). The jarosite was identified based on bands at 1.85 and 1.93 μm and an OH-feature near 2.26 μm and is most consistent with Fe-deficient H_3O -bearing jarosite (Fig. 3.8d). H_3O -bearing jarosite is consistent with precipitation under low temperature acidic conditions (Milliken et al. 2008). Jarosite is not as soluble as other sulfates, such as Mg-sulfates, and could be transported by fluids if they were already saturated with S and Fe. It would depend on the composition of the transporting fluid and the amount of time the mineral was in contact with the fluid. The jarosite could also be diagenetic, and this

cannot be ruled out since the CRISM data are too coarse to determine if the jarosite is cutting across bedding contacts. However, cementation is likely the most probable origin for the jarosite. The definitive sedimentary origin for the clinoforms implies that if this is a jarosite cement it would be of low temperature origin since the clinoforms are not a volcanic deposit. This provides a definitive constraint on paragenesis. The presence of

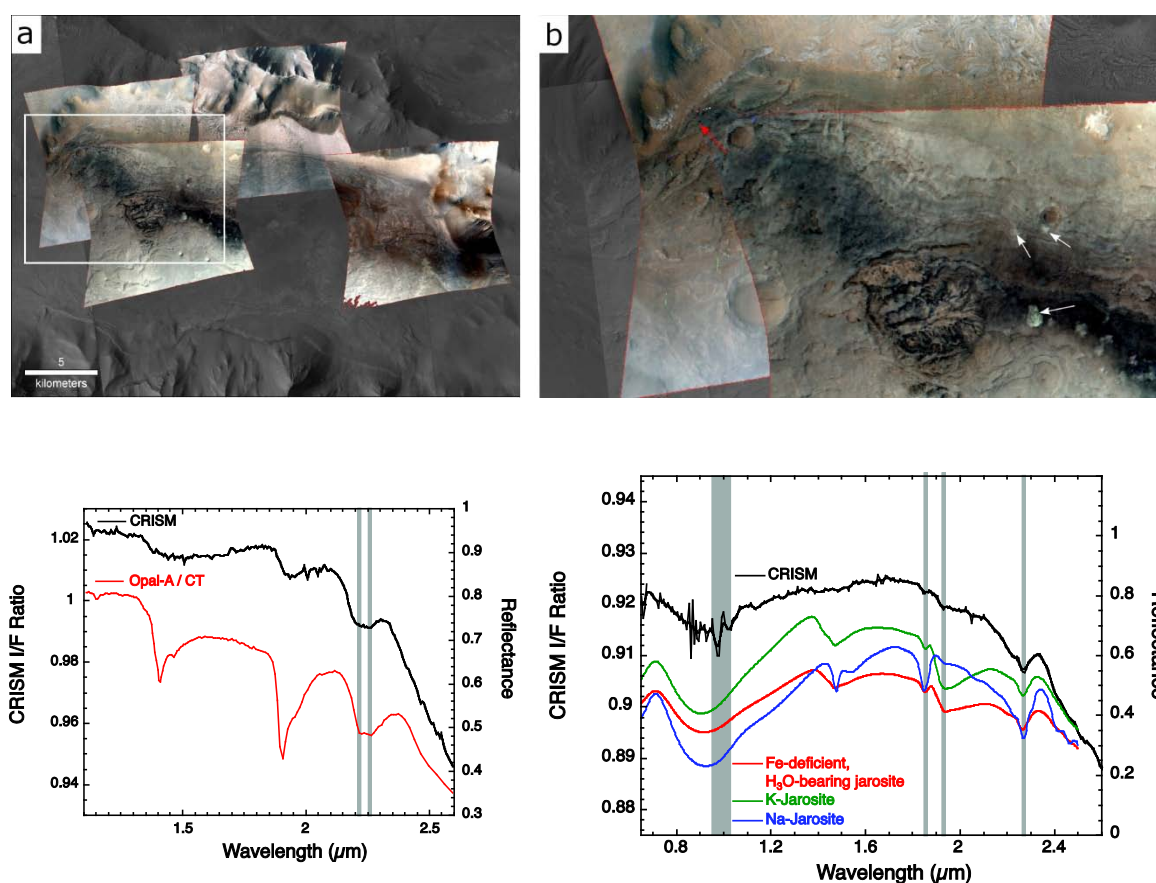


Figure 3.8 A.) CRISM targeted image overlain on a CTX mosaic of Southern Melas Basin. White box shows location of b. Light brown tones, such as on the eastern and western Melas fans, are indicative of dusty areas. B.) Close-up view of the area outlined in a. The white arrow shows the location of turquoise outcrops showing a good spectral match to opaline silica. Red arrow shows location of jarosite. C.) CRISM spectra (in black) of turquoise outcrops compared with library spectra of opaline silica A/CT (in red). Note good match of the double bands between 2.2 and 2.3 μm. D.) CRISM spectra (in black) of the clinoforms compared with library spectra of K-, Na- and H₂O-bearing jarosite.

these hydrous minerals implies that water was present when they formed, possibly as a lake or as pore fluids in pre-existing sediments (Milliken et al. 2008).

3.6 Discussion

Because the western Melas fans are a newly identified class of fan-like features on Mars, we compare them to common depositional fans found on both Earth and Mars to evaluate the most likely process responsible for their formation.

3.6.1 Depositional Fan Comparisons

3.6.1.1 Alluvial Fans

Alluvial fans, both on Mars and on Earth, are cone-shaped deposits radiating from a dominant source channel. They typically develop near the base of topographic highlands, thus fringing basin margins. The Melas fans, however, occur near the center of a basin. Alluvial fans typically have relatively steep slopes; the average surface slope of alluvial fans on Mars based on our compilation of existing data is 2.5° (see Table 3.4) (Moore and Howard 2005; Kraal et al. 2008a). Alluvial fans on Earth have average slopes of $2\text{--}12^\circ$ (Hashimoto et al. 2008; Blair and McPherson 1994b). Some authors have suggested that in humid areas alluvial fan formation is dominated by braided fluvial river processes and that these alluvial fans have more gentle slopes of 1° or less (Stanistreet and McCarthy 1993; Hashimoto et al. 2008). Other authors argue that these should not be classified as alluvial

fans and are actually braided stream systems (Blair and McPherson 1994b). The slope of the Melas fans ($\sim 1^\circ$) does, however, overlap with the slopes of humid alluvial fans. This would indicate that if the fan was not of sublacustrine origin that it would have formed by alluvial processes that required continuous rather than flashy or sporadic discharge, consistent with a wetter climate.

The processes observed to act on alluvial fans are debris flows, sheet floods, and shallow braided streams (Schumm 1977; Blair and McPherson 1994b; Harvey et al. 2005). The channels on the Melas fans are distinct and moderately sinuous, not braided. The Melas fans also have distinct depositional lobes from individual flows. Debris flow-dominated alluvial fans could be expected to have lobate deposits, but these typically have boulder-laced snouts (Whipple and Dunne 1992). The Melas fans do not show evidence for large boulders at the scale of HiRISE images (~ 25 cm/pixel). Also, debris flow-dominated fans typically have slopes above 5° while the Melas fans have much lower slopes (Harvey 1984; Wells and Harvey 1987; Blair and McPherson 1994a). Furthermore, the high branching angles of the lobes in the Melas fans are not seen in subaerial debris-flow dominated fans.

3.6.1.2 Gully Deposits

Gully deposits that have been identified on Mars have lobe-shaped terminations but are developed on steep rather than gentle slopes. The average slope on which gullies are developed is 27° based on over 200 measurements from recent studies (Malin et al. 2006; Dickson et al. 2007; Heldmann et al. 2007). These elongate deposits are thought to form

by dry mass wasting on steep slopes or perhaps by liquid water flows (Pelletier et al. 2008). The flows typically originated from a small region, and the flows did not diverge widely to create complex branching networks as seen in the Melas fans.

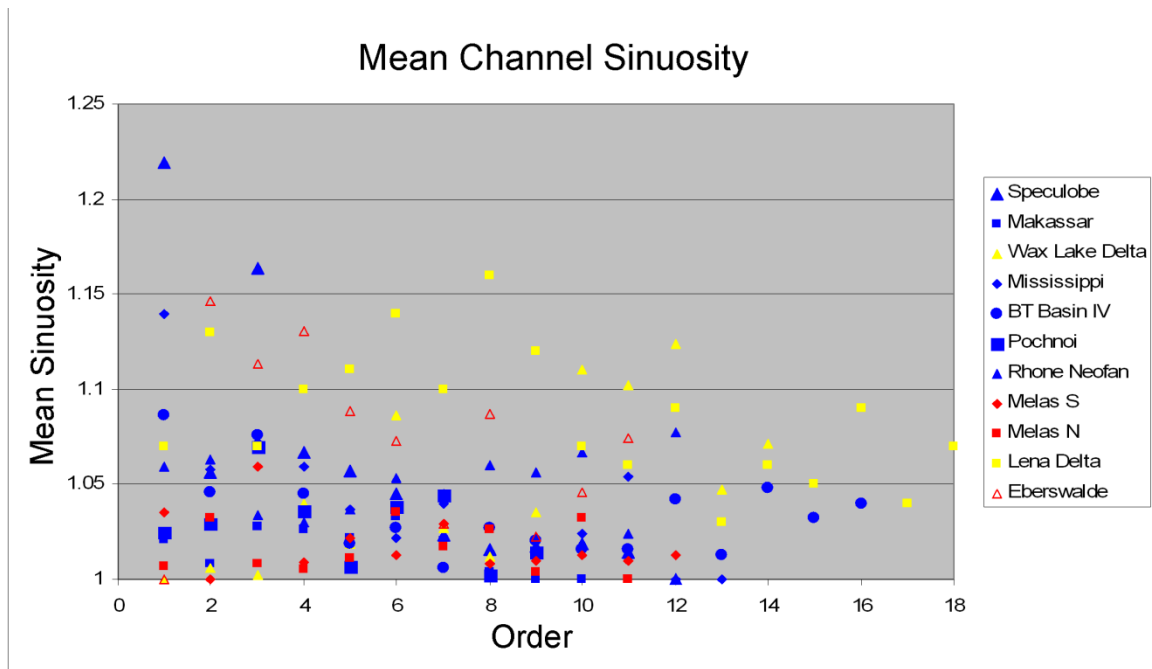


Figure 3.9. Plot showing how mean channel sinuosity changes down-fan (i.e. for increasing order) for six terrestrial submarine fans, two terrestrial deltas, and the two western Melas fans. Sinuosities were measured for channels on the distal portions of the terrestrial submarine fans.

3.6.1.3 Deltas

Deltas are partially subaerial masses of sediment deposited near where a river enters a standing body of water. The Eberswalde delta on Mars has a low surface slope that averages 2° (Lewis and Aharonson 2006), and many meandering and sinuous channels, scroll bars and branching terminations (Wood 2006). Terrestrial deltas also commonly

have low surface slopes ($<1^\circ$) and can show lobate stacking patterns from lobe buildup and switching (Coleman and Wright 1975). Delta channels show a range of sinuosities and can be meandering and sinuous (Wood 2006) or mildly sinuous (Fig. 3.9). The western Melas fans show low surface slopes and mildly sinuous channels (sinuosity of 1.02), which both fall within the range of values common for deltas (Table 3.3, Fig. 3.9). The Eberswalde delta is located at the margin of its crater, similar to terrestrial deltas which are located near the margins of basins. Jezero crater delta, southeast of Nili Fossae on Mars, is also located at the margin of its crater (Ehlmann et al. 2008). However, the western Melas fans are found near the center of the basin. The delta channels also have low branching angles, and its lobes do not lead into the high-angle fingers seen in the Melas fans.

Feature	Basin Position	Slope	Shape	Channels
Alluvial Fan	Margin	2.5°	Cone-shaped	Braided
Gully Deposit	Wall	27°	Elongate lobes	-
Delta	Margin	2.1° * $<1^\circ$ **	Fan-shaped, lobes	Sinuuous, meandering, mildly sinuous
Submarine Fan	Center	$\leq 1^\circ$	Elongate branching lobes, fingers	Mildly sinuous
Melas W. Fans	Center	$\sim 1^\circ$	Elongate branching lobes, fingers	Mildly sinuous

Table 3.3 Depositional fan characteristics. *This is the average slope reported for the Eberswalde Delta (Lewis and Aharonson 2006). **This is the average slope value for terrestrial deltas.

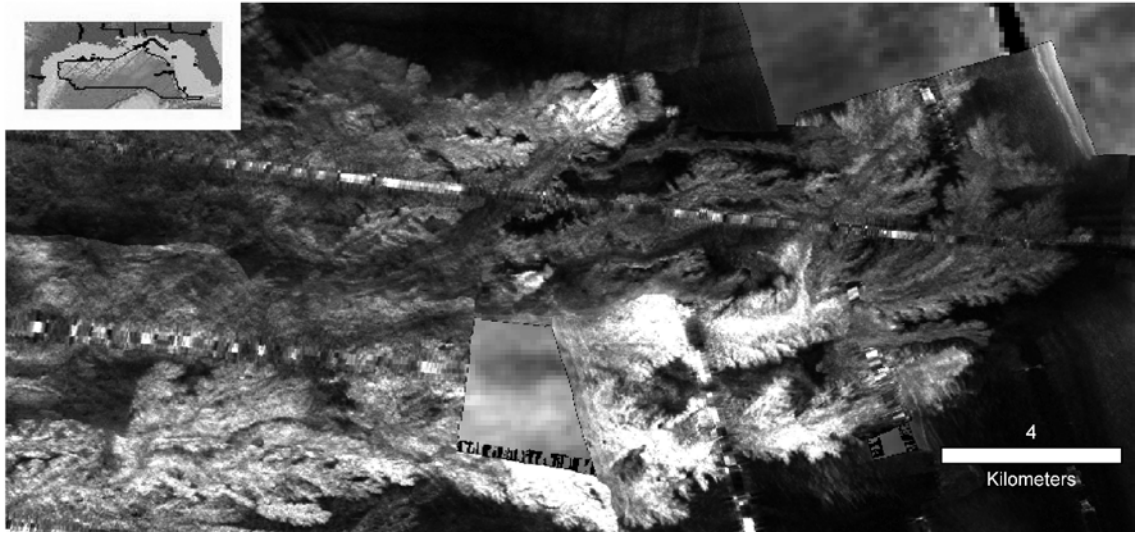


Figure 3.10 SeaMARC IA Side-scan sonar image of the Mississippi submarine fan showing the elongated nature of the lobes and the fingers that branch off at high angle (USGS). Inset shows location of the side-scan sonar image. High backscatter areas are composed of clay facies with interbedded sand and silts, whereas low backscatter areas are composed of clay facies with no siliciclastic sands or silts (Nelson et al. 1992).

3.6.1.4 Submarine Fans

The morphology of the Melas fans compares favorably with depositional features formed on the Mississippi submarine fan (Figs. 3.2, 3.10). The distal Mississippi submarine fan also has a lobate morphology with finger-like dendritic terminations, elongated lobes, and splays that branch off of the main deposit at high angles (up to 90°). The distal Mississippi submarine fan also has low relief mildly-sinuuous channels and is very flat, with a surface slope of $\sim 0.08^\circ$ based on our analysis of existing bathymetric data (Gardner 2007). Although the slope of the Melas fans ($\sim 1^\circ$) is somewhat higher than that of the Mississippi fan, it is possible that slight differential erosion of the surface of the

Melas fans could cause an increase in the slope. If the surfaces of the Melas fans were not an exact bedding plane, measured surface slopes would be higher than the true slope.

Submarine fans are densely channelized distributary systems and the distal Mississippi fan is composed of depositional lobes whose beds consist of graded sand and silt (Nelson et al. 1992). The detailed structure of these lobes shows a “finger-like” or high branching angle dendritic backscatter pattern in sidescan sonar which correlates to the sand-silt beds formed by abrupt deposition of channelized flows to form small lobes at their distal reaches (Fig. 3.10; Nelson et al. 1992; Klaucke et al. 2004). These finger-like lobes are commonly oriented at high angles to the channels which delivered the sediment to the lobes (except for the cluster of termination lobes). Similar finger-shaped deposits have been observed on the Monterey Fan and in the distal areas of Permian submarine fans preserved in the Tanqua Karoo basin, South Africa (van der Werff and Johnson 2003; Klaucke et al. 2004). The relatively abrupt terminations associated with the finger-like lobes are characteristic of sediment-gravity flow deposits. Full preservation of these lobes on subaerial fans is unlikely due to subsequent reworking and sediment transport by flowing water (Whipple and Dunne 1992). The unmodified preservation of sediment-gravity flow deposits such as those observed in Southern Melas Basin is consistent with accumulation in the distal reaches of a subaqueous fan. The channels present on distal submarine fans are mildly sinuous (<1.3), and the channels on the Melas fans show similar sinuosities (Fig. 3.9). These measurements show the channels on the Melas fans have properties that are consistent with channels on submarine fans.

The Melas fans are located near the center of the basin in the current topographically lowest area, which could be the result of subsequent erosion of the basin or the original depositional setting. Many submarine fans also occur on basin plains in the topographic lows of the basin, but this may not necessarily correspond to the center of the basin. For example, the Mississippi submarine fan is located at ~3300 m water depth and is over 500 km away from the Mississippi Canyon on a very low gradient surface (Schwab et al. 1996). It is bounded to the east by the Florida escarpment (Schwab et al. 1996). Although the Mississippi submarine fan is not located in the center of the Gulf of Mexico, it is located on the basin plain in a depositional low. Sublacustrine fans are also found in the deepest areas of lakes (Normark and Dickson 1976a). They typically occur on the basin plains near the centers of their lakes, such as in Lake Baikal, Siberia (Nelson et al. 1999) and Lakes Malawi and Tanganyika, east Africa (Scholz and Rosendahl 1990). Thus, the current basin position of the Melas fans is similar to that of terrestrial sublacustrine fans.

3.6.2 Formation of the Melas Western Fans

Based on their morphological similarity to the Mississippi submarine fan, the western Melas fans could be interpreted as sublacustrine fans. Sublacustrine fans commonly occur in deep lakes on Earth and form important depositional systems that commonly are fed by density underflows originating from regional drainage systems (Nelson et al. 1999). Turbidity current experiments in the laboratory have produced subaqueous fan deposits that are channelized with mildly sinuous, low-relief channels (Yu

et al. 2006). Thickness maps of these deposits show finger-shaped deposits that resemble the distal stretches of submarine fans.

In contrast to the small size of the Melas fans, the overall area and volume of the Mississippi submarine fan is $3 \times 10^5 \text{ km}^2$ and $2.9 \times 10^5 \text{ km}^3$, and the fan is 600 km long (Wynn et al. 2007). The much larger size of the Mississippi fan is expected since the size of a submarine fan is as much a function of sediment flux as its duration, and the Mississippi drains a large part of the North American continent. For Melas Chasma, the sediment flux must have been much smaller due to the small size of the catchment area which would have yielded the sediments which formed the fan. Terrestrial submarine fans comparable in size to the Melas fans do exist, such as the upper fan in Brazos-Trinity Basin IV and the Pochnoi fan (Kenyon and Millington 1995; Beaubouef et al. 2003), but they have not been imaged in as much detail as the Mississippi fan so their small-scale morphology cannot be compared.

The properties of the channels on the Melas fans (i.e. channel length, width, and sinuosity) are also consistent with the values measured for terrestrial submarine fans and deltas (Fig. 3.9, 3.11). The mean sinuosity of the channels on the six distal terrestrial submarine fans is low overall. Sinuosity ranges from 1.0 to 1.3 but the majority of the submarine fans have channels with a sinuosity less than 1.1. The Melas fan channels also have low sinuosity with most values below 1.05. The relationship between mean channel length and mean channel width for submarine fans and deltas roughly follows a power law distribution (Fig. 3.11). The channels on the Melas fans follow a similar trend. The

steepness of the power law trend does not appear to correlate with the dominant grain size present on the fan, the water depth of the fan, fan size, margin type or drainage basin size. It is possible that a combination of these factors determines how quickly or slowly the channel width decrease for a given decrease in channel length. We have not yet identified a good quantitative measure of channel properties that is able to distinguish between the submarine channels formed on submarine fans and the subaerial channels formed on deltas.

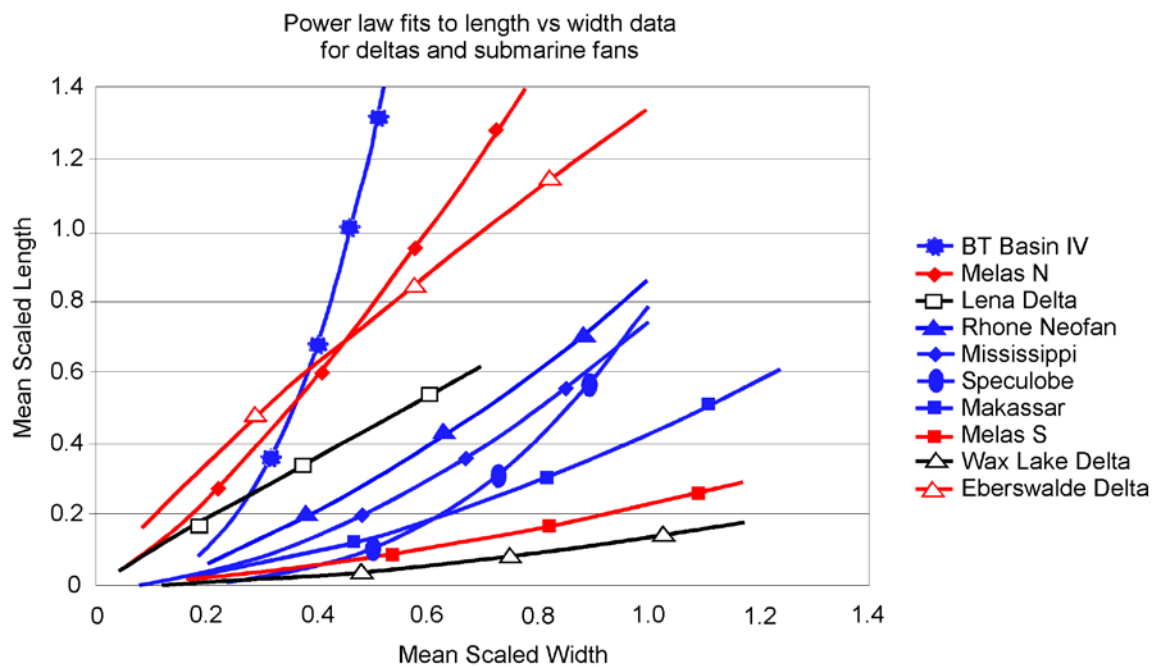


Figure 3.11 Plot showing power law fits to mean scaled channel length versus mean scaled channel width data. Fits for six terrestrial submarine fans, two terrestrial deltas, one Martian delta, and the two western Melas fans are plotted. This plot shows that the channel widths and lengths for the Melas fans fall within the typical range of values seen for terrestrial submarine fans and deltas.

Terrestrial submarine fans typically have only one active main channel at a time (Damuth et al. 1983b; Wynn et al. 2007). Each channel is eventually abandoned, probably

by avulsion, and a new channel is formed nearby. This may have been the case for the Melas fans as well. The northern fan was deposited first since it is located stratigraphically and topographically below the southern fan. Eventually, its feeder channel was abandoned, and the channel may have avulsed to a new course further south. This could have resulted in the deposition of the southern fan.

Many features of the Melas fans are also shared with deltas. However, based on detailed morphologic comparisons of the lobes as well as basin location, the Melas fans appear more similar to terrestrial submarine fans than to either terrestrial or Martian deltas.

3.6.3 Discriminating Between Deltas and Submarine Fans

Analysis of plan-view morphology and slopes provides broad constraints on interpretations of depositional fans, but does not uniquely constrain their origin. Morphology alone points to a sublacustrine origin, however, a deltaic origin cannot be excluded. The observed facies, as well as their stacking pattern, allows us to discriminate conclusively whether deposits were formed as part of a delta or a submarine fan.

Since most of the information necessary to distinguish different sedimentary facies is small-scale, orbital images do not provide the necessary resolution. Views of the deposit in cross-section that expose details at the centimeter to decimeter scale would be required to provide definitive evidence of sublacustrine sediment transport via turbidity currents. Obtaining this kind of data would require rover images, similar to those taken at Meridiani

Planum by the Mars Exploration Rover *Opportunity* (Grotzinger et al. 2005; Metz et al. 2009a) and at Gusev crater by Spirit (Lewis et al. 2008b).

Distinctive features that could be observed in a deltaic environment, but would not be expected in a submarine fan environment include point bar deposits, floodplain deposits, paleosols and mudcracks (MacNaughton et al. 1997). Submarine fans are largely composed of the deposits of turbidity currents. However, turbidity currents can also occur in the distal delta front and in prodeltas, and so the presence of these deposits alone is not diagnostic (Mutti et al. 2003; Pattison 2005). Distinguishing a prodelta from a submarine fan may require examination of the fan architecture. The study of detailed facies transitions and stacking patterns may be necessary to distinguish between submarine fans and distal deltaic facies.

3.6.4 Timescales

In an effort to obtain the most conservative estimate of fan formation time, we have calculated minimum durations. This calculation assumes a continuous sediment accumulation rate, but it is known from Earth that sedimentation is characteristically discontinuous in time, and that discontinuities are the rule not the exception (Sadler 1981). Minimum formation time can be constrained using several approaches; analyses of formation times for subaerial deposits of roughly comparable volume on Mars (Jerolmack et al. 2004; Kraal et al. 2008b), estimates of subaqueous fan formation on Earth provided by age dating fan deposits, and quantitative estimates of how long turbidity currents would have taken to deposit the fans.

The well-studied terrestrial deposit of the Brazos-Trinity fan in Basin IV is somewhat larger in size than the Melas fan and formed in no more than ~35,000 years (Behrmann et al. 2006; Mallarino et al. 2006). This measure is similar to ~17,000 years of sediment deposition leading to development of several submarine fans in the California Borderland (Covault et al. 2007). Together these examples constrain a millennial-scale estimate for the minimum time that water must have been present in Southern Melas Basin. This estimate includes within it intervals of non-deposition. Deposits which span longer time intervals have the opportunity to incorporate more and longer hiatuses (Sadler 1981). Removing this inactivity would shorten the formation time and duration for standing water in Melas basin.

Theoretical analyses of primarily subaerial fan deposition on Mars assuming no intermittency in construction place minimum formation times at the decadal to century scale (Jerolmack et al. 2004; Kraal et al. 2008b). Comparison of formation times between these relatively proximal depositional systems and the distal fan of Southern Melas Basin is reasonable because of differences in the efficiency with which these systems trap sediment. Proximal subaerial systems have more sediment moving through them but also have relatively low trapping efficiencies for this detritus (Trimble 1981; Allison et al. 1998; Goodbred and Kuehl 1998; Walling et al. 1999), while distal subaqueous fans are viewed as efficient sediment traps.

Formation times for the Melas fans were also estimated by calculating how long subaqueous turbidity currents would need to flow in order to deposit the volume of material

observed to compose the visible part of the fans. To estimate how long each lobe takes to form, we need to know the rate of sediment transport (Q_s). Fluid discharge through the channels is given by

$$Q_w = uBH \quad (1)$$

where u is the mean flow velocity, B is the channel width and H is the channel depth. Channel width and minimum depth (see discussion in the *Methods* section) can be measured from the Melas DEM. The flow velocity can be found by the Chezy flow resistance relation

$$u = (\tau_a^* R g D \alpha_r^2)^{1/2} \quad (2)$$

where τ_a^* is the dimensionless formative shear stress, R is the submerged specific density of grains ($R = \frac{\rho_s}{\rho} - 1$, where ρ_s is the sediment density and ρ is the fluid density), g is Martian gravity ($g = 3.7 \text{ m/s}^2$), D is the grain diameter, and α_r is the resistance coefficient for flow in a channel. In order to determine the values of these parameters, a grain size and composition must be assumed. We assumed sand sized quartz grains ($D=0.3 \text{ mm}$) which leads to $\tau_a^* = 1.8$, $R=1.65$, and $\alpha_r=15$ for active, mobile bed conditions (Parker et al. 1998). This yields a flow velocity of 0.8 m/s which is reasonable for turbidity currents. The characteristic velocity of turbidity currents can be related to the buoyancy flux by

$$B_f = R g u h B C \quad (3)$$

where B_f is the buoyancy flux, h is the flow thickness, and C is the concentration of sediment in the turbidity current. Britter and Linden (1980) related the buoyancy flux per unit width to the velocity of the current by

$$u_{front} = \Omega \left[\frac{B_f}{B} \right]^{1/3} \quad (4)$$

where u_{front} is the velocity of the head of the turbidity current and Ω is a proportionality factor. The densimetric Froude number is given by

$$Fr_{densimetric}^2 = \frac{u_{front}^2}{RghC} \quad (5)$$

(Middleton 1993), and can be related to Ω by

$$Fr_{densimetric}^2 \cong \Omega^3 = \frac{u_{front}^2}{RghC}. \quad (6)$$

For bed slopes between 0-10°, Ω^3 is between 1-1.5 (Britter and Lindon 1980). Since the slope of the southern Melas fan is $\sim 1^\circ$, Ω^3 and hence the densimetric Froude number should equal ~ 1 . In the case of small slopes, the front velocity of the turbidity current is the same as the characteristic velocity, so $u_{front} = u$ (Britter and Linden 1980). We can calculate the rate of sediment transport by

$$Q_s = Cu_{front}hB. \quad (7)$$

Typical sediment concentrations in turbidity currents range from 1-10%, and we assume a sediment concentration of 1% (Middleton 1993).

The timescale of formation is given by

$$t_{eq} = (1 - \lambda)V / Q_s \quad (8)$$

where V is the lobe volume and λ is the porosity (assume $\lambda=0.35$) (Jerolmack et al. 2004). The time for the formation of each of the ten lobes of the southern Melas fan was calculated, and these were added to get an estimated time of formation of ~106 years.

This calculation assumes that each lobe was formed by one turbidity flow event, which is conservative in that it likely would have taken several flows to develop lobes with levee-bounded channel networks (Yu et al. 2006). Experiments on turbidity currents show that multiple flow events are needed to form channel networks on the surfaces of submarine fans (Yu et al. 2006). Thus, what we recognize as a lobe in a plan-view of the Melas fans likely took several flow events to form. This could be tested by a rover mission, which could examine each lobe in cross-section to determine the number of flow events required to form each lobe.

Our calculation also assumes there was no hiatus between different turbidity flow events, and so the actual formation time is likely to be longer. Laboratory and field experiments show that although turbidite events appear to take place on the order of hours to days, the time between events is on the order of years to thousands of years (Rothman et al. 1994). If there was a hiatus of 10 years between each event, the southern fan would

have taken ~200 years to form, but if the hiatus was 1000 years then it would have taken ~10,000 years to form. The above timescale estimate does not take into account the formation time of the northern Melas fan, but assuming it took a comparable amount of time to form, this would double the amount of time standing water would have been required in the basin. By comparing analogous formation times for terrestrial submarine fans of comparable size, subaerial fan deposits on Mars, and our own calculations, we estimate a formation timescale of 10^2 to 10^4 years.

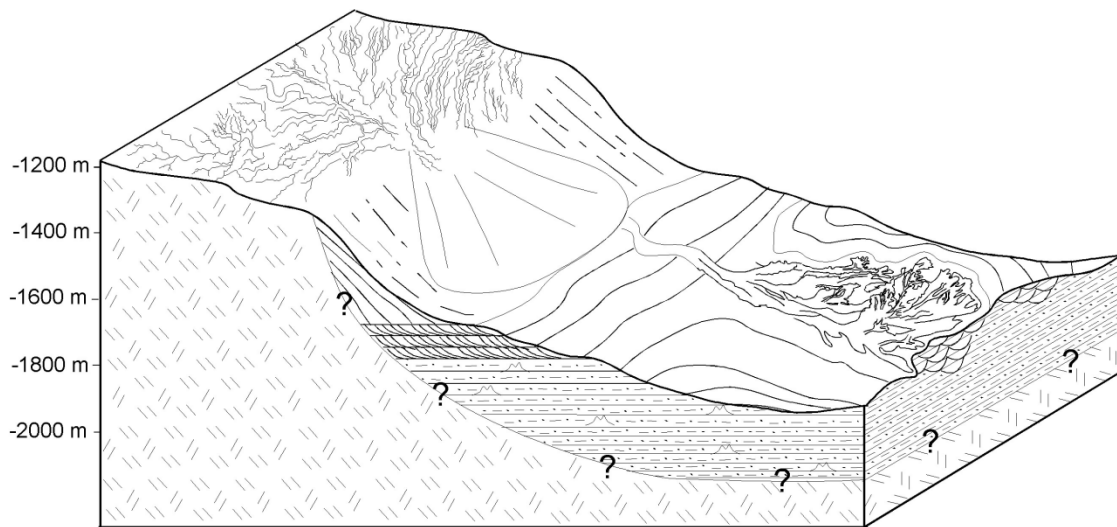


Figure 3.12 Ideal schematic arrangement of environments including sublacustrine fans, clinoforms, alluvial fan and incised channels; actual topography represented by white line in Fig. 3.2b. The inferred sublacustrine fans occur in the topographically lowest part of the basin.

6.5 Sublacustrine fans as terminal sediment sinks

We suggest that Southern Melas Basin could represent a complete erosional-to-depositional system, from the fluvially-incised source region in the surrounding highlands

to the terminal sediment sink formed by the sublacustrine fans in the topographically lowest part of the basin (Fig. 3.2b, 3.12). Sediments are moved from their source in the surrounding mountainous areas to their sink in depositional areas by the sediment transport system (Allen 2008). Fluvial incision of bedrock, interpreted to be caused by runoff from precipitation, drains the ridges bordering the western and eastern parts of the basin (Mangold et al. 2004; Quantin et al. 2005). Sediments generated during erosion of the upland areas were transported by fluvial drainage systems to form a classic, cone-shaped alluvial fan at the western edge of the basin where confined channel flow emerges onto the fan surface (Quantin et al. 2005). The preservation of sediments in the alluvial fan depends on whether there is accommodation space available to store the sediment over the long term. Accommodation space can be generated when the graded profile of these streams moves upwards in response to a rise in base level or to uplift of the source area (Viseras et al. 2003). The amount of sediment permanently stored in the alluvial fans is likely small compared to the total flux of sediment (Allen 2008). Sediments which pass through the alluvial fan could then be deposited as the clinoforms, which could record a potential shoreline or the upslope channel levee part of the submarine fan system (Dromart et al. 2007). The clinoforms give way further down the topographic profile to a sublacustrine fan, very similar in morphology to the Mississippi submarine fan (Fig. 3.2b, 3.12). This ultimate topographic low in the system then provides the terminal sink for the sediments (Leeder 1999).

The above interpretation assumes that the various elements of the geomorphic system are all the same age. If these features have different ages, then the linkages between

elements in the sediment transport system would not necessarily hold. However, even if not all of these elements are the same age, they still represent pieces of the sediment transport system. For example, cross-cutting relationships suggest there are several generations of valley networks preserved in the ridges surrounding Southern Melas Basin (Quantin et al. 2005). It is not possible to determine which generation of the drainages may have fed the depositional fans currently preserved in the bottom of the basin. Similar to the valley networks, perhaps the currently exposed clinoforms overlie a set of older buried clinoforms that are the same age as the depositional fan. As sediments were transported into the basin, the depositional system could have responded with retrogradation, aggradation, or progradation of the sediment depocenter further into the basin; these dynamic responses depend on how the incoming sediment flux balances with basin subsidence and lake level (Flemings and Grotzinger 1996; Hodgson et al. 2006).

We are assuming here that the sediments described in Southern Melas Basin post-date canyon formation and can therefore be linked to the modern geomorphic surface. If these sediments are actually older than the basin itself and have been exposed through erosion of the basin floor, then the depositional fans would predate, and thus not be related to the clinoforms, the alluvial fan, or the valley networks. Conclusive stratigraphic contacts that show that layered sediments underlie the volcanic material composing the ridges in Melas Chasma have not been observed. Areas where stratigraphic contacts are conclusive, such as to the east of Southern Melas Basin, show these layered materials onlap the ridges. Thus, there is no evidence to suggest that the layered materials in Southern Melas Basin are older than the basin.

3.7 Conclusions

The novel depositional fans in Southern Melas Basin have a unique morphology which includes multiple lobes with dendritic finger-like terminations that branch off at high angles in the downstream direction. The southern fan is located at a higher stratigraphic level than the northern fan, and layers near the fans show evidence for hydrated minerals including opaline silica and jarosite. The Melas fans appear morphologically similar to deltas and submarine fans; however, the details of the morphology and their basin position suggest that they are likely to be sublacustrine fans. Quantitative comparisons of the channel patterns present on the Melas fans show they are consistent with the channel patterns observed on terrestrial submarine fans, although the channel pattern on deltas is similar. A rover mission could acquire the detailed facies information necessary to conclusively discriminate between submarine fans and deltas. Estimates of minimum fan formation timescales suggest the fans formed in 10^2 to 10^4 years, and thus a stable body of water must have been present for at least this long. The preservation of valley networks in the topographic highs surrounding the basin, an alluvial fan where these valley networks drain into the basin, clinoforms, and depositional fans in the lowest part of the basin, suggest that the entire depositional system is preserved from the source area to the sink. This suggests that Mars was capable of supporting surface liquid bodies of water for a significant period of time during the initial stages of Valles Marineris formation.

Apex latitude (N)	Apex longitude (E)	Fan gradient (°)	Reference
-1.4	58.3	4.75	Kraal et al 2008
-1.46	58.39	4.06	Kraal et al 2008
-7.27	356.22	2.64	Kraal et al 2008
-18.09	322.89	2.66	Moore & Howard 2005
-18.32	340.11	2.21	Moore & Howard 2005
-18.41	323.35	5.67	Moore & Howard 2005
-20.1	123.2	6.41	Kraal et al 2008
-20.34	324.21	1.3	Moore & Howard 2005
-21.14	320.66	1.83	Moore & Howard 2005
-21.35	72.68	1.82	Moore & Howard 2005
-21.47	67.22	1.48	Moore & Howard 2005
-21.52	320.09	2.03	Moore & Howard 2005
-21.66	72.56	1.82	Moore & Howard 2005
-21.68	66.41	2.25	Moore & Howard 2005
-22.36	66.53	3.24	Moore & Howard 2005
-22.73	74.46	2.23	Moore & Howard 2005
-22.76	74.03	1.42	Moore & Howard 2005
-23.04	74.74	3.21	Moore & Howard 2005
-23.14	73.83	3.6	Moore & Howard 2005
-23.31	73.99	3.59	Moore & Howard 2005
-23.32	27.07	2.58	Moore & Howard 2005
-23.37	74.58	2.33	Moore & Howard 2005
-23.45	74.35	1.96	Moore & Howard 2005
-23.56	27.44	2.08	Moore & Howard 2005
-23.62	27.18	2.56	Moore & Howard 2005
-23.91	28.15	2.08	Moore & Howard 2005
-24.31	28.29	1.67	Moore & Howard 2005
-24.84	27.42	2.16	Moore & Howard 2005
-24.96	325.71	1.52	Moore & Howard 2005
-25.88	324.85	2.66	Moore & Howard 2005
-26.23	331.52	2.1	Moore & Howard 2005
-26.43	324.84	2.53	Moore & Howard 2005
-27	332.99	2.33	Moore & Howard 2005
-27.58	332.85	2.36	Kraal et al 2008
-27.65	332.93	1.58	Kraal et al 2008
-28.04	332.91	1.55	Kraal et al 2008
-28.09	332.77	2.26	Kraal et al 2008
-28.49	84.07	1.77	Moore & Howard 2005
-28.54	84.51	3.21	Moore & Howard 2005
-33	84.26	1.32	Kraal et al 2008
-33.02	84.19	1.58	Kraal et al 2008
-49.6	113.6	2.33	Kraal et al 2008
-51	114.3	1.85	Kraal et al 2008
-51	113.5	2.33	Kraal et al 2008
Average		2.5°	

Table 3.4 Compilation of Martian alluvial fan gradients. The average gradient is 2.5°.

Chapter 4

GEOMORPHIC CHANNEL PATTERNS OF DELTAS VERSUS DISTAL SUBMARINE FANS: IMPLICATIONS FOR SEDIMENTATION PROCESSES ON EARTH AND MARS

Abstract

Channel systems at the distal limits of submarine fans show variability in channel size and bifurcation patterns. This information is useful in constraining channel properties in static reservoir models, e.g. the mean and range of values typical for channel dimensions, sinuosity, and branching angles. Criteria were evaluated that might help discriminate between deltas and submarine fans based on the bifurcation pattern of the channels present on the fans, i.e. by using the properties of channel width, length, sinuosity, branching angle and gradients. Submarine fans and deltas show nonlinear decreases in mean channel width and channel length with increasing bifurcation order. Sinuosity is also found to decrease down fan. Channel branching angles appear to be stochastic and do not provide a meaningful measure to discriminate between fan types. The trends of mean channel length versus mean channel width follow a power law. The steepness of the power law trend does not appear to correlate with the dominant grain size present on the fan, the water depth of the fan, margin type or drainage basin size. The exponents of the power law fit for deltas are somewhat smaller than the exponents for submarine fans, but taking into account the uncertainties on the values, the two types of fans cannot be wholly distinguished.

We also characterized the channel patterns on a Martian submarine fan and delta and compared them to terrestrial fans. Channel lengths fall off slightly more slowly for a

given decrease in channel width on Mars possibly due to a longer advection length scale on Mars due to lower gravity.

4.1 Introduction

Understanding channel bifurcation patterns is important for understanding dynamics of sediment transport systems, in addition to providing constraints for reservoir models. The channels present on submarine fans are important hydrocarbon reservoirs in many areas of the world (Deptuck et al. 2007). Submarine channels form sand-rich channel complexes and the size, lateral continuity, connectivity and heterogeneity of sand bodies are important constraints in reservoir models (Clark and Pickering 1996; Labourdette 2007). Characterizing the variability in channel size and bifurcation pattern present in channel systems at the distal limits of submarine fans can be used to constrain channel properties in static reservoir models. We compare the channel bifurcation patterns present on submarine fans and deltas on both Earth and Mars to test whether the differences in sediment transport affect the channel bifurcation pattern.

If the channel patterns on deltas and submarine fans are indistinguishable, then this might provide a short-cut to modeling deepwater systems which, by virtue of their depositional setting, provide only difficult and expensive access for study. Instead, the scaling relationships from well-characterized deltas could be applied to submarine fan exploration prospects with only minor adjustments. In contrast, if the channel patterns on submarine fans and deltas are distinct, then this observation could provide an important criterion to interpret depositional environment for fans where the water depth is unknown.

A further application, of interest to planetary science, would be to provide a basis for separation of subaerial from fully subaqueous sediment bodies on planets like Mars.

This study tested whether it is possible to discriminate between deltas and submarine fans based on the bifurcation pattern of the channels present on the fans by using the properties of channel width, length, sinuosity, branching angle and gradients. Channels on six terrestrial submarine fans, two terrestrial deltas, two Martian submarine fans and one Martian delta were compared.

4.2 Background

One might expect the channel patterns on deltas and submarine fans to differ, since channels on deltas are fed by rivers whereas channels on submarine fans are fed by turbidity currents. These turbidity currents flow down sinuous deep-water channels through laterally extensive channel-levee systems that locally aggrade significantly above the low gradient fan surface (Wynn et al. 2007). These levees can build up to hundreds of meters above the submarine fan surface, and by definition this occurs on the upper and middle submarine fan (Flood and Damuth 1987). The channels are thought to avulse frequently with only one channel active at a time (Damuth et al. 1983b; Wynn et al 2007). Levees exist for channels in the upper and middle submarine but are not seen on lower submarine fans (Flood and Damuth 1987).

Many studies have examined submarine channels on the upper and middle regions of submarine fans (Flood and Damuth 1987; Clark et al. 1992; Deptuck et al. 2007; Kolla

et al. 2007; Wynn et al. 2007), but few studies focus on channels across lower submarine fans (Twitchell et al. 1992; Nelson et al. 1992). The channels on upper and middle submarine fans are similar to river channels in several aspects of their planform geometries (Clark et al. 1992; Flood and Damuth 1987). Also similar to subaerial river channels, submarine channels show high sinuosity, abandoned meander loops, lateral channel migration, crevasse splays and abandoned terraces (Damuth et al. 1983a, Pickering et al. 1986; Karl et al. 1989; Beaufouef et al. 2002). Yet, there is a lower occurrence of meander loop cutoffs and avulsions in submarine channels as compared to subaerial channels, which may be due to stabilization of the sinuosity by deposition on both the inner and outer bends of submarine channels (Kane et al. 2008). Strongly bypassing turbidity currents deposit on the inner channel bend, whereas weakly bypassing flows deposit on the outer channel bend, a case unique to submarine channels (Kane et al. 2008). Straub et al. (2008) conducted laboratory experiments on turbidity current deposition in sinuous channels and found high deposition rates on the outer banks of bends. They concluded that sedimentation rates were highest where near-bed sediment concentration was greatest, which occurs on the outer banks of channel bends. This contrasts with subaerial river channels where bedload transport dominates the evolution of channel morphology (Dietrich and Whiting 1989). Since bedload transport does not cover the steep outer banks of bends, the sidewalls are exposed to erosion by the moving fluid (Straub et al. 2008).

Distributary channel patterns on deltas are controlled by a combination of channel mouth bifurcations and avulsions, with channel bifurcations being more common (Slingerland and Smith 2004; Edmonds and Slingerland 2007; Jerolmack and Mohrig

2007; Edmonds et al. 2009). Recent studies that focus on understanding bifurcations of channels in deltas have debated whether bifurcations are caused by the buildup of mouth bars or the deceleration of jet plumes (Wright 1977; Wellner et al. 2005; Edmonds and Slingerland 2007). As discussed by Wright (1977), a sediment-laden flow enters a standing body of water as a turbulent jet at the mouth of a distributary channel and begins to spread laterally. As the turbulent jet decelerates, its transport energy diminishes, causing deposition of material. Bed friction in the shallow depths basinward of a river mouth causes rapid deceleration, lateral expansion and sediment deposition in a mouth bar.

Distributary channel bifurcation patterns will depend on where mouth bars form as well as their final location. Edmonds and Slingerland (2007) document bifurcation patterns on several deltas, and they show that distributary channel widths and lengths decrease nonlinearly with successive bifurcation number (order). Channel width decreases with increasing bifurcation order, defined as the number of bifurcations upstream of the channel in question, because the channels are adjusting to a decreasing discharge (Edmonds and Slingerland 2007). They suggest that channel length decreases are the result of jet momentum flux decreases. Since the distance to the river mouth bar is proportional to jet momentum flux, a decreased momentum flux would lead to smaller distances between successive mouth bars and hence more closely spaced channel bifurcations. Olariu and Bhattacharya (2006) document terminal distributary channels on several river-dominated deltas and measure the channel orientations with respect to the main trunk channel. They found that these angles were related to the overall dominant processes operating on the delta (eg. wave dominated, river dominated or tide dominated deltas). Since delta-plain

gradients are small and sedimentation rates are high, the direction of distributary channels can be easily changed (Olariu and Bhattacharya 2006). With each bifurcation of the channel, the discharge is split between the newly formed channels, and hence the channels become smaller in a downstream direction.

The purpose of this study was to compare morphometric data on submarine distributary networks to delta distributary networks to see if the patterns differ enough to allow discrimination between fan types where the environment of deposition is unknown. Our mapping of the channels on the distal limits of submarine fans and fluvial deltas on both Earth and Mars shows that the bifurcation patterns on the two types of fans are indistinguishable using simple parameters.

4.3 Study Sites

Six terrestrial submarine fans, two Martian submarine fans, two terrestrial deltas and one Martian delta were examined in this study. We selected the terrestrial submarine fans based on the availability of side-scan sonar or seismic images of sufficient quality to be able to distinguish the channel patterns. Wax Lake delta, LA, was selected since it has had relatively little human influence impacting its morphology. The Lena delta, Russia, was chosen since it is in a permafrost region, and conditions on Mars when the deltas and submarine fans formed may have been similar (Baker 2006). Table 4.1 lists basic properties of each fan. The locations of the terrestrial submarine fans and deltas are shown in Figure 4.1.

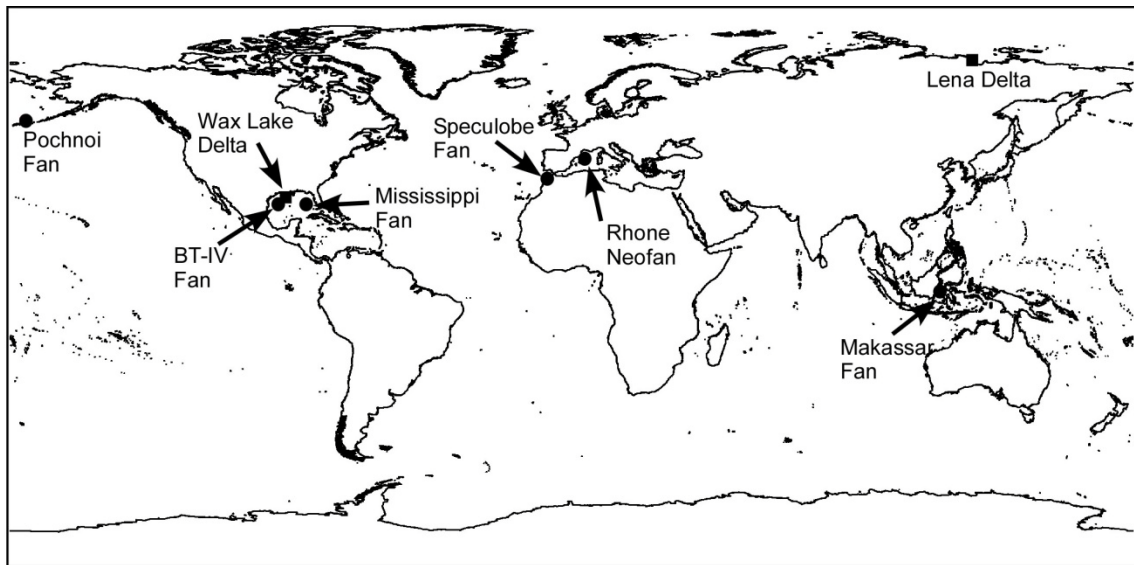


Figure 4.1 Map showing location of fans in this study. Squares represent the locations of deltas and circles represent the locations of submarine fans.

4.3.1 Submarine Fans

Speculobe

The Speculobe fan is a small (3 by 14 km) seafloor fan located in the Gulf of Cadiz offshore Spain. The fan is sand-rich and contains predominantly fine to medium grained sand and a low clay content <1.5 vol % (internal Shell data). It lies on the lower slope of the Gulf of Cadiz at a water depth of approximately 1500 m. The width of the lower slope varies from 50 km to 200 km, and this area has been tectonically active in the Quaternary (Hernandez-Molina et al. 2006).

Fan	Grain size	Water depth (m)	Fan Length (km)	Fan Width (km)	Fan Area (km ²)	Fan Volume (km ³)	Drainage Basin Area (km ²)	Tectonic State
Bering	?	?	400	190	20,000 ^f	?	1.2×10 ⁵	Active
BT Basin IV	sand	1500	16 ^c	8 ^c	128	12.8 [*]	1.2×10 ⁵	Passive
Makassar	mud	2400	65 ^a	50 ^a	2500 ^a	7.5 [‡]	7.5×10 ⁴	Active
Mississippi	mud	3200	600 ^b	500	300,000 ^b	290,000 ^b	4.76×10 ⁶	Passive
Rhone Neofan	sand	2400	100	14	1430 ^b	25 ^b	9.0×10 ⁴	Passive
Speculobe	sand	1500	14	3	48	0.3 [‡]	5.7×10 ⁴	Active ^e
Melas N	?	?	2.1	1.5	2.3 ^d	0.05 ^d	~500	-
Melas S	?	?	1.3	3	4.3 ^d	0.10 ^d	~500	-
Wax Lake Delta	sand	~0	11	12	40	0.08 ^{**}	?	Passive
Lena Delta	sand	~0	190	190	32,000	?	2.5×10 ⁶	Active
Eberswalde Delta	?	~0	13.7	11.5	102	?	4800	-

Table 4.1 Properties of the fan systems examined in this study. Grain size refers to the dominant grain size. Tectonic state refers to whether or not the area was tectonically active when the fan was deposited. †Shell cores show that the depth of the sand composing the fan near the centre is 8 m and is 2 m near the edges of the fan. An intermediate depth value of 6 m was used to calculate the volume (Shell Speculobe Report Phase II). ‡The longest core of the fan lobes described in Orange et al. (2006) is 3 m, so this value was used to calculate the volume of the fan, although the actual thickness is likely to be larger.

*Calculated assuming thickness of fan is 100 m (Beaubouef et al. 2003). **Thickness of sediments ranges between 0.5-3 m (Wellner et al. 2005); An intermediate value of 2 m was used for this volume calculation. a. Orange et al. 2006, b. Wynn et al. 2007, c. Beaubouef et al. 2003, d. Metz et al. 2009b, e. Hernandez-Molina et al. 2006, f. Herman et al. 1996.

Makassar Straits

The seafloor fan in Makassar Straits is a very low relief mud-rich submarine fan located between the islands of Borneo and Sulawesi. It is approximately 40 km wide by 60 km long and is located at a water depth of ~2400 m. Makassar Straits formed during the Eocene in response to crustal extension, and after Borneo was uplifted during the Neogene, the massive outbuilding of the Mahakam Delta occurred (Hall et al. 2009). Much of this deltaic sediment was redeposited as turbidites in the Makassar Basin (Jackson 2004; Konyukhov 2009). Differential uplift in the Late Pliocene changed the direction of sediment transport from eastward to westward when mini-basins associated with the long limbs of west-verging anticlines filled with coarse-grained turbidites (Jackson 2004).

Mississippi

The Mississippi submarine fan is a large (>600 km long), mud-rich seafloor fan with an area of ~300,000 km² and a volume of 290,000 km³ (Fig. 4.2A; Wynn et al 2007). This passive-margin submarine fan was sourced through a major submarine valley system at the shelf margin and upper slope, which in turn was fed by a large river (the ancestral Mississippi River) with its continental drainage system. It was largely constructed during the Plio-Pleistocene when sedimentation rates were as high as 6-11 m per 1000 years during the Pleistocene glacials (Wynn et al. 2007). Finger-shaped backscatter patterns on the edge of the fan correlated with restricted sand-silt beds suggest channelized flows may have been an important sediment-delivering process to the distal fan (Twitchell et al. 1992; Nelson et al. 1992).

Brazos-Trinity Basin IV

The Brazos-Trinity Basin IV ponded apron is located in the northwestern Gulf of Mexico and is formed in the terminal basin of four linked intraslope basins (Fig. 4.2B). The apron is of Pleistocene age (Beaubouef et al 2003), and is deposited on a relatively shallow synclinal ramp with no outlet (Mallarino et al 2006). The apron is located in ~1500 m of water depth and is 8 km wide by 16 km long with a maximum thickness of 100 m (Beaubouef et al 2003). Its oval-shaped basin is thought to be a salt withdrawal mini-basin and the main axis is oriented in a northeast-southwest direction (Mallarino et al

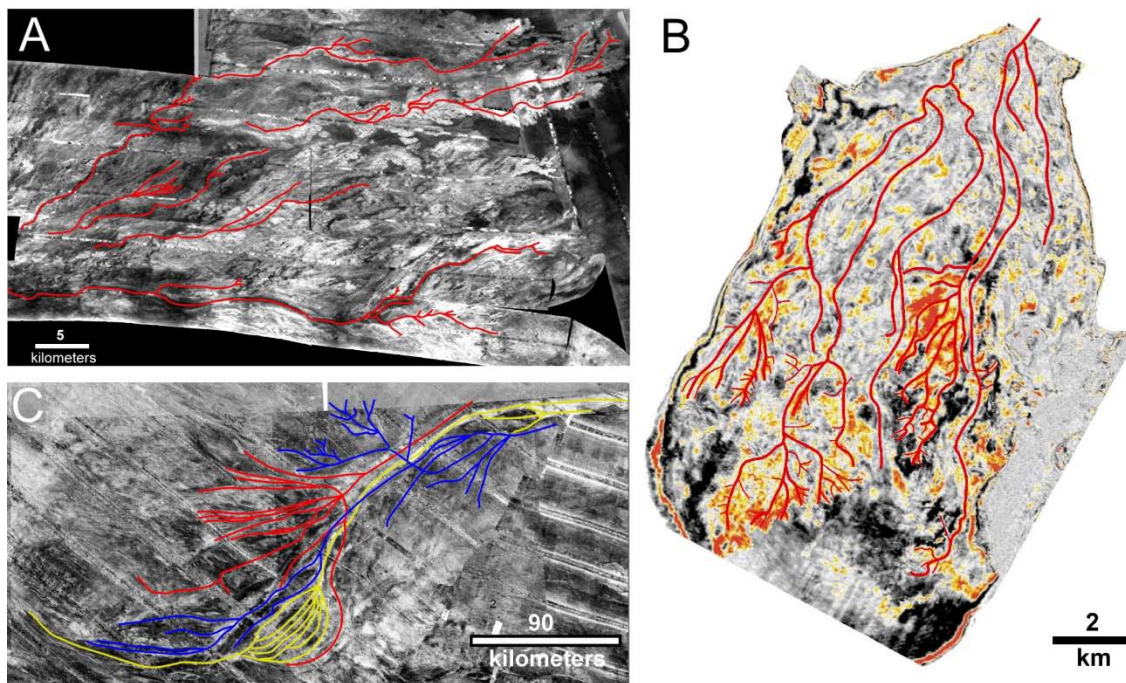


Figure 4.2 Examples of channel mapping on side-scan sonar and seismic images. A.) Side-scan sonar image of Mississippi submarine fan showing the channels mapped in red. B.) Horizon slice from 20 ms below the top of the fan extracted from a high-resolution 3D seismic volume of the Brazos-Trinity Basin IV ponded apron from Beaubouef et al. (2003). Channels are mapped in red. C.) 6.6 kHz side-scan sonar image of the Bering fan with the channels mapped in different colors which reflect the relative ages of the channels based on cross cutting relationships (yellow are oldest, blue are youngest).

2006). Sediment is supplied to the apron from an inlet channel to the northeast (Beaubouef et al 2003). Cores show the proximal fan is sand-rich while the periphery and areas further down-fan are more mud-rich (Beaubouef et al 2003; Mallarino et al 2006). The majority of the sand was deposited between 115-15 ka, with maximum accumulation rates during the Last Glacial Maximum (Mallarino et al 2006).

Rhone Neofan

The Rhone Neofan is part of the much larger Petit-Rhone Fan, formed from the most recent avulsion of the Rhone channel in the Gulf of Lion at a water depth of ~2400 m. The Gulf of Lion is a young passive margin with a high subsidence rate, and is supplied with sediments from the Rhone River (Droz et al. 2006). The continental shelf is 80 km wide, and the slope is strongly incised by canyons (Droz et al. 2006). Coring shows that the Neofan is composed of medium to fine-grained, well-sorted sand (Torres et al. 1997; Droz et al. 2001). The growth of the Neofan began at 80 ka BP and continued until 18 ka BP and is thought to have been controlled by Quaternary glacio-eustatic changes. The Rhone Neofan is up to 70 m thick, covers an area of 1430 km² and had a volume of 25 km³ (Wynn et al. 2007).

Bering Fan

The Bering fan is one of three main canyon-channel systems located in the Aleutian Basin in the Bering Sea (Fig. 4.2C; Herman et al., 1996). The area of the Bering fan is

20,000 km², and it is thought to be a very young feature, possibly of late Pliocene-Quaternary age (Herman et al., 1996).

4.3.2 Deltas

Wax Lake Delta

Wax Lake Delta is a modern bay head fan delta located at the mouth of the Wax

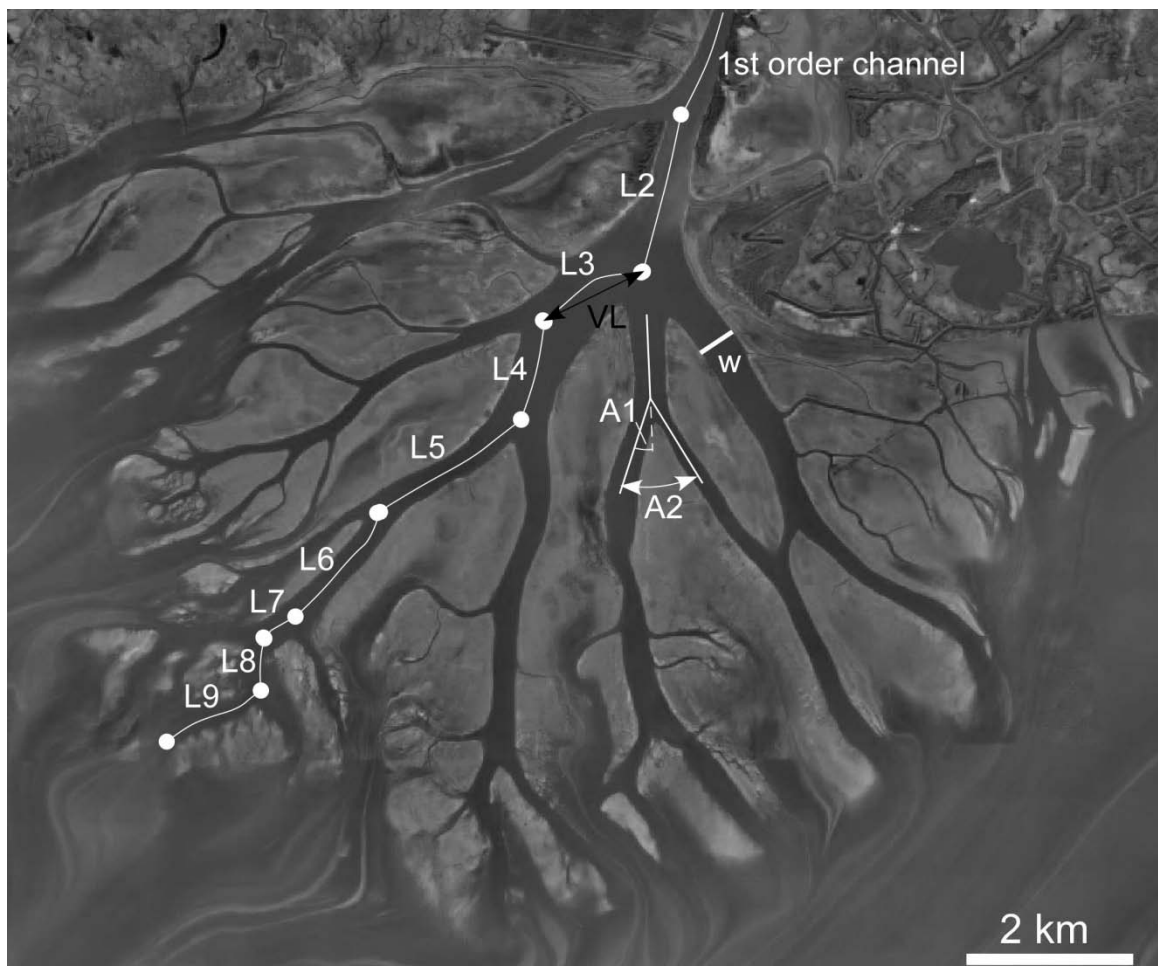


Figure 4.3. High-altitude aerial photograph of the Wax Lake Delta taken in 2002. The first order channel is noted along with bifurcation points (circles), channel lengths (L), valley lengths (VL), channel width (w), and branching angles (A1 and A2).

Lake outlet, LA, which is a man-made channel excavated in 1941 (Fig. 4.3; Wellner et al. 2005; Parker and Sequeiros 2006). Deltaic deposition at the Wax Lake Outlet was entirely subaqueous until 1972 when the tops of several deltaic sublobes were exposed at mean low tide (Wellner et al. 2005). The formation of this delta was tracked through time by images taken over the last thirty years. There have been negligible human influences on the delta since the original excavation of the channel.

Lena Delta

The Lena delta is a river-dominated delta located at the Laptev Sea coast in northeast Siberia in a permafrost region (Olariu and Bhattacharya 2006). The permafrost may affect river bank stability (Lawson 1983). The evolution of the delta has been strongly influenced by tectonic forces over the last 80,000 years (Are and Reimnitz 2000). A large fraction of the delta is underlain by Devonian bedrock which may control the channel distributary pattern (Are and Reimnitz 2000).

4.3.3 Mars Fans

Two submarine fans have been identified in southwest Melas Chasma in Valles Marineris on Mars (see Fig. 4.6). These submarine fans were identified based on their morphologic similarity to the Mississippi submarine fan complex. The Melas fans are composed of multiple channelized lobate deposits. The northern fan is 2.1 km long and has

an area of 2.3 km² while the southern fan is 1.3 km long with an area of 2.2 km² (Metz et al., 2009b).

The Eberswalde delta is located within a 65 kilometer diameter crater at 24.3° S latitude, 33.5° W longitude on Mars (Malin and Edgett 2003). The delta is an erosional remnant of a larger and thicker paleodeltaic deposit and is composed of six separate deltaic lobes (Lewis and Aharonson 2006; Wood 2006). The delta surface is covered by numerous channel forms and bifurcating distributaries that appear as present-day topographic highs after being elevated by erosion and deflation of the surrounding host sediments (Bhattacharya et al. 2005; Wood 2006).

4.4 Data

Side-scan sonar or seismic images of six terrestrial submarine fans were examined in this study along with aerial photographs and satellite images of two terrestrial deltas. Satellite images of Martian submarine fans and a delta were also examined.

4.4.1 Submarine Fans

Deep-towed 100 kHz high-resolution side-scan sonar collected by UK-TAPS during the TTR-12 cruise in 2002 of the Speculobe fan was used along with a 2 m contour interval bathymetric map compiled on the basis of this survey. A 100 kHz side-scan sonar survey of the Rhone Neofan collected by UK-TAPS was also used. We used high-resolution SeaMARC IA 27-30 kHz side-scan sonar images of the Mississippi submarine fan acquired in 1990 by the U.S. Geological Survey (Twitchell et al. 1992). 6.5 kHz Gloria

side-scan sonar images of the Bering fan acquired by the USGS between 1986-1987 were also used (EEZ-SCAN Scientific Staff 1991). We used multibeam backscatter images acquired by Unocal in 2003 to study the basin floor fan located in the Makassar Straits as well as a 10 m contour interval bathymetric map. A horizon slice from 20 ms below the top of the fan extracted from a high-resolution 3D seismic volume from Beaubouef et al. (2003) was used to study Basin IV in the Brazos-Trinity system.

Several factors can affect the backscatter pattern returned from side-scan sonar profiles including the geometry of the sensor-target system, the roughness of the seafloor, and the composition and grain size of the surface (Blondel and Murton 1997). Gardner et al. (1991) found that regional backscatter patterns correlate, at least qualitatively, with lithostratigraphy.

4.4.2 Deltas

The Wax Lake Delta was studied by using a high-altitude infrared aerial photograph (pixel size ~16 m) taken in 2002 at low tide and a 0.5 m contour interval bathymetric map (Wellner et al 2005). A Landsat 7 (ETM+) image was used to study the Lena Delta (spatial resolution of 30 m).

4.4.3 Mars Fans

The image of the Melas submarine fans used in this study was PSP_0007667_1700 taken by the HiRISE (High Resolution Imaging Science Experiment) camera onboard the

Mars Reconnaissance Orbiter. The image is in the visible spectral range, was acquired at ~3 pm local Mars time, and has a pixel size of 30 cm.

A Mars Global Surveyor Mars Orbiter Camera narrow angle mosaic of the Eberswalde delta was used to map the channels on the delta. The mosaic has a resolution of 1.5 m/pixel and was created by Malin Space Science Systems (M. C. Malin, et al., Distributary Fan Near Holden Crater, NASA's Planetary Photojournal, <http://photojournal.jpl.nasa.gov/>, PIA04869, 13 November, 2003).

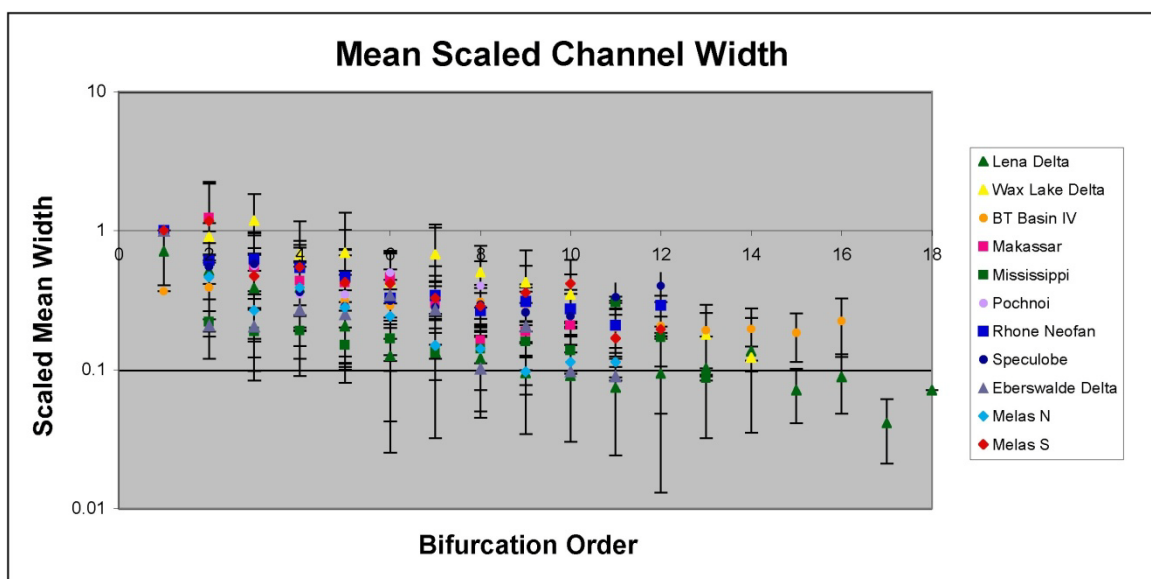


Figure 4.4 Plot of mean scaled channel width versus bifurcation order.

4.5 Methods

The properties of distributary channels were measured by hand in ArcGIS.

Channels that rejoin downstream were excluded from the analysis. We defined channels

similarly to Edmonds and Slingerland (2007) where the channel length (L) is defined as the distance between two bifurcation points along the channel centerline (Fig. 4.3). The valley length is the straight-line distance between two bifurcation points (Fig. 4.3). The channel width (W) is the average across-stream distance from water edge to water edge on the day the image was taken (Fig. 4.3).

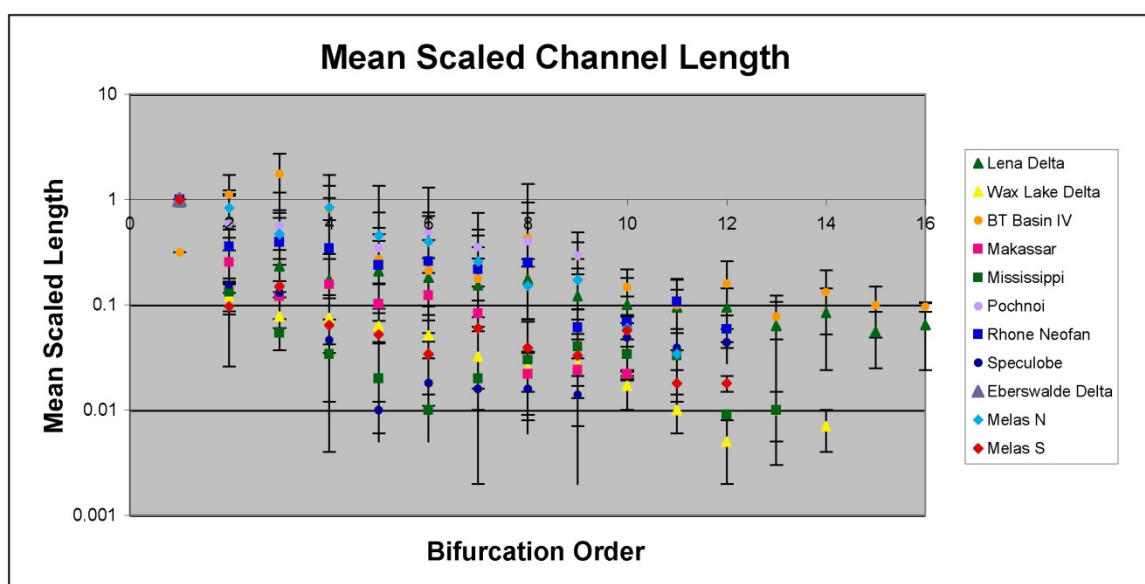


Figure 4.5 Plot of mean scaled channel length versus bifurcation order.

The mean channel widths and lengths reported are the average measurements for all channels of a particular order on a fan. The error bars in figures 4.5 and 4.7-4.8 and the uncertainties in Table 4.2 are the standard deviations of the population of channel measurements for each order. The standard deviations are fairly large due to the large range of variability in each of the parameters that were measured. The smallest channel

observed on a particular fan is limited by the resolution of the image used for analysis. The standard deviations reported for the fitted parameters n and a in Figure 4.6 were calculated using a montecarlo analysis with 1000 iterations.

The branching angle was measured in two different ways. In the first method, after each bifurcation point the angle that a channel veers off from the straight-line path of the trunk channel is measured (A1 in Fig. 4.3). The second method measures the angle between the two channels after a bifurcation (A2 Fig. 4.3). The lines used to measure the branching angles after the split are defined by an approximation of a straight line to the centerline over about three channel diameters as measured before the channel split. The channel gradient was calculated by dividing the difference in bed elevation between the beginning and end of a channel by the channel length, since densely-spaced bathymetric data were not available. The sinuosity was calculated by dividing the channel length by the valley length. Therefore, a sinuosity of 1 is a straight channel, and a sinuosity greater than 1 is sinuous.

The goal of this study was to compare channel systems on many different fans. To this end, we sought to remove the issue of scale when looking at many different sized systems. We accomplished this by comparing only non-dimensional parameters, such as sinuosity and branching angle, and scaling other parameters to make them non-dimensional. We divided the channel width by the width of the main river or submarine channel before it has split once (defined as a first order channel) and channel length by the length of the first order channel to make these parameters non-dimensional.

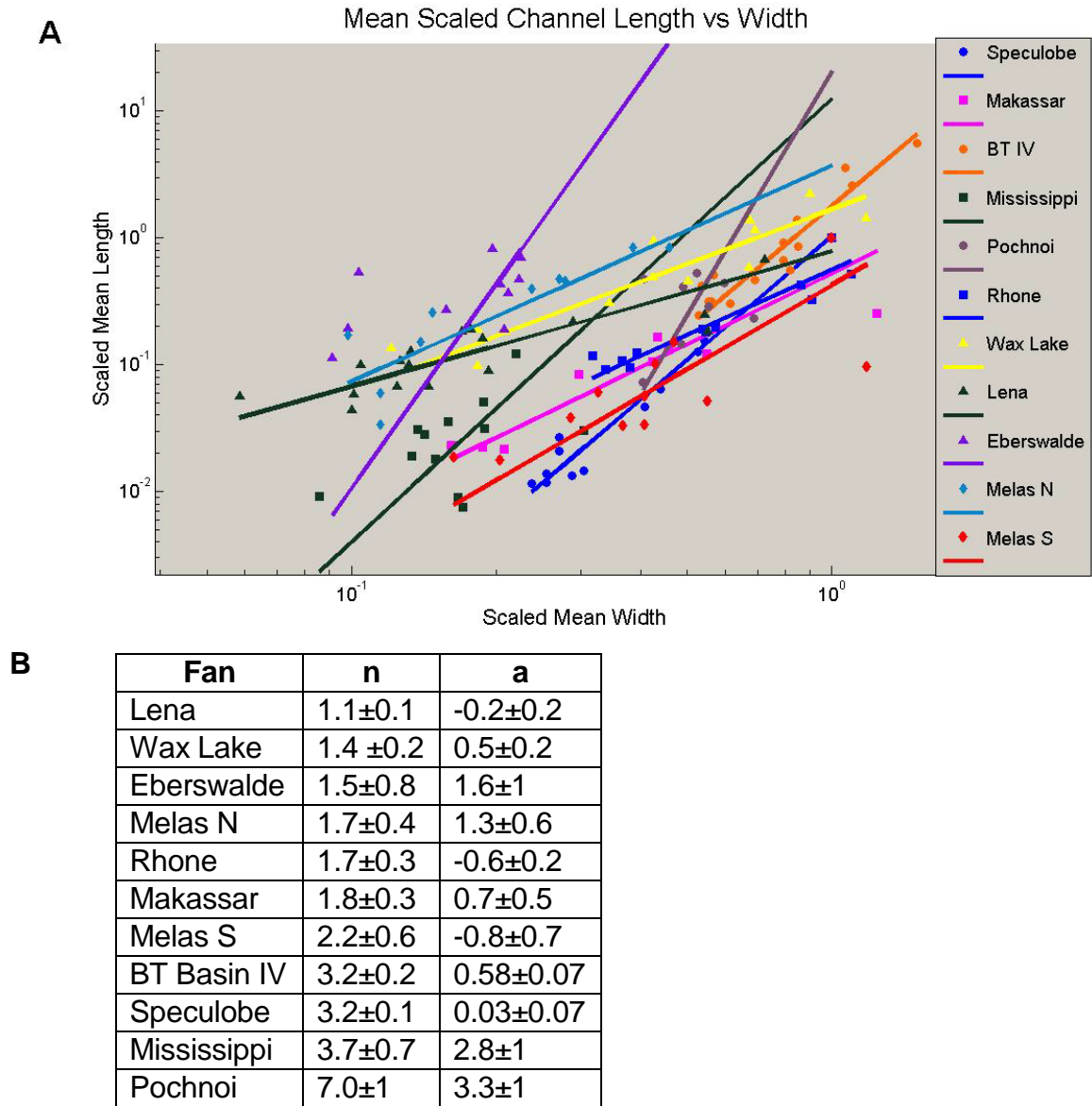


Figure 4.6. A.) Log-log plot of power law fits ($L=aW^n$) to mean scaled channel length (L) versus width data (W). B.) The fitted values for n and a are shown for each fan along with the standard deviations of the fitted parameters.

Fan	Order	N	Mean Channel Width (km)	Mean Channel Length (km)	Mean Channel Gradient (m/km)	Mean Channel Sinuosity

Bering	1	4	5.402±3	89.17±87	-	1.03±0.04
	2	11	2.196±1	41.985±53	-	1.03±0.05
	3	14	3.232±2	39.396±25	-	1.07±0.09
	4	15	2.823±2	46.725±33	-	1.04±0.06
	5	12	2.644±2	36.552±26	-	1.01±0.01
	6	7	3.71±2	20.769±21	-	1.04±0.04
	7	11	2.617±1	13.062±22	-	1.04±0.08
	8	6	2.987±1	25.711±29	-	1.00±0.01
	9	4	2.182±0.5	6.464±3	-	1.01±0.02
Brazos-Trinity	1	1	0.155±0.04	0.717±0.04	-	1.09±0.01
Basin IV	2	3	0.165±0.07	2.543±1	-	1.05±0.02
	3	6	0.233±0.1	3.970±2	-	1.18±0.03
	4	6	0.171±0.07	1.855±2	-	1.05±0.03
	5	13	0.132±0.07	0.613±0.6	-	1.02±0.03
	6	14	0.123±0.04	0.480±0.4	-	1.03±0.04
	7	12	0.127±0.05	0.401±0.2	-	1.01±0.01
	8	15	0.131±0.06	0.985±1	-	1.03±0.04
	9	15	0.123±0.05	0.659±0.4	-	1.02±0.04
	10	22	0.107±0.04	0.334±0.2	-	1.02±0.05
	11	23	0.086±0.04	0.226±0.1	-	1.02±0.05
	12	14	0.088±0.04	0.362±0.3	-	1.04±0.06
	13	20	0.082±0.04	0.176±0.1	-	1.01±0.04
	14	5	0.083±0.04	0.300±0.2	-	1.05±0.1
	15	6	0.087±0.04	0.224±0.1	-	1.03±0.05
	16	4	0.095±0.05	0.217±0.04	-	1.04±0.07
Makassar	1	3	3.189±0.1	54.857±3	1.658±0.02	1.02±0.01

	2	7	3.961±3.2	13.978±3	0.845±0.1	1.01±0.01
	3	12	1.753±1.4	6.709±2	0.746±0.2	1.03±0.03
	4	15	1.385±1	9.012±9	0.635±0.5	1.03±0.04
	5	14	1.349±1	5.757±3	0.568±0.3	1.02±0.03
	6	14	1.458±0.8	7.129±4	0.481±0.3	1.03±0.03
	7	10	0.947±0.8	4.582±3	0.496±0.3	1.02±0.02
	8	7	0.514±0.4	1.263±1	0.551±0.2	1.00±0.01
	9	4	0.598±0.4	1.237±0.4	0.739±0.3	1.00±0.01
	10	2	0.663±0.1	1.183±0.1	0.602±0.3	1.00±0.01
Mississippi	1	1	0.845±0.09	96.261±0.09	-	1.14±0.02
	2	7	0.186±0.1	11.838±5	-	1.06±0.03
	3	14	0.159±0.09	4.852±5	-	1.07±0.08
	4	22	0.160±0.09	2.994±3	-	1.06±0.08
	5	18	0.126±0.09	1.737±1	-	1.04±0.04
	6	12	0.141±0.09	0.873±0.4	-	1.02±0.03
	7	6	0.113±0.09	1.818±1	-	1.04±0.03
	8	6	0.120±0.09	2.724±4	-	1.03±0.04
	9	5	0.134±0.09	3.442±4	-	1.02±0.02
	10	2	0.116±0.09	2.944±2	-	1.02±0.02
	11	2	0.257±0.09	2.912±1	-	1.05±0.05
	12	2	0.144±0.09	0.727±0.1	-	1±0.02
	13	2	0.073±0.09	0.874±0.1	-	1±0.02
Rhone Neofan	1	2	0.145±0.04	3.300±0.3	-	1.06±0.02
	2	6	0.132±0.1	1.079±0.3	-	1.06±0.04
	3	8	0.159±0.1	1.696±2	-	1.03±0.03
	4	10	0.125±0.06	1.399±1	-	1.03±0.04

	5	17	0.083±0.04	0.647±0.5	-	1.04±0.04
	6	18	0.079±0.04	0.600±0.3	-	1.05±0.07
	7	14	0.078±0.04	0.631±0.4	-	1.05±0.05
	8	14	0.057±0.04	0.409±0.4	-	1.06±0.1
	9	12	0.055±0.04	0.313±0.2	-	1.06±0.08
	10	8	0.053±0.04	0.354±0.2	-	1.07±0.09
	11	7	0.046±0.04	0.386±0.2	-	1.02±0.03
	12	4	0.049±0.04	0.301±0.09	-	1.08±0.03
Speculobe	1	1	0.059±0.005	9.7±0.005	19.998±0.3	1.22±0.02
	2	2	0.032±0.005	1.504±0.8	8.749±0.3	1.06±0.02
	3	6	0.031±0.05	1.22±0.9	4.937±4.2	1.16±0.1
	4	9	0.026±0.008	0.622±0.6	3.219±4.8	1.07±0.05
	5	13	0.024±0.01	0.447±0.5	8.26±3.5	1.06±0.05
	6	19	0.016±0.006	0.201±0.1	5.338±4.7	1.05±0.05
	7	26	0.017±0.007	0.129±0.09	5.275±3.9	1.02±0.03
	8	27	0.015±0.005	0.115±0.09	3.807±4.4	1.02±0.03
	9	22	0.015±0.005	0.135±0.1	3.502±2.9	1.02±0.04
	10	10	0.014±0.005	0.112±0.06	6.776±4.7	1.02±0.03
	11	4	0.016±0.005	0.261±0.09	6.637±3.7	1.01±0.02
	12	2	0.018±0.008	0.142±0.02	9.697±1.9	1.00±0.02
Melas N	1	1	0.122±0.0008	0.417±0.0008	-	1.01±0.01
	2	3	0.056±0.03	0.347±0.2	-	0.032±0.04
	3	6	0.033±0.02	0.196±0.08	-	1.01±0.01
	4	5	0.047±0.03	0.349±0.09	-	1.01±0.006
	5	8	0.034±0.02	0.191±0.1	-	1.01±0.02
	6	15	0.029±0.03	0.165±0.1	-	1.04±0.06

	7	15	0.018±0.009	0.107±0.09	-	1.02±0.02
	8	14	0.017±0.009	0.063±0.03	-	1.03±0.07
	9	6	0.012±0.004	0.072±0.04	-	1.00±0.01
	10	4	0.014±0.003	0.025±0.008	-	1.03±0.06
	11	4	0.014±0.004	0.014±0.006	-	1.00±0.01
Melas S	1	1	0.049±0.0008	1.976±0.0008	-	1.04±0.01
	2	3	0.058±0.04	0.190±0.1	-	1.00±0.01
	3	6	0.023±0.01	0.297±0.2	-	1.06±0.04
	4	10	0.027±0.01	0.102±0.2	-	1.01±0.01
	5	14	0.021±0.01	0.201±0.2	-	1.02±0.03
	6	15	0.020±0.01	0.067±0.05	-	1.01±0.02
	7	24	0.016±0.007	0.119±0.1	-	1.03±0.04
	8	11	0.014±0.005	0.076±0.05	-	1.01±0.01
	9	2	0.018±0.009	0.066±0.04	-	1.01±0.01
	10	3	0.020±0.01	0.112±0.02	-	1.01±0.02
	11	4	0.008±0.004	0.037±0.01	-	1.01±0.02
	12	2	0.010±0.0008	0.035±0.005	-	1.01±0.01
Wax Lake Delta	1	1	0.355±0.09	1.399±0.09	0.357±0	1.00±0.01
	2	2	0.320±0.09	3.110±1.1	0.125±0.1	1.01±0.01
	3	5	0.417±0.2	1.993±1.1	0.319±0.2	1.00±0.01
	4	8	0.240±0.2	1.938±1.1	0.273±0.2	1.04±0.07
	5	7	0.245±0.1	1.630±0.6	0.236±0.2	1.02±0.03
	6	10	0.151±0.09	1.327±0.6	0.065±1	1.09±0.2
	7	8	0.239±0.2	0.826±0.6	0.412±0.7	1.03±0.05
	8	8	0.178±0.1	0.645±0.3	0.075±0.06	1.01±0.03
	9	16	0.150±0.1	0.685±0.4	0.552±0.5	1.04±0.05

	10	6	0.122±0.09	0.434±0.2	0.801±0.1.2	1.11±0.2
	11	4	0.074±0.09	0.255±0.1	0.057±0.08	1.10±0.1
	12	6	0.065±0.09	0.137±0.09	0.064±0.09	1.12±0.5
	13	6	0.065±0.09	0.268±0.1	0.556±1.1	1.05±0.05
	14	4	0.043±0.09	0.190±0.09	0.063±0.07	1.07±0.08
Lena Delta	1	2	4±2	66±40	-	1.07±0.002
	2	4	3.0±0.7	44±30	-	1.13±0.1
	3	6	2±2	16±8	-	1.07±0.06
	4	12	2±2	12±9	-	1.1±0.1
	5	20	1.2±0.6	14±10	-	1.11±0.2
	6	34	0.7±0.6	13±8	-	1.14±0.2
	7	40	0.8±0.6	11±11	-	1.1±0.2
	8	44	0.7±0.4	12±9	-	1.16±0.2
	9	43	0.6±0.4	9±7	-	1.12±0.2
	10	36	0.5±0.4	7±6	-	1.07±0.07
	11	42	0.4±0.3	7±5	-	1.06±0.06
	12	26	0.5±0.5	7±4	-	1.09±0.08
	13	26	0.6±0.4	4±4	-	1.03±0.06
	14	18	0.8±0.6	6±4	-	1.06±0.05
	15	12	0.4±0.2	4±2	-	1.05±0.05
	16	6	0.5±0.2	4±3	-	1.09±0.05
	17	4	0.24±0.09	4±1	-	1.04±0.03
	18	2	0.4±0.08	2.8±0.2	-	1.07±0.02
Eberswalde Delta	1	3	0.52±0.2	1.8±0.6	-	1±0.03
	2	14	0.10±0.1	1.6±0.7	-	1.15±0.3
	3	26	0.12±0.1	1.5±1	-	1.11±0.1

	4	33	0.12 ± 0.1	1.0 ± 1	-	1.13 ± 0.2
	5	33	0.11 ± 0.5	$0.87 \pm 1 = 0.7$	-	1.09 ± 0.2
	6	18	0.11 ± 0.06	0.73 ± 0.5	-	1.07 ± 0.1
	7	5	0.08 ± 0.7	0.50 ± 0.2	-	1.03 ± 0.03
	8	5	0.05 ± 0.5	1.1 ± 0.5	-	1.09 ± 0.05
	9	7	0.11 ± 0.1	0.36 ± 0.4	-	1.02 ± 0.03
	10	2	0.05 ± 0.01	0.37 ± 0.3	-	1.05 ± 0.05
	11	2	0.05 ± 0.01	0.21 ± 0.03	-	1.07 ± 0.03

Table 4.2 Number of channels in each bifurcation order, mean channel width, mean channel length, mean gradient and mean channel sinuosity. We did not have bathymetry data for fans with no channel gradient reported.

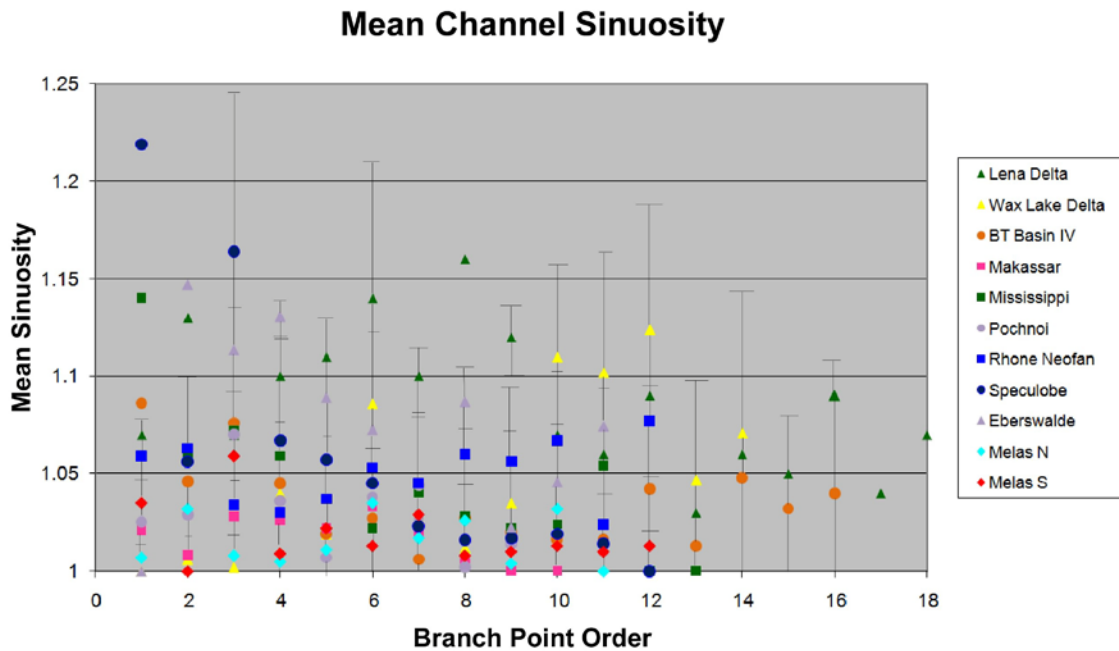


Figure 4.7 Plot of mean channel sinuosity versus bifurcation order.

4.6 Results

The channels were defined by the method described in section 4.3, and Table 4.2 shows the number of channels mapped in each system, the mean channel width, channel length, gradient, and sinuosity. A plot of the mean channel width for each order of channel is shown in Fig.4.4. This figure shows that the mean channel width generally decreases as the order increases, similar to the trends found by Edmonds and Slingerland (2007) for deltas, although for a few fans, the second and third order channels are wider than the main channel. The mean width tends to decrease by less than 50% with each decrease in channel order. Some channels also widen over the last few orders as seen on the Speculobe, Makassar, Brazos-Trinity-Basin IV and Melas South fans.

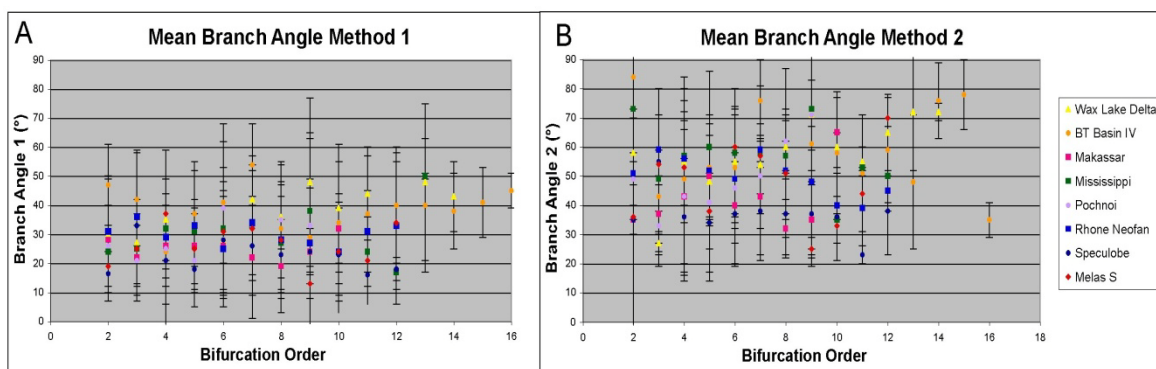


Figure 4.8 Channel branching angle versus bifurcation order. A.) Using method 1 to define branching angle. B.) Using method 2 to define branching angle.

The plot of mean scaled channel length for each order is shown in Fig. 4.5 and shows that the mean channel length decreases with increasing bifurcation order, similar to the trends found by Edmonds and Slingerland (2007) for deltas. The channel length decreases rapidly on the Makassar, Mississippi, and Melas S fans, and on the Wax Lake

Delta and then stays fairly constant. The decrease in channel length is smaller and fluctuates more widely on the Brazos-Trinity Basin IV, Melas N, Pochnoi, Rhone Neofan and Lena Delta.

Mean scaled channel length and mean scaled channel width appear to correlate. The mean channel length roughly decreases with decreasing mean channel width as shown in Fig. 4.6. The correlations of mean scaled channel width versus mean scaled channel length can be fit reasonably well with power laws as shown in Fig. 4.6a (R^2 values between 0.62-0.87). The power law fits can be represented by the equation $L=aW^n$, and the fitted values for a and n are shown in Fig. 4.6b along with the uncertainties on these parameters. The channel width versus length for the Pochnoi fan alone is not well fit by a power law. The three deltas in this study (the Lena delta ($n=1.1\pm0.1$), the Wax Lake delta ($n=1.4\pm.2$) and the Eberswalde delta ($n=1.5\pm0.8$)) have similar values for the fitted exponent n and exponents smaller than those found for the submarine fans. The exponent of the Pochnoi fan is significantly larger than the other fans ($n=7.0\pm1$), but this system was not well fit by a power law. The exponents of all the submarine fans fall within the range 1.7-3.7 which are higher those of the deltas, but with the uncertainties in these exponents, the two types of fans cannot be wholly distinguished.

The mean channel sinuosity is fairly low (<1.3) for all of the systems that were examined (Fig. 4.7). The Makassar fan has a roughly constant mean sinuosity of 1.03, whereas the Speculobe fan mean sinuosity varies between 1.05-1.23 and the Wax Lake Delta between 1.07-1.12.

The gradient (Table 4.2) has no systematic trend with channel order for the Makassar deep sea fan, the Speculobe fan or the Wax Lake Delta. The input channel has a larger gradient on the Makassar and Speculobe fans because the channel is only defined for the steeper part of the system and is not extended through the length of the entire system.

The mean branching angle for method 1 varies between 15-55° (Fig. 4.8A). There is no systematic trend in the dataset. The mean branching angle for method 2 varies between 20-85° (Fig. 4.8B). Again, there does not appear to be any systematic trend between branching angle and the order of the channel. There also does not appear to be a relation between mean branch angle and gradient.

4.7 Discussion

4.7.1 Nature of Channel Bifurcations

The decrease in channel width with increasing bifurcation order on delta distributary channels implies that the channel width is decreasing in a down-fan direction as the channels continue to bifurcate. This is not unexpected since a nonlinear decrease in channel width after channel bifurcation has been previously found in delta distributary channels and is expected by predictions of hydraulic geometry relations (Edmonds and Slingerland 2007). We found a similar trend of decreasing width with increasing bifurcation order on submarine fans. When a turbidity current is flowing through a channel and that channel splits, if both of the channel branches are active simultaneously one would expect the cross-sectional area of each of the channels after the split to be smaller than that

of the previous single channel. If the discharge of the turbidity current and the depth of the channels stay roughly constant, then the width of the channels should decrease after each split. This is observed for all of the fans examined. A decrease in channel width after channel bifurcation indicates that both branches of the channel were active simultaneously; otherwise the width after a bifurcation should be comparable to the width before the bifurcation. The method used to map the channels in this study does not distinguish between channel avulsion and channel bifurcation in most cases. Cross-sectional views were not available to determine whether the channel avulsed to a new path or simply bifurcated. In a few areas it was possible to see crosscutting relationships between channels, and in these instances, it was possible to distinguish between channel bifurcation and avulsion. However, the result that channel width decreases downfan does not necessarily imply that an original channel and a channel that formed during an avulsion were active simultaneously.

Studies of the channels on upper and middle submarine fans came to similar conclusions. Flood and Damuth (1987) found that both channel width and depth decrease down the submarine fan, and hence there was a decrease in the cross-sectional area of the channels down fan. They suggested that this implied a down-fan decrease in the maximum thickness and total volume of the turbidity currents that flow down the channels. Since the finer material in the turbidity current can spill over the edge of the channel more easily, they suggest that the remaining flows should become coarser and better sorted down-fan.

For the Speculobe, Makassar, Brazos-Trinity-Basin IV and Melas South fans, there appears to be a slight increase in channel width near the termination of the channel system (at the largest bifurcation orders). The slight increase in channel width at their distal limits could be due to shallowing of the channels and spreading of the flow. This is supported by sub-bottom profiles that transect the channels on the Makassar fan and show that the depth of the channels is less near the distal limit (Orange et al. 2006). These profiles show that channels near the distal limits of the fan have very little topographic signature.

Our study found that channel length decreases downfan with increasing bifurcation order on the three deltas examined. This is not unexpected since Edmonds and Slingerland (2007) also found that channel length decreases non-linearly with channel bifurcations and suggested that the channel length between bifurcations is proportional to the jet momentum flux and depends on the depth of the initial channel. Their modeling suggests that the distance between bifurcations is not a function of simple grain settling since this process does not account for mouth bar progradation observed in the field.

Channel length also decreases downfan on the submarine fans examined in this study. On several of the submarine fans (Rhone Neofan, Pochnoi, BT Basin IV and Melas North), the channel length is variable but continues to decrease down fan similar to the trend observed on deltas. This could imply a variable but increasing rate of sediment deposition from the turbidity current, which results in the variable but decreasing channel lengths seen on these submarine fans. On the other submarine fans (Mississippi, Melas South, Makassar, and Speculobe), the decrease in mean channel length with increasing

bifurcation order shows that the main trunk channel of submarine fans tends to be fairly long, and then the channel reaches a point where it begins to bifurcate after a short distance. After this point, the mean channel length stays roughly constant. In the submarine case, a channel will bifurcate when a lobe has built up high enough to divert the flow. The behavior of turbidity currents around obstructing topography depends on several factors including the velocity of the current, the obstacle height, the current density and the density stratification within the current (Kneller and Buckee 2000). Lane-Serff et al. (1995) found that part of the head of turbidity currents can surmount obstacles up to four or five times the ratio of the obstacle height to current body thickness or less than 1.5 times the flow thickness (Muck and Underwood 1990). This could imply that in the submarine fans where the length of the main channel is long and then subsequent channels rapidly decreases to a constant length, the turbidity current does not lose much material at first, since it takes a significant distance to build up a lobe high enough to divert the flow. Then once it has reached this state, the current should lose material at a roughly constant, but faster rate than previously, so that the subsequent channels bifurcate after a roughly equivalent distance. The trends in bifurcation length do not seem to correlate with the size of the fan, the dominant grain size present on the fan, or the water depth of the fan.

The branching angle of the channels appears to be highly variable. These angles do not seem to be related to the order of the channel (i.e. position on the fan) or to the slope of the fan surface. The branching angle varies over a wide range and may depend on a complicated set of factors that we are unable to separate. The method of measuring branching angles that Olariu and Bhattacharya (2006) used to differentiate among different

delta types was not meaningful when applied to submarine fans. No trends or patterns could be recognized in these branching angles.

4.7.2 Mean Channel Length versus Width Trends

The mean channel length versus width on the various fans follows a power law trend as discussed above. How quickly or slowly the channel widths decrease for a given decrease in channel length (i.e. in a steep trend the channel length falls off faster for a given decrease in channel width), does not appear to correlate with the dominant grain size present on the fan or the water depth. To first order both deltas and submarine fans show a similar range of length versus width trends, but the fitted exponent n for deltas is slightly less than those found on submarine fans. Taking into account the uncertainties on the values, the two types of fans overlap in their range of n . Large values of n ($n > 2.3$) are only found on submarine fans; however, the sample size of deltas investigated in this study is small and examination of additional deltas may find deltas with larger n .

The fact that the length versus width distributions of submarine fans and deltas overlap may be due to the amount of error in the data obscuring the differences in processes that lead to channel formation in each type of fan. Or, submarine fans and deltas might have similar advection length scales which could lead to overlapping length versus width trends.

4.7.3 Sinuosity

Unlike on upper and middle submarine fans, the mean channel sinuosity on lower submarine fans is quite low. In this study the mean sinuosity on lower submarine fans ranges from 1.0-1.23, but is typically less than 1.05. The sinuosity of the channels on the upper and middle Amazon submarine fan ranges from 1.05-2.6 (Flood and Damuth 1987). Clark et al. (1992) measured the sinuosity of channels on 16 different submarine fans and found values as high as 3 with average values appearing closer to 1.3-1.5. Thus, it appears that channels on the lower parts of submarine fans are much less sinuous than those farther up fan.

Laboratory experiments on sediment deposition by turbidity currents in sinuous channels show that sediment is preferentially deposited on the outer bends of channels, leading to an asymmetric channel cross-section and a relative straightening of the channel (Straub et al. 2008). This suggests that perhaps continued deposition in outer channel bends leads to straightening of the channels and the much lower sinuosities observed on lower submarine fans.

4.7.4 Reservoir Model Applications

The mean and range of values found for measurements of channel width and length as shown in Table 4.2 can be used to constrain the dimensions of sand bodies in static reservoir models of submarine channels and deltas. Our determination of stochastic branching angles indicates such branching angles can be used realistically in reservoir models, instead of just being assumed for simplicity's sake. Most reservoir models use the same value for sinuosity on lower submarine fans as was used for the upper fan, but our

results show that the channel sinuosity is lower on distal submarine fans and should be modeled with a lower value in reservoir models. The combination of these results helps to constrain the lateral connectivity of sand bodies that may serve as reservoirs.

4.7.5 Effects of Martian Gravity

Another potential application of channel bifurcation mapping is to help interpret depositional fans observed on other planets. If a depositional fan is observed on Mars, whether the fan formed subaqueously or at the air-water interface has different implications for the environmental conditions present when the fan formed. The observation of a submarine fan on Mars would imply a relatively deep and perhaps long-lived body of water whereas a delta could form in a much shallower body of water. Since one of the goals of Mars exploration is to understand the past extent of liquid water at the surface, this distinction has become relevant with the recent observation of a potential ancient submarine fan (chapter 3 of this thesis). If the channel patterns on submarine fans and deltas were distinct, then this observation would provide an important criterion to interpret depositional fans observed on other planets.

The Melas North and South fans on Mars are small fans, and the slope of their power law fits falls within the lower part of the range of values found on the larger terrestrial submarine fans. This means the Melas fans have channels that are slightly longer for a given width than the terrestrial submarine fans. This could be due to similar bifurcation behavior, but because Mars has lower gravity ($g=3.7 \text{ m/s}^2$) it could cause the sediment to be carried farther by a given flow on Mars than a similar flow on Earth. The

advection distance for a particle traveling in a turbidity current is given by

$$L = \frac{uh_s}{\omega_s} \quad (1)$$

where ω_s is the settling velocity, u is the flow speed and h_s is the height of the sediment particle above the bed (see Fig. 4.9). The flow speed of a turbidity current is given by

$$u = \left(\frac{\rho g H S}{C_f} \right)^{\frac{1}{2}} \quad (2)$$

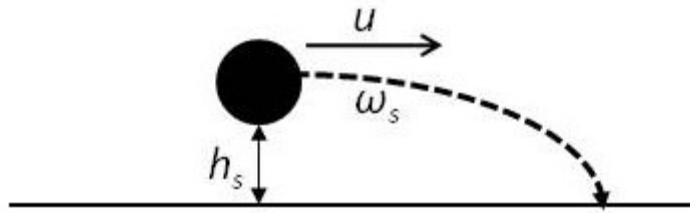


Figure 4.9 Diagram illustrating the settling of a particle at a height h_s above the bed in a flow traveling at a flow speed u .

where ρ is the density, g is the acceleration due to gravity, H is the flow depth, S is the slope, and C_f is the form drag coefficient. The settling velocity for small grains (< 1 mm) is given by

$$\omega_s = \frac{1}{18} \frac{RgD^2}{\nu} \quad (3)$$

where R is the submerged specific density of grains, D is the grain diameter, and ν is the kinematic viscosity. Substituting equations (2) and (3) into equation (1) yields $L \propto g^{-1/2}$.

Thus, for the same current, the ratio of the advection length of a particle on Mars to the

advection length of a particle on earth is $\frac{L_{Mars}}{L_{Earth}} \propto \frac{g_{Mars}^{-1/2}}{g_{Earth}^{-1/2}}$ which gives $L_{Mars} = 1.63 L_{Earth}$.

Our observation of longer channels on Mars agrees with the predictions of a longer advection length scale on Mars due to the lower gravity.

4.8 Conclusions

After mapping the terminal channel systems on six terrestrial submarine fans, two Martian submarine fans, two terrestrial deltas and one Martian delta, some trends are apparent. Mean channel width and length decrease nonlinearly down fan. The channel sinuosity on lower submarine fans is much lower than further up fan. Channel branching angles appear to be stochastic and do not provide a meaningful measure to discriminate between fans. The trends of mean channel length versus mean channel width follow power laws. The exponent in the fits of channel length versus channel width is slightly smaller for deltas than for submarine fans, but the range of values of n overlaps for the two types of fans. Channel lengths fall off slightly more slowly for a given decrease in channel width on Mars which may be the result of a longer advection length scale due to the lower gravity.

This study has allowed us to characterize the variability in channel size and bifurcation pattern present in channel systems at the distal limits of submarine fans. This information will be useful in constraining channel properties in static reservoir models, e.g. the mean and range of values typical for channel dimensions, sinuosity, and branching angles.

Chapter 5

THIN-SKINNED DEFORMATION OF SEDIMENTARY ROCKS IN VALLES MARINERIS, MARS

Abstract

Deformation of sedimentary rocks is widespread within Valles Marineris, characterized by both plastic and brittle deformation identified in Melas, Candor and Ius Chasmata. We have identified four deformation styles using HiRISE and CTX images: km-scale convolute folds, detached slabs, folded strata and pull-apart structures. Convolute folds are detached rounded slabs of material with alternating dark and light-toned strata that show refolded folds with a fold wavelength of about one kilometer. The detached slabs are also isolated rounded blocks of material, but exhibit only highly localized evidence of stratification. The third style, folded strata, comprises continuously folded layers that are not detached. Finally, pull-apart structures are composed of stratified rock that has broken off into small irregularly-shaped pieces showing evidence of brittle deformation. Some areas exhibit multiple styles of deformation and grade from one type of deformation into another, both laterally and vertically. The deformed rocks are observed over thousands of kilometers, are limited to discrete stratigraphic intervals, and occur over a wide range in elevations. All deformation styles appear to be of likely thin-skinned origin. The orientation of fold axes is bimodal and exhibits northeast-southwest and southeast-northwest components. CRISM reflectance spectra show that some of the deformed sediments contain a component of mono- and polyhydrated sulfates.

Several possible mechanisms could be responsible for the deformation of sedimentary rocks in Valles Marineris, such as subaerial or subaqueous gravitational slumping or sliding and soft-sediment deformation, where the latter could include impact- or seismically-induced liquefaction. These mechanisms are evaluated based on their expected pattern, scale and areal extent of deformation. Deformation produced from slow subaerial or subaqueous landsliding and liquefaction is consistent with the deformation observed in Valles Marineris.

5.1 Introduction

The relative timing between the formation of the Valles Marineris canyon system and the various light-toned stratified deposits observed within the different chasmata remains an outstanding question for the geologic history of Mars. Some of this ambiguity arises from the fact that light-toned deposits with similar morphologic traits are observed in large mounds within the canyon (interior layered deposits, hereinafter referred to as ILDs), on the floor of the chasmata, and occasionally in rock outcrops in the walls of the canyon system. The issue is complicated further because the tectonic activity responsible for the formation of the Valles Marineris likely occurred as several episodes over a long period of time. Thus, it is unclear if the stratigraphy of deposits in one chasm can be directly correlated to the stratigraphy in other chasmata. Although individual light-toned units are not traceable throughout the entire canyon system, some of them exhibit clear evidence of deformation. The relative age of the strata within Valles Marineris, both in the mounds of light-toned layers and in the layers exposed on the surrounding floor, is still debated.

Understanding the mechanism(s) responsible for this deformation, both within and between chasmata, could provide insight into the relative timing of events within the Valles Marineris system.

The ILD are large mounds or mesas believed to be composed primarily of sedimentary rocks. The ILD are found within many of the chasmata in Valles Marineris as well as the peripheral chasmata such as Hebes, Juventae and Ganges (Scott and Tanaka 1986). Some authors have suggested that the ILD predate chasma formation, because layered materials are found in some chasma wall spurs (Malin and Edgett 2000; Montgomery and Gillespie 2005; Catling et al. 2006). Other studies based on geomorphology and structural relationships have suggested that the ILD accumulated on top of Noachian-aged bedrock during or after chasma formation (Scott and Tanaka 1986; Lucchitta 1990; Peulvast et al. 1993; Lucchitta et al. 1994; Schultz 1998; Okubo et al. 2008). Unfortunately, most locations lack unambiguous stratigraphic contacts between the ILD and canyon walls, making a definitive determination of the relative age of strata within the chasma difficult. Several lithologic interpretations of the ILD have been suggested, including lacustrine deposits (Nedell et al. 1987; Komatsu et al. 1993; Malin and Edgett 2000), eolian deposits (Nedell et al. 1987), volcanic (ash) deposits (Lucchitta 1990; Lucchitta et al. 1994; Chapman and Tanaka 2001), and lithified mass-wasted wall rock material (Nedell et al. 1987; Lucchitta et al. 1994).

The stages and timing of events in the evolution of Valles Marineris are also still debated, but the general framework that has emerged is as follows (Lucchitta et al. 1994;

Mege and Masson 1996; Schultz 1998; Peulvast et al. 2001; Okubo et al. 2008): 1. During Late Noachian to Early Hesperian time, there was dike emplacement radial to Syria Planum and the formation of graben and pit craters in the future region of Valles Marineris. 2. After Early Hesperian time, localized subsidence and sedimentary basin formation occurred in association with the earlier radial dikes, grabens and pit craters. Subsidence may have been related to melting of subsurface ice, dissolution of pre-existing chemical precipitates and formation of the chaotic terrain. The ILD were deposited in the subsiding basins. 3. Rifting during the Amazonian in the area of the ancestral basins and the ILD associated with deep-seated faults; rifting may have been driven by Tharsis-related stresses and may have connected the ancestral basins to one another. Following rifting, landslides and erosion further widened the ancestral basins and rifts to their present form.

An alternative model for the formation of Valles Marineris was proposed by Montgomery et al. (2009). They interpreted the formation of Valles Marineris and the Thaumasia plateau as a "mega-slide" characterized by thin-skinned deformation involving gravity sliding, extension, and broad zones of compression. The gentle slope of 1° in the region makes gravitational body forces too small to drive deformation of basalt, but slip along a detachment could have occurred if geothermal heating and topographic loading of salt or mixtures of salt and ice allowed for development of a layer-parallel zone of weakness (Montgomery et al. 2009). They proposed that the Valles Marineris reflects extension, collapse and excavation along fractures radial to Tharsis. They also suggest that deformation represented by compressional features in the highlands on the southern margin of the Thaumasia Plateau and the wrinkle ridges on the plateau imply décollements at

multiple levels and several phases of deformation. Similar features are observed in terrestrial salt-based fold and thrust belts, which support regularly spaced folds of weak vergence and exhibit abrupt changes in deformational style at their margins (Davis and Engelder 1985).

Isolated occurrences of deformed strata were previously identified in western Melas and western Candor Chasmata and are thought to represent subaerial landslides of large interior layered deposits found in those chasmata (Okubo et al. 2008), subaqueous landslides of wallrock (Weitz et al. 2003), dry debris avalanches (Skilling et al. 2002), or gravity gliding of ILD (Lucchitta 2008). However, Context Camera (CTX) images provide nearly complete coverage of Valles Marineris and have revealed many more exposures of deformed strata that were identified and mapped during the course of this study. Recent High Resolution Imaging Science Experiment (HiRISE) images and HiRISE-based digital elevation models (DEMs) allowed a detailed look at the morphology of these deposits as well as their stratigraphic position.

In this study we identify many more occurrences of deformed strata on the floors of Ius, Melas and Candor Chasmata in Valles Marineris. The morphology and composition of these deposits are examined in detail to evaluate how the sediments were deformed and the relative timing of the deformation with respect to the formation of Valles Marineris.

5.2. Geologic Setting

Candor Chasma is a large depression (lowest elevation is approximately -5 kilometers) located in the northern part of Valles Marineris; it was mapped previously by Scott and Tanaka (1986) and Lucchitta (1999). Candor has several occurrences of ILD that have been studied using both spectral (Mangold et al. 2008b; Murchie et al. 2009; Roach et al. 2009a) and structural data (based on image-derived digital elevation models; Fueten et al. 2006; Fueten et al. 2008; Okubo et al. 2008). Lucchitta (1999) mapped the ILD as Hesperian or Amazonian in age, and Fueten et al. (2006) showed that the layers in the ILD (near the two white circles in Fig. 5.1A) dip away from the peak of the deposits and are subhorizontal in the surrounding plains. Fueten et al. (2006) interpreted this structural pattern as indicating that the ILD drape preexisting topography and lack evidence of large scale faulting indicative of chasma formation; this implies that the layers post-date chasma formation. Folded strata near the southern margin of Candor (locations C1 and C2 in Fig. 5.1A) generally dip towards the center of the chasma which is consistent with deposition in a preexisting basin (Okubo et al. 2008, Okubo 2010). Okubo et al. (2008) interpret the folds in this area as the result of southward-directed landsliding of the ILD.

Murchie et al. (2009) found that the lower and middle parts of the ILD in western Candor are dominated by monohydrated sulfate whereas the upper beds are dominated by polyhydrated sulfates. Roach et al. (2009a) found that the ILD in eastern Candor are composed of interlayered mono- and polyhydrated sulfates. Changes in the hydration state of these sulfates (mono or poly) have not been detected over several years of observations, which indicates that the monohydrated sulfates are not actively being altered to

polyhydrated phases or polyhydrated phases dehydrated to monohydrated phases on short timescales (Roach et al. 2009a).

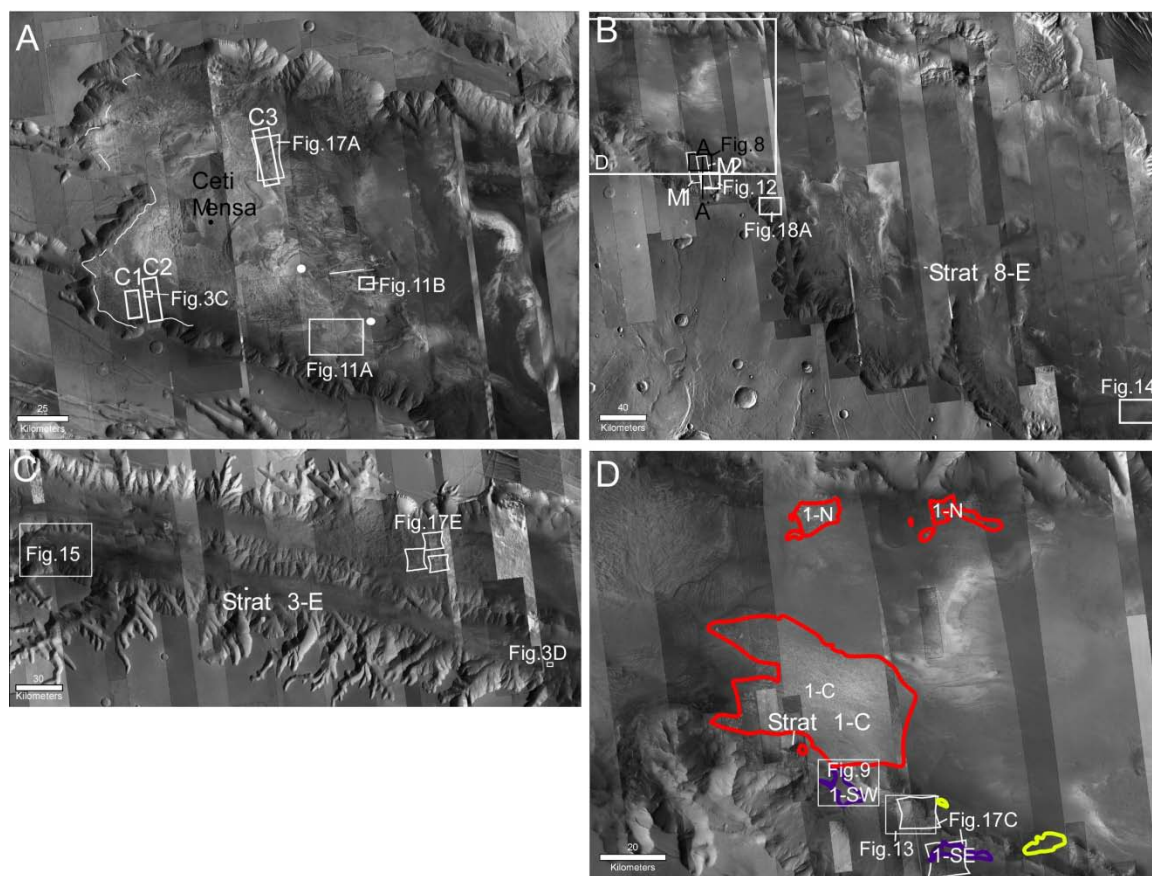


Fig 5.1. A.) Location map in Candor Chasma. White boxes labeled C1, C2 and C3 represent locations of DEM's discussed in the text. White boxes show locations of Figs. 5.11A and 5.11B and the CRISM image in Fig. 5.17A. White line traces out the topographic bench. Black circle indicates location of Ceti Mensa mound, and the two white circles indicate two other topographic highs in western Candor. B.) Location map in Melas Chasma with white boxes showing the locations of Figs. 5.1D, 5.12, 5.14 and 5.18A and black box showing location of Fig. 5.8. White rectangles labeled M1 and M2 represent locations of DEM's discussed in text. The black line shows the location where cross-section A-A' was measured and the white line where stratigraphic column 8-E was measured. White line shows location of cross-section A-A' from Fig. 5.6. C.) Location map in Ius Chasma with white boxes showing the locations of Figs. 5.3D, 5.15 and the CRISM images in 5.17E. The white circle shows where stratigraphic column 3-E was measured. D.) Zoomed in portion of Melas Chasma indicated in B. White boxes show locations of Figs. 5.9, 5.13 and the CRISM images from 5.17C. White line shows where

stratigraphic column 1-C was measured. Purple outlines show locations of outcrops showing convolute folds, yellow shows folded strata and red shows detached slabs. Outcrops are labeled with designations referred to in Table 5.1.

Melas Chasma is another deep depression (lowest elevation is approximately -5 km) that is located within central Valles Marineris. Several large ILD are located along the southern portion of Melas Chasma and OMEGA data of these ILD exhibit spectral signatures consistent with the presence of monohydrated (kieserite) and polyhydrated sulfates (Gendrin et al. 2005). Several interesting features have been discovered in a small basin in southwestern Melas Chasma (informally called southern Melas basin) including dense valley networks (Quantin et al. 2005), clinoforms (Dromart et al. 2007), and possible sublacustrine fans (Metz et al. 2009b). These features indicate the presence of liquid water and a potentially deep lake in the basin. Large exposures of detached slabs have been identified on the floor of western Melas Chasma (Skilling et al. 2002; Weitz et al. 2003) and have been interpreted to be the result of landsliding.

Ius Chasma is a large trough (lowest elevation is approximately -4.5 km) in western Valles Marineris that shows a regular, nearly rectangular geometry (Schultz 1991). This trough is thought to have formed by normal faulting and to postdate the ILD (Schultz 1998). No mounds of layered material are observed in Ius Chasma, but spectral signatures of kieserite, polyhydrated sulfates, clays and hydrated silica have been identified on the floor of eastern Ius Chasma (Gendrin et al. 2005; Roach et al. 2009b).

5.3. Methods

A mosaic of projected CTX (5 m/pixel) and HiRISE images (0.25-0.5 m/pixel) covering Valles Marineris was overlain onto a base map of THEMIS daytime IR images using ArcGIS®. CTX coverage over Valles Marineris is nearly complete, but HiRISE images cover only select locations. The entire Valles Marineris canyon was examined and areas showing deformation were identified and mapped (Fig. 5.2). Four primary styles of deformation were noted: large-scale convolute folds, detached slabs, folded strata and pull-apart structures (Fig. 5.3). Detached slabs are rounded blocks of detached material that only locally show evidence of layering (Fig. 5.3A), and convolute folds are defined similarly but are composed of alternating dark and light-toned strata that exhibit disharmonic folding (Fig. 5.3B). Folded strata are defined as laterally continuous layered materials, and the trend of their fold axial traces is not uniform (Fig. 5.3C). Pull-apart structures are composed of fragments of strata that have broken off into small irregularly-shaped pieces (Fig. 5.3D). Deformed areas were separated into eight regions as shown in Fig. 5.2. Regions are defined as groupings of nearby outcrops of various types of deformed strata, whereas outcrops are continuous exposures of one type of deformed strata.

The styles of deformation called detached slabs and convolute folds are composed of detached blocks. These blocks are inferred to have a sedimentary origin, though this is difficult to confirm with the exception of a few cases. Supporting a sedimentary origin are the observations that some of the blocks contain finely-stratified deposits and the spectroscopic signature of evaporite minerals, including kieserite and polyhydrated sulfates. In general, we regard these materials to now be (at least partly) lithified rocks; at the time of deformation they could have been strata formed of unconsolidated loose

sediments, water-saturated sediments, loosely cemented sediments, or fine-grained sediments with high cohesion. The major and minor axes of the detached slabs and convolute folds were measured, and histograms of the size distributions for each region are shown in Figure 5.4. Many of the regions consist of several outcrops of deformed strata and in these cases the size distribution of blocks for each outcrop are reported separately (e.g. Fig 5.1D). The ratio of the major to minor axis of each block was computed and the areal size of each block was also measured. Statistics on the sizes of the blocks are shown in Table 5.1. In areas with only a few blocks exposed, the sizes of all blocks were measured. In areas with many blocks exposed, the size of blocks in areas with HiRISE coverage was measured.

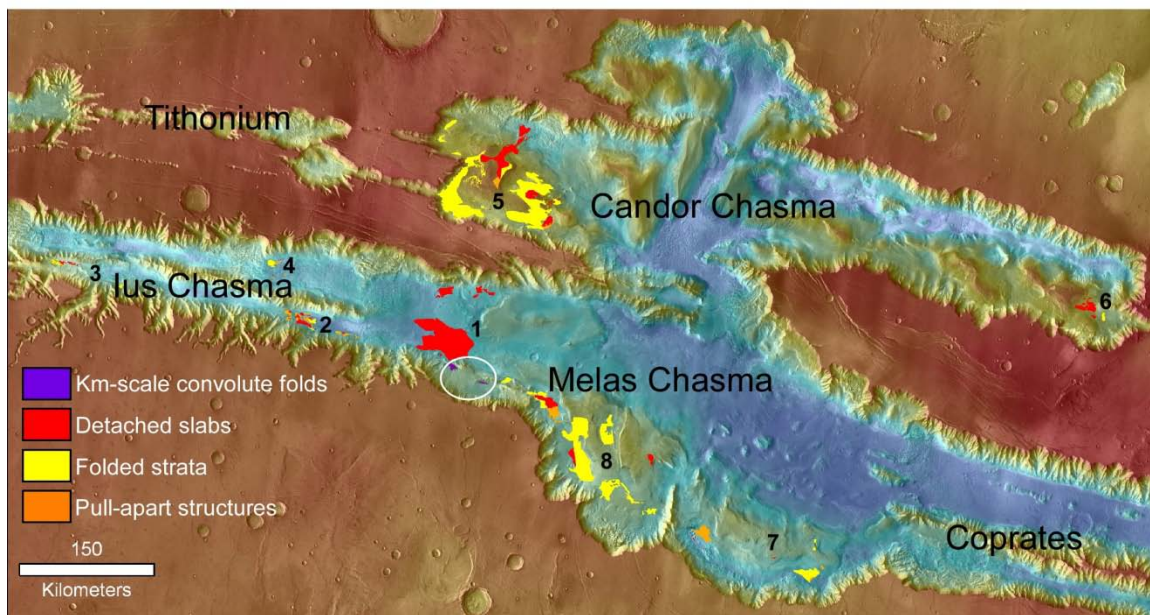


Fig 5.2. MOLA colorized elevation base map with eight regions of deformation mapped and labeled. Four styles of deformation were observed, km-scale convolute folds (purple), detached slabs (red), folded strata (yellow), and pull-apart structures (orange). Deformation was observed in Ius, Melas and Candor Chasmata, but not in Coprates or Tithonium Chasmata. White circle shows locations of km-scale convolute folded outcrops.

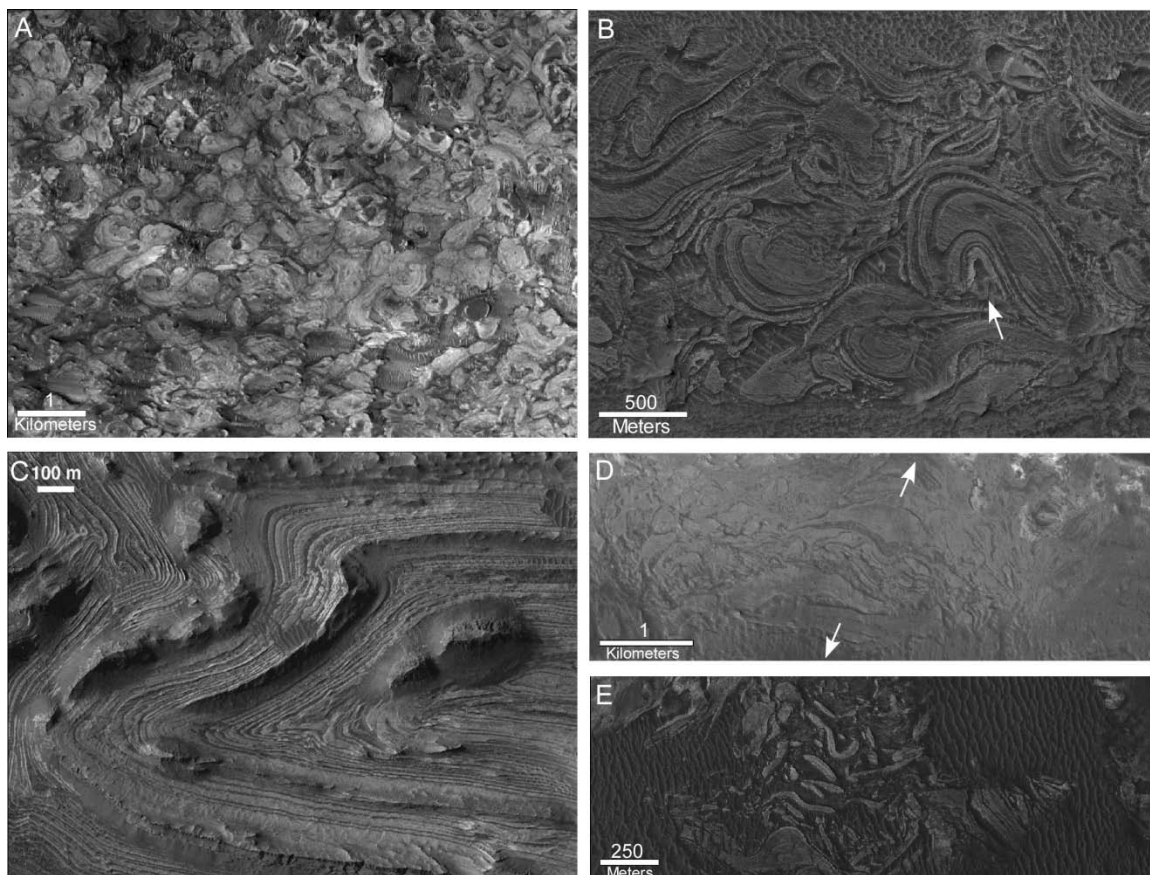


Fig 5.3. Four deformation styles were observed in Valles Marineris. A.) Detached slabs; this example is from Melas Chasma (P05_002828_1711). B.) Km-scale convolute folds which are observed only in two exposures in southern Melas basin (PSP_007087_1700). This example is from the easternmost exposure. White arrow shows location of disharmonic fold. C.) Folded strata; this example is from Candor Chasma (PSP_001918_1735). D.) Pull-apart structures; this example is from Ius Chasma (P07_003606_1727). Note how the strata look as if they have been pulled apart in the direction of the arrows. E.) Pull-apart structures; here the strata have been pulled apart to a greater extent than in d. The strata are expressed as irregularly shaped pieces (PSP_003593_1725).

Five Digital Elevation Models (DEMs) were constructed using the methods of Kirk et al. (2008) and cover three separate deformed areas (Fig. 5.1). These DEMs were evaluated to understand the three-dimensional geometry of the various deformation

patterns. Three DEMs were produced based on images obtained in Candor Chasma. These consisted of the following stereo pairs (C1) PSP_001918_1735 (28.5 cm/pixel) and PSP_001984_1735 (26.2 cm/pixel) centered at -6.444° N, 283.221° E and with a vertical precision of 0.13 m; (C2) PSP_003474_1735 (27.5 cm/pixel) and PSP_003540_1735 (26.4 cm/pixel) centered at -6.433° N, 283.216° E and with a vertical precision of 0.12 m; (C3) PSP_008023_1745 (26.4 cm/pixel) and PSP_010238_1745 (27.3 cm/pixel) centered at -5.295° N, 284.166° E and with a vertical precision of 0.12 m. Two DEMs were in Melas Chasma and consisted of stereo pairs (M1) PSP_007087_1700 (26.7 cm/pixel) and PSP_007667_1700 (28.8 cm/pixel) centered at -9.816° N, 283.503° E and with a vertical precision of 0.13 m and (M2) PSP_007878_1700 (26.5 cm/pixel) and PSP_008735_1700 (28.9 cm/pixel) centered at -9.755° N, 283.4° E and with a vertical precision of 0.13 m. With a stereo convergence angle of 25° and assuming 1/5 pixel correlations, the vertical precision of the DEM is $x/(5\tan 25^{\circ})$ where x is the size of the pixel. The precision is limited by the DEM's 1 m postings in steep areas.

Two stratigraphic columns were measured in the southeastern outcrop exposure of convolute folds in region 1 (in Melas Chasma) using DEM's M1 and M2 (Fig. 5.1B, D and 5.5). A stratigraphic column was measured in the northern section of region 5 in Candor Chasma using DEM C3 (Fig. 5.1A and 5.5). The dips of bedding in these areas were obtained by using planar fits to bedding visible in the HiRISE images associated with the derived DEMs. Linear segments were traced out along well-exposed layers with some natural curvature to provide constraints on the three-dimensional geometry of the layer. We employed the method of Lewis et al. (2008b), which uses principal component analysis

to ensure that the layers are well-fit by a plane. Additional stratigraphic columns in areas without DEM coverage were estimated using a combination of Mars Orbital Laser Altimeter (MOLA) data and visual images. This method was used for the stratigraphic columns measured in the southwest and central outcrops in region 1, the outcrops in region 3, and the outcrops in region 7 and 8 (Fig. 5.5). MOLA contour lines were used to estimate the thickness of stratigraphic units and elevations of contacts. True bed thicknesses in these columns are not known, because the dips of the bedding in these areas cannot be properly calculated without a high-resolution DEM. A cross-section was constructed for the southeastern outcrop in region 1 using a MOLA topographic profile from the north to the south end of southern Melas basin (Figs. 5.1B and 5.6). The DEM of this area was used to measure the true dips of beds shown in this section.

The exposed area of each deformed unit was measured in ArcGIS. For several of the areas, both lower and upper contacts for the deformed strata were visible and a thickness for the deformed units could be calculated. For other areas the thickness was estimated using gridded MOLA data. For regions where an upper or lower contact was not visible, a minimum thickness was estimated using MOLA data. The volume of each area was calculated by multiplying the measured area by the measured or estimated thickness. The length of each deformed area was measured in a direction perpendicular to the nearest chasma wall.

The axial traces of folds in the deformed regions were mapped wherever they were visible. The orientations of these folds with respect to north were measured, and rose

diagrams of the directions were constructed (Fig. 5.7). Parts of the southern portion of region 5 were covered by DEM's C1 and C2, and the fold axes in these areas were mapped by Okubo et al. (2008) and (Okubo 2010), who measured the trend and plunge of fold axes in these areas and found the plunges were relatively shallow ($\sim 5^\circ$).

Region	Outcrop	Mean long dimension (m)	Mean short dimension (m)	Long dimension range (m)	Short dimension range (m)	Mean Area (m ²)	Mean Ratio	N
1	SE	647	451	394-1157	220-826	234,310	1.5	6
1	SW	459	247	160-1005	95-439	114,621	1.96	41
1	C	466	265	110-1086	64-665	124,507	1.81	107
2	E	192	107	91-298	51-175	17,740	1.91	21
2	W	349	209	92-777	55-557	74,139	1.81	63
3	E	-	-			-	-	-
3	W	397	249	143-796	106-369	94,531	1.63	18
4	C	135	83	80-214	41-118	9,849	1.68	15
1	N	413	272	119-686	84-514	100,299	1.56	40
5	E	347	195	80-993	59-599	89,632	1.79	18
5	W	-	-			-	-	-
5	N	265	146	63-815	29-307	44,882	1.82	37
5	C	581	269	204-867	96-544	114,325	2.22	38
6	C	208	123	90-464	55-229	24,320	1.73	35
7	E	-	-			-	-	-
7	W	-	-			-	-	-
8	E	470	259	171-847	98-538	113,051	1.98	22
8	W	394	254	159-823	113-442	86,089	1.62	33

Table 5.1. The mean sizes and the range in sizes of the blocks of material forming the detached slabs and convolute folds are listed for each region. Some regions have been subdivided into several outcrops (C-central, E-east, W-west, N-north, S-south). Ratio is the ratio of mean long dimension to mean short dimension. N is the number of blocks measured in each outcrop. Regions without entries did not have any exposures of detached slabs or convolute folds. Convolute folds are only observed in the SE and SW outcrops of region 1; all other measurements are for detached slabs.

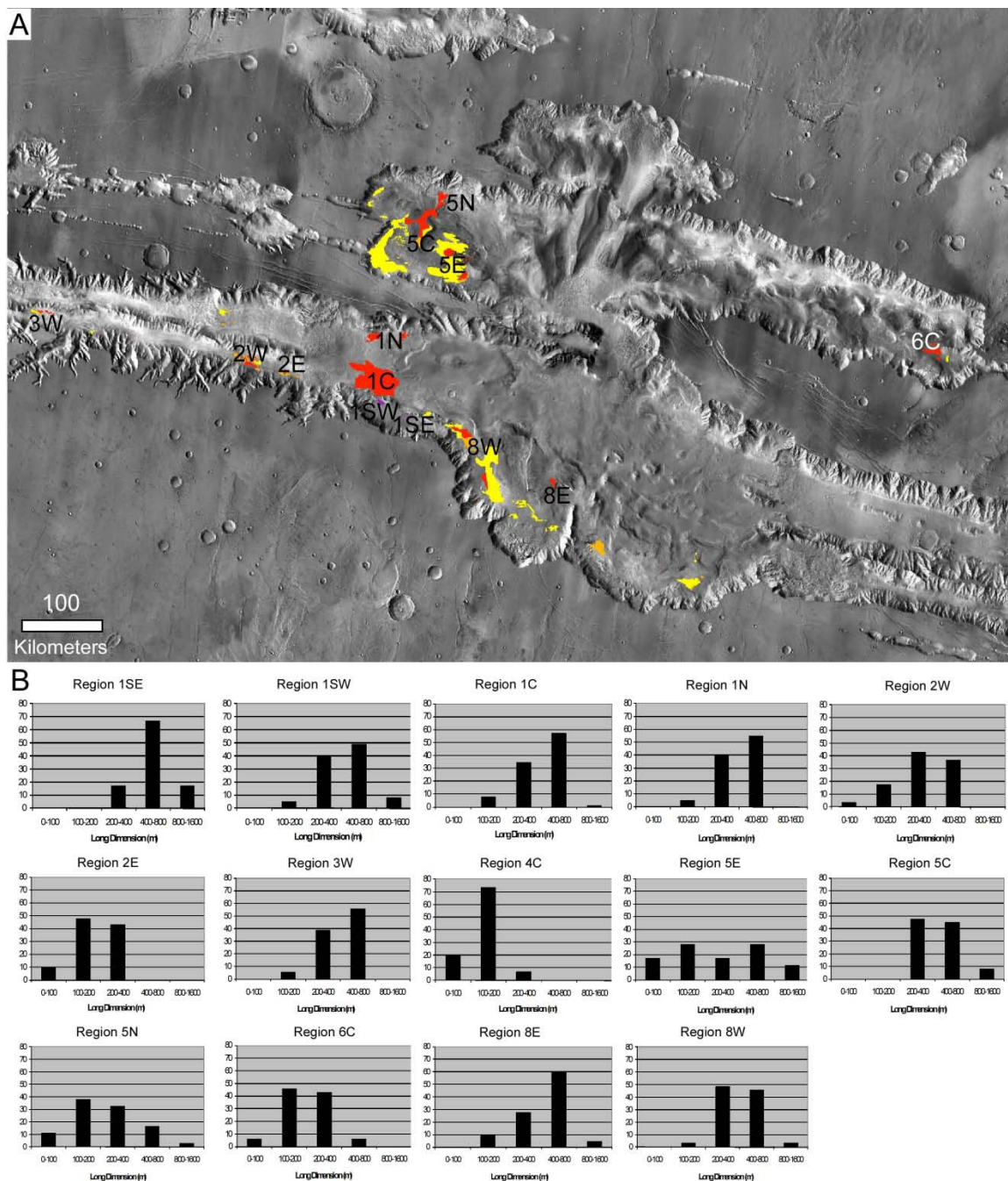


Fig 5.4. A.) THEMIS IR basemap with locations of outcrops labeled where block sizes were measured. B.) Histograms of the long dimension of the convolute folds and the detached slabs. The axes for each histogram are the same; the vertical axis is the percent of blocks that falls into a particular size range, and the horizontal axis are bins of long block dimension. Blocks are larger in Melas Chasma, smaller in Ius Chasma and show a more even distribution of size classes in Candor Chasma.

CRISM full-resolution target images (FRTs) exist for many of the deformed areas and were examined in this study to determine the composition of the beds (CRISM images listed in Table 5.2 and locations of key images shown in Fig. 5.1). These images have 544 spectral bands with 6.55 nm sampling and a resolution of ~18 m/pixel. The CRISM data were converted to I/F using the methods of Murchie et al. (2007, 2009). The data were corrected for photometric effects by dividing I/F values by the cosine of the solar incidence angle and atmospheric attenuation was accounted for by dividing by a scaled atmospheric transmission spectrum obtained during an observation crossing Olympus Mons (Mustard et al. 2008). The latter step corrects for atmospheric gases but does not account for aerosols. Map-projected CRISM images were imported into ArcGIS to integrate with HiRISE, CTX, and MOLA data. CRISM spectra presented here are I/F ratio spectra created by averaging pixels (spectra) corresponding to distinct geologic units and dividing those average spectra by an average of pixels (spectra) from a spectrally 'bland' area that usually corresponds to Mars dust (e.g., Milliken et al, 2008).

Melas Chasma	Ius Chasma	Candor Chasma
FRT000043C6	FRT00008950	FRT0000400F
FRT00006347	FRT00009445	FRT000039F3
FRT0000AC5C	FRT0000D5F8	FRT0000593E
FRT0000AD3D	FRT0000B347	HRL000033B7
FRT0000C00F	FRT0000CAE2	FRT000103C5
FRT0000A244	FRT0000873F	HRL00007C86
FRT0000AA51	FRT000027E2	FRT0000BE37
FRT0000A3E9	FRT0000905B	
FRT000061BD	FRT0000A396	
HRL000123C5		
FRT000136D3		
FRT0001070E		

Table 5.2. List of CRISM targeted images examined in this study.

5.4. Results

5.4.1 Deformation Styles

Mapping of deformed strata in Valles Marineris yields four primary deformation styles: km-scale convolute folds, detached slabs, folded strata, and pull-apart structures (Fig. 5.3). Some areas exhibit multiple styles of deformation and grade from one type of deformation into another, both laterally and vertically. Deformed strata have been identified in eight different regions throughout Ius, Melas and Candor Chasmata. Tithonium and Coprates Chasmata were also examined for this study, but deformed strata have not yet been observed in these locations. Regions are defined as groupings of nearby outcrops of various types of deformed strata. Outcrops are continuous exposures of one type of deformed strata.

Km-scale convolute folds were only observed in two exposures in Melas Chasma, both in relatively small outcrops in a small basin in southwestern Melas Chasma (SE and SW outcrops of region 1). The convolute folds are detached rounded slabs of alternating dark and light-toned strata that exhibit disharmonic folding with a fold wavelength of about one kilometer (Fig. 5.3A). The strata that appear dark-toned may be more friable and have been preferentially eroded out and filled in with dark-toned sand. Sequences of strata can be traced between some of the slabs (Fig. 5.8). Several fold geometries are observed

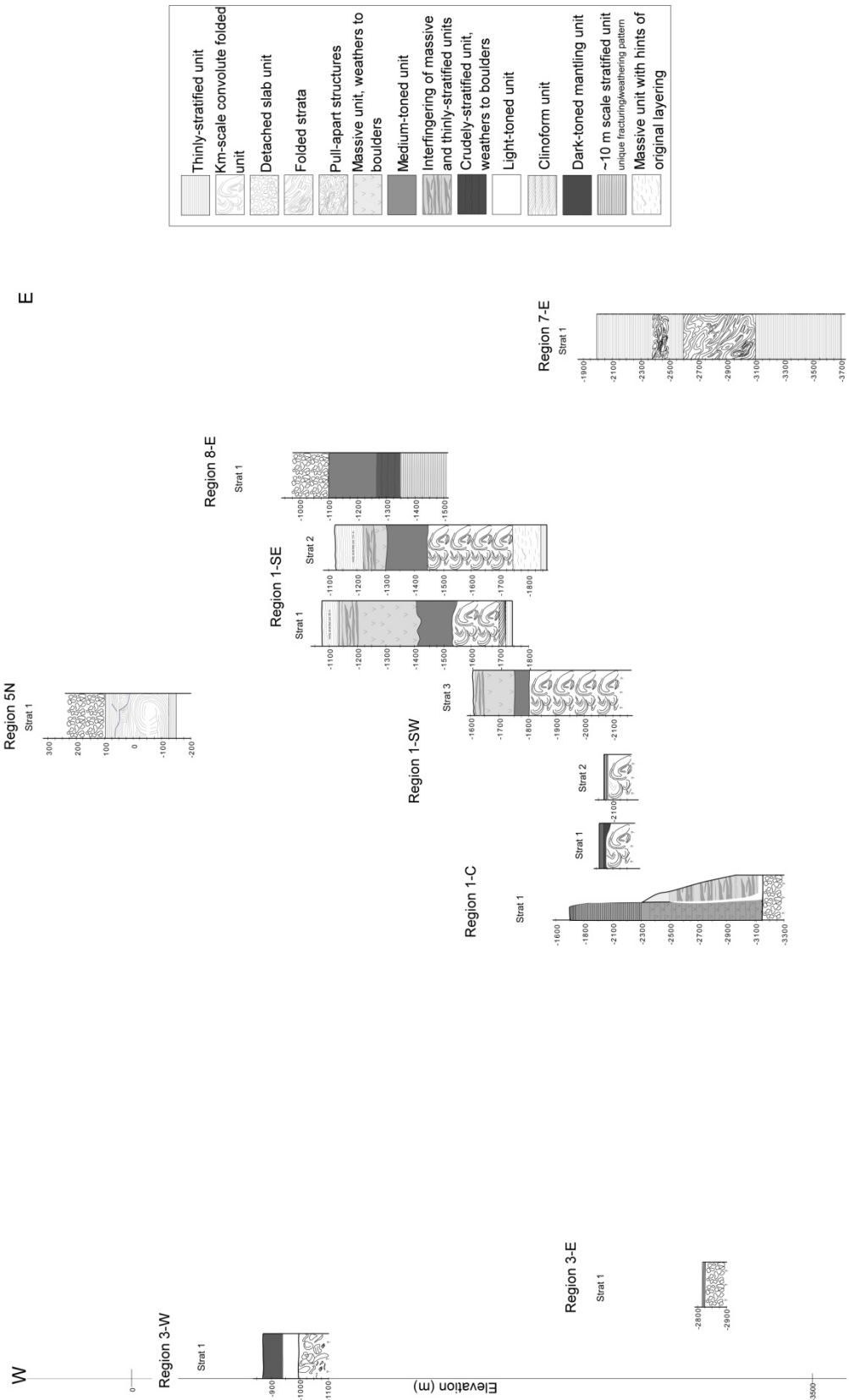


Fig 5.5. Eleven stratigraphic columns were measured based on HiRISE DEM's and MOLA gridded data in Ius, Melas, and Candor Chasmata. Stratigraphic columns are labeled by region number and outcrop location and are arranged from west to east. Stratigraphic columns are arranged vertically such that relative elevations correlate (except for stratigraphic columns from regions 1-C and 7-E which are on a different vertical scale than the other sections - these two sections are correlated so that they line up at only at - 2100 m, and the stratigraphic section from region 5N which occurs at a much higher elevation than the other sections).

including parallel, disharmonic and similar folds (Fig. 5.3A). In the southwestern outcrop of region 1, the km-scale convolute folds grade into detached slabs (Figs. 5.1D and 5.9). Table 5.1 shows the range and mean block sizes of the convolute folds as well as the mean ratio of the long to short dimension. Most blocks are elliptical in shape, and the convolute folds tend to be larger than the detached slabs.

The detached slabs are also rounded blocks of detached material, but they only locally show evidence of layering (Fig. 5.3B). These have previously been classified as 'blocky deposits' by Weitz et al. (2003). In most areas the slabs appear featureless, but in a few locations the slabs do show folded strata and appear to flow around each other (see Fig. 6 in Weitz et al. 2003). Some of the blocks show resistant edges (Fig. 5.10). Detached slabs are found in many exposures in Ius, Melas and Candor Chasma (Fig. 5.2). The mean and range of sizes of detached slabs are given in Table 5.1. Similar to the convolute folds, detached slabs tend to be elliptical, but the detached slabs have a larger range of sizes, including some small slabs (~30 m).

The folded strata are laterally continuous layered materials and the trend of their fold axial traces is not uniform (Fig. 5.3C). Folded strata exhibit many geometries including both similar folds and concentric folds, in addition to domes, basins, crescents, mushrooms and other interference patterns. Where fold axes can be determined in detail, they indicate non-cylindrical fold geometry (Okubo 2010). Fold wavelengths range in size from 250 m to 2700 m. There are large exposures of folded strata in Candor Chasma, some of which were studied by Okubo et al. (2008) and Okubo (2010). Folded strata also occur throughout Ius and Melas Chasmata.

The pull-apart structures are areas that show evidence of possible brittle deformation and appear to be composed of fragments of strata that have broken off into small irregularly-shaped pieces. In some areas the fragmented strata look as if they could be fit back together similar to puzzle pieces, whereas in other areas the fragmentation proceeded to a larger degree and only irregularly shaped fragments of strata remain (Fig. 5.3 D-E). It is possible that some of these structures may have originally been detached slabs that have experienced differential erosion to produce irregularly shaped blocks. Pull-apart structures occur in Ius, Melas and Candor Chasmata.

In some areas the different styles of deformation can be seen to grade into each other (Fig. 5.11). Thus, the four types appear to form a continuum of deformation styles that likely depend on the orientation of the principal stresses and the strain rate. The grading in deformation styles occurs laterally as well as vertically, with folded strata

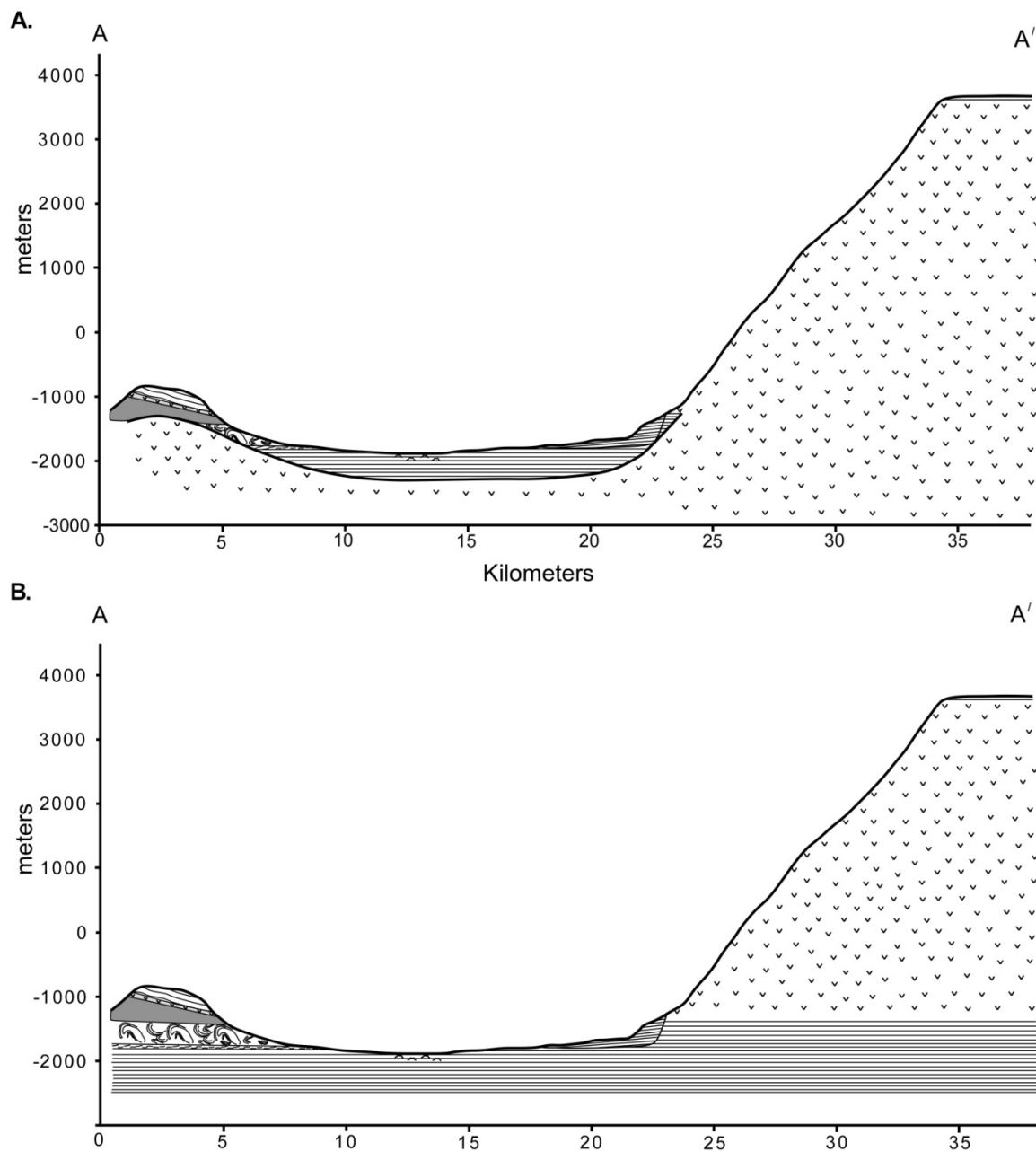


Fig 5.6. Cross-section constructed using MOLA topographic profile taken from A to A' in southern Melas basin (Fig. 5.1B) Vertical axis is in meters and horizontal axis is in kilometers. Two possible scenarios are shown. A.) Stratigraphy is shown assuming units currently exposed at surface were deposited in a pre-existing basin. It is not known how deep this pre-existing basin may have been nor to what elevation the northern basin wall might extend. In this case the strata should onlap the basin walls at the margins of the basin. B.) Stratigraphy is shown assuming units at surface were deposited before the formation of Valles Marineris and have been exposed due to subsequent erosion. In this case, the strata should not be observed to onlap the basin walls in any location.

transitioning into blocky deposits in several locations as one moves up the stratigraphic section (Fig. 5.11).

5.4.2 Map distribution and stratigraphy of deformed regions

5.4.2.1 Melas Chasma

Three regions of deformed strata occur in western and southern Melas Chasma (Fig 5.2).

The two outcrops of convolute folds in region 1 occur on a slope near the northern ridge bounding southern Melas basin (Fig. 5.1D). The convolute folded strata in the southwestern outcrop of region 1 appear to extend over a low point in the ridgeline where

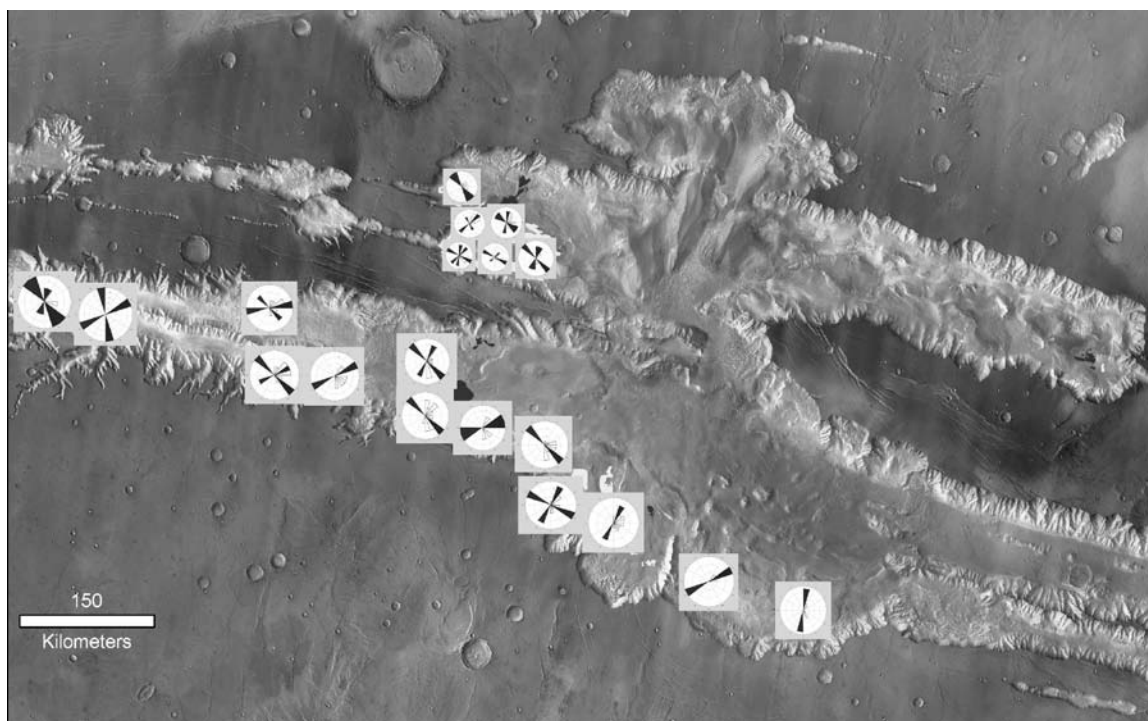


Fig 5.7. Rose diagrams of fold axial trace orientations plotted on deformation map in the locations they were measured. Fold axial trace orientations are bimodal with a component to the NE-SW and a component to the SE-NW.

they transition into a large outcrop of detached slabs in the central portion of region 1 (Fig. 5.9). There are two smaller outcrops of detached slabs at the base of the northern ridge bounding Melas Chasma (labeled 1-N in Fig. 5.1D). The central and northern outcrops in region 1 are likely part of a continuous outcrop of detached slabs, although no definitive exposures of detached slabs are identified in the area between them (Fig. 5.1D).

Regions 7 and 8 are exposed in the low areas near the chasma walls on the south wall of Melas Chasma (Fig. 5.2). Deformed strata are mostly located topographically below the interior layered deposits on materials previously mapped as interior massive deposits (Avm, Amazonian Valles Marineris younger massive material) and Avme (Amazonian Valles Marineris etched massive material) and interior floor materials (Avfr, Amazonian Valles Marineris rough floor material) by Scott and Tanaka (1986). Small areas of regions 7 and 8 do occur on the lower parts of the interior layered deposit mounds. The large southern outcrops of deformation in regions 7 and 8 appear to be close to the same stratigraphic horizon.

Two stratigraphic columns were measured in the southeastern outcrop of convolute folds in region 1 in southern Melas basin where DEMs were available (Fig. 5.8). The lowest portion of the basin is filled with a thinly-stratified unit with bedding dips between $0.6 \pm 0.1^\circ$ and $1.4 \pm 1^\circ$. Two features interpreted as sublacustrine fans occur in the topographic low of the basin, suggesting the basin was once filled with water (Metz et al. 2009). At the position of stratigraphic column 2, the thinly-stratified unit is overlain by a

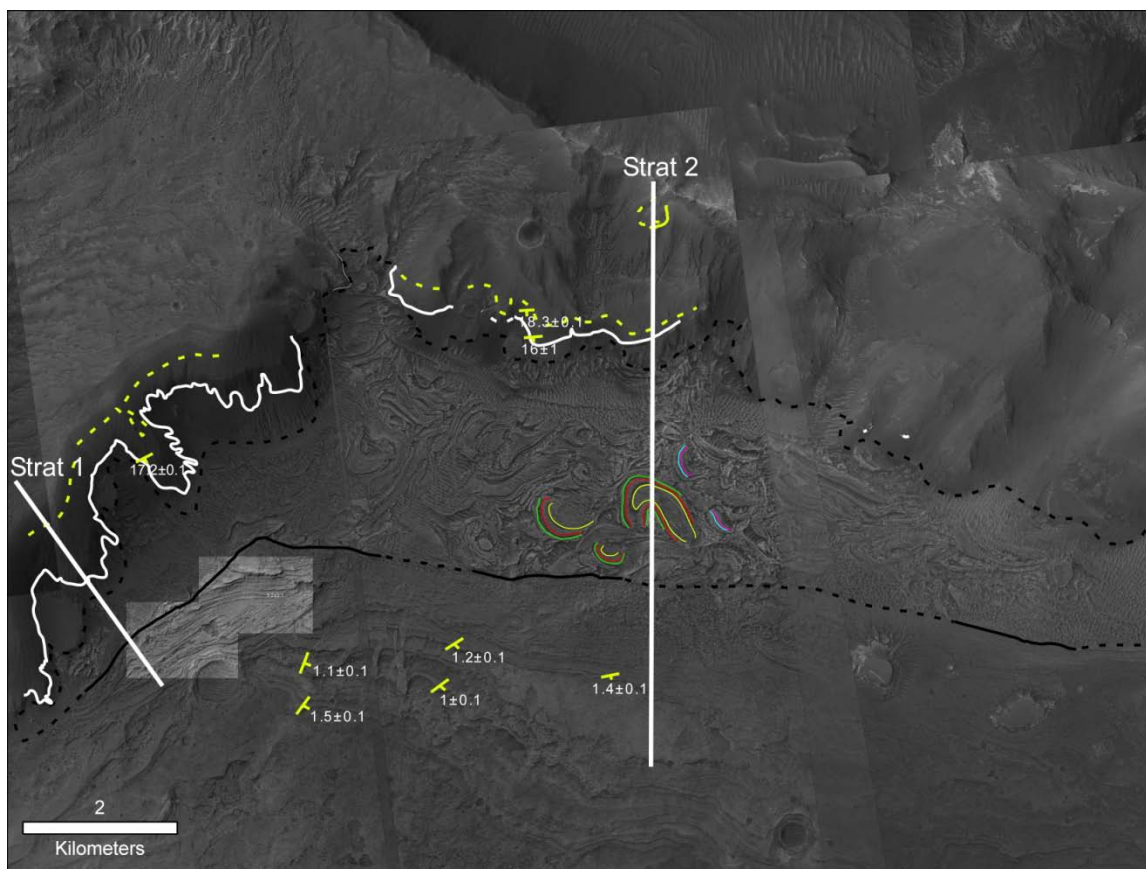


Fig 5.8. Map showing locations of stratigraphic sections measured in region 1-SE (labeled Strat 1 and Strat 2). Contacts between units identified in this region are also indicated: contact between flat-lying strata and km-scale convolute folds is mapped as a black line (lines are dashed where contact is inferred), contact between folds and medium toned unit is shown as a white line, and the contact between the massive unit that weathers to boulders and the thinly-stratified unit is shown as a dashed yellow line (gradational contact). Representative dips are shown in yellow. Several strata that are repeated through multiple fold blocks in the km-scale convolute folded unit are traced in various colors. Each color represents one bed that could be followed through multiple blocks.

96 m thick massive unit with hints of undisturbed layering. The massive unit is overlain by a 280 m thick convolute-folded unit. Further to the west at the position of stratigraphic column 1, a 23.9 m thick set of clinoforms lies above the thinly-stratified unit and is overlain by a 146 m thick convolute folded unit. No massive unit is observed below the

convolute folds in this location. The convolute folded unit may be a relatively thin unit deposited on a paleo-slope or it may fit conformably into the stratigraphy. However, there is no evidence for onlap of the slope by the convolute folded unit. Above the convolute folded unit is a 148 m-thick medium-toned unit that lacks signs of bedding. At the position of stratigraphic column 1, the medium-toned unit is overlain by a 44 m-thick massive unit that weathers into boulders, and this unit thickens to the west to 282 m at the position of stratigraphic column 1. The medium-toned unit interfingers and grades into a 131 m-thick thinly stratified unit that caps the ridge on the north side of southern Melas basin. On the west side of southern Melas basin this thinly-stratified unit is only 56 m thick and has been eroded via fluvial incision.

On the south chasma wall of southern Melas basin, a unit that appears to have slumped down the chasma wall is observed (Fig. 5.12). This unit contains bedding that dips to the north at $\sim 7^\circ$ which is steeper than the $\sim 1^\circ$ dips of strata present on the basin floor. A large section of rock appears to have slid away from the chasma wall, including a small stratified section of rock (Fig. 5.12B). An S-fold is observed where the section of 'sliding' rock has likely collided with the layered sediments on the basin floor (Fig. 5.12B). A set of isolated elliptical patterns is exposed in a several hundred meter long vertical exposure of rock near where the sliding block collided with the basin floor sediments (Fig. 5.12C).

A cross-section from the north to south end of southern Melas basin was measured at the location of stratigraphic column 2 (Figs. 5.1B and 5.6). This shows how the

stratigraphy fits into the regional topography of the basin. There are at least two possible interpretations for the stratigraphy at depth in southern Melas basin as shown in Fig. 5.6A and B. The strata observed at the surface could onlap the side of an older buried depositional basin (Fig. 5.6A). One constraint that could favor this interpretation is that bedding in the northern wall of southern Melas basin dips at $\sim 19^\circ$ to the south. If these beds were deposited on a pre-existing slope, they would be expected to dip to the south. In the second possible interpretation, the strata observed at the surface are older than the wall-

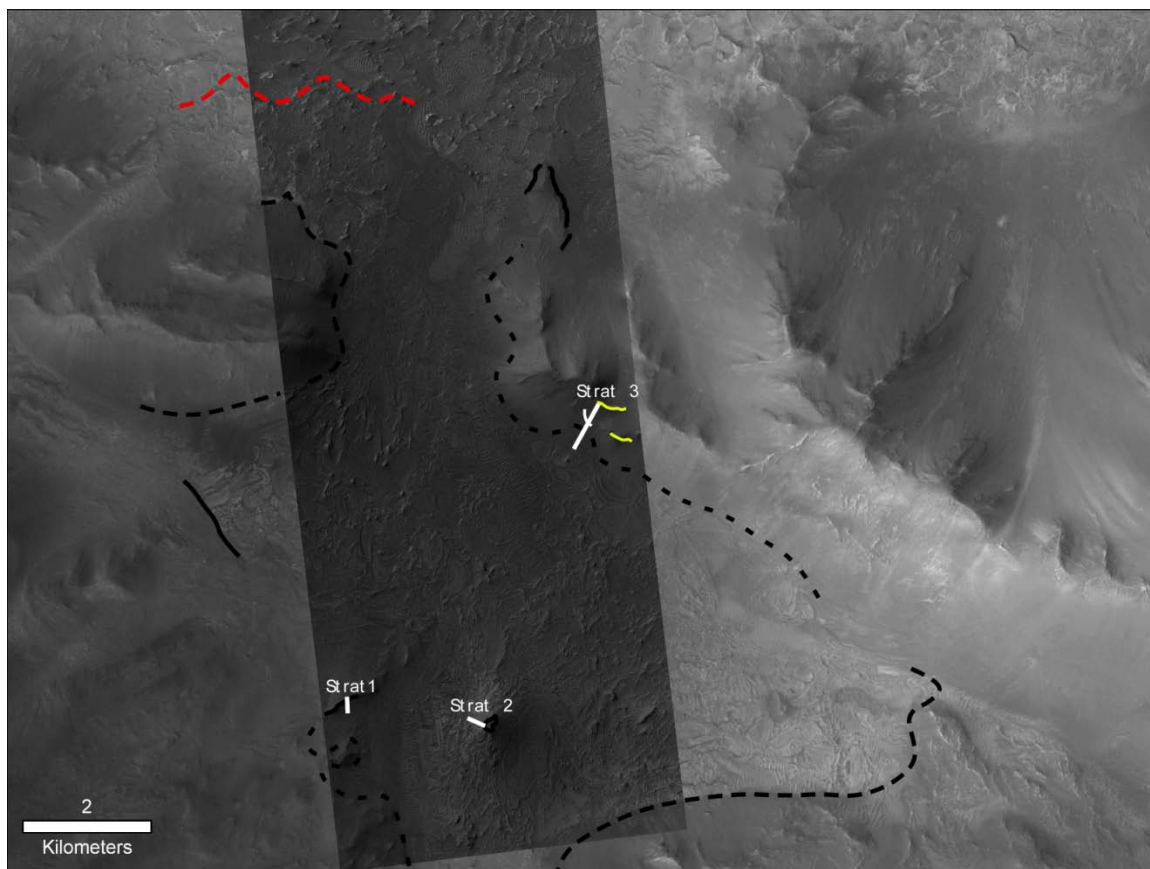


Fig 5.9. Map showing locations of stratigraphic sections measured in region 1-SW (labeled Strat 1-3). Contacts between units are indicated using the same color scheme as Fig 5.8. Dashed red line shows gradational contact between convolute folds and detached slabs.

rock composing the chasma walls of Valles Marineris and are exposed through erosion (Fig. 5.6B). The exposed stratigraphy and contacts within southern Melas basin do not allow discrimination between these two options. However, just to the east of southern Melas basin, layered sediments are observed to onlap the wall of the basin, suggesting at least some deposition of layered sediments occurred after the formation of the basin.

In the southwestern outcrop of convolute folds in region 1, which is ~27 km to the west of the southeastern outcrop (Fig. 5.1D), a similar stratigraphy to the southeastern outcrop was observed. Three stratigraphic columns were constructed for the southwestern outcrop using MOLA data (Fig. 5.9). At the position of stratigraphic column 3, a thick interval (~325 m) of km-scale convolute folds is observed. The deformed unit is overlain by the same three units observed to overlie the folds in region 1, a medium-toned unit, a massive unit and a laterally interfingering massive and thinly-stratified unit. The two other stratigraphic columns measured in the area show ~100 m thick exposures of convolute folds. In stratigraphic column 2, the folds are covered with a thin medium-toned unit that is overlain by a thin light-toned unit. In stratigraphic column 1, the folds are covered by a thin (~15 m thick), dark-toned stratified unit overlain by a thin (~15 m thick), medium-toned and stratified unit.

A stratigraphic column was estimated using MOLA data in the central outcrop of region 1 in western Melas Chasma (Fig. 5.1D). The lowest unit is a ~150 m-thick exposure of detached slabs. There is a thin, light-toned deposit that drapes the detached slabs and the

ridge adjacent to the detached slabs. The light toned drape appears similar in tone and texture to a light-toned draping deposit seen on the ridge in the western part of southern Melas basin (Fig. 5.13). The light-toned drape also appears similar to the material composing the convolute folds. However, because the light-toned unit drapes detached slabs that can be seen to grade into the convolute folds, the light-toned unit must be stratigraphically younger.

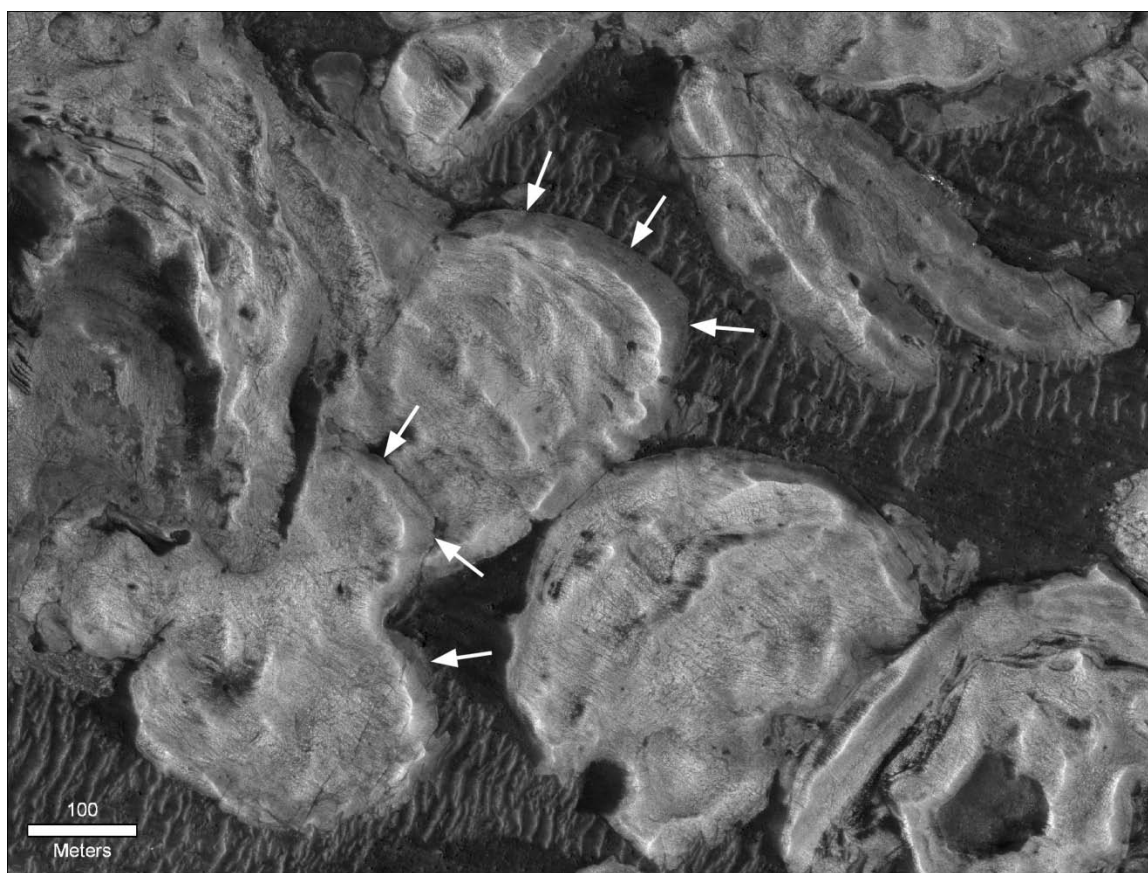


Fig 5.10. Some of the detached slabs show resistant edges as is illustrated by the white arrows (ESP_014339_1710).

A stratigraphic column was constructed for the southeastern outcrop of deformed strata in region 7 in southeastern Melas Chasma (Figs. 5.5 and 5.14). The base of the column consists of ~600 m of stratified deposits. A ~500 m thick unit with a weathering pattern that makes it difficult to determine the type of bedding occurs above the layered strata in the location where the stratigraphic column was measured. However, farther to the west at the same stratigraphic interval the deposits consist of folded strata (Fig. 5.14 A and B). These folds are largely elongated in a downslope direction. We have tentatively assumed the unit with the lattice-like weathering pattern also consists of folded strata. Above the unit with the lattice-like weathering pattern is another 100 m of stratified deposits. Above these are ~125 m of pulled-apart strata (Fig. 5.14 A and C). The eastern boundary of the areal exposure of the pulled-apart strata is very linear and may be a fault. At the top of the section are ~375 m of stratified deposits.

In the stratigraphic columns measured in the southeastern outcrops in region 1 and region 7, both the lower and upper contacts of the deformed units could be identified. In the other outcrops, either the lower or upper contact was observed, but not both in the location where the stratigraphic column was measured. However, in many regions these missing upper or lower contacts were observed in other outcrops within the region. The fact that both lower and upper contacts are observed in many areas implies that the deformation is restricted to a limited, relatively thin stratigraphic interval. The thickness of the deformed unit ranges



Fig 5.11. Several styles of deformation can be seen to grade into each other. Dashed black lines show gradational contacts. A.) Lateral gradation between deformation types. Location of image shown in Fig. 5.1A. B.) Vertical transition between folded strata and detached slabs. Location of image shown in Fig. 5.1A.

from 100 m to 350 m thick, although in many areas only minimum thicknesses could be estimated, since both the lower and upper contacts were not observed.

5.4.2.2 Ius Chasma

Regions 2-4 occur in Ius Chasma. All of the outcrops in Ius occur on the floor of the chasma in areas previously mapped as interior floor (Avfr) and surface materials (Avsd (Amazonian Valles Marineris dark surface material)) by Scott and Tanaka (1986). There are no interior layered deposits or mounds near the deformed strata in Ius Chasma, suggesting the origin of the latter is not linked to the former. In region 2, the deformed strata are exposed in the lowest topographic areas, and in the eastern part of the region are covered by a terraced alluvial fan. Sediment eroded from the southern wall of Ius overlies the southern end of the deformed unit. In the western part of the region deformed strata are observed up to the level of a resistant bed in the northern wall of Ius. The areas above the resistant bed are mantled with eolian sediments. The southern portion of the deformed strata is covered with materials derived from erosion of the southern wall of Ius. Roach et al. (2009b) also examined the strata in this topographic low and found that they were composed of kieserite, polyhydrated sulfate and hydrated silicate with the polyhydrated sulfates found at higher elevations than the kieserite. In region 4 in the northern portion of

Ius Chasma, several types of deformed strata are observed and are partially covered by Amazonian landslide deposits. CRISM image FRT0000A396 examined by Roach et al (2009b) shows that the deformed strata in this area are composed of non-hydrated material.

Several different types of deformed strata are exposed in Region 3 at the bottom of the floor of western Ius Chasma (Fig. 5.15). Stratigraphic sections for this area are shown in Fig. 5.5. In the western outcrop of this region grading between detached slabs, pull-apart strata and folded strata is observed. The deformed strata occur in topographic lows and are exposed in an erosional window; several landslides overlie the deformed strata. A stratigraphic column was measured in this area and consists of ~100 m of deformed strata at the base overlain by a ~50 m thick light-toned unit (Fig. 5.15). At the top of the section is ~150 m of a dark toned mantling unit. The deformed strata are covered by eolian dunes in some of the low areas where the dark-toned unit has been eroded away.

5.4.2.3 Candor Chasma

Region 5 is located in western Candor Chasma and region 6 in eastern Candor Chasma. They occur in areas previously mapped as massive deposits (Avme), surface materials (Avsd), floor materials (Avfs, Amazonian Valles Marineris smooth floor material), and layered materials (Hvl, Hesperian Valles Marineris layered material) (Scott and Tanaka 1986). The deformed strata are observed up to the elevation of a topographic bench that runs around western Candor Chasma and is shown by the white line in Fig 5.1. The bench was interpreted by Lucchitta (2008) as a shoreline and by Okubo (2010) as forming through eolian erosion. Several large outcrops of the folded strata are found in the

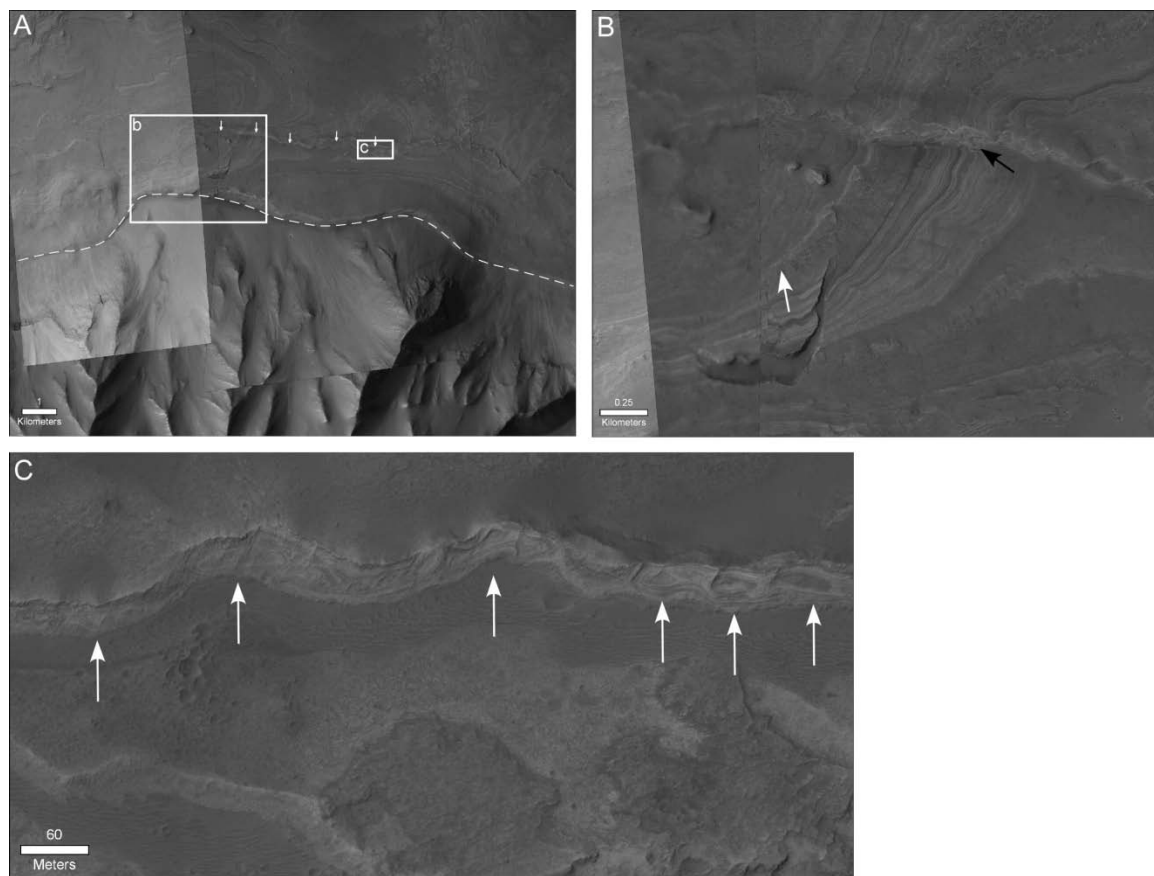


Fig 5.12. A.) Location of slump in southern Melas basin. Dashed line shows edge of slump. White arrows show where slump block slid into pre-existing basin floor strata. White boxes show locations of b and c. B.) Zoomed-in portion of slump showing a small stratified block that has pulled away from the main slump mass (white arrow). Black arrow shows S-fold where the slump collides with basin-floor strata. C.) Vertical section where hypothesized slump folds are shown in cross-section. White arrows highlight folds. B and C are from PSP_002828_1700.

western portion of region 5 in Candor at the base of the chasma wall and up to the level of the topographic bench. Another large exposure of deformed strata is found in the topographic low to the east of Ceti Mensa. In several areas in the eastern outcrops of region 5, detached slabs overlie folded strata (Fig. 5.11B). Much of the outcrop of deformed strata in the central portion of region 5 is located on the lower portion of Ceti

Mensa. A light-toned unit covers much of the central part of western Candor and appears to overlie the deformed strata. In some areas the deformed strata are exposed in erosional windows through the light-toned unit. Exposures of detached slabs cap elongated mesas in several areas. One example is shown in Fig. 5.16A.

A stratigraphic column was measured within a crater in the northern part of region 5 using DEM C3 (Figs. 5.5 and 5.16). At the base of the section is 25 m of undeformed sediments. At -125 m elevation, there is a low-angle fault and the layers above the fault were folded into an overturned concentric fold. There are several additional folds and many high-angle faults in the 225 m above the low-angle fault at -125 m (Fig 5.16). In the southwestern portion of the deformed unit is a potential interval of repeated stratigraphy. There is another 25 m of stratified sediments above the deformed interval. The top of the section is 125 m thick and consists of detached slabs that form a resistant cap. Faults were mapped in the crater wall and the orientations of the faults indicated in Fig. 5.16 B are shown in the equal-area stereonet in Fig. 5.16C.

5.4.3 Elevations of deformed strata

The deformed units are observed to occur at a variety of elevations, including as low as -4100 m in Melas Chasma and up to 3400 m in Candor Chasma. The elevations of the deformed strata range from -4200 to -1000 m in Ius Chasma, from -4100 to 400 m in Melas Chasma, and from -2500 to 3400 m in Candor Chasma. There does not seem to be a pattern in the elevations where deformed strata are observed.



Fig 5.13. Light-toned unit that drapes the ridge in the western part of southern Melas basin (PSP_009025_1705).

5.4.4 Fold orientations

Orientations of fold axial traces were measured wherever possible (i.e. for folded strata and convolute folds) and have largely bimodal trends as shown in Fig. 7. There is

one set of fold axes with a NE-SW orientation and another set with a SE-NW orientation. This trend holds well for the folds in western Candor Chasma and for those in Ius Chasma. Folds in Melas Chasma exhibit more variation, with the fold axes in eastern Melas Chasma having primarily a NE-SW orientation, which is roughly perpendicular to the nearest chasma wall.

5.4.5 Composition of deformed strata inferred from CRISM spectra

CRISM images covering the deformed strata exhibit spectral signatures consistent with the presence of sulfates. Monohydrated sulfate (likely the Mg-variety kieserite) and polyhydrated sulfates are detected in spectra of deformed beds in Ius, Candor and Melas Chasmata (Fig. 5.17). Another type of material that does not show a good spectral match to any library spectra is detected in Ius and Melas Chasmata (Fig. 5.17 C, E). Ratio spectra of this unknown material has absorption bands at 1.4 μm , 1.91 μm and a 'doublet' near 2.21 and 2.27 μm (Fig. 5.17 D, F). Roach et al. (2009b) previously identified this material in Ius and Coprates Chasmata and Noctis Labrynthus and discuss its spectral characteristics in detail. We also note that the strength of the 1.4 μm band for this material is variable, and the relative strengths of the 2.21 and 2.27 bands also vary (Fig. 5.17 D, F). This suggests that the material is a mixture of at least two different phases, similar to the findings of Roach et al. (2009b). Laboratory experiments by Tosca et al. (2008b) formed a material which may be jarosite mixed with poorly crystalline clays or silica, and it has similar spectral properties to this unknown phase. The material precipitated in the Tosca et al. (2008b) experiments formed at a moderate pH of 6-7 and was XRD amorphous. This

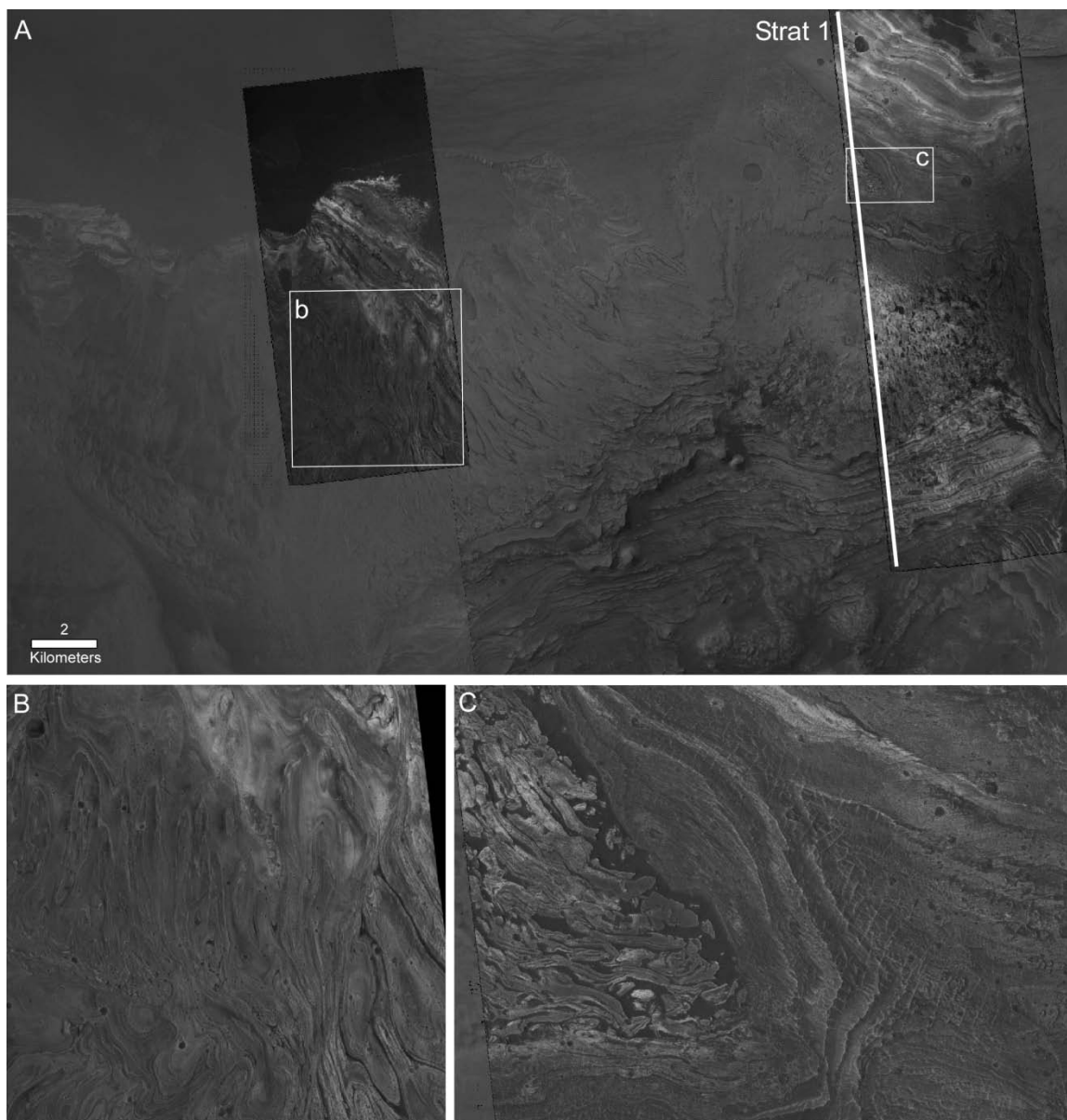


Fig. 5.14 A.) Multiple types of deformation exposed in region 7-W (P07_003909_1686, P17_007535_1688). White boxes show locations of b and c. White line shows location where stratigraphic column was estimated. B.) Folded strata (ESP_013719_1665). C.) Pull-apart strata (ESP_013508_1665).

material is also seen in layered material that onlaps the ridgelines to the west of region 8.

This novel material is not identified in any of the ILD mesas in Candor or Melas Chasma,

instead these ILD show strong spectral signatures consistent with the presence of kieserite and polyhydrated sulfates (Roach et al. 2009a). The deformed units in region 7 also do not show the novel material.

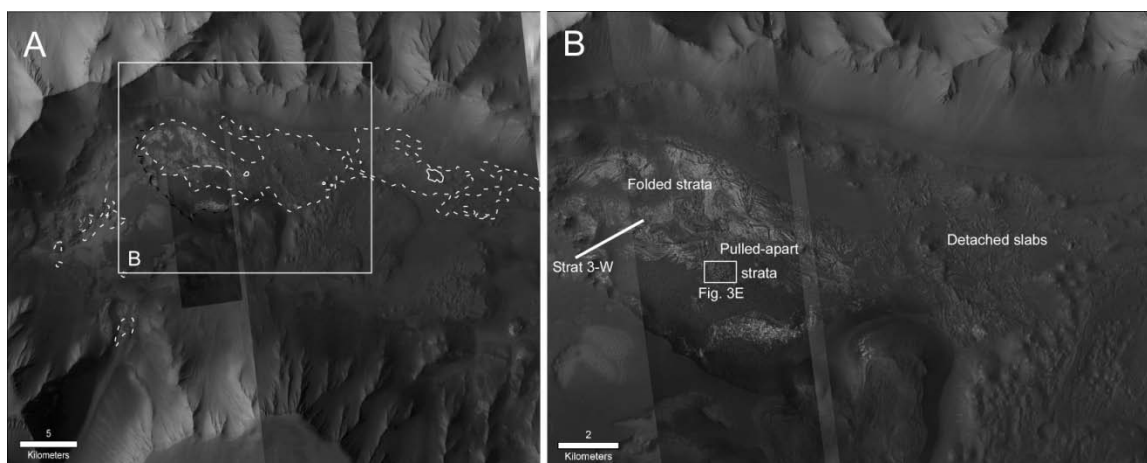


Fig 5.15. Deformation exposed in region 3. A.) White and black dashed lines show extent of deformed strata. White box shows location of B. B.) Grading between detached slabs, pull-apart strata and folded strata is observed. The white box shows the location of Fig. 5.3E. The location where stratigraphic column 1 was measured is shown by the white line.

5.5. Discussion

5.5.1 Rheology of deformed strata

The styles of deformation observed in Valles Marineris suggest that much of the deformation occurred in the plastic regime. The exception to this is the pull-apart structures that likely were deformed in the brittle regime. Because the deformed strata appear to be largely composed of several types of sulfates, including kieserite ($\rho=2.57 \text{ g cm}^{-3}$) and polyhydrated sulfates, it is important to consider the deformational behavior of these minerals. Though published data on the material properties of sulfates is limited, the density of gypsum ($\rho=2.32 \text{ g cm}^{-3}$) is less than that of most sedimentary and volcanic rocks,

so given this flow-strength contrast it should theoretically deform in a fashion similar to halite at low strain rates (Williams-Stroud and Paul 1997). Halite is weak and easily mobilized by solid state flow and can flow at low temperatures and differential stresses (Jackson and Talbot 1986). Some work has been done on the deformation of gypsum which shows that at very slow strain rates the strength of gypsum approaches that of halite, which deforms plastically at shallow depths at strain rates of 10^{-8} - 10^{-14} s⁻¹ (Williams-Stroud and Paul 1997; Jackson and Talbot 1986). Gypsum undergoes creep at faster strain rates if water is present (de Meer and Spiers 1995). In order for water to be trapped with the gypsum during deformation, it would need to be covered with low permeability rock, such as clay-rich mudstones (Heard and Rubey 1966). The strength of these sulfates increases with water loss. Anhydrite requires two orders of magnitude larger differential stress than gypsum in order to attain diapiric strain rates (Williams-Stroud and Paul 1997).

The deformed sediments in Ius and Melas could also consist of volcanic ash that was deposited rapidly over a large area and became water saturated and subsequently altered. This interpretation could fit with the spectral detection of the material that may be jarosite mixed with poorly crystalline altered clays or silica. Studies of ash rheology show that the transition from brittle to ductile deformation occurs between 800-850 °C but shifts to lower temperatures with increasing water pressure or with lower rates of displacement (Robert et al. 2008).

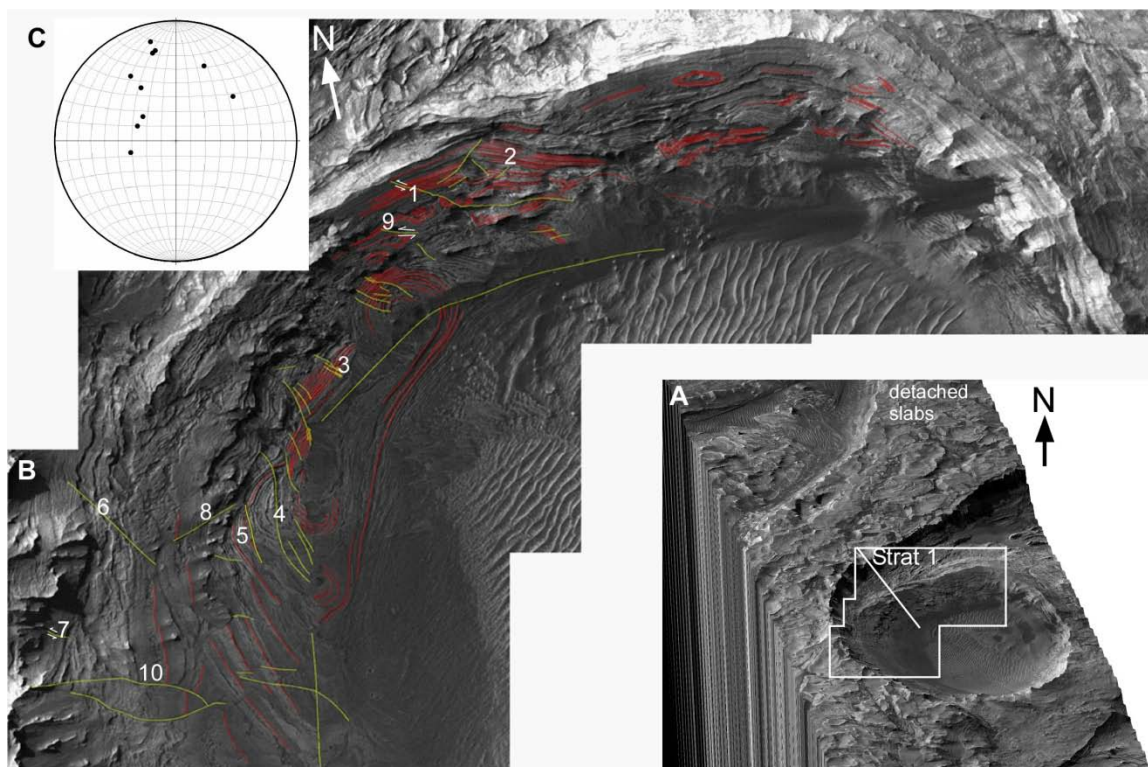


Fig 5.16. A.) Perspective view of DEM showing that the detached slabs form a resistant mesa. White box shows location of b. B.) Portion of crater wall in DEM with key strata to help visualize deformation mapped in red and faults in yellow. Faults whose orientation was measured are numbered 1-10. C.) Equal-angle stereonet of orientations of faults indicated in B (n=10).

5.5.2 Relative age of deformed strata

An important consideration is whether the strata on the floor of Valles Marineris, both the mounds of light-toned strata (ILD) and the surrounding sediments, pre- or post-date chasma formation. This question has been debated in the literature with several authors suggesting the light-toned layered rock predates chasma formation and is being exhumed from below the wallrock (Malin and Edgett 2000; Montgomery and Gillespie 2005; Catling et al. 2006) and most others suggesting the sediments postdate or were contemporaneous with chasmata formation (Lucchitta et al. 1992; Peulvast and Masson

1993; Lucchitta et al. 1994; Chapman and Tanaka 2001; Weitz et al. 2001; Komatsu et al. 2004; Fueten et al. 2006; Fueten et al. 2008; Okubo et al. 2008; Okubo 2010). Much of this controversy arises from the fact that there are very few clear, unambiguous contacts between the light-toned layered deposits, which are often near the centers of chasmata, and the canyon wallrock. Here we review the evidence presented in previous literature to support relative age interpretations for the ILD (cited images are listed in Table 5.3).

From the first images sent back by the Mariner and Viking spacecraft, the wallrock of Valles Marineris was seen as distinct from the light-toned layered rock found on the floors of the chasmata. Wallrock is described as showing 'spur and gully' morphology or smooth talus slopes and as giving rise to landslides, whereas the ILD are described as showing light-colored smooth surfaces with fluted topography distinctly different from wallrock (Lucchitta et al. 1992). An early study based on Viking images (Viking Orbiter 1 frames 913A11 and 913A13, 20-125 m/pixel) observed that the ILD in the divide between Ophir and central Candor Chasma onlap the spur and gully morphology of the canyon wall (Nedell et al. 1987). Lucchitta et al. (1994) observed that in east Candor, the ILD abuts and buries wallrock already eroded into spurs and gullies along the south part of the chasma. Witbeck et al. (1991) suggest that in Juventae and Ganges Chasmata layered deposits overlie conical hills that are similar to chaotic terrain farther west. In Melas Chasma, Peulvast and Masson (1993) state that 'no direct contact can be seen between the smooth

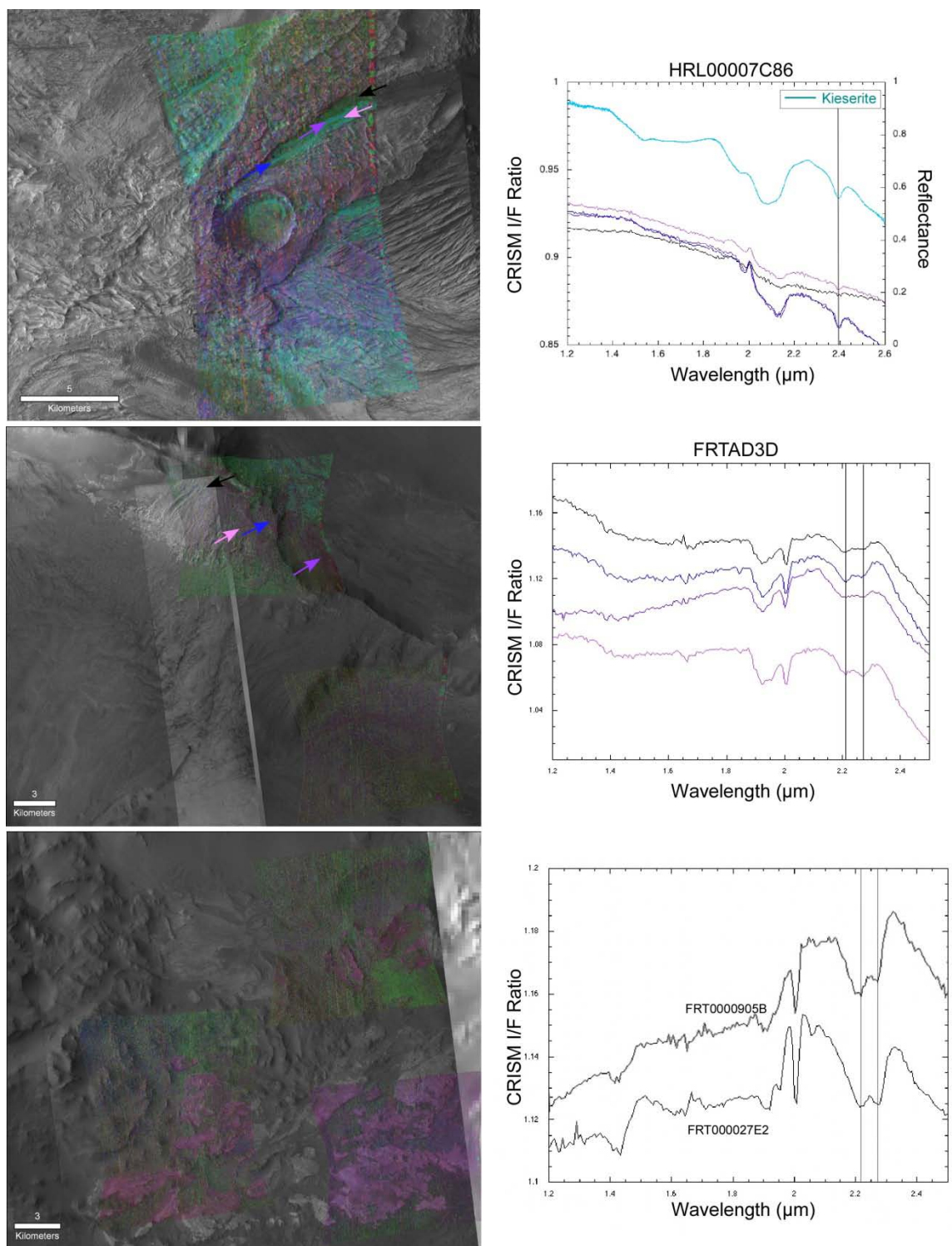


Fig 5.17. A.) Band parameter map from CRISM targeted image HRL00007C86 overlaid on CTX image from region 5 in Candor Chasma. Red channel is BD 2210, green channel is BD 2100 and blue channel is SINDEK. Green areas show kieserite. B.) Four CRISM

spectra (from areas indicated by arrows) show a good spectral match to the laboratory spectrum of kieserite. C.) Band parameter map from CRISM targeted image FRT0000AD3D overlayed on CTX image from region 1 in Melas Chasma. Red channel is BD 2210, green channel is BD 2100 and blue channel is SINDEXT. D.) Four CRISM spectra (from areas indicated by arrows) show the unknown material with bands near 1.9 μm , and a doublet at 2.21 and 2.27 μm . The drop in reflectance near 2.01 μm is due to incomplete removal of atmospheric CO_2 and is not a surface absorption. E.) Band parameter map from CRISM targeted images FRT0000905B, FRT000027E2 and FRT0000A396 overlayed on CTX image from region 4 in Ius Chasma. Purple areas show the unknown material. Red channel is BD 2210, green channel is BD 2100 and blue channel is BD 1900. F.) CRISM spectra from FRT0000905B and FRT000027E2 show the unknown material in the purple areas with bands at 1.43 μm , 1.91 μm and a doublet at 2.21 and 2.27 μm . The relative strength of the bands in the doublet varies. The drop in reflectance near 2.01 μm is due to incomplete removal of atmospheric CO_2 and is not a surface absorption.

surfaces (of the ILD) and the south Melas Chasma wall, as a 15-50 km 'moat' separates them.' They further note that landslides from the south Melas wallrock partly fill the moat and cover the base of the ILD bench, obscuring the contact. Peulvast and Masson (1993) suggest that the layered sediments in south Melas embay the wide reentrants and ridges, and thus formed in a basin whose walls already had their present outline.

When the Mars Orbiter Camera (MOC) on the Mars Global Surveyor began sending back images (4-10 m/pixel), new details of the ILD and wallrock were evident. Malin and Edgett (2000) suggest that several MOC images show that light-toned layered strata underlie the wallrock. They cite MOC images (M17-000468, M17-00467 and M20-01506) covering the eastern part of the wall of northwest Candor as evidence that the ILD continue under the chasma walls. While light-toned material can be seen high up on the wallrock in this location, a direct stratigraphic contact between the light-toned layered material and the wallrock is obscured by an eolian mantle, making the stratigraphic

relationship ambiguous. It is possible the light-toned layers could underlie the wallrock here, but they could also onlap the wallrock. Additional images from west Candor (M14-00631, M-18-00099 and M19-00784) are cited as the best locations where layered units can be seen going into and under the chasm walls (Malin and Edgett 2000). In these areas, light-toned layered rocks are observed up to the level of a topographic bench, as described earlier in this paper. However, the direct stratigraphic contacts are also obscured here by eolian mantles and talus deposits. Their other examples from Coprates (M20-00380, M20-01760, M21-00103) and Ius (M08-07173) are also ambiguous with the actual contacts obscured by eolian mantle or talus deposits. Montgomery and Gillespie (2005) cite additional areas in Candor (R07-00897) and southwest Melas (R04-01897, R08-00286 and R08-00287) where they interpret wallrock as underlain by light-toned layered deposits. These areas also show ambiguous contacts that could represent onlap or wallrock underlain by light-toned strata.

Catling et al. (2006) examined many MOC images (Table 3) in Juventae Chasma which they state show that the ILD are older than the wallrock and chaos material. Many of these images do show promising contacts, and HiRISE images (PSP_005557_1755 and PSP_003790_1755, ~25 cm/pixel) confirm that light-toned strata do underlie wallrock near mound A of Catling et al. (2006). In this location, the HiRISE images resolve a relatively long exposure of a contact between the light-toned strata and the wallrock (Fig. 5.18B). This exposure occurs along a ridgeline in a spur and shows a sharp, irregular contact that cuts across elevation. The light-toned strata are less resistant to erosion than the dark-toned

wallrock material which caps the ridge. The contact appears to be an erosional unconformity and shows that the local wallrock directly overlies the light-toned strata.

Other authors have described locations in MOC imagery where layered deposits appear to onlap chasma walls. Chapman and Tanaka (2001) observed layered deposits 'plastered onto' the chasma walls in Coprates (MOC image AB-106306). Komatsu et al. (2004) observed that an ILD mound overlaid the chaotic terrain in Juventae (MOC image M10-00466) and that the ILD are covered by younger landslides and eolian material. MOC image M10-00466 was later cited by Catling et al. (2006) to show that light-toned strata underlie the wallrock. Flauhaut et al (In Press) similarly observe ILD to overlie chaotic mounds in Capri. Chojnacki and Hynek (2008) suggest light-toned layers are 'pasted-on' to wallrock in Ophir Chasma (S04-01271). We regard these interpretations as ambiguous, because the contacts are mostly obscured by eolian mantles, talus deposits, and landslides; in areas where there may be direct contacts (such as Juventae), these contacts are not fully resolved in MOC imagery.

Structural relationships have also been used to argue the relative ages of the ILD. Using High Resolution Stereo Camera (HRSC)-derived DEMs, Fueten et al. (2006) measured the dips of layers in the ILD mounds of southwestern Candor Chasma and found that they were parallel to local slopes. Similar results were found for the ILD in Ophir (Zegers et al. 2006), Hebes (Hauber et al. 2006), Iani (Sowe et al. 2007), and Coprates Chasma (Hamelin et al. 2008). Okubo et al. (2008) and Okubo (In Press) used HiRISE DEMs to measure the dips of strata to the south of the ILD mounds in southwest Candor

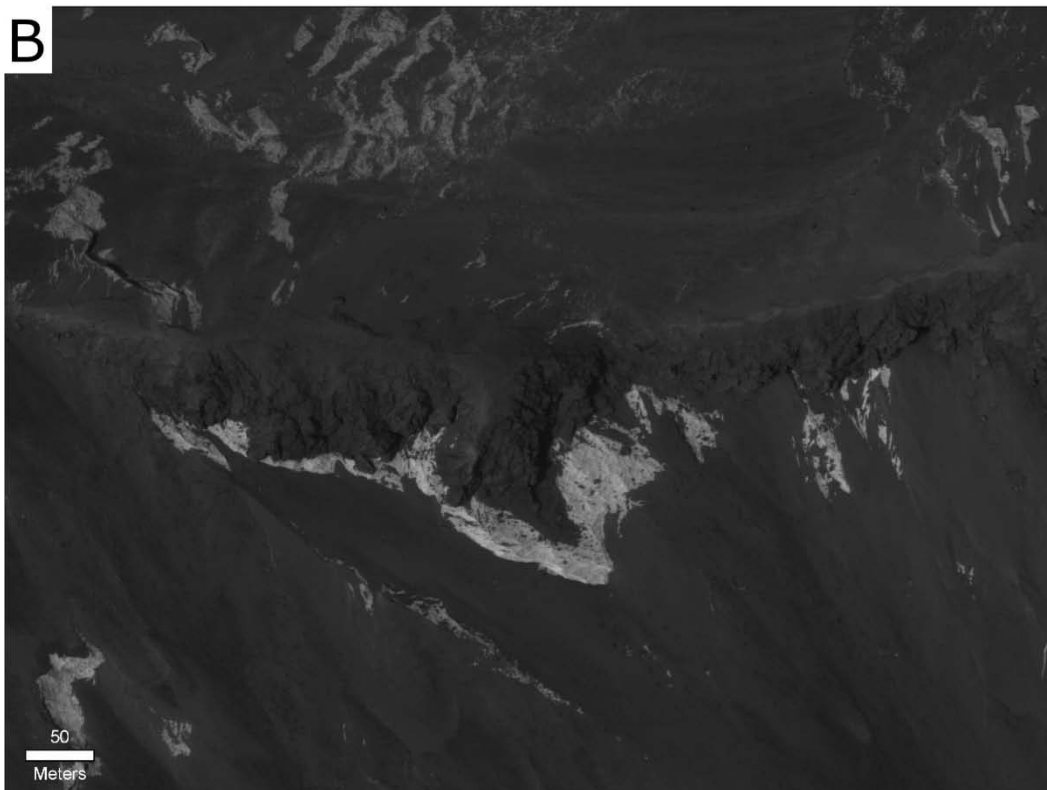
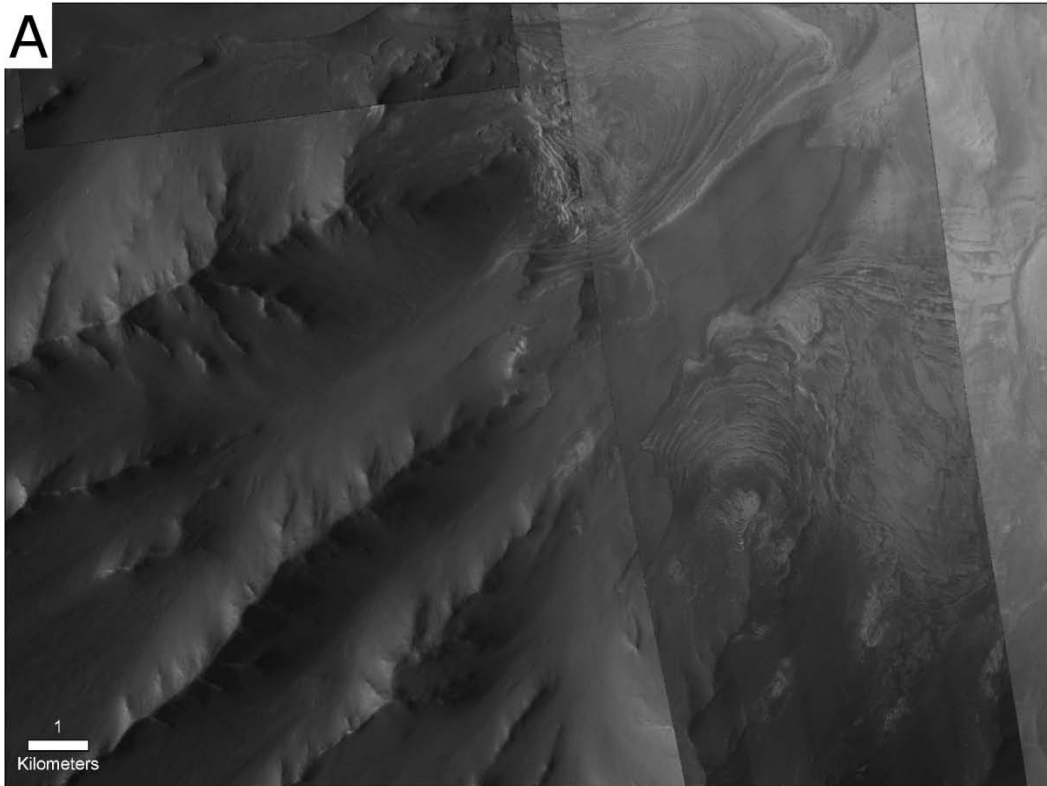


Fig. 5.18 A.) Onlap relationship between the light-toned stratified deposits and the wallrock in south Melas Chasma. The light-toned layers fill in the topographic lows between the ridgelines (P05_002907_1706, PSP_004397_1695). B.) Contact between wallrock and light-toned layers in a ridgeline in Juventae Chasma (PSP_5557_1755).

and found that they generally dip toward the center of Candor, suggesting they postdate formation of the ancestral basin.

A search for unambiguous contacts between wallrock and light-toned stratified deposits was made in a separate effort by J. Metz and R. Milliken (unpublished analysis) using CTX and HiRISE imagery, but none were found in central Valles Marineris. In virtually every location, these contacts are obscured by eolian mantles, talus deposits, or landslides. In southern Melas Chasma, just to the east of southern Melas basin, there is a convincing area where the light-toned stratified deposits clearly onlap and fill in the topographic lows between ridges of wallrock (Fig. 5.18A). Structural data also seems to support a younger age for the light-toned deposits. The exception to this is in Juventae Chasma, where promising contacts showing wallrock overlying light-toned layers are observed. These few relatively unambiguous examples illustrate that the relative ages may differ in each chasma. Locally, light-toned layers may underlie wallrock, but in other locations the light-toned strata may have infilled pre-existing basins. Thus, resolving the controversy in the ages of the wallrock and light-toned layers may have to wait until landed missions can use absolute age-dating techniques in multiple chasmata.

Camera	Image	Location	Resolution	Reference
Candor				
Viking Orbiter 1	913A11	Ophir-Candor	63 m/pixel	Nedell et al. 1987
Viking Orbiter 1	913A13	Ophir-Candor	63 m/pixel	Nedell et al. 1987
MOC	M17-00468	5.56°S, 74.20°W	244 m/pixel	Malin and Edgett 2000
MOC	M17-00467	5.52°S, 74.56°W	5.8 m/pixel	Malin and Edgett 2000
MOC	M20-01506	5.17°S, 74.52°W	2.9 m/pixel	Malin and Edgett 2000
MOC	M14-00631	5.10°S, 77.1°W	5.71 m/pixel	Malin and Edgett 2000
MOC	M18-00099	4.98°S, 77.33°W	4.29 m/pixel	Malin and Edgett 2000
MOC	M19-00784	5.17°S, 77.36°W	4.29 m/pixel	Malin and Edgett 2000
MOC	R07-00897	4.90°S, 76.80°W	3.02 m/pixel	Montgomery and Gillespie 2005
Coprates				
MOC	M20-00380	14.64°S, 53.86°W	4.25 m/pixel	Malin and Edgett 2000
MOC	M20-01760	13.04°S, 65.13°W	5.68 m/pixel	Malin and Edgett 2000
MOC	M21-00103	14.64°S, 56.58°W	2.84 m/pixel	Malin and Edgett 2000
MOC	AB-106306	10.26°S, 69.31°W	5.97 m/pixel	Chapman and Tanaka 2001
Ius				
MOC	M08-07173	8.10°S, 84.30°W	5.7 m/pixel	Malin and Edgett 2000
Melas				
MOC	R04-01897	11.11°S, 75.45°W	5.96 m/pixel	Montgomery and Gillespie 2005
MOC	R08-00286	10.48°S, 75.77°W	4.48 m/pixel	Montgomery and Gillespie 2005
MOC	R08-00287	10.52°S, 75.40°W	250 m/pixel	Montgomery and Gillespie 2005
Juventae				
MOC	M10-00466	4.58°S, 63.43°W	2.87 m/pixel	Komatsu et al. 2004; Catling et al. 2006
MOC	E22-00455	2.31°S, 62.00°W	6.03 m/pixel	Catling et al. 2006
MOC	R03-00948	4.84°S, 63.50°W	2.87 m/pixel	Catling et al. 2006
MOC	E02-02546	4.15°S, 62.67°W	4.33 m/pixel	Catling et al. 2006
MOC	M11-02064	3.33°S, 62.01°W	1.43 m/pixel	Catling et al. 2006
MOC	E22-01273	2.46°S, 62.28°W	4.53 m/pixel	Catling et al. 2006
MOC	M10-00466	4.58°S, 63.43°W	2.87 m/pixel	Catling et al. 2006
MOC	E23-01035	4.47°S, 62.60°W	3.01 m/pixel	Catling et al. 2006
MOC	M04-00651	3.60°S, 61.98°W	4.3 m/pixel	Catling et al. 2006
MOC	E16-00591	2.37°S, 62.21°W	4.54 m/pixel	Catling et al. 2006
MOC	E11-02581	4.63°S, 63.39°W	3.02 m/pixel	Catling et al. 2006
MOC	E11-01370	4.28°S, 62.55°W	3.02 m/pixel	Catling et al. 2006
MOC	M21-00460	3.42°S, 61.93°W	5.75 m/pixel	Catling et al. 2006
MOC	E16-00591	2.37°S, 62.21°W	4.54 m/pixel	Catling et al. 2006

MOC	R02-00160	4.61°S, 63.30°W	3.01 m/pixel	Catling et al. 2006
MOC	M07-02818	3.37°S, 61.92°W	2.87 m/pixel	Catling et al. 2006
MOC	E14-01770	2.34°S, 62.15°W	3.02 m/pixel	Catling et al. 2006
MOC	E22-00892	2.28°S, 62.15°W	4.52 m/pixel	Catling et al. 2006
MOC	E22-00455	2.31°S, 62.00°W	6.03 m/pixel	Catling et al. 2006
MOC	R15-02329	2.27°S, 62.12°W	4.53 m/pixel	Catling et al. 2006
MOC	M08-04669	2.75°S, 61.70°W	5.74 m/pixel	Catling et al. 2006
MOC	E17-01902	2.85°S, 61.76°W	4.52 m/pixel	Catling et al. 2006
MOC	R05-00012	4.49°S, 64.07°W	3.01 m/pixel	Catling et al. 2006
MOC	R05-01255	4.44°S, 64.12°W	3.01 m/pixel	Catling et al. 2006
HiRISE	PSP_005557_1755	4.69°S, 63.20°W	27.1 cm/pixel	This paper
HiRISE	PSP_003790_1755	4.61°S, 63.10°W	26.7 cm/pixel	This paper
Ophir				
MOC	S04-01271	4.75°S, 73.43°W	3.01 m/pixel	Chojnacki and Hynek 2008

Table 5.3. Images cited in the literature as showing the contact between light-toned deposits and wallrock in Valles Marineris.

5.5.3 Possible causes of deformation

There are several possible mechanisms that could explain the observed deformation features in the strata of Valles Marineris. The salient features which need to be explained are (1) the lateral distribution pattern of deformation, including exposures as large as 1800 km² across spanning ~1000 km of Valles Marineris; (2) the deformational styles, including convolute folds, detached slabs, folded strata and pull apart structures and their gradations, both laterally and vertically, between different styles; (3) fold axis orientations which are largely bimodal with NE-SW and SE-NW orientations; (4) the scale of the deformation features, including km-scale convolute folds and 60 m to 1 km-sized detached slabs; (5) the thickness of the deformed intervals which range up to 350 m; (6) confinement of deformation to discrete stratigraphic intervals that occur at widely different elevations

throughout the Valles Marineris system; and (7) composition of the deformed strata, which includes at least a component of sulfates.

Salt diapirism has been previously invoked to explain the folding in Candor and Melas Chasma (Beyer et al. 2000; Milliken et al 2007) . However, subsequent examination of new localities showed that undeformed strata are found directly beneath the folds in several areas in Candor and Melas and suggests that this mechanism is not consistent with all observations. Deformation caused by salt diapirism should show evidence of vertical motions, but the deformation observed in Valles Marineris does not show this, and where the orientations of fold axes can be measured, they are found to dip shallowly, consistent with subhorizontal shear. Due to this evidence, we will not consider salt diapirism any further.

Alternative mechanisms that may explain many of the observed features include liquefaction, landsliding, and gravity gliding.

5.5.3.1 Liquefaction

Liquefaction occurs when metastable, loosely packed grains become temporarily suspended in their pore fluid, and the drag exerted from the moving pore fluid exceeds the weight of the grains, lifting the grains and destroying the framework; this reduces the sediment strength to nearly zero (Lowe 1975). Liquefaction arises in unconsolidated sediments either before or soon after burial (Fernandes et al. 2007). On Earth, liquefaction is often triggered by seismic shaking associated with surface waves generated by large

earthquakes; the deformed deposits that result are called "seismites" (Seilacher 1969). Seismic induced liquefaction typically occurs when a liquefiable sand layer is overlain by a thin, nonliquefiable stratum and the water table is shallow; this causes the pore fluid pressure to increase (Obermeier 1996). Other factors that increase the susceptibility of sediments to liquefaction include: (1) recent deposition; (2) rapid deposition; (3) water-saturation; (4) presence of homogenous fine-grained sediment; (4) shallow-burial; and (5) absence of cements (Allen 1986; Montenat et al. 2007). Sediments are commonly undeformed below the seismites, since these sediments have already been consolidated or cemented and are no longer susceptible to liquefaction (Pope et al. 1997).

Criteria that are used to recognize seismites include (1) restriction of deformation to a stratigraphic interval separated by undeformed beds; (2) occurrence in potentially liquefiable sediments; (3) zones of structures correlatable over large areas; and (4) presence of structures that suggest liquefaction (Sims 1975). The deformation observed in Valles Marineris meets many of the criteria used to recognize seismites. The deformation is confined to a discrete interval with undeformed overlying and underlying beds. The deformation occurs over a large area and the deformational structures are consistent with those commonly reported to form from liquefaction. Seismites show a variety of deformational features including: ball-and-pillow structures, convoluted folded strata, sand blows, sand dikes, sedimentary breccias, homogenized beds, pull-apart structures, and slumps and slides (Davenport and Ringrose 1987; Roep and Everts 1992; Mohindra and Bagati 1996; Pope et al. 1997; Rodríguez-Pascua et al. 2000; Fernandes et al. 2007; Montenat et al. 2007). Earthquakes can cause strata to fail and shear on gently inclined

slopes as low as 0.1-5% causing separation between individual slide blocks of as much as several meters (Obermeier 1996). The deformational structures observed in Valles Marineris are similar to many of those reported in seismites on Earth, such as convolute folded strata, detached slabs and pull-apart structures. The variation in seismite types is thought to be related to the stage of lithification, sediment characteristics and lithostatic pressure (Roep and Everts 1992; Monentat et al. 2007). The style of deformation can be seen to vary laterally in seismites, as is also observed in the deformation in Valles Marineris (Mohindra and Thakur 1998).

The cyclic shaking required to cause liquefaction is a horizontal acceleration of at least $0.1 \times g$, and features caused by earthquake-induced liquefaction have been observed to occur from earthquakes greater than magnitude 5.5 (Obermeier 1996). The distance at which liquefaction features have been observed to occur from earthquakes of various magnitudes has been recorded. From Allen (1986) the relationship between earthquake magnitude (M) and distance (X) is

$$M = 0.499 \ln \left(\frac{X}{3.162 \times 10^{-5}} \right) \quad (1)$$

Because the deformation that we observe in Valles Marineris occurred across a distance of 1180 km, this implies that if this deformation was caused by earthquake-induced liquefaction then the 'marsquake' may have been at least magnitude 8.7, subject to the caveat that the effect of different crustal properties of Mars on this empirical relation is unknown. Another possibility is that the liquefaction was not caused by a marsquake, but by seismic energy generated from an impact event. Several seismites on Earth are suggested to have been induced from impact events, including deformation in the Carmel

Formation and Slickrock Member of the Entrada Sandstone in southeastern Utah (Alvarez et al. 1998); in the Cotham Member of Penarth Group in the United Kingdom (Simms 2003); and in the Alamo breccia in southern Nevada (French 2004). The Cretaceous-Tertiary impact is suggested to have generated a magnitude 13 earthquake which could have deformed unlithified sediments over several thousand kilometers (Collins et al. 2005). If an impactor was the source of the seismic energy that caused the deformation in Valles Marineris, it would likely have been at least 3 km in size to generate magnitude 8.7 marsquakes (calculated using Impact Effects Program from Collins et al. 2005). The crater formed by this impact would be about 36 km in size. There are several impact craters of this size or larger surrounding central Valles Marineris.

On Earth, liquefaction caused by earthquakes commonly arises at a depth ranging from a few meters to about 15 m and becomes increasingly difficult at depth; this is because the vertical stress applied by the overburden increases the resistance of the sediment to shearing and deformation (Obermeier 1996). The thickness of deformed sediments is thus limited by the maximum depth of sediments susceptible to liquefaction at the time of the earthquake (Simms 2003). On Earth, seismites are typically on the order of tens of centimeters to ten meters thick (Roep and Everts 1992, Mohindra and Bagati 1996, Pope et al. 1997, Mohindra and Thakur 1998, Jones and Omoto 2000, Rodríguez-Pascua et al. 2000, Simms 2003, Fernandes et al. 2007). This contrasts with the exposures of deformed beds in Valles Marineris which are up to 350 m thick. If these are seismites, it would require that sediments compact and lithify much more slowly on Mars. Sediments may not compact as easily on Mars due to the lower gravity; the mass of overburden would need to be about a third larger in order to have a similar weight of overburden with depth as

on Earth. If seismites are indeed up to 350 m thick on Mars, it may also imply that cementation occurs more slowly there than on Earth. The degree of lithification would be lower if water in groundwater systems on Mars was less abundant on average than in groundwater systems on Earth. This is consistent with the evidence of incomplete lithification of the rocks observed in Meridiani Planum (McLennan et al. 2005).

Another challenge to interpreting the deformation in Valles Marineris as seismites is that the wavelength of folds in seismites on Earth is typically tens of centimeters to a couple of meters. The wavelength of folding observed on Mars is ~50 m to a kilometer. The factors controlling the wavelength of folding in seismites on Earth are uncertain, but Rodríguez-Pascua et al. (2000) suggest that folding is the result of the upward flow of liquefied sand at more or less regularly spaced sites. The wavelength may also depend on the thickness of the deforming layer or on the amplitude of the seismic waves. Pope et al. (1997) found that the fold axes of seismites were randomly oriented, although Simms (2003) found seismite fold axes had a strong preferred orientation. Simms (2003) suggests the preferred fold axes orientations are perpendicular to the direction of travel of seismic waves. Rodríguez-Pascua et al. (2000) observed that the axes of seismite convolute folds were bimodal with the two directions roughly perpendicular to each other. They suggest this is related to the directions of maximum compression and maximum stress from the paleostress ellipse.

Overall, many of the properties of the deformed sediments observed in Valles Marineris fit with a seismite interpretation. The observation of the deformation covering a broad region, the styles of deformation, and the confinement of the deformation to discrete intervals all fit well with an interpretation as seismites. However, the thickness of the

deformed interval may be difficult to achieve in seismites and would imply an unusually thick stack of unlithified sediments on Mars. This would imply lithification occurred more slowly on Mars. The scale of the folding and the orientations of the fold axes are not well understood on Earth, and thus evaluating these constraints on Mars is difficult.

5.5.3.2 Landslides

Landslide deposits are common in Valles Marineris and represent some of the youngest geologic activity in this area (Late Hesperian to Amazonian) (Harrison and Grimm 2003; Quantin et al. 2004). These landslides were originally thought to be wet debris flows because of their long runout distances (Lucchitta 1979; Lucchitta 1987). However, recent work has suggested the role of interstitial fluid was negligible, and the runout distances are consistent with dry terrestrial landslides (McEwen 1989; Lajeunesse et al. 2006; Soukhovitskaya and Manga 2006). The morphology of these landslides includes slump blocks at the head, hummocky material farther out, and a vast apron of longitudinally ridged material extending to the toe (Lucchitta 1978).

Landslides are also suggested to have occurred at much earlier times in Valles Marineris. Okubo et al. (2008) suggests that folded strata in southwestern Candor Chasma are the result of a subaerial or subaqueous landslide that has been eroded such that the characteristic surface morphology is no longer present. They suggest that the folds reflect compression at the toe of a southward directed slide/slump from the nearby ILD. It has also been suggested that the detached slabs in Melas Chasma may be the result of landsliding (Skilling et al. 2002; Weitz et al. 2003).

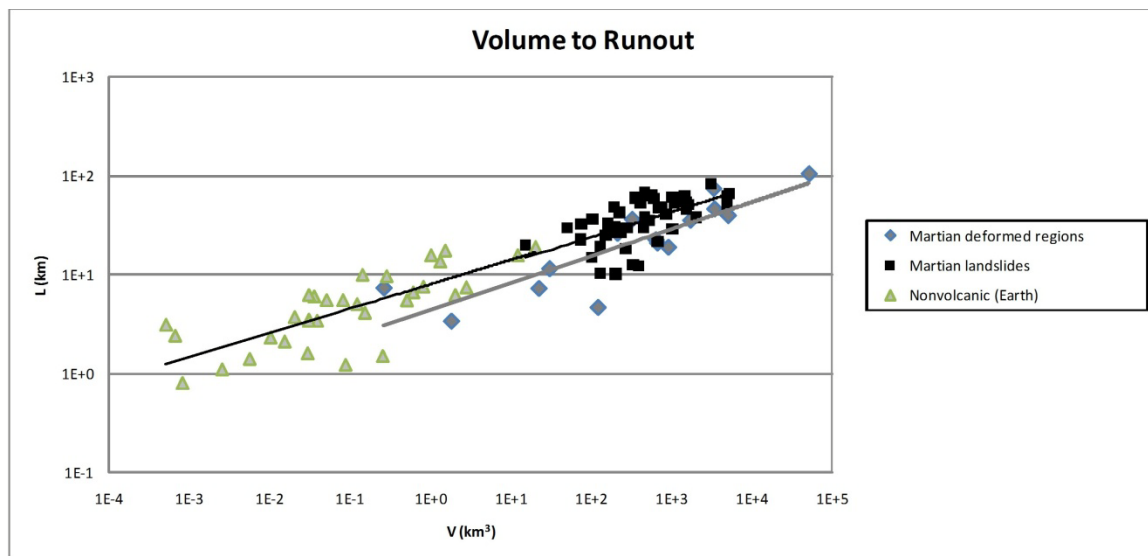


Fig 5.19. Plot showing landslide volume (V) on horizontal axis in km^3 and landslide runout (L) on vertical axis in km. Data for Martian landslides is taken from Quantin et al. 2004 (squares) and for terrestrial nonvolcanic landslides from Hayashi and Self 1992 (triangles). The volume to runout of the Martian deformed regions are from this study (diamonds).

Interpreting the deformed strata observed in Valles Marineris as the result of ancient landsliding does fit with the limited stratigraphic extent observed for the deformed strata. One would expect the beds stratigraphically below a landslide unit to be undeformed, because beds below the detachment surface of a landslide as well as beds below the surface over which the landslide runs out are not affected by the slide. The beds above a landslide deposit should also be undeformed, because they are deposited after the landslide occurs. The strata both underlying and overlying the deformed beds are undisturbed in Valles Marineris, as expected for a landslide origin. This interpretation also fits with the variety of elevations in which the deformation is observed to occur, because landslides could occur at any elevations in the chasma. The large size of the deformed units is also possible for landslide deposits. Fig. 5.19 shows the runout distance versus

volume for recent Martian landslides, terrestrial nonvolcanic landslides, and the deformed units observed in Valles Marineris. The recent Martian landslides fit along the same trend as the terrestrial nonvolcanic landslides. The deformed regions in Valles Marineris fall close to the range of volume versus runout measurements from recent Martian landslides, although not along the same trend. The length for the deformed regions is actually the length of the deposit, not the runout length, because headscarp source regions for these deposits are not observed. Thus, if this deformation is the result of landsliding, the runout lengths would be expected to be longer than the values presented in Fig. 19, which would shift the fit for the deformed regions closer to the other Martian landslides.

The variety of deformational morphologies observed in Valles Marineris is also consistent with morphologies observed in large terrestrial submarine landslides (Lucente and Pini 2003; Lucente and Pini 2008). In the Miocene age Casaglia-Monte della Colonna landslide in the Northern Apennines, large detached stratified slabs and many types of folding, including overturned, recumbent, asymmetric, disharmonic, box, and refolded folds are identified (Lucente and Pini 2003). These are similar to the deformational morphologies of the detached slabs and folded strata observed in Valles Marineris. Detached slabs are observed in the upper part of terrestrial submarine slides, and these are commonly composed of undeformed strata but can also have folded strata (Lucente and Pini 2003). The slabs overlie a several meter thick strongly deformed set of beds that show isoclinal folds and overfolds; this unit acted as a shear zone (Lucente and Pini 2003). These characteristics are similar to the observation that detached slabs in Valles Marineris overlie folded strata in several areas in Candor Chasma (region 5) and in Melas Chasma (region 7). Lucente and Pini (2003) also found that the size of the slabs decreases towards

the distal portion of the slide. The sizes of the slabs observed in Candor Chasma do show a decrease in average slab size on the northern and eastern part of the region. In the other regions, the size of the slabs shows no particular trend with location within a particular exposure, although the sizes of the slabs are a bit larger in Melas and a bit smaller in Ius.

The scale of the slabs observed in terrestrial submarine landslides can be hundreds of meters in size (Lucente and Pini 2003), which is of the same order as the slabs observed in Valles Marineris. The wavelength of the folding observed in terrestrial submarine landslide deposits is on the order of fifty centimeters to tens of meters in size (Lucente and Pini 2003), much smaller than the kilometer scale folds observed in Valles Marineris. However, this may in part be due to a sample bias, because it is difficult to observe kilometer scale folds in the terrestrial submarine slides.

Slabs that have an appearance similar to the detached slabs observed in Valles Marineris are also found in very slow landslides and are called 'block spreads'. Block spreads form when a thick layer of rock overlying a softer material fractures and separates due to liquefaction (Cruden and Varnes 1996). Blocks in spreads can be hundreds of meters thick and can occur over wide areas (Cruden and Varnes 1996). This type of feature would not require a body of water, but only enough pore water for liquefaction to be possible.

One of the challenges in interpreting the deformation as the result of landsliding is locating the source for each of the putative slides. The deformed regions in Ius Chasma are not adjacent to ILD, so if these are slides, the source must either be the sides of the chasma walls, or an ILD that has completely eroded away. There are ILD in Candor and Melas Chasma within ~100 km of the deformed units in those chasmata. The deformed strata are

mostly topographically lower than the ILD, which means the ILD may have been able to serve as sources for potential slides. It could also mean that the deformed units are stratigraphically below the ILD and hence older. If the deformed strata were formed by landslides and these slides did originate from the ILD, then one might expect slides to have occurred around multiple sides of the ILD, which is not observed in Melas. One would also expect the orientation of the fold axes to be perpendicular to the direction of slide movement (or parallel to the walls of the ILD, if they were the source for the slides) (Lucente and Pini 2003). Also, some of the deformed strata are found on part of the Ceti Mensa ILD in Candor, so again the sources for these slides are unclear. The slides may have originated from the chasma walls of Valles Marineris, but if that were the case then no remnants of the layered material remains in many of the areas where the slides should have originated. Fold axes are oriented parallel to the chasma walls in many locations which would be expected if they were the source for the slides. However, some exceptions to this do occur and most areas exhibit a second set of fold axes that are perpendicular to the chasma walls. Although some dispersion of fold axes orientations are expected in slides due to rotation of fold hinges and sheath folds, fold axes are not typically bimodal (Lucente and Pini 2003).

Mechanisms that can trigger submarine landslides include volcanic activity; seismic activity, either faulting or impact induced; and fluid overpressurization, which occurs when rapid deposition of low permeability sediments traps pore fluid that cannot escape as the sediment compacts (Flemings et al. 2008; Lucente and Pini 2008). The same triggering mechanisms have been suggested to have caused the Amazonian landslides on Mars

(Quantin et al. 2004; Neuffer and Schultz 2006; Soukhovitskay and Manga 2006) and could have provided a triggering mechanism for potential ancient landslides.

5.5.3.3 Regional gravity gliding

Montgomery et al. (2009) suggest that the patterns of deformation surrounding the Thaumasia Plateau are indicative of a gravity-driven mega-slide. They suggest that extensional deformation in Syria Planum and Noctis Labryinthis connect to zones of transtension and strike-slip in Claritas Fossae and Valles Marineris and to compressional uplift along the Coprates Rise and Thaumasia highlands. They propose that the large-scale thin-skinned gravity spreading would have occurred above a detachment along a buried weak layer of salts or ice. In their model, Valles Marineris reflects extension, collapse, and excavation along fractures radial to Tharsis as part of one lateral margin of the Thaumasia gravity-spreading system. Their model predicts that a décollement or detachment should exist at some depth beneath the Thaumasia plateau. Because Valles Marineris is up to 8 km deep in some locations, this detachment surface might be exposed in some areas. Perhaps the deformation observed in Valles Marineris formed along the detachment surface as a result of shear from gravity gliding. This interpretation presupposes that the sediments exposed on the floor of Valles Marineris are older than the chasma itself.

If the deformation formed as a result of this potential mechanism, then one would expect that the deformation would be confined to a discrete slip surface. This surface need not correspond to a particular elevation and could have a complex 3D geometry. However, given a physically plausible geometry for the detachment, it might be expected to dip to the

east near Syria Planum and dip to the west near the Thaumasia highlands, and the detachment surface might dip to the south at its northern boundary. This predicts that deformation within Valles Marineris would be located within the salt layer and should follow the detachment surface. We do find that the deformed strata in Valles Marineris have a component of salts, both mono- and polyhydrated sulfates, which could fit with the gravity-gliding model. In addition, sulfates should be easily deformed, because they are weak and prone to viscous creep. Deformation caused by gravity gliding should be confined to a limited stratigraphic interval as observed in Valles Marineris, but the elevations of the deformed strata in Valles Marineris do not convincingly delineate a discrete surface as might be expected for gravity gliding (Fig. 5.5).

The deformational morphologies expected from gravity gliding might be similar to a large landslide. Folding would be expected landward of the distal pinchout of the original salt layer as well as at the distal portion of the slide where the compressive stresses are greatest (Rowan et al. 2004). Irregular topography along the initial slide plane could cause convergent and divergent movement and cause broadly arcuate fold belts and dome and basin structures (Rowan et al. 2004). The trend of the folds may be highly variable (Rowan et al. 2004). Detached folds are observed to result from gravity gliding, but refolded folds (which could be indicative of one phase of disharmonic folding, similar to the convolute folds observed in Melas) are not documented (Rowan et al. 2004). The structural style of the folding that results from gravity gliding is highly dependent on the rheology and thickness of the décollement layer as well as the thickness of the overburden (Rowan et al. 2004). Thin overburden generally produces folds with shorter wavelengths and shorter amplitudes (Rowan et al. 2004). The wavelength of folding in Valles Marineris is

somewhat smaller than for folds observed in terrestrial analog gravity glides, which would imply that the overburden on Mars was thinner than typical terrestrial glides. In gravity gliding, features somewhat similar to the detached slabs may result from many fault bounded blocks gliding down the detachment surface (Schultz-Ela 2001). Gravity-gliding would be expected to induce deformation over a broad area and this could explain the large areal exposures of deformation in Valles Marineris.

Overall, gravity gliding does fit several of the observations of deformation in Valles Marineris, including large areal extent of deformation, confinement to discrete stratigraphic interval, and some of the observed morphologies. However, the geometry of the surface defined by the deformation (at different elevations) is not consistent with what a detachment would predict. Also, the details of the deformational morphologies and grading between deformation types have not been described in terrestrial gravity-glide deposits.

6. Conclusions

Four styles of deformation including convolute folds, detached slabs, folded strata, and pull-apart structures were observed in Ius, Candor and Melas Chasmata. The deformed units are on the order of hundreds of meters thick, are underlain and overlain by undeformed strata, and occur in large exposures over broad areas and a wide range in elevation. Fold-axis orientations exhibit a bimodal distribution, with one set oriented NE-SW and another set oriented NW-SE. Visible-near infrared reflectance spectra of the deformed strata are consistent with the presence of a sulfate component, including mono- and polyhydrated varieties.

Overall, liquefaction and landsliding both provide the most parsimonious explanations for the cause of deformation observed in Valles Marineris. The morphology, limited stratigraphic interval, and large aerial distribution of the deformation fit well with liquefaction, but the scale of the features is much larger than similar features observed on Earth. Submarine or slow subaerial landsliding fits with the morphology, limited stratigraphic interval, and scale of the slabs observed in Valles Marineris, but the details of the areal distribution make identifying a source for the slides challenging. It is possible that a combination of liquefaction and landsliding may have been responsible for the formation of these features, possibly induced by local tectonic activity or a large impact. If sediments were deposited fairly rapidly in a submarine setting, then an impact could have triggered liquefaction and submarine landsliding over a broad region in Valles Marineris. Gravity gliding was considered but does not appear to be as good of a fit to the observations as the other mechanisms.

The only mechanism considered that requires the deformed strata to be deformed before the formation of Valles Marineris is gravity gliding, and this mechanism is not a good fit to our observations. If landsliding of ILD mounds was responsible for forming the deformed strata, then this could have occurred anytime after the deposition of the ILD and before the Amazonian landslides which overlie the deformed beds. If the strata deformed as a result of liquefaction, then this would imply the deformation happened soon after deposition of the sediments since liquefaction occurs in water-saturated unlithified sediments.

REFERENCES

- Aharonson, O., M. T. Zuber, and D. H. Rothman (2001), Statistics of Mars' topography from the Mars Orbiter Laser Altimeter: Slopes, correlations, and physical models, *Journal of Geophysical Research*, 106, 23723-23735.
- Ahlbrandt, T. S. ,and S. G. Fryberger (1981), Sedimentary features and significance of interdune deposits, in *Recent and Ancient Non-Marine Depositional Environments: Models for Exploration: SEPM, Special Publication 31*, edited by Flores, R.M. , 293-314.
- Albarède, F., and J. Blichert-Toft, (2007), The split fate of the early Earth, Mars, Venus, and Moon, *Comptes Rendus Geoscience*, 339, 917-927.
- Allen, J. R. L. (1986), Earthquake magnitude-frequency, epicentral distance, and soft-sediment deformation in sedimentary basins, *Sedimentary Geology*, 46, 67-75.
- Allen, P. A. (2008), From landscapes into geological history, *Nature*, 451, 274-276.
- Allison, M. A., S. A. Kuehl, T. C. Martin, A. Hassan (1998), Importance of flood-plain sedimentation for river sediment budgets and terrigenous input to the oceans; insights from the Brahmaputra-Jamuna River *Geology*, 26, 175-178.
- Alvarez, W., E. Staley, D. O'Connor, and M. A. Cham (1998), Synsedimentary deformation in the Jurassic of southeastern Utah- A case of impact shaking?, *Geology*, 26, 579-582.
- Andrews-Hanna, J. C., R. J. Phillips, and M. T. Zuber (2007), Meridiani Planum and the global hydrology of Mars, *Nature*, 446, 163-166.

- Anderton, R. (1976), Tidal-shelf sedimentation: An example from the Scottish Dalradian, *Sedimentology*, *23*, 429-458.
- Are, F., and E. Reimnitz (2000), An overview of the Lena River delta setting: geology, tectonics, geomorphology, and hydrology, *Journal of Coastal Research*, *16*, 1083–1093.
- Arvidson, R. E., F. P. Seelos, K. S. Deal, W. C. Koeppen, N. O. Snider, J. M. Kieniewicz, B. M. Hynek, M. T. Mellon, and J. B. Garvin (2003), Mantled and exhumed terrains in Terra Meridiani, Mars, *Journal of Geophysical Research*, *108*, 8073.
- Arvidson, R. E., R. C. Anderson, P. Bartlett, J. F. Bell, P. R. Christensen, P. Chu, K. Davis, B. L. Ehlmann, M. P. Golombek, S. Gorevan, E. A. Guinness, A. F. C. Haldemann, K. E. Herkenhoff, G. Landis, R. Li, R. Lindemann, D. W. Ming, T. Myrick, T. Parker, L. Richter, F. P. Seelos, L. A. Soderblom, S. W. Squyres, R. J. Sullivan, and J. Wilson (2004), Localization and physical property experiments conducted by opportunity at Meridiani Planum, *Science*, *306*, 1730-1733.
- Arvidson, R. E., F. Poulet, R. V. Morris, J. P. Bibring, J. F. Bell, S. W. Squyres, P. R. Christensen, G. Bellucci, B. Gondet, B. L. Ehlmann, W. H. Farrand, R. L. Fergason, M. Golombek, J. L. Griffes, J. Grotzinger, E. A. Guinness, K. E. Herkenhoff, J. R. Johnson, G. Klingelhöfer, Y. Langevin, D. Ming, K. Seelos, R. J. Sullivan, J. G. Ward, S. M. Wiseman, and M. Wolff (2006), Nature and origin of the hematite-bearing plains of Terra Meridiani based on analyses of orbital and Mars Exploration rover data sets, *Journal of Geophysical Research*, *111*, E12S08, doi:10.1029/2006JE002728.
- Ashley, G. M., J. B. Southard, and J. C. Boothroyd (1982), Deposition of climbing-ripple

- beds: a flume simulation, *Sedimentology*, 29, 67-79.
- Back, S., M. de Batist, P. Kirillov, M. R. Strecker, P. Vanhauwaert (1998), The Frolikha Fan: A large Pleistocene glaciolacustrine outwash fan in northern Lake Baikal, Siberia, *Journal of Sedimentary Research*, 68, 841-849.
- Bagnold, R. A. (1941), *The Physics of Blown Sand and Desert Dunes*, London, Chapman & Hall, 265 p.
- Baker, V. R. (2001), Water and the Martian landscape, *Nature*, 412, 228-236.
- Baker, V. R., (2006), Geomorphological evidence for water on Mars, *Elements*, 2, 139-143.
- Bal, A., and D. W. Lewis (1994), A Cretaceous-early Tertiary macrotidal estuarine-fluvial succession: Puponga Coal Measures in Whanganui Inlet, onshore Pakawau Sub-basin, northwest Nelson, New Zealand, *New Zealand Journal of Geology and Geophysics*, 37, 287.
- Beales, F. W. (1972), Dolomitic mottling in Palliser (Devonian) limestone, Banff and Jasper National Parks, Alberta, in *Carbonate Rocks I: Classifications--Dolomite--Dolomitization*, AAPG Reprint Series no 4.
- Beaubouef, R. T., J. C. Van Wagoner, N. L. Adair (2003), Ultra-High Resolution 3-D Characterization of Deep-Water Deposits-II: Insights into the Evolution of a Submarine Fan and Comparisons with River Deltas, extended abstract *AAPG Annual Meeting*, Salt Lake City, UT.
- Behrmann, J. H., et al. (2006), Rapid Sedimentation, Overpressure, and Focused Fluid Flow, Gulf of Mexico Continental Margin, *Scientific Drilling*, 3, 12-17.
- Bell, J. F., S. W. Squyres, K. E. Herkenhoff, J. N. Maki, H. M. Arneson, D. Brown, S. A. Collins, A. Dingizian, S. T. Elliot, E. C. Hagerott, A. G. Hayes, M. J. Johnson, J. R.

- Johnson, J. Joseph, K. Kinch, M. T. Lemmon, R. V. Morris, L. Scherr, M. Schwochert, M. K. Shepard, G. H. Smith, J. N. Sohl-Dickstein, R. J. Sullivan, W. T. Sullivan, and M. Wadsworth (2003), Mars Exploration Rover Athena Panoramic Camera (Pancam) investigation, *Journal of Geophysical Research*, 108, E12.
- Beyer, R. A., H. J. Melosh, A. McEwen, and R. D. Lorenz (2000), Salt diapirs in Candor Chasma, Mars?, LPSC XXXI abstract, League City, TX.
- Bhattacharya, J. P., and R. G. Walker (1991), River- and wave-dominated depositional systems of the Upper Cretaceous Dunvegan Formation, northwestern Alberta, *Bulletin of Canadian Petroleum Geology*, 39(2), 165-191.
- Bhattacharya, J. P., and R. G. Walker (1992), Deltas, in *Facies Models: A Response to Sea Level Change*, edited by R. G. Walker and N. P. James, pp. 157-177, Geological Association of Canada, Stittsville, Ontario.
- Bhattacharya, J. P., T. H. D. Payenberg, S. C. Lang, and M. C. Bourke (2005), Dynamic river channels suggest a long-lived Noachian crater lake on Mars. *Geophysical Research Letters*, 32, L10201, doi:10.1029/2005GL022747.
- Blair, T. C., and J. G. McPherson (1994a), Alluvial fan processes and forms, in *Geomorphology of Desert Environments*, edited by A. D. Abrahams and A. J. Parsons, pp. 354-402, Chapman & Hall, London.
- Blair, T. C., and J. G. McPherson (1994b), Alluvial fans and their natural distinction from rivers based on morphology and, hydraulic processes, sedimentary processes and facies assemblages, *Journal of Sedimentary Research*, A64, 450-489.
- Blondel, P., and B. J. Murton (1997), *Handbook of Seafloor Sonar Imagery*, Chichester, England, John Wiley & Sons, 314 p.

- Bouma, A. H. (1962), *Sedimentology of Some Flysch Deposits; A Graphic Approach to Facies Interpretation*, 168 pp., Elsevier, Amsterdam.
- Branney, M. J., and P. Kokelaar (2002), *Pyroclastic density currents and the sedimentation of ignimbrites*, Geological Society of London Memoir 27, 143 p.
- Breuer, D., and T. Spohn (2003), Early plate tectonics versus single-plate tectonics on Mars: Evidence from magnetic field history and crust evolution, *Journal of Geophysical Research*, 108, 5072.
- Bristow, C. S. (1993), *Sedimentary structures exposed in bar tops in the Brahmaputra River, Bangladesh*, Geological Society of London Special Publications, 75, 277-289.
- Britter, R. E., and P. F. Linden (1980), The motion of the front of a gravity current traveling down an incline, *Journal of Fluid Mechanics*, 99, 531-543.
- Brookfield, M. E. (1977), Origin of bounding surfaces in ancient aeolian sandstones, *Sedimentology*, 24, 303-332.
- Bullen, S. B., and D. F. Sibley (1984), Dolomite selectivity and mimetic replacement, *Geology*, 12, 655-658.
- Catling, D. C., S. E. Wood, C. Leovy, D. R. Montgomery, H. M. Greenberg, C. R. Glein, and J. M. Moore (2006), Light-toned layered deposits in Juventae Chasma, Mars, *Icarus*, 181, 26-51, doi:10.1016/j.icarus.2005.10.020.
- Chakraborty, C., and P. K. Bose (1992), Ripple/dune to upper stage plane bed transition: some observations from the ancient record, *Geological Journal*, 27, 349-359.
- Chapman, M. G., and K. L. Tanaka (2001), Interior trough deposits on Mars: Subice volcanoes?, *Journal of Geophysical Research*, 106, 10087-10100.

- Cheel, R. J., and G. V. Middleton (1986), Horizontal laminae formed under upper flow regime plane bed conditions, *Journal of Geology*, *94*, 489-504.
- Chojnacki, M., and B. M. Hynek (2008), Geological context of water-altered minerals in Valles Marineris, Mars, *Journal of Geophysical Research*, *113*, E12005, doi:10.1029/2007JE003070.
- Christensen, P. R., J. L. Bandfield, R. N. Clark, K. S. Edgett, V. E. Hamilton, T. Hoefen, H. H. Kieffer, R. O. Kuzmin, M. D. Lane, M. C. Malin, R. V. Morris, J. C. Pearl, R. Pearson, T. L. Roush, S. W. Ruff, and M. D. Smith (2000), Detection of crystalline hematite mineralization on Mars by the Thermal Emission Spectrometer: Evidence for near-surface water, *Journal of Geophysical Research*, *105*, 9623-9642.
- Clark, B. C., R. V. Morris, S. M. McLennan, R. Gellert, B. Joliff, A. H. Knoll, S. W. Squyres, T. K. Lowenstein, D. W. Ming, N. J. Tosca, A. Yen, P. R. Christensen, S. Gorevan, J. Bruckner, W. Calvin, G. Dreibus, W. Farand, G. Klingelhöfer, H. Waenke, J. Zipfel, J. F. Bell, J. P. Grotzinger, H. Y. McSween, and R. Rieder (2005), Chemistry and mineralogy of outcrops at Meridiani Planum, *Earth and Planetary Science Letters*, *240*, 73-94.
- Clark, J. D., N. H. Kenyon, K. T. Pickering (1992), Quantitative analysis of the geometry of submarine channels: Implications for the classification of submarine fans, *Geology*, *20*, 633-636.
- Clark, J. D., and K. T. Pickering, (1996), Architectural elements and growth patterns of submarine channels: Applications to hydrocarbon exploration. *AAPG Bulletin*, *80*, 194-221.
- Clemmensen, L. B., H. Olsen, and R. C. Blakey (1989), Erg-margin deposits in the Lower

Jurassic Moenave Formation, Wingate Sandstone, south Utah, *GSA Bulletin*, 101, 759-773.

Coleman, J. M., and L. D. Wright (1975), Modern river deltas: Variability of processes and sand bodies, in *Deltas: Models for exploration*, edited by M. L. Broussard, Houston Geological Society, Houston, 99-149.

Coleman, J. M., D. B. Prior, J. F. Lindsay (1983), Deltaic influences on shelf-edge instability processes, in *The Shelfbreak: Critical Interface on Continental Margins*, edited by D. J. Stanley and G. T. Moore, Society of Economic Paleontologists and Mineralogists, Tulsa, 121-137.

Collins, G. S., H. J. Melosh, and R. A. Marcus (2005), Earth impact effects program: A web-based computer program for calculating the regional environmental consequences of a meteoroid impact on Earth, *Meteoritics & Planetary Science*, 40, 817-840.

Covault, J. A., W. R. Normark, B. W. Romans, S. A. Graham (2007), Highstand fans in the California borderland: The overlooked deep-water depositional systems, *Geology*, 35, 783-786.

Cruden, D. M., and D. J. Varnes, (1996), Landslide types and processes, in *Landslides: Investigation and Mitigation*, edited by Turner, A.K., and Schuster, R.L., Special Report 247, Washington, DC, National Academy Press, 36-75.

Dalrymple, R. W. (1992), Tidal depositional systems, in *Facies Models: Geological Society of Canada*, edited by R. G. Walker and N. P. James, N.P., St. John's, 195-218.

- Damuth, J. E., V. Kolla, R. D. Flood, R. O. Kowsmann, M. C. Monteiro, M. Gorini, J. J. C. Palma, R. H. Belderson (1983a), Distributary channel meandering and bifurcation patterns on the Amazon deep-sea fan as revealed by long-range side-scan sonar (GLORIA). *Geology*, *11*, 94-98.
- Damuth, J. E., R. O. Kowsmann, R. D. Flood, R. H. Belderson, M. A. Gorini (1983b), Age relationships of distributary channels on Amazon deep-sea fan: Implications for fan growth pattern, *Geology*, *11*, 470-473.
- Damuth, J. E., and R. D. Flood (1984), Morphology, sedimentation processes, and growth pattern of the Amazon deep-sea fan, *Geo-Marine Letters*, *3*, 109-117.
- Dardis, G. F. (1985), Genesis of Late Pleistocene cross-valley moraine ridges, south-central Ulster, Northern Ireland, *Earth Surface Processes and Landforms*, *10*, 483-495.
- Dasgupta, P. (2003), Sediment gravity flow- the conceptual problems, *Earth-Science Reviews*, *62*, 265-281.
- Davenport, C. A., and P. S. Ringrose (1987), Deformation of Scottish Quaternary sediment sequences by strong earthquake motions, in *Deformation of Sediments and Sedimentary Rocks*, edited by M. E. Jones, and R. M. F. Preston, Geological Society Special Publication No. 29, 299-314.
- Davis, D. M., and T. Engelder, (1985), The role of salt in fold and thrust belts, *Tectonophysics*, *119*, 67-88.
- de Meer, S., and C. J. Spiers, (1995), Creep of wet gypsum aggregates under hydrostatic loading conditions, *Tectonophysics*, *245*, 171-183.
- De Pater, I., and J. J. Lissauer (2001), *Planetary Sciences*, Cambridge University Press, Cambridge, U. K., 568 p.

- Demicco, R. V., and L. Hardie (1994), *Sedimentary Structures and Early Diagenetic Features of Shallow Marine Carbonate Deposits*, SEPM, Atlas, v. 1.
- Deptuck, M. E., Z. Sylvester, C. Pirmez, and C. O'Byrne, (2007), Migration-aggradation history and 3-D seismic geomorphology of submarine channels in the Pleistocene Benin-major Canyon, western Niger Delta slope. *Marine and Petroleum Geology*, 24, 406-433.
- Dickson, J. L., J. W. Head, M. Kreslavsky (2007), Martian gullies in the southern mid-latitudes of Mars: Evidence for climate-controlled formation of young fluvial features based upon local and global topography, *Icarus*, 188, 315-323.
- Dietrich, W. E. and P. J. Whiting (1989), Boundary shear stress and sediment transport in river meanders of sand and gravel, in *River Meandering*, edited by K. Ikeda and G. Parker, American Geophysical Union Water Resources Monograph 12, 1-50.
- Dromart, G., C. Quantin, O. Broucke (2007), Stratigraphic architectures spotted in southern Melas Chasma, Valles Marineris, Mars, *Geology*, 35, 363-366.
- Droz, L., R. Kergoat, P. Cochonat, S. Berné (2001), Recent sedimentary events in the western Gulf of Lions (western Mediterranean), *Marine Geology*, 176, 23-37.
- Droz, L., A. T. dos Reis, M. Rabineau, S. Berne, G. Bellaiche (2006), Quaternary turbidite systems on the northern margins of the Balearic Basin (Western Mediterranean): a synthesis, *Geo-Marine Letters*, 26, 347-359.
- Edgett, K. (2005), The sedimentary rocks of Sinus Meridiani: Five key observations from data acquired by the Mars Global Surveyor and Mars Odyssey orbiters, *Mars*, 1, 5-58.
- Edgett, K. S., and M. C. Malin (2002), Martian sedimentary rock stratigraphy: Outcrops

and interbedded craters of northwest Sinus Meridiani and southwest Arabia Terra,
Geophysical Research Letters, 29, 2179.

Edmonds, D. A., and R. L. Slingerland, (2007), Mechanics of river mouth bar formation: Implications for the morphodynamics of delta distributary networks, *Journal of Geophysical Research*, 112, F02034, doi:10.1029/2006JF000574.

Edmonds, D. A., D. C. J. D. Hoyal, B. A. Sheets, and R. L. Slingerland (2009), Predicting avulsions: Implications for coastal wetland restoration, *Geology*, 37, 759-762, doi: 10.1130/G25743A.

EEZ-SCAN Scientific Staff (1991), Atlas of the U.S. Exclusive Economic Zone, Bering Sea: U.S. Geological Survey Miscellaneous Investigations, I-2053, 145 p.

Ehlmann, B. L., J. Mustard, C. I. Fassett, S. C. Schon, J. W. Head, D. J. Des Marais, J. Grant, S. Murchie (2008), Clay minerals in delta deposits and organic preservation potential on Mars, *Nature Geoscience*, 1, 355-358.

Fassett, C. I., and J. W. Head (2005), Fluvial sedimentary deposits on Mars: Ancient deltas in a crater lake in the Nili Fossae region, *Geophysical Research Letters*, 32, L14201, doi:10.1029/2005GL023456.

Fernandes, L. A., A. B. de Castro, and G. Basilici (2007), Seismites in continental sand sea deposits of the Late Cretaceous Caiua Desert Bauru Basin, Brazil, *Sedimentary Geology*, 199, 51-64.

Fischer, A. G. (1964), The Lofer Cyclothems of the Alpine Triassic, in *Symposium on Cyclic Sedimentation*, edited by D. F. Merriam, Kansas State Geological Survey, Bulletin 169, 107-149.

- Flauhaut, J., C. Quantin, P. Allemand, and P. Thomas, *In Press*, Morphology and geology of the ILD in Capri/Eos Chasma (Mars) from visible and infra-red data, *Icarus*, 10.1016/j.icarus.2009.11.019.
- Flemings, P. B., and J. P. Grotzinger (1996), STRATA: Freeware for analyzing classic stratigraphic problems *GSA Today*, 6, 1-7.
- Flemings, P. B., H. Long, B. Dugan, J. Germaine, C. M. John, J. H. Behrmann, D. Sawyer, and I. E. Scientists (2008), Erratum to "Pore pressure penetrometers document high overpressure near the seafloor where multiple submarine landslides have occurred on the continental slope, offshore Louisiana, Gulf of Mexico", *Earth and Planetary Science Letters*, 274, 269-283, 10.1016/j.epsl.2008.06.027.
- Flood, R. D., and J. E. Damuth (1987), Quantitative characteristics of sinuous distributary channels on the Amazon Seep-Sea Fan, *GSA Bulletin*, 98, 728-739.
- Frederiksen, K. S., L. B. Clemmensen, H. S. Lawaetz (1998), Sequential architecture and cyclicity in Permian desert deposits, Brodick Beds, Arran, Scotland, *Journal of the Geological Society of London*, 155, 677-683.
- French, B. M. (2004), The importance of being cratered: The new role of meteorite impact as a normal geological process, *Meteoritics & Planetary Science*, 39, 169-197.
- Fryberger, S. G., and C. J. Schenk (1988), Pin stripe lamination - a distinctive feature of modern and ancient eolian sediments, *Sedimentary Geology*, 55, 1-15.
- Fryberger, S. G., T. S. Ahlbrandt, and S. Andrews (1979), Origin, sedimentary features, and significance of low-angle eolian "sand sheet" deposits, Great Sand Dunes National Monument and vicinity, Colorado, *Journal of Sedimentary Petrology*, 49, 733-746.

- Fryberger, S. G., A. M. Al-Sari, and T. J. Clishamp (1983), Eolian dune, interdune, sand sheet and siliciclastic sabkha sediments of an offshore prograding sand sea, Dhahran Area, Saudi Arabia, *AAPG Bulletin*, 67, 280-312.
- Fuete, F., R. Stesky, P. MacKinnon, E. Hauber, K. Gwinner, F. Scholten, T. Zegers, G. Neukum (2006), A structural study of an interior layered deposit in southwestern Candor Chasma, Valles Marineris, Mars, using high resolution stereo camera data from Mars Express, *Geophysical Research Letters*, 33, L07202, doi:10.1029/2005GL025035.
- Fuete, F., R. Stesky, P. MacKinnon, E. Hauber, T. Zegers, K. Gwinner, F. Scholten, and G. Neukum (2008), Stratigraphy and structure of interior layered deposits in west Candor Chasma, Mars, from High Resolution Stereo Camera (HRSC) stereo imagery and derived elevations, *Journal of Geophysical Research*, 113, E10008, doi:10.1029/2007JE003053.
- Galloway, W. E. (1975), Process framework for describing the morphologic and stratigraphic evolution of deltaic depositional systems, in *Deltas: Models for Exploration*, edited by M. L. Broussard, Houston Geological Society, Houston.
- Gardner, J. V., M. E. Field, H. Lee, and B. E. Edwards (1991), Ground-truthing 6.5-kHz side scan sonographs: What are we really imaging? *Journal of Geophysical Research*, 96, 5955-5974.
- Gardner, J. V. (2007), Law of the Sea Mapping Program, http://www.ccom-jhc.unh.edu/index.php?p=39|46&page=law_of_the_sea.php, edited.
- Glotch, T. D., and P. R. Christensen (2005), Geologic and mineralogic mapping of Aram Chaos: Evidence for a water-rich history, *Journal of Geophysical Research*, 110.

E09006, doi:10.1029/2004JE002389.

- Goodbred, S. L., and S. A. Kuehl (1998), Floodplain processes in the Bengal Basin and the storage of Ganges–Brahmaputra river sediment: an accretion study using ^{137}Cs and ^{210}Pb geochronology *Sedimentary Geology*, *121*, 239-258.
- Grant, J. A., R. P. Irwin, J. P. Grotzinger, R. E. Milliken, L. L. Tornabene, A. S. McEwen, C. M. Weitz, S. W. Squyres, T. D. Glotch, B. J. Thomson (2008), HiRISE imaging of impact megabreccia and sub-meter aqueous strata in Holden Crater, Mars, *Geology*, *36*, 195-198.
- Griffes, J. L., J. P. Grotzinger, and R. E. Milliken (2010), Working towards a classification scheme for sedimentary rocks on Mars, Lunar and Planetary Science Conference, abstract, Woodlands, TX.
- Grotzinger, J. P., R. E. Arvidson, J. F. Bell, W. Calvin, B. C. Clark, D. A. Fike, M. Golombek, R. Greeley, A. Haldemann, K. E. Herkenhoff, B. L. Jolliff, A. H. Knoll, M. Malin, S. M. McLennan, T. Parker, L. Soderblom, J. N. Sohl-Dickstein, S. W. Squyres, N. J. Tosca, and W. A. Watters (2005), Stratigraphy and sedimentology of a dry to wet eolian depositional system, Burns formation, Meridiani Planum, Mars, *Earth and Planetary Science Letters*, *240*, 11-72.
- Grotzinger, J. P., J. Bell, K. Herkenhoff, J. Johnson, A. Knoll, E. McCartney, S. McLennan, J. Metz, J. Moore, S. Squyres, R. Sullivan, A. Aharonson, R. Arvidson, B. Jolliff, M. Golombek, K. Lewis, T. Parker, and L. Soderblom (2006), Sedimentary textures formed by aqueous processes, Erebus crater, Meridiani Planum, Mars, *Geology*, *34*, 1085-1088.

- Hamelin, N., H. Racher, F. Fueten, R. Stesky, P. MacKinnon, E. Hauber, K. Gwinner, F. Scholten, and T. Zegers, (2008), Structural analysis of an interior layered deposit in northern Coprates Chasma, Mars, Lunar and Planetary Science Conference XXXIX, Abstract 1424, Woodlands, TX.
- Harrison, K. P., and R. E. Grimm (2003), Rheological constraints on Martian landslides, *Icarus*, 163, 347–362.
- Hartmann, W. K. (2005), Martian cratering 8: Isochron refinement and the chronology of Mars, *Icarus*, 174, 294-320.
- Harvey, A. M. (1984), Debris flow and fluvial deposits in Spanish Quaternary alluvial fans: Implications for fan morphology, in *Sedimentology of Gravels and Conglomerates, Memoir 10*, edited by E. H. Koster and R. J. Steel, Canadian Society of Petroleum Geologists, Calgary, 123-132.
- Harvey, A. M. A. E. Mather, M. Stokes (2005), Alluvial fans: geomorphology, sedimentology, dynamics, *Geological Society of London, Special Publications 251*, 1-7.
- Hashimoto, A., T. Oguchi, Y. Hayakawa, Z. Lin, K. Saito, T. A. Wasklewicz (2008), GIS analysis of depositional slope change at alluvial-fan toes in Japan and the American Southwest, *Geomorphology*, 100, 120-130.
- Hauber, E., K. Gwinner, A. Gendrin, F. Fueten, R. Stesky, S. M. Pelkey, H. Wulf, D. Reiss, T. Zegers, P. MacKinnon, G. Michael, R. Jaumann, J. P. Bibring, G. Neukum, and H. C. -I. Team (2006), An integrated study of interior layered deposits in Hebes Chasma, Valles Marineris, Mars, using MGS, MO and MEX data, Lunar and Planetary Science Conference XXXVII, Abstract 2022, League City, TX.

- Hayashi, J. N., and S. Self (1992), A comparison of pyroelastic flow and debris avalanche mobility, *Journal of Geophysical Research*, 97, 9063-9071.
- Head, J. W., D. R. Marchant, M. C. Agnew, C. I. Fassett, and M. A. Kreslavsky (2006), Extensive valley glacier deposits in the northern mid-latitudes of Mars: Evidence for Late Amazonian obliquity-driven climate change, *Earth and Planetary Science Letters*, 241, 663-671.
- Heard, H. C., and W. M. Rubey (1966), Tectonic implications of gypsum dehydration, *GSA Bulletin*, 77, 741-760.
- Heldmann, J. L., E. Carlsson, H. Johansson, M. T. Mellon, O. B. Toon (2007), Observations of Martian gullies and constraints on potential formation mechanisms II. The northern hemisphere, *Icarus*, 188, 324-344.
- Herman, A. K., P. R. Carlson, J. V. Gardner (1996), Aleutian Basin of the Bering Sea: Styles of sedimentation and canyon development, in *Geology of the United States Seafloor: The view from GORIA*, edited by J. V. Gardner, et al., Cambridge University Press, Cambridge, 305-332.
- Hernandez-Molina, F. J., E. Llave, D. A. V. Stow, M. Garcia, L. Somoza, J. T. Vazquez, F. J. Lobof, A. Maestrob, V. Diaz del Rio, R. Leonb, T. Medialdeab, J. Gardnerh (2006), The contourite depositional system of the Gulf of Ca'diz: A sedimentary model related to the bottom current activity of the Mediterranean outflow water and its interaction with the continental margin, *Deep-Sea Research II*, 53, 1420-1463.
- Hodgson, D. M., S. S. Flint, D. Hodgetts, N. J. Drinkwater, E. P. Johannessen, S. M. Luthi (2006), Stratigraphic evolution of fine-grained submarine fan systems, Tanqua Depocenter, Karoo Basin, South Africa, *Journal of Sedimentary Research*, 76, 20-

40.

- Hummel, G., and G. Kocurek (1984), Interdune areas of the back-island dune field, North Padre Island, Texas, *Sedimentary Geology*, 39, 1-26.
- Hunter, R. E. (1977a), Basic types of stratification in small eolian dunes, *Sedimentology*, 24, 361-387.
- Hunter, R. E. (1977b), Terminology of cross-stratified sedimentary layers and climbing-ripple structures, *Journal of Sedimentary Petrology*, 47, 697-706.
- Hunter, R. E. (1981), Stratification styles in eolian sandstones: some Pennsylvanian to Jurassic examples from the western interior U.S.A., in *Recent and Ancient Nonmarine Depositional Environments: Models for Exploration*, edited by F. G. Ethridge, and R. M. Flores, SEPM, Special Publication 31, 315-329.
- Hynek, B. M. (2004), Implications for hydrologic processes on Mars from extensive bedrock outcrops throughout Terra Meridiani, *Nature*, 431, 156-159.
- Jackson, B. A. (2004), Seismic evidence for gas hydrates in the North Makassar Basin, Indonesia, *Petroleum Geoscience*, 10, 227-238.
- Jackson, M. P. A., and C. J. Talbot (1986), External shapes, strain rates, and dynamics of salt structures, *GSA Bulletin.*, 97, 305-323.
- Jerolmack, D. J., D. Mohrig, M. T. Zuber, S. Byrne (2004), A minimum time for the formation of Holden Northeast fan, Mars, *Geophysical Research Letters*, 31, L21701, doi:10.1029/2004GL021326.
- Jerolmack, D. J., D. Mohrig, J. P. Grotzinger, D. A. Fike, and W. A. Watters (2006), Spatial grain size sorting in eolian ripples and estimation of wind conditions on planetary surfaces: Application to Meridiani Planum, Mars, *Journal of Geophysical*

- Research*, 111, E12S02, doi:10.1029/2005JE002544.
- Jerolmack, D., and D. Mohrig (2007), Conditions for branching in depositional rivers, *Geology*, 35, 463-466, doi: 10.1130/G23308A.1.
- Johnson, K. S. (2005), Subsidence hazards due to evaporite dissolution in the United States, *Environmental Geology*, 48, 395-409.
- Jones, A. P., and K. Omoto (2000), Towards establishing criteria for identifying trigger mechanisms for soft-sediment deformation: a case study of Late Pleistocene lacustrine sands and clays, Onikobe and Nakayamadaira Basins, northeastern Japan, *Sedimentology*, 47, 1211-1226.
- Jones, G. H. S. (1978), Coherently overturned flaps surrounding craters, *Nature*, 273, 211-213.
- Kane, I. A., W. D. McCaffrey, J. Peakall (2008), Controls on sinuosity evolution within submarine channels, *Geology*, 36(4), 287-290.
- Karl, H. A., M. A. Hampton, N. H. Kenyon (1989), Lateral migration of Cascadia deep-sea channel in response to accretionary tectonics, *Geology*, 17, 144-147.
- Kenyon, N. H., and J. Millington (1995), Contrasting deep-sea depositional systems in the Bering Sea., in *Atlas of deep water environments: architectural style in turbidite systems*, edited by K. T. Pickering, et al., Chapman and Hall, London, 196–202.
- Kirk, R. L., E. Howington-Krause, M. R. Rosiek, J. A. Anderson, B. A. Archinal, K. J. Becker, D. A. Cook, D. M. Galuszka, P. E. Giessler, T. M. Hare, I. M. Holmberg, L. P. Keszthelyi, B. L. Redding, W. A. Delamere, D. Gallagher, J. D. Chapel, E. M. Eliason, R. King, and A. S. McEwen (2008), Ultrahigh resolution topographic mapping of Mars with MRO HiRISE stereo images: Meter-scale slopes of

- candidate Phoenix landing sites, *Journal of Geophysical Research*, *113*, E00A24, doi: 10.1029/2007JE003000.
- Klaucke, I., D. G. Masson, N. H. Kenyon, J. V. Gardner (2004), Sedimentary processes of the lower Monterey Fan channel and channel-mouth lobe, *Marine Geology*, *206*, 181-198.
- Knauth, L. P., D. M. Burt, and K. H. Wohletz (2005), Impact origin of sediments at the opportunity landing site on Mars, *Nature*, *438*, 1123-1128.
- Kneller, B. C., and C. Buckee (2000), The structure and fluid mechanics of turbidity currents: a review of some recent studies and their geological implications, *Sedimentology*, *47*, 62-94.
- Knoll, A., B. Joliff, W. Farrand, J. Bell, B. Clark, R. Gellert, M. Golombek, J. Grotzinger, K. Herkenhoff, J. Johnson, S. McLennan, R. Morris, S. Squyres, R. Sullivan, N. Tosca, A. Yen, and Z. Learner (2008), Veneers, Rinds, and Fracture Fills: Relatively Late Alteration of Sedimentary Rocks at Meridiani Planum, Mars, *Journal of Geophysical Research*, *113*, E06S16, doi:10.1029/2007JE002949.
- Kocurek, G. (1981), Significance of interdune deposits and bounding surfaces in aeolian dune sands, *Sedimentology*, *28*, 753-780.
- Kocurek, G. (1991), Interpretation of ancient eolian sand dunes, *Annual Reviews of Earth and Planetary Science*, *19*, 43-75.
- Kocurek, G., and J. Nielson (1986), Conditions favourable for the formation of warm-climate aeolian sand sheets, *Sedimentology*, *33*, 795-816.
- Kolla, V. H. W. Posamentier, and L. J. Wood (2007), Deep-water and fluvial sinuous channels – Characteristics, similarities and dissimilarities, and modes of formation,

Marine and Petroleum Geology, 24, 388-405.

Komatsu, G., P. E. Geissler, R. G. Strom, and R. B. Singer (1993), Stratigraphy and erosional landforms of layered deposits in Valles Marineris, Mars, *Journal of Geophysical Research*, 98, 11105-11121.

Komatsu, G., G. G. Ori, P. Ciarcelluti, Y. D. Litasov (2004), Interior layered deposits of Valles Marineris, Mars: analogous subice volcanism related to Baikal Rifting, Southern Siberia, *Planetary and Space Science*, 52, 167-187.

Konyukhov, A. I. (2009), Geological structure, sedimentation conditions, and petroleum potential of sedimentary basins in Southeast Asia, *Lithology and Mineral Resources*, 44, 427-440.

Kraal, E. R., E. Asphaug, J. M. Moore, A. Howard, A. Brecht (2008a), Catalogue of large alluvial fans in Martian impact craters, *Icarus*, 194, 101-110.

Kraal, E. R., M. van Dijk, G. Postma, M. G. Kleinhans (2008b), Martian stepped-delta formation by rapid water release, *Nature*, 451, 973-976.

Labourdet, R. (2007), Integrated three-dimensional modeling approach of stacked turbidite channels, *AAPG Bulletin*, 91, 1603-1618, doi: 10.1306/06210706143.

Lajeunesse, E., C. Quantin, P. Allemand, and C. Delacourt (2006), New insights on the runout of large landslides in the Valles-Marineris canyons, Mars, *Geophysical Research Letters*, 33, L04403.

Lane-Serff, G. F., L. M. Beal, and T. D. Hadfield (1995), Gravity current flow over obstacles, *Journal of Fluid Mechanics*, 292, 39-53

Langford, R. P. (1989), Fluvial-aeolian interactions part 1, modern systems, *Sedimentology*, 36, 1023-1035.

- Langford, R., and B. Bracken (1987), Medano Creek, Colorado, a model for upper flow-regime fluvial deposition, *Journal of Sedimentary Petrology*, 57, 863-870.
- Lawson, D. E. (1983), Erosion of perennially frozen streambanks, US Army Corps of Engineers, Cold Regions Research & Engineering Laboratory, CRREL Report 83-29.
- Leclair, S. F. (2002), Preservation of cross-strata due to the migration of subaqueous dunes: an experimental investigation, *Sedimentology*, 49, 1157-1180.
- Leeder, M. R. (1999), *Sedimentology and Sedimentary Basins*, Blackwell, Oxford, 592 pp.
- Lewis, K. W., and O. Aharonson (2006), Stratigraphic analysis of the distributary fan in Eberswalde crater using stereo imagery, *Journal of Geophysical Research*, 111, doi:10.1029/2005JE002558.
- Lewis, K. W., O. Aharonson, J. P. Grotzinger, R. L. Kirk, A. S. McEwen, and T. A. Suer (2008a), Quasi-periodic bedding in the sedimentary rock record of Mars, *Science*, 322, 1532-1535.
- Lewis, K. W., O. Aharonson, J. P. Grotzinger, S. W. Squyres (2008b), Structure and stratigraphy of Home Plate from the Spirit Mars Exploration Rover, *Journal of Geophysical Research*, 113, E12S36, doi:10.1029/2007JE003025.
- Link, M. H. (2003), Depositional systems and sedimentary facies of the Miocene-Pliocene Ridge Basin Group, Ridge Basin, southern California, in *Evolution of Ridge Basin, Southern California*, edited by J. C. Crowell, The Geological Society of America, Boulder, Colorado, 17-87.
- Lowe, D. R. (1975), Water escape structures in coarse-grained sediments, *Sedimentology*, 22, 157-204.

- Lozinsky, R. P. (1994), Cenozoic stratigraphy, sandstone petrology, and depositional history of the Albuquerque Basin, central New Mexico, in *Basins of the Rio Grande Rift: Structure, Stratigraphy, and Tectonic Setting*, edited by G. R. Keller and S. M. Cather, GSA, Boulder, 73-81.
- Lucchitta, B. K. (1978), A large landslide on Mars, *GSA Bulletin*, 89, 1601-1609.
- Lucchitta, B. K. (1979), Landslides in Valles Marineris, Mars, *Journal of Geophysical Research*, 84, 8097-8113.
- Lucchitta, B. K. (1987), Valles Marineris, Mars: Wet debris flows and ground ice, *Icarus*, 72, 411-429.
- Lucchitta, B. K. (1990), Young volcanic deposits in the Valles Marineris, Mars? *Icarus*, 86(2), 476-509.
- Lucchitta, B. K., A. S. McEwen, G. D. Clow, P. E. Geissler, R. B. Singer, R. A. Schultz, and S. W. Squyres (1992), The canyon system on Mars, in *Mars*, edited by H. H. Kieffer, B. M. Jakosky, C. W. Snyder, and M. Matthews, Tucson, University of Arizona Press, 453-492.
- Lucchitta, B. K., N. K. Isbell, and A. Howington-Kraus (1994), Topography of Vallis Marineris: Implications for erosional and structural history, *Journal of Geophysical Research*, 99, 3783-3798.
- Lucchitta, B. K. (1999), Geologic map of Ophir and central Candor Chasmata (MTM-05072) of Mars, U.S. Geological Survey Investment Series, I-2568, Denver, USGS Information Services.
- Lucchitta, B. K. (2008), HiRISE images of layered deposits in west Candor Chasma, Mars (II): Unconformities and possible gravity tectonics, *Lunar and Planetary Science*

XXXIX, League City, TX, 2317.

Lucente, C. C., and G. A. Pini, (2003), Anatomy and emplacement mechanism of a large submarine landslide within a Miocene foredeep in the northern Apennine, Italy: A field perspective. *American Journal of Science*, 303, 565-602.

Lucente, C. C., and G. A. Pini (2008), Basin-wide mass-wasting complexes as markers of the Oligo-Miocene foredeep-accretionary wedge evolution in the Northern Apennines, Italy. *Basin Research*, 20, 49-71, doi: 10.1111/j.1365-2117.2007.00344.x.

MacNaughton, R. B., R. W. Dalrymple, G. M. Narbonne (1997), Early Cambrian braid-delta deposits, MacKenzie Mountains, north-western Canada, *Sedimentology*, 44, 587-609.

Malin, M. C., and K. S. Edgett (2000), Sedimentary rocks of early Mars, *Science*, 290, 1927-1937.

Malin, M. C., and K. S. Edgett (2001), Mars Global Surveyor Mars Orbiter Camera: Interplanetary cruise through primary mission, *Journal of Geophysical Research*, 106, 23429-23570.

Malin, M. C., and K. S. Edgett (2003), Evidence for persistent flow and aqueous sedimentation on early Mars, *Science*, 302, 1931-1934.

Malin, M. C., G. E. Danielson, A. P. Ingersoll, H. Masursky, J. Veverka, M. A. Ravine, and T. A. Soulanille (1992), The Mars Observer Camera, *Journal of Geophysical Research*, 97, 7699-7718.

Malin, M., K. S. Edgett, L. V. Posiolova, S. M. McColley, E. Z. N. Dobrea (2006), Present-day impact cratering rate and contemporary gully activity on Mars, *Science*, 314,

1573-1577.

- Malin, M., J. F. Bell, B. A. Cantor, M. A. Caplinger, W. M. Calvin, R. T. Clancy, K. S. Edgett, L. Edwards, R. M. Haberle, P. B. James, S. W. Lee, M. A. Ravine, P. C. Thomas, and M. J. Wolff (2007), Context Camera Investigation on board the Mars Reconnaissance Orbiter, *Journal of Geophysical Research*, *112*, E05S04, doi:10.1029/2006JE002808.
- Mallarino, G., R. T. Beaubouef, A. W. Droxler, V. Abreu, L. Labeyrie (2006), Sea level influence on the nature and timing of a minibasin sedimentary fill (northwestern slope of the Gulf of Mexico), *AAPG Bulletin*, *90*, 1089-1119.
- Mangold, N., C. Quantin, V. Ansan, C. Delacourt, P. Allemand (2004), Evidence for precipitation on Mars from dendritic valleys in the Valles Marineris area, *Science*, *305*, 78-81.
- Mangold, N., V. Ansan, P. Masson, C. Quantin, and G. Neukum (2008a), Geomorphic study of fluvial landforms on the northern Valles Marineris Plateau, Mars, *Journal of Geophysical Research*, *113*, E08009, doi:10.1029/2007JE002985.
- Mangold, N., A. Gendrin, B. Gondet, S. LeMouelic, C. Quantin, V. Ansan, J. P. Bibring, Y. Langevin, P. Masson, and G. Neukum (2008b), Spectral and geologic study of the sulfate-rich region of West Candor Chasma, Mars, *Icarus*, *194*, 519-543.
- McCollom, T. M., and B. M. Hynek (2005), A volcanic environment for bedrock diagenesis at Meridiani Planum on Mars, *Nature*, *438*, 1129-1131.
- McEwen, A. S. (1989), Mobility of large rock avalanches: Evidence from Valles Marineris, Mars, *Geology*, *17*, 1111-1114.
- McEwen, A. S., E. M. Eliason, J. W. Bergstrom, N. T. Bridges, C. J. Hansen, W. A.

- Delamere, J. A. Grant, V. G. Gulick, K. E. Herkenhoff, L. P. Keszthelyi, R. L. Kirk, M. T. Mellon, S. W. Squyres, N. Thomas, and C. M. Weitz (2007), Mars Reconnaissance Orbiter's High Resolution Imaging Science Experiment (HiRISE), *Journal of Geophysical Research*, *112*, E05S02, doi:10.1029/2005JE002605.
- McLennan, S. (2003), Sedimentary silica on Mars, *Geology*, *31*, 315-318.
- McLennan, S. M., and J. P. Grotzinger (2008), The sedimentary rock cycle of Mars, in *The Martian Surface: Composition, Mineralogy, and Physical Properties*, edited by J. F. Bell, Cambridge University Press, 541-577.
- McLennan, S. M., J. F. Bell, W. M. Calvin, P. R. Christensen, B. C. Clark, P. A. De Souza, J. Farmer, W. H. Farrand, D. A. Fike, R. Gellert, A. Ghosh, T. D. Glotch, J. P. Grotzinger, B. Hahn, K. E. Herkenhoff, J. A. Hurowitz, J. R. Johnson, S. S. Johnson, B. Jolliff, G. Klingelhöfer, A. H. Knoll, Z. Learner, M. C. Malin, H. Y. McSween, J. Pockock, S. W. Ruff, L. A. Soderblom, S. W. Squyres, N. J. Tosca, W. A. Watters, M. B. Wyatt, and A. Yen (2005), Provenance and diagenesis of the evaporite-bearing Burns formation, Meridiani Planum, Mars, *Earth and Planetary Science Letters*, *240*, 95-121.
- Mege, D., and P. Masson (1996), Amounts of crustal stretching in Valles Marineris, Mars, *Planetary and Space Science*, *44*, 749-782.
- Melosh, H. J. (1989), *Impact Cratering: A Geologic Process*, Oxford Monographs on Geology and Geophysics, Oxford University Press, New York, 245 p.
- Metz, J. M., J. P. Grotzinger, D. M. Rubin, K. W. Lewis, S. W. Squyres, J. F. Bell (2009a), Sulfate-rich eolian and wet interdune deposits, Erebus crater, Meridiani Planum, Mars, *Journal of Sedimentary Research*, *79*, 247-264.

- Metz, J. M., J. P. Grotzinger, D. Mohrig, A. McEwen, C. Weitz, C. Pirmez, B. Prather (2009b), Sublacustrine depositional fans in Melas Chasma, *Journal of Geophysical Research* 114, E10002, doi:10.1029/2009JE003365.
- Miall, A. D. (1992), Alluvial deposits, in *Facies Models: Geological Society of Canada*, edited by R. G. Walker, and N. P. James, St. John's, 119-142.
- Middleton, G. V. (1993), Sediment deposition from turbidity currents, *Annual Reviews of Earth and Planetary Science*, 21, 89-114.
- Milliken, R. E., J. Grotzinger, R. A. Beyer, S. Murchie, and A. McEwen (2007), Evidence for salt tectonics in Valles Marineris, Mars, Seventh International Conference on Mars, Pasadena, CA.
- Milliken, R. E., G. A. Swayze, R. E. Arvidson, J. L. Bishop, R. N. Clark, B. L. Ehlmann, R. O. Green, J. P. Grotzinger, R. V. Morris, S. L. Murchie, J. F. Mustard, C. M. Weitz (2008), Opaline silica in young deposits on Mars, *Geology*, 36, 847-850.
- Mohindra, R., and T. N. Bagati (1996), Seismically induced soft-sediment deformation structures (seismites) around Sumdo in the lower Spiti valley (Tethys Himalaya), *Sedimentary Geology*, 101, 69-83.
- Mohindra, R., and V. C. Thakur (1998), Historic large earthquake-induced soft sediment deformation features in the Sub-Himalayan Doon valley, *Geology Magazine*, 135, 269-281.
- Montenat, C., P. Barrier, P. Ott d'Estevou, and C. Hilbsch (2007), Seismites: An attempt at critical analysis and classification, *Sedimentary Geology*, 196, 5-30, doi:10.1016/j.sedgeo.2006.08.004.
- Montgomery, D. R., and A. Gillespie (2005), Formation of Martian outflow channels by

catastrophic dewatering of evaporite deposits, *Geology*, 33, 625-628.

Montgomery, D. R., M. Som, M. P. A. Jackson, B. C. Schreiber, A. R. Gillespie, J. B.

Adams (2009), Continental-scale salt tectonics on Mars and the origin of Valles Marineris and associated outflow channels, *GSA Bulletin*, 121, 117-133.

Moore, J. M., and A. D. Howard (2005), Large alluvial fans on Mars, *Journal of Geophysical Research*, 110, E04005.

Mountney, N. P., and B. D. Thompson (2002), Stratigraphic evolution and preservation of aeolian dune and damp/wet interdune strata: an example from the Triassic Helsby Sandstone Formation, Cheshire Basin, UK, *Sedimentology*, 49, 805-833.

Murchie, S., R. Arvidson, P. Bedini, K. Beisser, J. P. Bibring, J. L. Bishop, J. Boldt, P. Cavender, T. Choo, R. T. Clancy, E. H. Darlington, D. J. Des Marais, R. Espiritu, D. Fort, R. Green, E. Guinness, J. Hayes, C. Hash, K. Heffernan, J. Hemmler, G. Heyler, D. Humm, J. Hutcheson, N. Izenberg, R. Lee, J. Lees, D. Lohr, E. Malaret, T. C. Martin, J. A. McGovern, P. McGuire, R. Morris, J. Mustard, S. M. Pelkey, E. Rhodes, M. Robinsson, T. L. Roush, E. Schaefer, G. Seagrave, F. Seelos, P. Silvergate, S. Slavney, M. Smith, W. -J. Shyoong, K. Strobehn, H. Taylor, P. Thompson, B. Tossman, M. Wirzburger, and M. Wolff (2007), Compact Reconnaissance Imaging Spectrometer for Mars (CRISM) on Mars Reconnaissance Orbiter (MRO), *Journal of Geophysical Research*, 112, E05S03, doi:10.1029/2006JE002682.

Murchie, S. L., J. F. Mustard, B. L. Ehlmann, R. E. Milliken, J. L. Bishop, N. K. McKeown, E. Z. N. Dobreá, F. P. Seelos, D. L. Buczkowski, S. M. Wiseman, R. E. Arvidson, J. J. Wray, G. Swayze, R. N. Clark, D. J. D. Marais, A. S. McEwen, and

- J. -P. Bibring (2009), A synthesis of Martian aqueous mineralogy after 1 Mars year of observations from the Mars Reconnaissance Orbiter, *Journal of Geophysical Research*, *114*, E00D06, doi:10.1029/2009JE003342.
- Mustard, J. F., C. D. Cooper, and M. K. Rifkin (2001), Evidence for recent climate change on Mars from the identification of youthful near-surface ground ice, *Nature*, *412*, 411-414.
- Mustard, J., S. L. Murchie, S. M. Pelkey, B. L. Ehlmann, R. E. Milliken, J. A. Grant, J. -P. Bibring, F. Poulet, J. Bishop, E. N. Dobreá, L. Roach, F. Seelos, R. E. Arvidson, S. Wiseman, R. Green, C. Hash, D. Humm, E. Malaret, J. A. McGovern, K. Seelos, T. Clancy, R. Clark, D. D. Marais, N. Izenberg, A. Knudson, Y. Langevin, T. Martin, P. McGuire, R. Morris, M. Robinson, T. Roush, M. Smith, G. Swayze, H. Taylor, T. Titus, and M. Wolff (2008), Hydrated silicate minerals on Mars observed by the Mars Reconnaissance Orbiter CRISM instrument, *Nature*, *454*, 305-309, doi:10.1038/nature07097.
- Mutti, E., R. Tinterri, G. Benevelli, D. di Biase, G. Cavanna (2003), Deltaic, mixed and turbidite sedimentation of ancient foreland basins, *Marine and Petroleum Geology*, *20*, 733-755.
- Nedell, S. S., S. W. Squyres, and D. W. Anderson (1987), Origin and evolution of the layered deposits in the Valles Marineris, Mars, *Icarus*, *70*, 409-441.
- Nelson, C. H., D. C. Twitchell, W. C. Schwab, H. J. Lee, N. H. Kenyon (1992), Upper Pleistocene turbidite sand beds and chaotic silt beds in the channelized, distal, outer fan lobes of the Mississippi fan, *Geology*, *20*, 693-696.
- Nelson, C. H., E. B. Karabanov, S. M. E. Colman (1999), Tectonic and sediment supply

- control of deep rift lake turbidite systems: Lake Baikal, Russia, *Geology*, 27, 163-166.
- Neuffer, D. P., and R. A. Schultz (2006), Mechanisms of slope failure in Valles Marineris, Mars. *Quarterly Journal of Engineering Geology & Hydrogeology*, 39, 227-240.
- Normark, W. R., and F. H. Dickson (1976a), Sublacustrine fan morphology in Lake Superior, *AAPG Bulletin*, 60, 1021-1036.
- Normark, W. R., and F. H. Dickson (1976b), Man-made turbidity currents in Lake Superior, *Sedimentology*, 23, 815-831.
- Obermeier, S. F. (1996), Use of liquefaction-induced features for paleoseismic analysis - An overview of how seismic liquefaction features can be distinguished from other features and how their regional distribution and properties of source sediment can be used to infer the location and strength of Holocene paleo-earthquakes, *Engineering Geology*, 44, 1-76.
- Okubo, C. H., K. W. Lewis, A. McEwen, R. L. Kirk (2008), Relative age of interior layered deposits in southwest Candor Chasma based on high-resolution structural mapping, *Journal of Geophysical Research*, 113, E12002, doi:10.1029/2008JE003181.
- Okubo, C. H., 2010, Structural geology of Amazonian-aged layered sedimentary deposits in southwest Candor Chasma, Mars, *Icarus*, doi: 10.1016/j.icarus.2009.11.012.
- Olariu, C., and J. P. Bhattacharya (2006), Terminal distributary channels and delta front architecture of river-dominated delta systems, *Journal of Sedimentary Research*, 76, 212-233.
- O'Neill, C., A. M. Jellinek, and A. Lenardic (2007), Conditions for the onset of plate

tectonics on terrestrial planets and moons, *Earth and Planetary Science Letters*, 261, 20-32.

Orange, D. L., J. Decker, P. A. Teas, R. D. Schneider, A. H. Saller, A. Heffernan, N. Maher, and M. Levey (2006), A modern basin-floor fan imaged in the Makassar Straits, Indonesia: Insights from high-resolution multibeam bathymetry and backscatter, sub-bottom profiler data and USBL-navigated cores, AAPG Annual Convention, Houston TX., April 9-12, 2006.

Parker, G., C. Paola, K. X. Whipple, D. Mohrig (1998), Alluvial fans formed by channelized fluvial and sheet flow. I: Theory, *Journal of Hydraulic Engineering-Asce*, 124, 985-995.

Parker, G., and O. Sequeiros (2006), Large scale river morphodynamics: Application to the Mississippi Delta, in *RiverFlow 2006 Conference*, edited by R. M. L. Ferreria, Lisbon, Taylor and Francis, New York, 1067–1076.

Pattison, S. A. J. (2005), Storm-influenced prodelta turbidite complex in the lower Kenilworth Member at Hatch Mesa, Book Cliffs, Utah, USA: Implications for shallow marine facies models, *Journal of Sedimentary Research*, 75, 420-439.

Pelkey, S. M., and B. M. Jakosky (2002), Surficial geologic surveys of Gale crater and Melas Chasma, Mars: integration of remote-sensing data, *Icarus*, 160, 228-257.

Pelkey, S. M., B. M. Jakosky, P. R. Christensen (2003), Surficial properties in Melas Chasma, Mars, from Mars Odyssey THEMIS data, *Icarus*, 165, 68-89.

Pelkey, S. M., J. F. Mustard, S. Murchie, R. T. Clancy, M. Wolff, M. Smith, R. E. Milliken, J. P. Bibring, A. Gendrin, F. Poulet, Y. Langevin, and B. Gondet (2007), CRISM multispectral summary products: Parameterizing mineral diversity on Mars

- from reflectance, *Journal of Geophysical Research*, *112*, E08S14, doi:10.1029/2006JE002831.
- Pelletier, J. D., K. J. Kolb, A. S. McEwen, R. L. Kirk (2008), Recent bright gully deposits on Mars: Wet or dry flow? *Geology*, *36*, 211-214.
- Peulvast, J. P., and P. L. Masson (1993), Melas Chasma: Morphology and tectonic patterns in central Valles Marineris (Mars), *Earth, Moon, and Planets*, *61*, 219-248.
- Peulvast, J. P., D. Mege, J. Chiciak, F. Costard, P. Masson (2001), Morphology, evolution and tectonics of Valles Marineris wall slopes (Mars), *Geomorphology*, *37*, 329–352.
- Pickering, K. T. et al. (1986), A high-sinuosity, laterally migrating submarine fan channel-levee-overbank: Results from DSDP Leg 96 on the Mississippi Fan, Gulf of Mexico, *Marine and Petroleum Geology*, *3*, 3-18.
- Plint, A. G., and J. A. Wadsworth (2003), Sedimentology and palaeogeomorphology of four large valley systems incising delta plains, western Canada Foreland Basin: implications for mid-Cretaceous sea-level changes, *Sedimentology*, *50*, 1147-1186.
- Pope, M. C., J. F. Read, R. Bambach, and H. J. Hofmann (1997), Late Middle to Late Ordovician seismites of Kentucky, southwest Ohio and Virginia: Sedimentary recorders of earthquakes in the Appalachian basin, *GSA Bulletin*, *109*, 489-503.
- Quantin, C., P. Allemand, and C. Delacourt (2004), Morphology and geometry of Valles Marineris landslides, *Planetary and Space Science*, *52*, 1011-1022.
- Quantin, C., P. Allemand, N. Mangold, G. Dromart, C. Delacourt (2005), Fluvial and lacustrine activity on layered deposits in Melas Chasma, Valles Marineris, Mars, *Journal of Geophysical Research*, *110*, E12S19, doi:10.1029/2005JE002440.

- Roach, L. H., J. F. Mustard, S. L. Murchie, J. -P. Bibring, F. Forget, K. W. Lewis, O. Aharonson, M. Vincendon, and J. L. Bishop (2009a), Testing evidence of recent hydration state change in sulfates on Mars, *Journal of Geophysical Research*, *114*, doi:10.1029/2008JE003245.
- Roach, L. H., J. F. Mustard, G. A. Swayze, R. E. Milliken, J. L. Bishop, S. L. Murchie, and K. Lichtenberg (2009b), Hydrated mineral stratigraphy of Ius Chasma, Valles Marineris, *Icarus*, doi:10.1016/j.icarus.2009.09.003.
- Robert, G., J. K. Russell, and D. Giordano (2008), Rheology of porous volcanic materials: High-temperature experimentation under controlled water pressure, *Chemical Geology*, *256*, 216-230.
- Rodriguez, J. A. P., J. S. Kargel, D. A. Crown, L. F. Bleamaster, K. L. Tanaka, V. R. Baker, H. Miyamoto, J. M. Dohm, S. Sasaki, G. Komatsu (2006), Headward growth of chasmata by volatile outbursts, collapse, and drainage; Evidence from Ganges chaos, Mars, *Geophysical Research Letters*, *33*, L18203, doi:10.1029/2006GL026275.
- Rodríguez-Pascua, M. A., J. P. Calvo, G. De Vicente, and D. Gómez-Gras (2000), Soft-sediment deformation structures interpreted as seismites in lacustrine sediments of the Prebetic Zone, SE Spain, and their potential use and indicators of earthquake magnitudes during Late Miocene, *Sedimentary Geology*, *135*, 117-135.
- Røe, S. -L. (1987), Cross-strata and bedforms of probable transitional dune to upper-stage plane-bed origin from a Late Precambrian fluvial sandstone, northern Norway, *Sedimentology*, *34*, 89-101.
- Roep, T. B., and A. J. Everts (1992), Pillow-beds: a new type of seismites? An example

- from an Oligocene turbidite fan complex, Alicante, Spain, *Sedimentology*, 39, 711-72.
- Rothman, D. H., J. Grotzinger, P. B. Flemings (1994), Scaling in Turbidite Deposition, *Journal of Sedimentary Research*, A64, 59-67.
- Rowan, M. G., F. J. Peel, and B. C. Vendeville (2004), Gravity-driven fold belts on passive margins, in *Thrust Tectonics and Hydrocarbon Systems*, edited by K. R. McClay, AAPG Memoir 82, 157-182.
- Rubin, D. (1987), *Cross-Bedding, Bedforms, and Paleocurrents*, SEPM, Concepts in sedimentology and paleontology, 1, 187 p.
- Rubin, D. M., and R. E. Hunter (1982), Bedform climbing in theory and nature, *Sedimentology*, 29, 121-138.
- Sadler, P. M. (1981), Sediment accumulation rates and the completeness of stratigraphic sections, *Journal of Geology*, 89, 569-584.
- Scherer, C. M. S., and E. L. C. Lavina (2005), Sedimentary cycles and facies architecture of aeolian-fluvial strata of the Upper Jurassic Guara Formation, southern Brazil, *Sedimentology*, 52, 1323-1341.
- Scholz, C. A., and B. R. Rosendahl (1990), Coarse-clastic facies and stratigraphic sequence models from Lakes Malawi and Tanganyika, East Africa, in *Lacustrine Basin Exploration: Case Studies and Modern Analogs*, Memoir 50, edited by B. J. Katz, American Association of Petroleum Geologists, Tulsa, 151-168.
- Schwartz, R. K. (1982), Bedform and stratigraphic characteristics of some modern small-scale washover sand bodies, *Sedimentology*, 29, 835-849.
- Schultz, R. A. (1998), Multiple-process origin of Valles Marineris basins and troughs,

- Mars, *Planetary and Space Science*, 46, 827-834.
- Schultz-Ela, D. D. (2001), Excursus on gravity gliding and gravity spreading, *Journal of Structural Geology*, 23, 725-731.
- Schumm, S. A. (1963), Sinuosity of alluvial rivers on the Great Plains, *GSA Bulletin*, 74, 1089-1099.
- Schumm, S. A. (1977), *The Fluvial System*, John Wiley and Sons, Inc., New York.
- Schwab, W. C., H. J. Lee, D. C. Twitchell, J. Locat, C. H. Nelson, W. G. McArthur, N. H. Kenyon (1996), Sediment mass-flow processes on a depositional lobe, outer Mississippi fan, *Journal of Sedimentary Research*, 66, 916-927.
- Scott, D. H., and K. L. Tanaka (1986), Geologic map of the western equatorial region of Mars, USGS, Reston VA.
- Seilacher, A. (1969), Fault-graded beds interpreted as seismites, *Sedimentology*, 13, 155-159.
- Sharp, R. P. (1973), Mars: Fretted and chaotic terrains, *Journal of Geophysical Research*, 78, 4073-4083.
- Shaw, J. (1972), Sedimentation in the ice-contact environment, with examples from Shropshire (England), *Sedimentology*, 18, 23-62.
- Simms, M. J. (2003), Uniquely extensive seismite from the latest Triassic of the United Kingdom: Evidence for bolide impact? *Geology*, 31, 557-560.
- Sims, J. D. (1975), Determining earthquake recurrence intervals from deformational structures in young lacustrine sediments, *Tectonophysics*, 29, 141-152.
- Skilling, I. P., M. G. Chapman, and B. K. Lucchitta (2002), Young, blocky flows in east Ius/west Melas and west Candor Chasmata, Mars: Debris avalanche deposits

derived from interior layered deposits (ILD) mounds? Lunar and Planetary Science Conference XXXIII: League City, Texas, 1361.

- Slingerland, R.L., and N. D. Smith (2004), River avulsions and their deposits, *Annual Reviews of Earth and Planetary Science* 32, 257–285, doi:10.1146/annurev.earth.32.101802.120201.
- Sohn, Y. K., C. W. Rhee, and B. C. Kim (1999), Debris flow and hyperconcentrated flood-flow deposits in an alluvial fan, northwestern part of the Cretaceous Yongdong Basin, central Korea, *Journal of Geology*, 107, 111-132.
- Sowe, M., E. Hauber, R. Jaumann, K. Gwinner, F. Fueten, R. Stesky and G. Neukum (2007), Interior layered deposits in the eastern Valles Marineris and chaotic terrains on Mars, Lunar and Planetary Science Conference XXXVIII, Abstract 1568, League City, TX.
- Soukhovitskaya, V. and M. Manga (2006), Martian landslides in Valles Marineris: Wet or dry? *Icarus*, 180, 348–352.
- Smith, D. E., M. T. Zuber, H. V. Frey, J. B. Garvin, J. W. Head, D. O. Muhleman, G. H. Pettengill, R. J. Phillips, S. C. Solomon, H. J. Zwally, W. B. Banerdt, T. C. Duxbury, M. P. Golombek, F. G. Lemoine, G. A. Neumann, D. D. Rowlands, O. Aharonson, P. G. Ford, A. B. Ivanov, C. L. Johnson, P. J. McGovern, J. B. Abshire, R. S. Afzal, and X. Sun (2001), Mars Orbiter Laser Altimeter: Experiment summary after the first year of global mapping of Mars, *Journal of Geophysical Research*, 106, 23689-23722.
- Spencer, J. R., and F. P. Fanale (1990), New models for the origin of Valles Marineris closed depressions, *Journal of Geophysical Research*, 95, 14301-14313.

- Squyres, S. W., R. E. Arvidson, E. T. Baumgartner, J. F. Bell, P. R. Christensen, S. Gorevan, K. E. Herkenhoff, G. Klingelhofer, M. B. Madsen, R. V. Morris, R. Rieder, and R. A. Romero (2003), Athena Mars rover science investigation, *Journal of Geophysical Research*, *108*, E12, doi:10.1029/2003JE002121.
- Squyres, S. W., J. P. Grotzinger, R. E. Arvidson, J. F. Bell, C. W. Calvin, P. R. Christensen, B. C. Clark, J. A. Crisp, W. H. Farrand, K. E. Herkenhoff, J. R. Johnson, G. Klingelhöfer, A. H. Knoll, S. M. McLennan, H. Y. McSween, R. Morris, J. W. Rice, R. Rieder, and L. A. Soderblom (2004), In situ evidence for an ancient aqueous environment at Meridiani Planum, Mars, *Science*, *306*, 1709-1714.
- Squyres, S. W., A. H. Knoll, R. E. Arvidson, B. C. Clark, J. P. Grotzinger, B. L. Jolliff, S. M. McLennan, N. J. Tosca, J. F. Bell, W. M. Calvin, W. H. Farrand, T. D. Glotch, M. P. Golombek, K. E. Herkenhoff, J. R. Johnson, G. Klingelhöfer, H. Y. McSween, and A. S. Yen (2006), Two years at Meridiani Planum: Results from the Opportunity Rover, *Science*, *313*, 1403-1407.
- Squyres, S., O. Aharonson, B. Clark, B. A. Cohen, L. Crumpler, P. A. De Souza, W. H. Farrand, R. Gellert, J. Grant, J. P. Grotzinger, A. F. Haldemann, J. R. Johnson, G. Klingelhöfer, K. Lewis, R. Li, T. McCoy, A. S. McEwen, H. Y. McSween, D. W. Ming, J. M. Moore, R. V. Morris, T. J. Parker, J. W. Rice, S. W. Ruff, M. Schmidt, C. Schröder, L. A. Soderblom and A. Yen (2007), Pyroclastic activity at Home Plate in Gusev Crater, Mars, *Science*, *316*, 738-742.
- Stanistreet, I. G., T. S. McCarthy (1993), The Okavango Fan and the classification of subaerial fan systems, *Sedimentary Geology*, *85*, 115-133.
- Stolper, D., M. Kennedy, and J. Grotzinger (2007), Scale of lamination in sedimentary

rocks as a guide to depositional process on Mars (Abstract), Geological Society of America.

- Straub, K. M., D. Mohrig, B. McElroy, J. Buttles, and C. Pirmez (2008), Interactions between turbidity currents and topography in aggrading sinuous submarine channels: A laboratory study, *GSA Bulletin*, 120, 368-385, doi: 10.1130/B25983.1.
- Torres, J., L. Droz, B. Savoye, E. Terentieva, P. Cochonat, N. H. Kenyon, and M. Canals (1997), Deep-sea avulsion and morphosedimentary evolution of the Rhine Fan Valley and Neofan during the Late Quaternary (north-western Mediterranean Sea), *Sedimentology*, 44, 457-477.
- Tosca, N. J., S. M. McLennan, B. C. Clark, J. P. Grotzinger, J. A. Hurowitz, A. H. Knoll, C. Schröder, and S. W. Squyres (2005), Geochemical modeling of evaporation processes on Mars: Insight from the sedimentary record at Meridiani Planum, *Earth and Planetary Science Letters*, 240, 122-148.
- Tosca, N., A. Knoll, A., and S. McLennan (2008a), Water activity and the challenge for life on early Mars, *Science*, 320, 1204-1207.
- Tosca, N. J., R. E. Milliken, M. B. Wyatt, and S. M. McLennan (2008b), Clay minerals and poorly crystalline silicates: Unraveling paleo-acidity at the Martian surface, Lunar and Planetary Science Conference XXXIX: League City, TX.
- Trimble, S. W. (1981), Changes in sediment storage in the Coon Creek Basin, Driftless Area, Wisconsin, *Science*, 214, 181-183.
- Twitchell, D. C., W. C. Schwab, N. H. Nelson, N. H. Kenyon, H. J. Lee (1992), Characteristics of a sandy depositional lobe on the outer Mississippi Fan from SeaMARC 1A sidescan sonar images, *Geology*, 20, 689-692.

- van der Werff, W., and S. D. Johnson (2003), Deep-sea fan pinch-out geometries and their relationship to fan architecture, Tanqua Karoo basin (South Africa), *International Journal of Earth Sciences*, 92, 728-742.
- Viseras, C., M. L. Calvache, J. M. Soria, J. Fernández (2003), Differential features of alluvial fans controlled by tectonic or eustatic accommodation space. Examples from the Beltic Cordillera, Spain., *Geomorphology*, 50, 181-202.
- Walker, R. G. (1992), Turbidites and Submarine Fans, in *Facies Models: Response to Sea Level Change*, edited by R. G. Walker and N. P. James, Geological Association of Canada, Ontario, 239-263.
- Walling, D. E., P. N. Owens, G. J. L. Leeks (1999), Rates of contemporary overbank sedimentation and sediment storage on the floodplains of the main channel systems of the Yorkshire Ouse and River Tweed, UK, *Hydrological Processes*, 13, 993-1009.
- Wellner, R., R. T. Beaubouef, J. C. Van Wagoner, H. Roberts, T. Sun (2005) Jet-plume depositional bodies - the primary building blocks of Wax Lake Delta, *Gulf Coast Association of Geological Societies Transactions*, 55, 867-909.
- Weitz, C. M., T. J. Parker, F. S. Anderson, and J. A. Grant (2001), The interior layered deposits of Valles Marineris: Layering, erosional processes, and age relationships, Lunar and Planetary Science Conference XXXII, Abstract 1629, League City, TX.
- Weitz, C. M., T. J. Parker, M. H. Bulmer, F. S. Anderson, and J. A. Grant (2003), Geology of the Melas Chasma landing site for the Mars Exploration Rover mission, *Journal of Geophysical Research*, 108, 8082, doi:10.1029/2002JE002022.
- Weitz, C., R. E. Milliken, J. A. Grant, A. S. McEwen, R. M. E. Williams, J. L. Bishop,

- and B.J. Thompson (2009) Mars Reconnaissance Orbiter observations of light-toned layered deposits and associated fluvial landforms on the plateaus adjacent to Valles Marineris, *Icarus*, 205, 73-102, doi: 10.1016/j.icarus.2009.04.017
- Wells, S. G., and A. M. Harvey (1987), Sedimentologic and geomorphic variations in storm-generated alluvial fans, Howgill Fells, northwest England, *GSA Bulletin*, 98, 182-198.
- Whipple, K. X., and T. S. Dunne (1992), The influence of debris-flow rheology on fan morphology, Owens Valley, California, *GSA Bulletin*, 104, 887-900.
- Williams, G. E. (1971), Flood deposits of the sand-bed ephemeral streams of central Australia, *Sedimentology*, 17, 1-40.
- Williams-Stroud, S. C., and J. Paul (1997), Initiation and growth of gypsum piercement structures in the Zechstein Basin, *Journal of Structural Geology*, 19, 897-907.
- Winston, D. (1978), Fluvial systems of the Precambrian Belt Supergroup, Montana and Idaho, U.S.A., in *Fluvial Sedimentology*, edited by A. D. Miall, Canadian Society of Petroleum Geologists Memoir 5, 343-359.
- Witbeck, N. E., K. L. Tanaka, and D. H. Scott (1991), *Geologic Map of Valles Marineris Region, Mars, MAP I-2010*, U. S. Geological Survey, Reston, VA.
- Wohletz, K. H., and M. F. Sheridan (1979), Model of pyroclastic surge, Geological Society of America Special Paper, 180, 177-194.
- Wood, L. J. (2006), Quantitative geomorphology of the Mars Eberswalde delta, *GSA Bulletin*, 118, 557-566.
- Wynn, R. B., B. T. Cronin, J. Peakall (2007), Sinuous deep-water channels: Genesis, geometry and architecture, *Marine and Petroleum Geology*, 24, 341-387.

- Yu, B., A. Cantelli, J. G. Marr, C. Pirmez, C. O'Byrne, G. Parker (2006), Experiments on self-channelized subaqueous fans emplaced by turbidity currents and dilute mudflows, *Journal of Sedimentary Research*, 76, 889-902.
- Zegers, T. E., W. Dabekaussen, E. Hauber, K. Gwinner, F. Scholten, F. Fueten, R. Stesky, P. MacKinnon, G. Neukum, and H. C. -I. Team (2006), 3D Structural analysis of Ophir Chasma based on HRSC data and stereo-derived DTM, Lunar and Planetary Science Conference XXXVII, Abstract 1605, League City, TX.